Analysis of Carrier Dynamics in Photocatalytic Materials Using Ultrafast Spectroscopy

(超高速分光法をもちいた光触媒材料内のキャリアダイナミクスの解析)

Fumihiko Ichihara

Graduate School of Chemical Sciences and Engineering

Hokkaido University

2020

Abstract

Photocatalytic hydrogen evolution and carbon dioxide reduction using photocatalysts are expected as promising technologies for the realization of a sustainable society. However, high efficiency and stability under sunlight is required to fulfill the industrial demand. There are various approaches to improve photocatalytic activity, such as element doping, surface structure modification, implanting defect sites on the surface, using a photosensitizer, and loading of a cocatalyst as an active site. Since the mechanism of activity improvement has not been elucidated, it is not easy to obtain a guideline for developing new materials. Photocatalytic reaction is driven by photo-generated electron hole pairs. Thus, understanding the reaction mechanism and the carrier dynamics right after light irradiation in photocatalytic materials by using ultra-fast spectroscopy is highly desired. In this study, transient absorption spectroscopy was applied to evaluate the effect of dopants in oxide based photocatalyst and the interaction between cocatalysts and inorganic, and organic photocatalytic materials. This dissertation is composed of 6 chapters, including introduction and conclusions.

In Chapter 2, the configuration of the transient absorption spectroscopy used in this study was described, and the conventional fitting method of the transient decay curve and the fitting method adopted in this study were outlined.

Chapter 3 describes the doping effects over the carrier dynamics of La, Cr-doped $SrTiO_3$, which is a visible light responsive photocatalyst. Element doping is a method often used for making a wide gap semiconductor visible light responsive, and is a method of forming an impurity level between bands and promoting light excitation using visible light. Indeed, doping can make photocatalyst visible light responsive and shows photocatalytic activity under visible light. However, the doped photocatalyst has lost the high photocatalytic activity under ultraviolet light, which originally possessed by wide-gap semiconductors. In order to clarify the mechanism of this problem, we selected La and Cr-doped $SrTiO_3$ as model materials, and measured the effects of La and Cr dopants using transient absorption spectroscopy. Based on the results, it can be inferred that La doping would extend the lifetime of photogenerated charge carriers due to the hybridization of La 5d band with conduction band of $SrTiO_3$ which could contribute to secure the excited electrons and thus increased total photocatalytic performance. Interestingly, after Cr doping, the transient feature of $SrTiO_3$ has been changed under UV light irradiation, which displayed less reactivity and lifetime, could account for decreasing the photocatalytic activity. Accordingly, in order to design a superior photocatalyst for effective solar energy harvesting, one should strive for enhancing the electron reactivity as well as retaining the excitation state of $SrTiO_3$.

Chapter 4 describes the carrier dynamics in $Pt/SrTiO_3$. Pt is a typical cocatalyst indispensable for improving photocatalytic hydrogen evolution activity. A cocatalyst represented by a noble metal element has a function of greatly reducing the overpotencial of hydrogen generation and a function as an active site. Therefore novel metal cocatalysts are an indispensable element for designing a highly active photocatalyst. Furthermore, loading cocatalysts are expected to improve charge separation ability. However,

theoretical calculations suggests that the broad density of states of Pt over rapping with conduction band and valence band of the wide gap semiconductors, and capturing electrons and holes from conduction band and valence band, respectively. In this study, to examine the loading effect of Pt cocatalysts, the transient absorption spectra were measured over different amount of Pt and Ni loaded $SrTiO_3$ as a comparison. Focusing on the transient signal derived by hole in the $SrTiO_3$, it is found that with the increase Pt cocatalyst loading amount, the decay constant which represent the speed of carrier consumption linearly increase. While in the case of Ni loading, the decay constant was almost constant. This linear relationship between Pt loading amount and decay constant suggests that Pt cocatalyst on $SrTiO_3$ capture both photogenerated electron and hole. Therefore, for the cocatalyst, the localized density of state and an appropriate hydrogen absorption/desorption energy property are highly desired for efficient overall water splitting.

Chapter 5 proposes the charge carriers transfer process of conjugate polymer photocatalysts for carbon dioxide reduction reaction. Monomers and polymers with similar structures were synthesized using Suzuki-Miyaura coupling and Sonogashira coupling, and their photocatalytic activity and carrier dynamics were evaluated. By measuring time-resolved microwave conductivity, it is found that in the polymer synthesized by the Sonogashira coupling reaction, electrons generated by photoexcitation are delocalized due to the alkyl bond between molecules. Whereas in the polymer synthesized by the Suzuki-Miyaura coupling, a single bond is formed between the molecules, the photoexcited electrons can be localized with in benzene part of the conjugate polymer. Also, in ps-ns transient absorption spectroscopy, photoexcited electrons can easily attract strong interaction with cocatalyst through a C-C single bond in the material, thus electron can easily transfer to the cocatalyst. On the other hand, conjugate polymer composed by alkyl bonds, the electron transfer is difficult between conjugate polymer and cocatalyst. Furthermore, the sample prepared using the Suzuki-Miyaura coupling has evaluated by using the time-resolved PL spectrometry. The results shows the greatly shorten of the PL lifetime with the presence of the cocatalyst and carbon dioxide, indicating that electrons generated in the conjugated polymer are consumed in the carbon dioxide reduction reaction. As described above, the charge transfer process during the reaction was proposed by observing the interaction with the cocatalyst due to the bonding state in the conjugated polymer semiconductor. This result suggests that different polymer materials composed of C-C single bond may be useful for carbon dioxide reduction reaction.

Chapter 6 summarizes the above works and give an outlook for the future. As described above, the carrier dynamics in a typical oxide photocatalyst has been discussed for searching further active photocatalysts. In the doping method, by observing charge carriers dynamics, the advantage and disadvantage of doping an element into the semiconductor has been clarified. In the cocatalyst loading, by tracing the trapping process of holes into the Pt cocatalyst, it is found that there is the trade-off relationship between active site of the reaction and recombination center. In addition, the mechanism of the carbon dioxide reduction reaction using a conjugate polymer has evaluated. The electrons transfer process were tracked by various types of ultra-fast spectroscopy to obtain guidelines for material design based on the state of intermolecular bonding.

Contents

Chapter 1 . Introduction

1.1 Overview of photocatalysis

In recent years, the increase in the use of fossil fuels due to modernization and population growth has provoked severe environmental problems, and the development of alternative energy has become an urgent task for the realization of a sustainable society. Among various alternative energy technologies, artificial photosynthesis using a photocatalyst is a promising technology that can convert water or CO_2 into storable chemical energy by solar energy. In recent decades, research on photocatalysts is steadily progressing in various fields such as water and air purification,[1] H_2 or O_2 generation by water decomposition,[2] CO_2 photoreduction,[3] N_2 fixation reaction,[4] and photoelectrochemical conversion.[5]

Despite photocatalysts can be used for various reactions, the intrinsic mechanism is identical. Generally, as shown in Figure 1.1, photocatalytic reactions consist of three steps.[6–8] First, when the incident light energy exceeds the bandgap of semiconductor photocatalyst, the electrons located in the valence band (VB) are excited to the conduction band (CB) with the equivalent amount of the positively charged holes left in the VB. Secondary, the photo-generated electron-hole pair migrates to the surface of the semiconductor photocatalyst. Finally, the holes in the valence band that reach the surface act as oxidizing agents (electron donor $D \rightarrow D^+$), and the electrons in the conduction band act as reliable reducing agents (electron acceptor $A \rightarrow A^+$). These cause redox reactions with adsorbed molecules such as water and organic substances on the semiconductor surface. Details of each step are given below for further understanding.

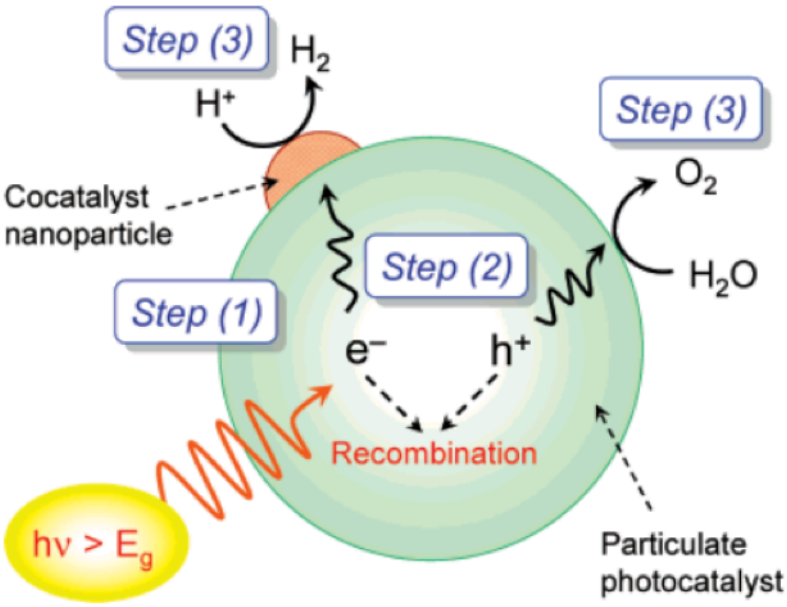

Figure 1.1. Schematic illustration of the basic mechanism of the semiconductor photocatalytic reaction process.[9]

First, the semiconductor photocatalyst absorbs light energy, which has higher energy than its bandgap and consequently generates photoexcited electron-hole pairs. In the initial stage, the irradiated light energy is stored in the semiconductor as photoexcited charge carriers. These photoexcited charge carriers are converted into chemical energy via a series of electronic processes and surface/interface reactions. From conventional thermal catalysis, spontaneous catalytic reaction (the photocatalytic reaction can drive $\Delta G<0$, ΔG means Gibbs free energy) as well as non-spontaneous catalysis ($\Delta G>0$) can be driven by photocatalysis. In the former case, the irradiated light energy is used to surmount the activation energy barrier of the reaction via electrons, excited in the photocatalyst. In the latter case, apart from the reaction activation process, light energy is converted to chemical energy and stored as the final reaction product.[6] In an actual photocatalytic reaction, more photons are generated when the photocatalysts absorb more photons. In order to achieve more efficient light-harvesting, there are several methods to extend the light absorption region of the semiconductor photocatalysts. One of the methods is tuning the electronic structure by doping foreign elements in the periodic table.[10–12] Other methods such as electron injection using localized surface plasmon resonance[13–15] and dye sensitization using metal complex dyes[16,17] have also been widely studied. In the second step, for taking part in the photocatalytic reaction, the photo-generated electron-hole pairs need to move to the surface of the photocatalyst. However, the large amount of photo-generated charge carriers induce electron-hole pairs recombination in the bulk or surface before reacting with the surface absorbed molecules, losing absorbed energy by heat or light emission. To prevent this recombination, loading co-catalysts such as Pt,[6,10,18–20] Pd,[19] RuO_2,[21] and NiO_x[2,21] on the semiconductor surface is a widely used effective approach. An internal electric field

is generated at the interface between the co-catalyst and the photocatalyst, promoting charge separation and promptly inducing carrier movement. Furthermore, since these co-catalysts have higher electrical conductivity, lower over-potential, and higher catalytic activity than general semiconductor photocatalysts, they function as an ideal photocatalytic active site.[6] In addition to loading the co-catalyst, the charge separation efficiency can be increased by fabricating composite photocatalytic materials such as TiO_2/CdS,[22] CdS/MoS_2,[23,24] and $SrTiO_3$: Rh/$BiVO_4$.[25] Besides, in smaller particle, the distance between the bulk and the surface is reduced, and the charge carriers can easily reach the active site so that the probability of recombination can be decreased.[26]

The carriers thus undergo charge separation and reach the surface can react with the adsorbed molecules, causing photo-oxidation / reduction reactions. Here, the following two typical photocatalytic reactions are mentioned.

(1)Photocatalytic splitting of water: $2H^+ + 2e^- \rightarrow H_2$ (E^0_{red} = 0 V vs. NHE) or $2H_2O + 4h^+ \rightarrow O_2 + 4H^+$ (E^0_{ox} = 1.23 V vs. NHE); thus, the total amount of H_2 or O_2 evolution is primarily determined by the amount of excited electrons or holes in the water/photocatalyst interface, respectively.[27]

(2) CO_2 photoreduction: The photo-generated holes in the valence band oxidize water to produce hydrogen ions ($H_2O + 2h^+ \rightarrow 1/2\ O_2 + 2H^+$, E^0_{ox} = 1.23 V vs. NHE), and the photogenerated electrons in the conduction band reduce CO2 into hydrocarbons such as CH_4 ($CO_2 + 8e^- + 8H^+ \rightarrow CH_4 + 2H_2O$, E^0_{red} = −0.24 V vs. NHE); the lager number of electrons take part in the reaction, the lager energetic solar fuels (e.g. CH_4, HCHO) can be generated.[3,28]

Considering sunlight as a free, abundant, and clean energy source, any photocatalytic reactions can be sustainable energy resource. Besides, approximately 3,850,000 EJ (exa-joules; 1 EJ = 108 J) of solar radiation shines on the earth every year, which is several orders of magnitude higher than the current energy consumption in the human society (about 474 EJ per year). It is essential for the development of human society to efficiently use this enormous abundant energy via artificial photocatalyst to provide enough clean and renewable energy.

1.2 Potencial application of photocatalysts

1.2.1 Photocatalytic water splitting

Hydrogen (H_2) production by photocatalytic water splitting is the main purpose of the photocatalytic reaction. H_2 has been considered as an ideal energy source because of its high specific energy density (around 140 kJ g^{-1}; about four times higher than that of methane) and clean combustion products.[29] To date, the main industrial H_2 production technology is steam reforming from hydrocarbon. 95% of the commercial H_2 is produced by the steam methane reforming at high temperatures (700-1100 °C):[30] ((1) $CH_4 + H_2O \rightarrow CO + 3H_2$, +191.7 kJ/mol; (2) $CO + H_2O \rightarrow CO_2 + H_2$, -40.4 kJ/mol.). However, this method requires much higher reaction temperature and is considered to be heavily energy-exhausting. Electrolysis is another way to produce H_2, in which the solid oxide electrolysis cells operate at high temperature (around 800 °C), alkaline electrolysis cells work at high concentrated alkaline electrolyte

(KOH or K_2CO_3) and the requested temperature of 200 °C, while polymer electrolyte membrane cells can promote reaction below 100 °C thus becoming more commercial by available. However, all those electrolysis process requires large amounts of electrical energy. Therefore, it is eager to pursue some environmental-friendly and low-cost strategy to obtain hydrogen. In comparison, photocatalytic water splitting might be a promising way to produce hydrogen from solar energy. In 1972, Fujishima and Honda discovered the hydrogen evolution through the photoelectrochemical splitting of water on the n-type TiO_2 electrode under UV-visible light irradiation. The schematic illustration of the electrochemical cell is shown in Figure 1.2. It consists of an n-type TiO_2 anode and a Pt black cathode. When the surface of the TiO_2 electrode was irradiated by the UV light from a 500 W Xe lamp, O_2 evolution occurred at the TiO_2 anode under applying of some bias. Concomitant reduction led to the H_2 evolution at the Pt counter electrode. This important discovery, which emerged from the use of photoelectrochemical cells with semiconductor electrodes, later inspired Bard to design the photocatalytic system by using semiconductor particles or powders as photocatalysts. In my Ph.D. study, I focus on the mechanism in the photocatalytic HER and CO_2 reduction.

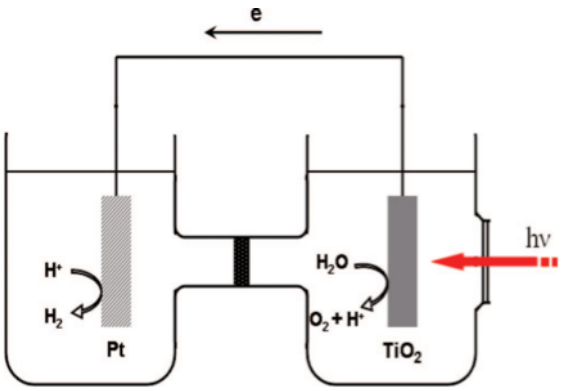

Figure 1.2. Schematic illustrations of the photoelectrochemical cell (PEC). Reproduced from Ref.[31]

Water splitting into H_2 and O_2 is an uphill reaction. It requires the standard Gibbs free energy charge ΔG_0 of 237 kJ/mol or 1.23 eV, as shown in Equation 1.

$$H_2O \rightarrow 1/2O_2 + H_2; \Delta G = +237 kJ/mol \tag{1.1}$$

Therefore, the bandgap energy (Eg) of the photocatalyst should be > 1.23 eV (λ < 1000 nm) to realize water splitting. To facilitate both the reduction and oxidation of H_2O by the photoexcited electrons and holes, respectively, the match of the bandgap and the potentials of the conduction/valence bands are important. Particularly, for a semiconductor photocatalyst, the bottom level of the conduction band should be more negative than the reduction potential of H^+/H_2 (0 V vs. NHE), whereas the top level of the valence band should be more positive than the oxidation potential of O_2/H_2O (1.23 V).

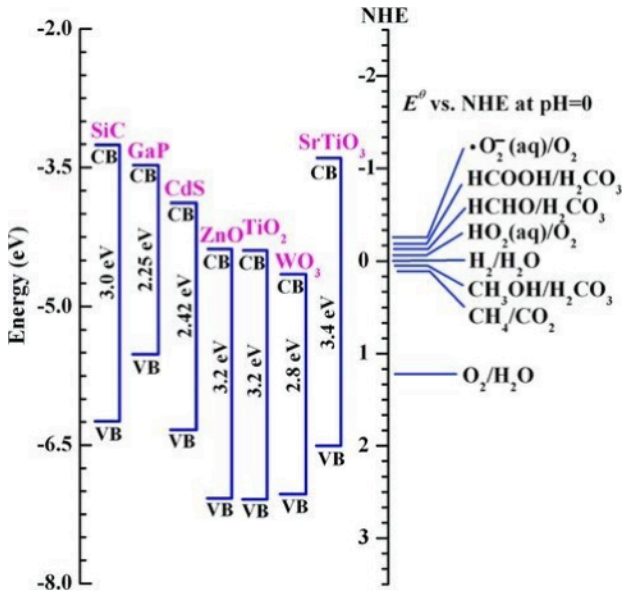

Figure 1.3. Band positions of some common semiconductor photocatalysts.[6]

Figure 1.3 shows the conduction band edge and valence band edge of some semiconductor photocatalyst candidates. There are many semiconductor materials whose electronic structures match well with the redox potential of water into H_2 and O_2. However, the band structure requirement is only the thermodynamic requirement for water splitting. Other factors, such as over-potentials, charge separation, mobility, and lifetime of photogenerated electrons and holes, can also affect the photocatalytic water splitting.

1.2.2 Photocatalytic CO_2 reduction reaction

With industrialization and the consumption of fossil fuel growth, CO_2 emission is increasing year by year and becomes the major origin of global warming. Photocatalytic CO_2 reduction to produce hydrocarbon fuels not only realizes the solar energy storage and conversion, but also offers a promising solution to CO_2 over-emission induced environmental crises, and therefore intensively attracts the attention from researchers.[32] However, the developing of this technology remains challenges. On the one hand, CO_2 molecules present linear symmetric structures, and they are so thermodynamically stable that the molecules ' activation is rather difficult to achieve. On the other hand, the reduction of CO_2 into hydrocarbon compounds is a typical proton-coupled electron transfer process and, therefore, also suffers from the kinetic limitation due to the involving of multiple e^- /H^+ transfer. Below is the potentials (vs. NHE, pH = 7) for CO_2 reduction into various hydrocarbon compounds.[33]

$$CO_2 + 2H^+ + 2e^- \rightarrow HCOOH(E^0 = -0.61V) \quad (1.2)$$

$$CO_2 + 2H^+ + 2e^- \rightarrow CO + H_2O(E^0 = -0.53V) \quad (1.3)$$

$$CO_2 + 4H^+ + 4e^- \rightarrow C + 2H_2O(E^0 = -0.20V) \quad (1.4)$$

$$CO_2 + 4H^+ + 4e^- \rightarrow HCHO + H_2O(E^0 = -0.48V) \quad (1.5)$$

$$CO_2 + 6H^+ + 6e^- \rightarrow CH_3OH + H_2O(E^0 = -0.38V) \quad (1.6)$$

$$CO_2 + 8H^+ + 8e^- \rightarrow CH_4 + H_2O(E^0 = -0.24V) \quad (1.7)$$

$$2CO_2 + 12H^+ + 12e^- \rightarrow C_2H_5OH + H_2O(E^0 = -0.33V) \quad (1.8)$$

From the above reaction, though the eight-electron reduction of CO_2 to CH_4 or CH_3OH requires a much lower potential than that for the two-electron reduction to CO or HCOOH, it does not mean that the former reaction is more easily achieved relative to the latter. This is because, the common reactions might require a higher potential; secondly, the intermediate processes might have to overcome a high energy barrier; also, the former reaction suffers from a higher kinetic limitation due to the more complex multi-proton-coupled electron transfer process. Organometallic complex compounds generally possess multiple and accessible redox states and therefore exhibit multi-electron transfer reactivity. Furthermore, through the modification of the organic ligands, the multiple redox potentials could be controlled. These features make organometallic complexes promising candidates for CO_2 reduction. Also, considering the slightly negative potential for CO_2 reduction and also the somewhat positive potential for water oxidation, a photocatalyst that might realize the concurrent CO_2 reduction and water oxidation must possess a very lager band gap as well as suitable band positions. Kudo et al. reported that $ALa_4Ti_4O_{15}$ (A = Ca, Sr, and Ba) photocatalysts with 3.79 - 3.85 eV of band gaps and layered perovskite structures could photo reduce CO_2 to form CO and HCOOH and simultaneously oxidize water to produce O_2 under UV light irradiation.[34] Ag was used as the co-catalyst in the case. Additionally, other semiconductor photocatalysts like Zn_2GeO_4, TiO_2, and ZnS were also applied for CO_2 photoreduction, but they are all UV active.[32] The development of visible-light sensitive photocatalysts for this application is highly desired.

1.3 Typical photocatalytic materials

Photocatalysts have been intensively researched for constructing further elaborate materials. In principle, photocatalytic reaction on the surface is able to occur only when the reduction and oxidation potential are more positive and negative than CBM and VBM potentials, respectively. Currently, various photocatalysts including metal oxide, sulfide and carbon based materials are being explored for solar fuel conversion. These can be classified into two main groups: inorganic and organic photocatalysts. The traditional inorganic semiconductors, such as TiO_2, $SrTiO_3$, ZnO, WO_3, CdS, and $BiVO_4$, can be active photocatalysts after absorb the incident photons with higher energy than their band gap to excite

electrons into CB from VB and left holes in VB. When these electons and holes succesfuly migrate to the surface, they can initiate the reduction and oxidation and oxidation reaction, respectively. In these inorganic materials, their band structure can be tuned by doping or co-doping with foreign elements, and creating vacancies. Likewise, carbon based materials, such as g-C_3N_4, polymers, and graphene, also can be active photocatalysts by light absorption. In organic semiconductor, after light absoption, the spatially separated photogenerated electron hole pair in their lowest unoccupied molecular orbital (LUMO) and highest occupied molecular orbital (HOMO) initiate photocatalytic reaction. For tuning the property of organic photocatalysts, besides elemental doping, the molecular exchange can be employed to explore the suitable energy band structure. In the following subchapter, I will give an overview of each inorganic and organic photocatalysts.

1.3.1 Inorganic photocatalysts

Almost all inorganic semiconductor materials are composed of metal cations including transition metals and anions such as oxygen, nitrogen, and sulfur. In many inorganic semiconductor based photocatalytic materials, the d-orbit of the transition metal forms a conduction band and an anion forms the valence band. Alkaline earth metals and lanthanoids do not affect the conduction band minimum and are often chosen as A sites with perovskite or spinel structures (ABO_3 and AB_2O_4). Table 1.1 summarize the inorganic semiconductors based photocatalytic materials which exhibited relatively high water splitting or hydrogen generating reactions in the presence of sacrificial reagent. The major similarity is that most materials consist of Ti, Ta, and Nb elements to form a conduction band and have a (layered) perovskite structure. Thus in this dissertation, $SrTiO_3$, the most basic compound containing Ti and having a perovskite structure, was used as a model material of inorganic photocatalysts for mechanism analysis. The following subchapter describes the perovskite structure, the physical properties of $SrTiO_3$, and attempts to make it visible light responsive photocatalysts.

Perovskite structure

In the past decades, large variety of metal oxide photocatalysts have been found and the photocatalytic performance have been intensively studied by the researchers. Although TiO_2 based materials are the most studied material for photocatalytic applications, ternary and other complex oxide systems, have been increasingly explored as photocatalysts. Among the various classes of materials studied, perovskites-based photocatalysts have unique photophysical properties and offer distinct advantages. Perovskites are the class of oxides with the general formula ABO_3. Generally, in this crystal structure, the A site is occupied by the larger cation such as an alkaline earth metal, while the B site is occupied by the smaller cation such as a transition metal from the first raw of the periodic table. Perovskites are one of the most prominent families of materials exhibiting properties suitable for numerous technological applications.[35] The origin of such properties lies in the crystal structure of perovskites. The perovskite crystal structure has corner connected BO_6 octahedra and 12 oxygen coordinated A sites, located in between the eight

Table 1.1. Various inorganic photocatalytic materials for water splitting and hydrogen generation.[36]

					Activity / μ mol h^{-1}	
Photocatalyst	Crystal structure	co-catalyst	Light source	Reactant solution	H_2	O_2
TiO_2	anatase	Rh	Hg	Water vapor	449	
TiO_2	anatase	Pt	Hg	2.2 M K_2SO_3	568	287
TiO_2	anatase	Pt	Hg	Pure water	106	53
$CaTiO_3$	Perovskite	NiO_x	Hg	0.2 M NaOH	30	17
$SrTiO_3$	Perovskite	NiO_x	Hg	5 M NaOH	40	19
$SrTiO_3$	Perovskite	Rh	Hg-Xe	Pure water	27	14
$NaTaO_3$	Perovskite	NiO_x	Hg	Pure water	2180	1100
$NaTaO_3$:La	Perovskite	NiO	Hg	Pure water	19800	9700
$NaTaO_3$:Sr	Perovskite	NiO	Hg	Pure water	9500	4700
$SrTiO_3$	Perovskite	Pt	Hg	MeOH solution	3200	-
$Sr_3Ti_2O_7$	Layered Perovskite	NiO_x	Hg	Pure water	144	72
$Sr_4Ti_3O_{10}$	Layered Perovskite	NiO_x	Hg	Pure water	170	4.5
$K_2La_2Ti_3O_{10}$	Layered Perovskite	NiO_x	Hg	0.1 M KOH	2186	1131
$Rb_2La_2Ti_3O_{10}$	Layered Perovskite	NiO_x	Hg	0.1 M RbOH	869	430
$Cs_2La_2Ti_3O_{10}$	Layered Perovskite	NiO_x	Hg	Pure water	700	340
$CsLa_2Ti_2NbO_{10}$	Layered Perovskite	NiO_x	Hg	Pure water	115	50
La_2TiO5	Layered Perovskite	NiO_x	Hg	Pure water	442	
$La_2Ti_3O_9$	Layered Perovskite	NiO_x	Hg	Pure water	386	
$La_2Ti_2O_7$	Layered Perovskite	NiO_x	Hg	Pure water	441	
$La_2Ti_2O_7$:Ba	Layered Perovskite	NiO_x	Hg	Pure water	5000	
$Ba_5Nb_4O_{15}$	Layered Perovskite	NiO_x	Hg	Pure water	2366	1139
$Sr_5Ta_4O_{15}$	Layered Perovskite	NiO	Hg	Pure water	1194	722
$Ba_5Ta_4O_{15}$	Layered Perovskite	NiO	Hg	Pure water	2080	910
$Na_2Ti_6O_{13}$	Tunnel Structure	RuO_2	Xe	Pure water	7.3	3.5
$BaTi_4O_9$	Tunnel Structure	RuO_2	Xe	Pure water	33	16
$Gd_2Ti_2O_7$	Cubic pyrochlore	NiO_x	Hg	Pure water	400	98
$Y_2Ti_2O_7$	Cubic pyrochlore	NiO_x	Hg	Pure water	850	420
$Na_2Ta_2O_6$	Pyrochlore	NiO	Hg	Pure water	960	490
$K_2Ta_2O_6$	Pyrochlore	NiO	Hg	Pure water	629	303
$LaTaO_4$	Fergusonite	NiOx	Hg	Pure water	116	52
La_3TaO_7	Cubic fluorite	NiO_x	Hg	Pure water	164	80
$Ga2O_3$:Zn	Corundum Structure	Ni	Hg	Pure water	2403	1400
Ge_3N_4	Spinel Structure	RuO_2	Hg	Pure water	1400	700
GaN	Wurtzite	$Rh_{2-x}Cr_xO_3$	Hg	H_2SO_4 (pH 4.5)	19	9.5
GaN:Mg	Wurtzite	RuO_2	Hg	Pure water	730	290
$(Ga_{0.88}Zn_{0.12})(N_{0.88}O_{0.12})$	Wurtzite	$Rh_{2-x}Cr_xO_3$	Hg	H_2SO_4 (pH 4.5)	800	400
$Zn_{1.44}GeN_{2.08}O_{0.38}$	Wurtzite	RuO_2	Hg	Pure water	14.2	7.4
CdS	Wurtzite	Pt	Hg >390	K_2SO_3	13000	
CdS	Wurtzite	WS_2	Xe >420	Lactic acid + NaOH	500	
CdS	Wurtzite	MoS_2	Xe >420	Lactic acid + NaOH	397.2	
$AgGaS_2$	Chalcopyrite	Rh	Xe >420	Na_2S + K_2SO_3	1340	
$NaInS_2$	Chalcopyrite	Pt	Xe >420	K_2SO_3	470	
$ZnIn_2S_4$	Spinel Structure	Pt	Xe >420	Na_2S + Na_2SO_3	77	
$Cu_{0.09}In_{0.09}Zn_{1.82}S_2$	Wurtzite	Pt	Xe >420	Na_2S + K_2SO_3	1200	
$Cu_{0.25}Ag_{0.25}In_{0.5}ZnS_2$	Chalcopyrite	Ru	Xe >420	Na_2S + K_2SO_3	2300	

BO_6 octahedra (Figure 1.4). The perfect structure of the octahedral connection results in a cubic lattice. However, depending on the ionic radii and electronegativity of the A and B site cations, the tilting of the octahedra takes place, which gives rise to lower symmetry structures. As seen from the crystal structure, B site cations are strongly bonded with the oxygen while A site cations have relatively weaker interactions with oxygen. Depending on the type of the cations occupying the lattice sites, these interactions could be altered to yield the different perovskite crystal geometries.

In an ideal cubic perovskite structure, if the lattice constant is a, the relationship with the bond distance is

$$\sqrt{2}(r_B + r_O) = r_A + r_O \tag{1.9}$$

where r_A, r_B, and r_O are the empirical ionic radii at room temperature. When the oxidation state and coordination number of each element are determined, the bond distance is a value within a fairly limited range. Goldschmidt[36] has introduced a tolerance factor (t), defined by the equation:

$$t = \frac{(r_A + r_O)}{\sqrt{2}(r_B + r_O)} \tag{1.10}$$

The bond distance has a certain width, and the cubic perovskite is formed in the range of 0.9 <t <1.1. In the ideal structure, the t values of $SrTiO_3$ is calculated to be 0.9986. The factor becomes smaller than 1 if the A ion is smaller than the ideal value or when the B ion is too large. As a result, the BO_6 octahedral part will tilt in order to fill space, and the symmetry of the crystal structure is lowered. For example, $CaTiO_3$ with t = 0.82 possess orthorhombic symmetry. On the other hand, if the t factor is larger than 1 due to a large A or small B ion, then tetragonal and hexagonal variants of the perovskite structure are stable, e.g., $BaTiO_3$ (t = 1.062) and $BaNiO_3$ (t = 1.13) type structures. In these cases, the close-packed layers are stacked in tetragonal and hexagonal manners in contrast to the cubic one formed for $SrTiO_3$. Since perovskites are not truly ionic compounds and since the values are taken for the ionic radii, the tolerance factor is only a rough estimate indicating compounds with a high degree of ionic bonding.

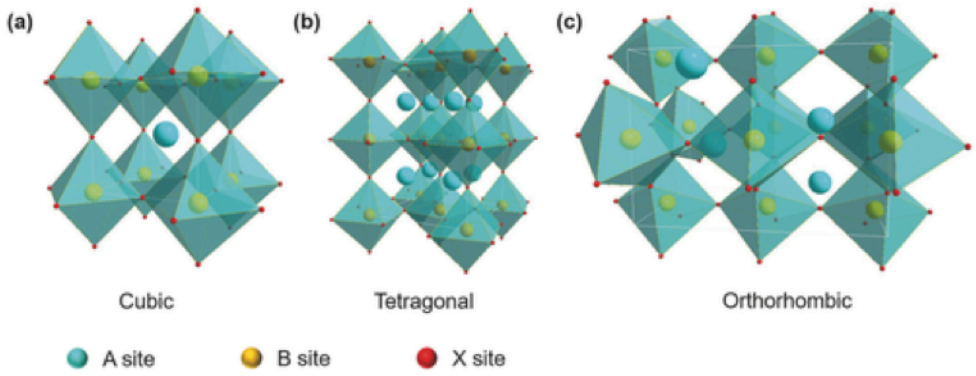

Figure 1.4. The crystal structures of perovskite materials with different symmetries: (a) cubic phase (t ≃ 1), (b) tetragonal phase (0.9 < t < 0.8), and (c) orthorhombic phase (0.8 < t < 0.7).[37]

As photocatalysts, perovskite structures may offer significant advantages over the corresponding binary oxides for several reasons. The perovskite structure could offer favorable band edge potentials, which allow various photocatalytic reactions. For example, as compared to the binary oxides, several perovskites have sufficiently cathodic CB potential for hydrogen evolution.[38] Secondly, A and B cation sites in the lattice offer a broader scope for the design and alteration of the band structure as well as other photophysical properties.

Photocatalytic activity of $SrTiO_3$ based materials

Titanate perovskites $ATiO_3$ (A = Ca, Sr, Ba, etc.) have been studied for photocatalytic applications for a long time. Most of the titanate perovskites have bandgap energy (Eg) values more than 3.0 eV. They only show excellent photocatalytic properties under UV radiation.[2,39] Using titanate perovskite as a host material, doping is widely used to alter the optical properties and induce visible light absorption. TiO_2 (anatase) single-crystal has a bandgap of 3.0-3.2 eV, and its CB potential is -0.4 eV above the water reduction level.[40] Certain perovskite titanates have CB energies more negative than TiO_2, making them more suitable candidates for hydrogen generation. Titanates also offer excellent photostability and corrosion resistance in aqueous solutions. $SrTiO_3$ is among the most promising pure titanate perovskite for photocatalytic applications.[2,41] It is a cubic perovskite (Pm3m, a = 3.905 Å) n-type semiconductor, with the direct and indirect band-gap energies between Ti-3d CB and O-2p VB are 3.4 and 3.2 eV, respectively.[42] The single-crystal $SrTiO_3$ shows photocatalytic H_2 evolution from alkaline condition ([NaOH] > 5M) under 500 W high-pressure mercury lamp irradiation.[43] The OH- group on the $SrTiO_3$ surface was suggested as a facile hole scavenger to increase a lifetime of electrons in $SrTiO_3$, which contributes to protons reduction. Prereduced Ti^{3+} was considered to take part in the HER under UV light irradiation.[44] In the same year, Domen et al. also reported the photocatalytic water vapor splitting by using $SrTiO_3$ with loading NiO as a co-catalyst.(Figure 1.5)[45] Later, they demonstrated HER performance of these materials shows three times higher in the liquid water. The loading amount of NiO co-catalyst is one of

the critical parameters for water splitting performance. The optimized amount (1.7 wt%) enhances water splitting performance 100 times. More importantly, Domen et al. revealed that the NiO co-catalyst form the core/shell structure during the pretreatment process. The NiO on the surface of $SrTiO_3$ experiences reduction and re-oxidation process, thus while NiO shell partially changes into $Ni(OH)_2$, the interface between $SrTiO_3$ and co-catalyst remains Ni metal state upon irradiation.[46]

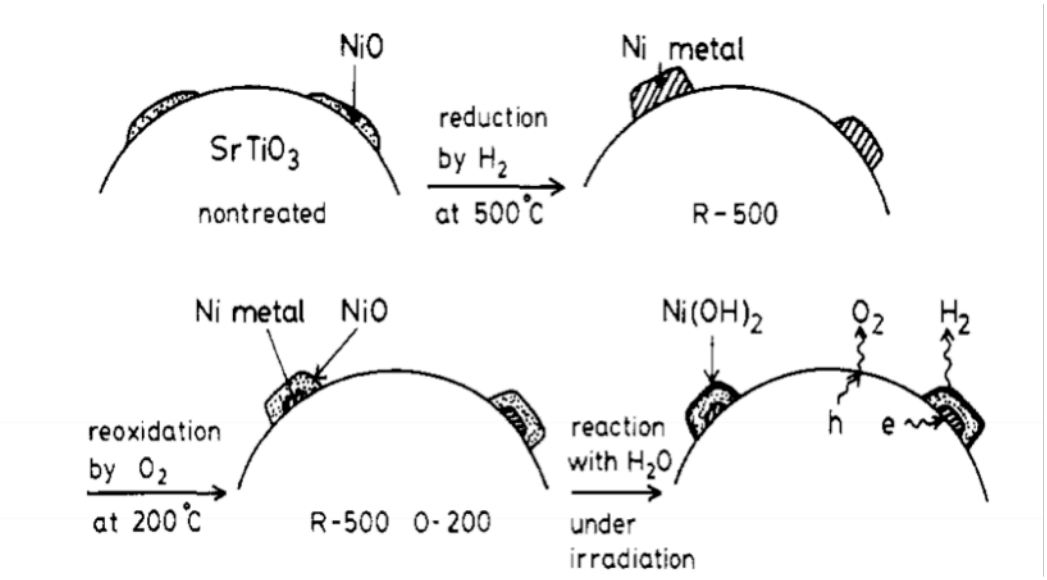

Figure 1.5. Schematic illustrations of the core/shell structure of NiO on the $SrTiO_3$ catalyst. from ref.[47]

These results guarantee the excellence of the photocatalytic performance over $SrTiO_3$ under UV light irradiation.

The bandgap energy renders $SrTiO_3$ an excellent photocatalyst only under UV light, which accounts for about 4-5% of the solar spectrum. The modification of $SrTiO_3$ to absorb the visible light spectrum is necessary to enhance photocatalytic activity. Among the strategies including photosensitization,[16,17] doping,[41,48] localized surface plasmon resonance,[13,49] extrinsic elemental doping into the semiconductor-based photocatalysts to narrow the bandgap is a conventional and useful method widely engaged by the researchers. Doping of single metal elements such as Cr,[50,51] Fe,[52,53] Ir,[54] Mn,[54] Ru,[54] Rh,[25,54] Pd[54] and Ti(III),[55,56] and non-metal elements such as N,[53,57] S,[53] C[53] have been reported for the photocatalytic activity under visible light irradiation. It is reported that by doping, impurity bands are created, which enable the absorption of visible-light to excite electrons. Among the different noble metal ions, Rh doping exhibited the best performance than the others like Ru and Ir. The donor level located at ca. 1.0 eV above valence band was formed by the Rh^{3+} doping, which acts as a surface reaction center for the oxidation of methanol.[54] Also, Cr-doped $SrTiO_3$ was evaluated for photocatalytic hydrogen production under visible light irradiation. By synthesizing with the hydrothermal method, the $Sr_{0.95}Cr_{0.05}TiO_3$ shows visible light absorption up to 540 nm and exhibited three times higher activity than that synthesized by a solid-state reaction due to the increased surface area.[51] It should be noted that the Cr^{3+} substitution

of Ti^{4+} sites in BO_6 octahedra would create oxygen defects and Cr^{6+} ions to maintain the charge neutralization, which may decrease the photocatalytic activity. The positive doping effect for Cr^{3+} mono-doping was suggested only for the substitution of Sr^{2+} sites in $SrTiO_3$. Recently to restrain the detrimental drawbacks of the lattice mismatching or valence state unbalance by mono-doping, codoping is often used beyond mono-doping. It is demonstrated that in one of the well-known codoped photocatalyst Cr, Sb-codoped $SrTiO_3$, codoping of Sb^{5+} is able to maintain Cr ions valence state to Cr^{3+}. As a result, a stable photocatalytic H_2 evolution rate was achieved.[41] In addition to the doping of foreign element into crystal geometry, self-doped $SrTiO_{3-x}$ was proposed to dope Ti(III) and oxygen vacancy. In the early period of history, the oxygen vacancy was believed, acts as recombination center. However recently, it is found that the oxygen vacancy may play several beneficial roles such as enhancing visible light absorption and chemisorption of CO_2 onto catalyst, which improved the photocatalytic reaction efficiency of converting CO_2 to hydrocarbon fuels.[55] As mentioned above, a numerous number of great effort has been done over the doping method, one of the critical problems but rarely addressed is the change of the light absorption and photocatalytic activity under UV-light region. The photocatalytic activity under UV-light is drastically decreased after doping even though their performance under visible-light could be enhanced, resulting in a lower total photocatalytic activity under the full spectrum of solar-light irradiation (Figure 1.6).[58–60] The only exception is that doping of lanthanides and alkali earth metals into $SrTiO_3$ seems to enhance the photocatalytic activities under UV light irradiation, leading to improve total photocatalytic activity under the full solar spectrum.[48,61]

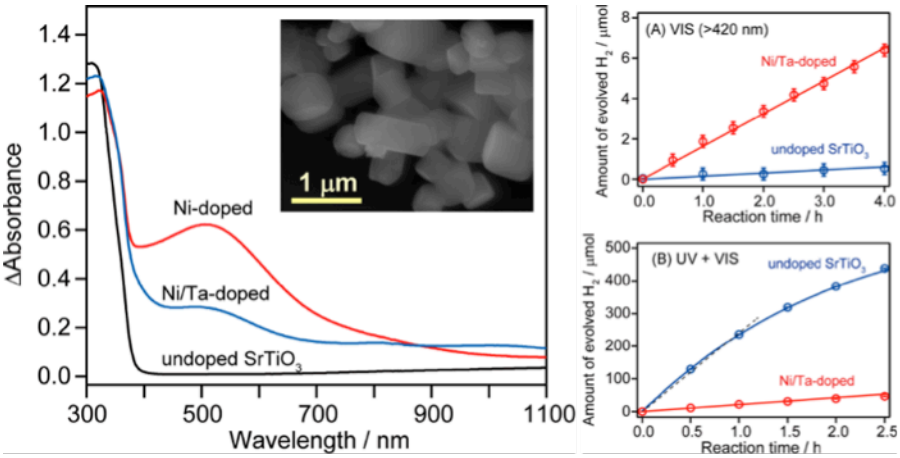

Figure 1.6. Diffuse reflection absorption spectra of undoped, 1% Ni-doped, and 1% Ni and 2% Ta co-doped $SrTiO_3$ are shown. Inset: SEM image of Ni/Ta co-doped $SrTiO_3$. Photocatalytic H_2 evolution from 10 vol % aq MeOH over 0.6 wt % Pt undoped and Ni/Ta co-doped $SrTiO_3$ under (A) VIS(>420 nm) and (B) UV + VIS light (>250 nm).

It is widely believed that the unoccupied d-orbital of transition metals may form some mid-gap states which can capture electrons and holes together, acting as a recombination center.[1,63] But the actual role of dopants and how they affect the charge carriers dynamics has not yet been fully elucidated. To design

more sophisticated photocatalysts over inorganic semiconductors, it is necessary to understand the hidden reaction mechanism, especially charge carriers dynamics in photocatalytic reaction.

1.3.2 Organic semiconductor based photocatalysts

In recent years, organic semiconductors typified by OLEDs have begun to show prominence in photocatalysis. g-C_3N_4 is known as the most famous organic semiconductor photocatalyst. This material has stable H_2 and O_2 generation performance under visible light and in the presence of sacrificial reagents.[64] The graphitic planes consisted of tri-s-triazine units linked by planar amino groups, as shown in Figure 1.7 (a). The XRD pattern and UV-vis absorption spectrum of g-C_3N_4 were shown in Figure 1.7 (b) and (c), respectively.

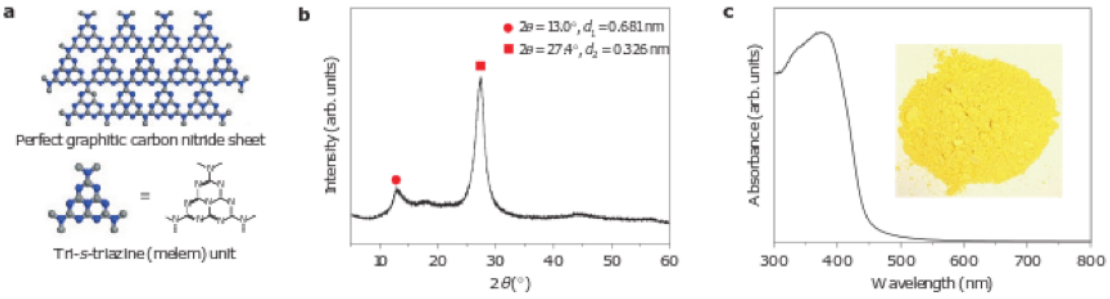

Figure 1.7. Schematic diagram of a perfect graphitic carbon nitride sheet constructed from melem units. (b) XRD pattern and (c) UV-vis absorption spectrum of g-C_3N_4 Inset in (c) is the photograph of g-C_3N_4 powder. From Ref.[64]

Besides, as shown in Figure 1.8, g-C_3N_4 has a high potential to be multifunction photocatalysts due to its electronic properties and nucleophilic properties. Further, highly elaborate g-C_3N_4 has been studied by using unique techniques of organic semiconductors such as functional group replacement, molecule doping, and copolymerization.[65] Also, as same as inorganic semiconductors, doping foreign elements into g-C_3N_4 has attempted to enhance the photocatalytic activity.[66,67] However, It has been difficult to tune the energy level of the HOMO-LUMO level derived from the structure.[65]

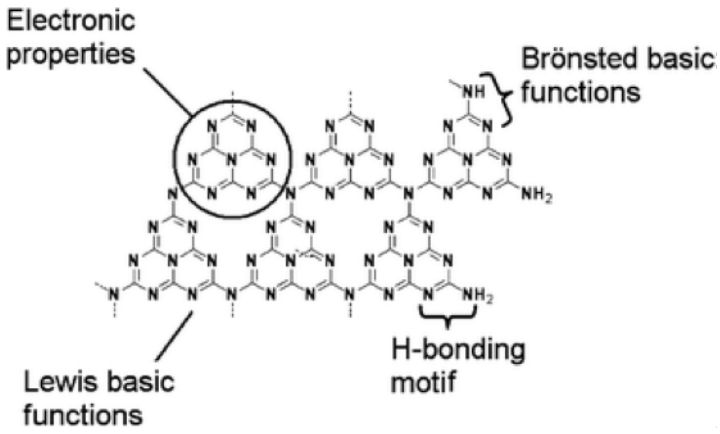

Figure 1.8. Structural feature of g-C_3N_4 From Ref.[65]

Besides g-C_3N_4, conjugated polymer semiconductors are also essential materials toward highly elaborated photocatalysts in organic materials. Conventional inorganic semiconductors have inherent conduction band and valence band energy levels derived from the crystal structure and elements of each material, and it is challenging to design inorganic semiconductors with arbitrary light absorption characteristics by changing these potentials. On the contrary, organic semiconductors have the feature that molecular design is quickly addressed, molecules with various HOMO-LUMO energy levels can be adjusted, and the organic semiconductors with potential suitable for various photocatalytic reactions can be efficiently designed. Furthermore, in the case of inorganic semiconductors, the generation of defects is unavoidable, especially in powder samples, whereas in the case of organic semiconductors, it is readily to fabricate as designed for desired photocatalytic reactions with very few defects. However, there are few research reports on photocatalysts using organic semiconductors, and the mechanism is not fully understood. The first organic semiconductor for photocatalytic HER using poly (p-phenylene) was reported in 1985 by Yanagida et. al. In this study, it was shown that H_2 was generated under irradiation with UV light ($\lambda >$ 290 nm) using Diethylamine as a sacrificial reagent.[68] Okemoto et al. found that Picene can decompose photocatalytic water from the estimation of oxidation/reduction levels of organic semiconductors by DFT calculation. The authors also experimentally confirmed the photocatalytic hydrogen evolution activity by using Picene. (Figure 1.9)[69] However, both of these organic semiconductors are driven only by UV light.

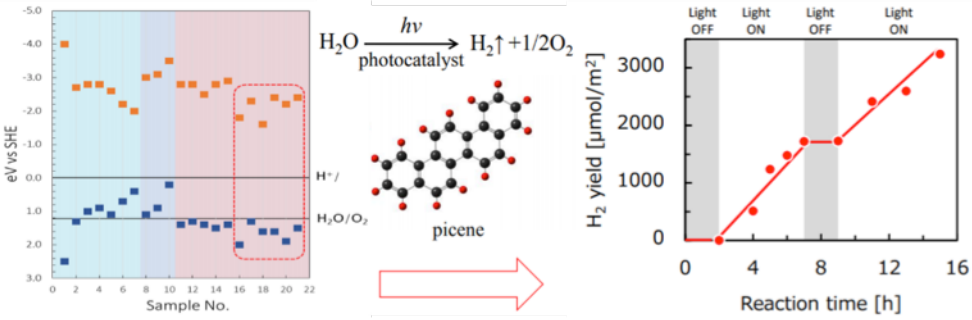

Figure 1.9. DFT calculation and proposed organic semiconductor for HER under UV light irradiation. From Ref.[69]

Sprick et al. have demonstrated that photocatalytic HER could be achieved in the presence of sacrificial reagents even under visible light using various conjugated polymers.(Figure 1.10) This work dramatically expands the options for photocatalytic materials.[70] The conjugated polymer materials have been energetically studied in the photocatalytic reactions, and it can be expected to be an essential material especially in photocatalytic CO_2 reduction.[71] However, like many other photocatalytic materials, the carbon based conjugated polymer material alone has no active sites useful for CO_2, so co-catalysts are needed to reduce the activation energy of CO_2.[71,72]

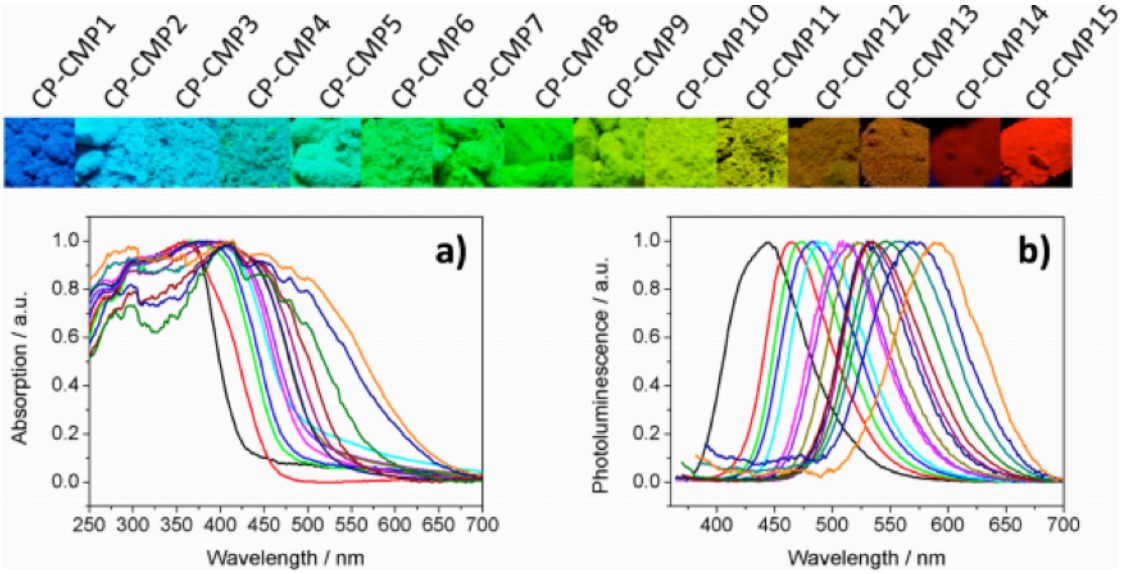

Figure 1.10. Statistical copolymerization allows continuous tuning of the photophysical properties of the photocatalysts. (top) Photographs of the series of copolymers (CP-CMP1-15), imaged under irradiation with UV light (λ= 365 nm); (a) UV-visible absorption spectra of the copolymers measured (intensities normalized); (b) normalized photoluminescence spectra of the copolymers (λ= 360 nm) A systematic redshift is observed as the pyrene monomer incorporation is increased.[70]

To date, many cocatalysts have been utilized for photocatalytic CO_2 photoreduction reactions.[73] Among them, one successful strategy for cocatalysts is the use of certain kinds of organometallic complexes developed from the molecular catalysis system.[74–76] These Ru-complexes, Ni-complexes, Re-complexes, and Co-complexes usually absorb on the surface of semiconductor by Van der Waals 'force. Hence these systems possess both advantages of heterogeneous catalysis and homogeneous catalysis.[77–81] The low oxidation states metal centers that exist in these complexes are mono-disperse on the semiconductor surface as countless active sites, and CO_2 is reduced using electrons flowing from the semiconductor.[81] Recently, Wang et al demonstrated CO_2 reduction reaction with CPs photocatalysts under visible light irradiation.[82] The authors selected 2, 4, 6-tris(4-bromophenyl)-1, 3, 5-triazine with three different building block, 1,4-phenylene diboronic acid (B), 2,5-thiophenediboronic acid (Th), and 2,1,3-benzothia-diazole-4,7 bis (BT), here authors classified these tree building block as reference, electron-donor, and electron-acceptor building block, respectively. This coupling was carried out using Suzuki-Miyaura coupling to form the corresponding conjugate polymer networks CPs-B, CPs-Th, and CPs-BT, respectively.(Figure 1.11) By incorporation electoron donor and acceptor, the photocatalytic CO_2 reduction reaction activity has enhanced under visible light irradiation with the presence of $CoCl_2$ and dipyridyl as cocatalysts. After composed with electron-acceptor building block CPs-BT, the CO evolution rate increased to 18.2 μmol/h from that of CPs-B (4 μmol/h). The authors demonstrated the effect of the different building block for the photocatalytic CO_2 reduction activity, however the electron delivery mechanism is still unclear.[82] Thus, understanding the mechanism of the electron transfer in the CPs photocatalysts is necessary for designing further elaborate CPs photocatalysts.

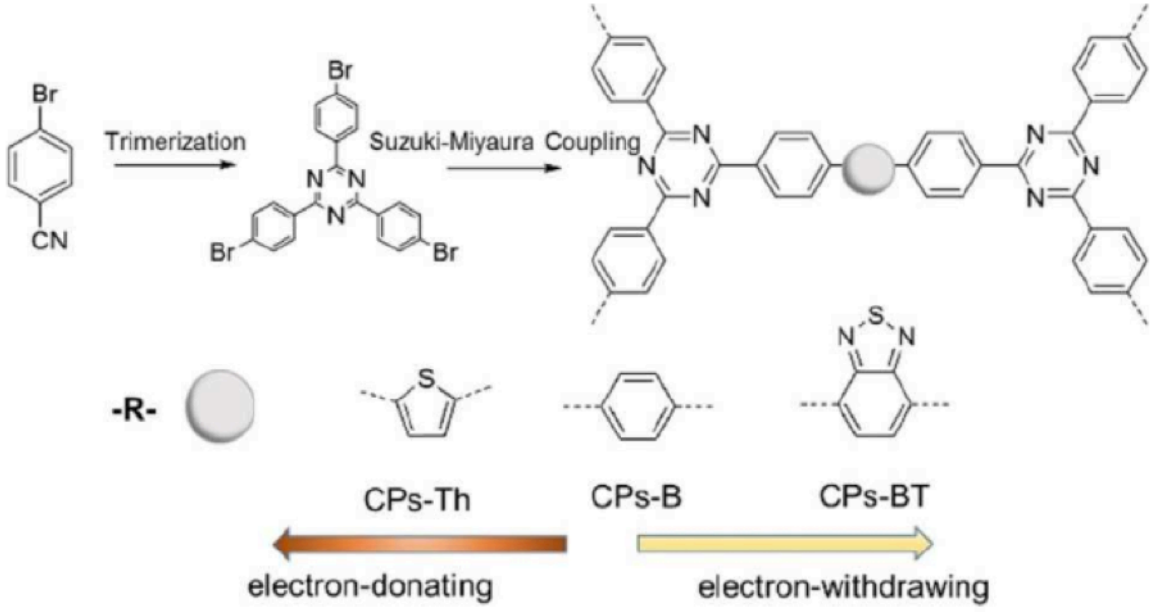

Figure 1.11. Design and synthesis pathway of three triazine ‐ based polymers with different molecular structures for photocatalytic CO_2 reduction.[82]

In CPs for photocatalytic CO_2 reduction, the reaction efficiency is rate-determined by the photoexcited electrons delivery from CPs to the surface loaded cocatalyst (adsorb and active CO_2 molecule). However, a limitation still exists in finding an appropriate way to promote the delivery of photoexcited electrons to cocatalyst due to a higher energy barrier of the out-of-plane Ohm or Schottky contact than the intramolecular cascade between cocatalyst and CPs.[72,83] Photoinduced intermolecular charge transfer through molecules by non-covalent interactions is a well-known efficient process in photochemistry.[84] To achieve kinetically favorable electron transfer from CPs to cocatalyst and make a breakthrough in CO_2 photoreduction, an intermolecular cascaded channel between the CPs and cocatalyst is desirable to be established for oriented delivery of photoexcited electrons to overcome a lower energy barrier and a less carrier.[73,85–87] Thus, in this dissertation we focus on the electrons delivery dynamics in the different bonding structure of CPs to reveal the effect of bonding condition, interaction with cocatalysts, reaction with CO_2 molecules over cocatalysts by using several ultra-fast spectroscopy.

1.4 The photocatalytic reaction mechanism study

As shown in Figure 1.1, the photocatalytic reaction comprises three substantial steps: (1) harvesting light with energy larger than band gap of the semiconductor to generate electron/hole pairs in CB and VB, respectively. (2) The charge carrier separation and subsequent migration to accumulate on the surfaces, or recombination of electron-hole pair in the bulk or surface. (3) Initiating reductive/oxidative reactions involving these charges carriers to generate certain products with the assistance of the cocatalysts. These three substantial process determine their photocatalytic activities, and take place within several milliseconds.

1.4.1 Charge carriers dynamics

Understanding the dynamics of photoexcited carriers in semiconductors is very important when evaluating photocatalysis, photoelectrochemistry, and photo voltaic reactions.[63,88,89] In the actual photocatalytic reaction, reaction process can be observed only when the carriers generated by light irradiation reach the surface by diffusion and react with molecules adsorbed on the surface. Similarly, the photo voltaic reaction can be detected as a photocurrent only when the carriers generated by light irradiation have a sufficient diffusion length.[88] In this way, carrier dynamics evaluation is indispensable in understanding and evaluating the phenomena caused by carrier diffusion and carrier transfer to molecules.

1.4.2 Charge carriers dynamics in photocatalysis

After photoirradiation onto photocatalysts, the photo excitation of electrons into the conduction band is a femtosecond process,[90] and both electron-hole pairs are trapped in a shallow trapping state. The trapping processes occurring afterward can be subdivided into fast surface trapping of photogenerated electron-hole pairs and slower deep electron trapping in the bulk. For instance, carriers trapping at the

surface requires only ~50 fs. Since shallowly trapped electrons at the surface and bulk are energetically equivalent and probably very close to the conduction edge, electrons are capable of migrating between surface trap site and shallow trap site in bulk that are in equilibrium. Relaxation of shallowly trapped electrons into a deeper trapping site occurs within ~500 ps through a hopping process involving energetically distributed trapping sites.[90,91] Carriers that reach the surface start to react in the ns-s range and return to a steady state in ms-s.[92] The trapped carriers could not contribute to the reaction in ns-s.[92,93] It has been reported that when the co-catalysts is loaded on the surface, the photogenerated charge carrier moves to the co-catalysts within few picoseconds in the case of an efficient photocatalyst.[20,90,94,95] In general, approximately 90% of electron-hole pairs recombine within 10 ns,[96] and this high recombination probability is considered to be the main cause of relatively low photocatalytic activity.[97] On the other hand, most trapped carriers have a long enough life to be able to participate in the photocatalytic reaction, and this trapping process will extend the carrier life and thus contribute to the improvement of the photocatalytic activity.[98,99] Trapping increases the lifetime of photoexcited carriers, which improves the photocatalytic activity, but at the same time reduces the reactivity of the trapped photoexcited carriers.[63] Bahnemann et al., reported that some trapped hole species in TiO_2 are incapable of oxidizing adsorbed anions, which are usually oxidized in photocatalytic reactions on TiO_2 surfaces.[100] Hence, stabilization of the charge carriers at trapping sites can be essential for the prevention of charge carrier recombination but decreases the inherent energetic driving force for the photocatalytic reactions. Chemically, as same as in TiO_2, trapped electrons and holes in $SrTiO_3$ are represented as Ti^{3+} and $^{\bullet}OH$ radicals, respectively.[63] The $^{\bullet}OH$ radicals are generated by oxidation of OH groups adsorbed on the surface and Ti^{3+} centers by reduction of Ti^{4+}. (Equations. 1.11 and 1.12).

$$H_2O_{abs} + h^+{}_{trap} \rightarrow {}^{\bullet}OH + H^+ \tag{1.11}$$

$$Ti^{4+} + e^-_{trap} \rightarrow Ti^{3+} \tag{1.12}$$

In addition, the sufficiently negative CB potential of TiO_2 and $SrTiO_3$ reacts with dissolved oxygen in the photocatalytic reaction system and electrons in CB or trapped electrons (Ti^{3+} center) to generate superoxo radicals. (Equation 1.13).[101]

$$O_2 \rightarrow O_2^{\bullet -} \tag{1.13}$$

Oxygen-based radicals such as $^{\bullet}OH$ radicals, $^{\bullet}O_2$, and H_2O_2 formed by photoirradiation of photocatalysts are considered to be reactive oxygen spiecies and have a strong oxidizing power and participate in various photocatalytic reactions.[102] According to a study by Ohotani et al., these radicals have a relatively long lifetime and are likely to be involved in many photocatalytic reactions.

1.4.3 Ultrafast spectroscopy for understanding the photocatalytic reaction

The photocatalytic reaction occurs through various transient reactions. Ultra-fast spectroscopy is a powerful tool for profoundly understanding this photocatalytic reaction. In ultrafast spectroscopy, a phenomenon occurring in a photocatalytic material after laser light irradiation can be measured. In Pump-probe spectroscopy, spectroscopy is basically performed using two light sources. First, the semiconductor surface is irradiated with a pulsed laser called " pump " to generate electron-hole pairs and then measured by irradiating the probe with a time difference from the pump irradiation. By selecting various wavelengths as the probe light, various physical and chemical properties of the material can be observed and evaluated. Typical pump-probe spectroscopy methods include transient absorption spectroscopy (TAS), time-resolved X-ray absorption spectroscopy (TR-XAS), time-resolved microwave conductivity (TRMC), and time-resolved terahertz spectroscopy (TR-THz). As shown in Figure 1.12, various reactions in the material after photoexcitation can be traced and observed depending on the wavelength of the applied probe light. Besides pump-probe spectroscopy, time-resolved photoluminescence that observes the emission decay after laser irradiation is known for analyzing radiative recombination kinetics. This section describes research aimed at elucidating the mechanism of photocatalytic reactions using ultrafast spectroscopy.

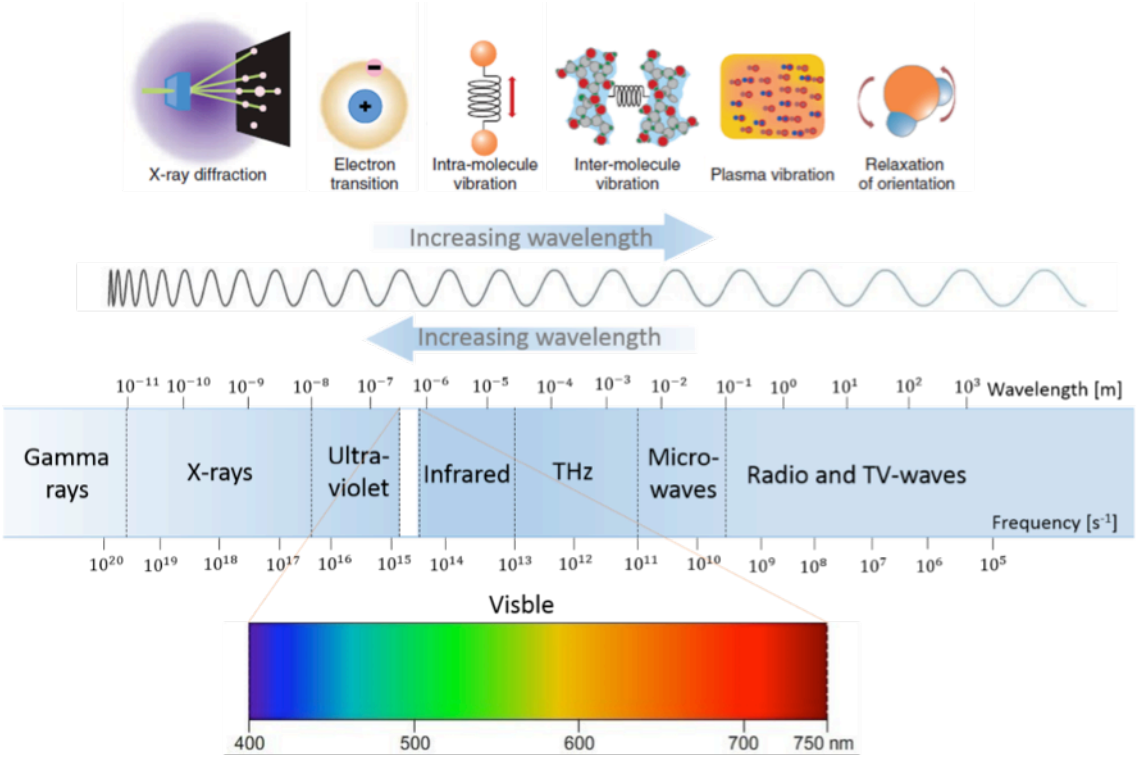

Figure 1.12. The electromagnetic spectram and corresponding photo-physical reaction.[103]

Transient absorption spectroscopy (TAS)

The ultrafast spectroscopy most used for elucidating the photocatalytic reaction is transient absorption spectroscopy in the visible-IR region.[90, 99, 104, 105] TAS can measure non-luminescent processes such as trapping of carriers generated by photoexcitation, charge transfer,[20, 94] carrier reaction,[94, 104] and recombination.[90, 105] In the photocatalytic reaction, usually a powder shape materials with the size of μm or smaller which possess a large number of surface defects show a higher photocatalytic performance compared with a single crystal due to its large specific surface area. However, this surface defect is believed to promote trapping of photoexcited charge carriers and reduce photocatalytic activity. To understand this discrepancy, Yamakata et al. reported TAS measurements on $SrTiO_3$ single crystals and powders.[99] $SrTiO_3$ single crystal has very few defects, so it does not show any significant traps in the Vis-NIR range and shows only signals derived from free electrons in CB. On the other hand, $SrTiO_3$ powder has abundant surface defects. The TAS signal reflects the trapped photoexcited charge carrier in the Vis-NIR range. Furthermore, since these trapped photoexcited charge carriers are trapped in defects, the mobility and the recombination probability decreases, resulting in relatively long life. The TAS measurement with the presence of oxygen and methanol indicate the trapped charge carriers still possess reactivity against these sacrificial agent. Thus, it is possible to verify the mechanism that has been predicted so far by ultrafast spectroscopy.[94, 99, 104]

Similarly, observation of charge transfer between $LaTiO_2N$ and cocatalyst has been studied by TAS. Figure 1.13 (A-C) shows the transient absorption spectra after excitation at 355 nm with $LaTiO_2N$ and with the loading Pt or CoO_x. In $LaTiO_2N$, broad transient absorption peaks with half-widths of about 2000 and 4000 cm^{-1} were observed at 17000 and 6000 cm^{-1} (580, 1700 nm). The peak at 17000 cm^{-1} can be attributed to absorption by trapped holes, and the peak at 6000 cm^{-1} can be attributed to absorption by trapped electrons. Subsequently, the effect of loading Pt cocatalyst was investigated on $LaTiO_2N$ sample. Pt is the material most commonly used as a hydrogen generation cocatalyst. As shown in Figure 1.13 (B), Over Pt loaded $LaTiO_2N$, two peaks are observed at 17000 and 6000 cm^{-1}. However, these transient absorption intensity ratios change by loading Pt, the intensity of 17000 cm^{-1} decreased, and conversely, the intensity of 6000 cm^{-1} increased. The change in the intensity ratio of trapped holes and trapped electrons indicates that the ratio of the number of photogenerated electrons and holes in the $LaTiO_2N$ photocatalyst has changed. Figure 1.13 (D) shows the results of a more detailed investigation of the decay process of trapped holes, trapped electrons, and free electrons by loading Pt. As shown in the figure, although the decay rate of free electrons at 2000 cm^{-1} and trapped electrons at 6000 cm^{-1} are increased by loading Pt, the decay rate of trapped holes at 17000 cm^{-1} was slowed by loading Pt. These results suggest that Pt cocatalyst capture the photoexcited electrons. When photoexcited electrons are trapped by Pt, the probability that holes recombine with electrons will decreases. Therefore, the lifetime of holes is considered to be longer. At this time, the decay of photoexcited electrons is more pronounced for free electrons of 2000 cm^{-1} than for trapped electrons of 6000 cm^{-1}. This result suggests that free electrons are easier to move to Pt than trapped electrons. The authors also confirmed the dependence of Pt on the loading amount. Transient absorption spectra show that when the loading amount of Pt is

increased from 0.5 wt% to 2 wt%, the signal intensity derived from holes decreases and becomes smaller than 0.5 wt%. This decrease in the signal intensity of the holes suggests that the holes have moved from $LaTiO_2N$ to Pt.

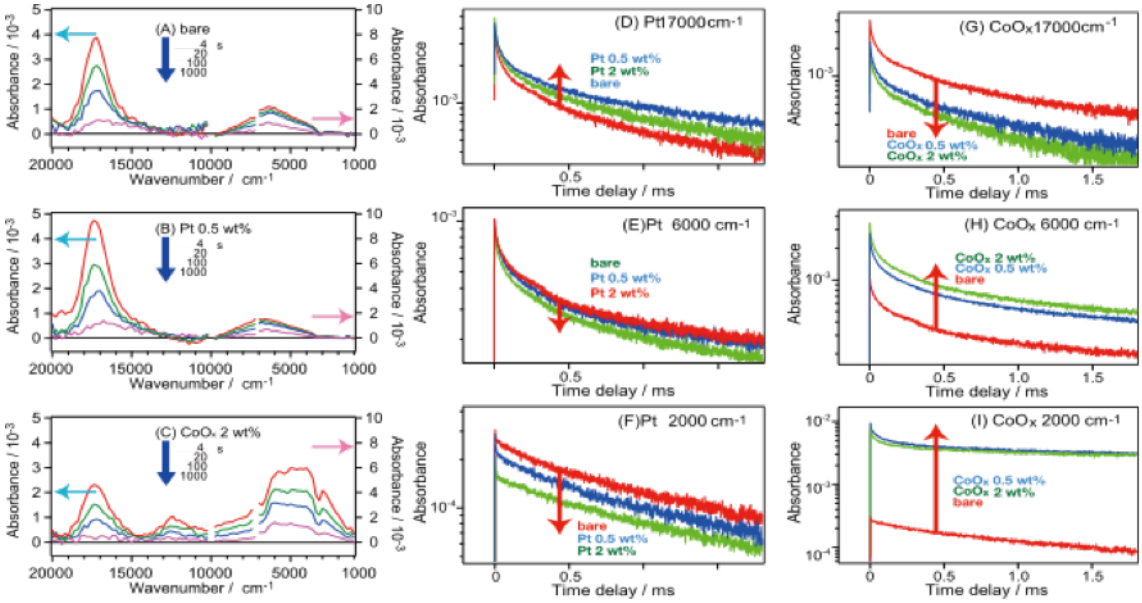

Figure 1.13. Time-resolved absorption spectra of $LaTiO_2N$ photocatalyst irradiated by UV laser pulses (355 nm, 6 ns duration, 0.5 mJ cm^{-2}, 5 Hz). (A) bare $LaTiO_2N$, (B) 0.5 wt% Pt-loaded $LaTiO_2N$, and (C) 2 wt% CoO_x-loaded $LaTiO_2N$. Decay of transient absorption of Pt-loaded LaTiO2N. The transient absorption was measured at 17000, 6000, and 2000 cm^{-1}. Decay of transient absorption of CoO_x loaded $LaTiO_2N$. The transient absorption was measured at 17000, 6000, and 2000 cm^{-1}. The sample was excited by 355nm laser pulses.[20]

A similar phenomenon is found in n-type GaN with loading Pt, where some Pt particles trap electrons but some Pt particles trap holes.[106] The selectivity of whether Pt particles capture electrons or holes is thought to depend on differences in the particle size and structure of the Pt cocatalysts. This result suggests that if over loading Pt cocatalysts trigger hole transfer which is not desired to occur. Generally, there is an optimum value for the amount of cocatalyst loading, and the steady-state reaction activity decreases after this amount, the TAS measurement presumptively suggested that excessive Pt loading cause hole transfer to Pt particle, leading the decreased steady-state reaction activity. However the dynamics of this hole transfer with the Pt loading is still not clear. Subsequently, the loading effect of CoO_x was investigated. CoO_x is a cocatalysts that promotes oxygen evolution. The authors have already reported that when CoO_x is supported on $LaTiO_2N$, water is oxidized with a quantum efficiency of about 30% in visible light below 600 nm. Figure 1.13 (C) shows the transient absorption spectra measured by exciting the band gap of CoO_x loaded $LaTiO_2N$. In the case of CoO_x loading, three peaks appeared at 17000, 12500, and 5000 cm^{-1}. The peaks of 17000 and 5000 cm^{-1} are observed for bare $LaTiO_2N$ and Pt loaded $LaTiO_2N$ catalysts. However, when CoO_x is loaded, the absorption intensity at 17000 cm^{-1} due to holes

decreases and the absorption intensity at 5000 cm^{-1} due to trapped electrons increases. These results indicate that the loading of CoO_x decreases the hole concentration and increases the number of electrons in $LaTiO_2N$. Interestingly, the absorption peak of trapped electrons shifts from 6000 to 5000 cm^{-1} when CoO_x is loaded. This wavelength shift suggests that the depth from the conduction band to shallower the electrons trap level. This result indicates that the depth of the trap level due to surface defects changes with surface treatment, and such information may be useful for the development of higher activity photocatalysts. Figure 1.13(G-I) shows the detailed decay process of photoexcited carriers. As the loading amount of CoO_x increases, the number of holes at 17000 cm^{-1} decreases monotonously. This decrease in the number of holes means that holes are trapped in CoO_x. On the other hand, in the case of 5000 cm^{-1} trapped electrons, increasing the loading amount of CoO_x increases the signal intensity and indicates that the lifetime of photoexcited electrons is increased. It can be seen that the change in free electrons at 2000 cm^{-1} increases more than 10 times by loading CoO_x. This results indicate that the recombination rate is suppressed by CoO_x cocatalyst capturing photoexcited hole. In another word, after excitation of CoO_x loaded $LaTiO_2N$, the electrons and holes are localized in $LaTiO_2N$ and CoO_x, respectively. As a result, recombination is suppressed and the lifetime of the electron is extended. A similar increase in electron lifetime due to hole trapping can be observed by introducing a hole trapping agent such as methanol. These results show that CoO_x traps holes very efficiently as well as hole trapping agents. The trapping of holes by CoO_x can also be confirmed from the shape of the transient absorption spectra in Figure.1.13 (C). When CoO_x is loaded, a new absorption peak appears at 12500 cm^{-1}, due to an increase in the oxidation state of Co. CoO_x has been reported to change color from yellow to gray when oxidized from Co (II) to Co (III).[107, 108] Therefore, the appearance of this 12500 cm^{-1} (800 nm) peak strongly suggests that holes have been trapped by CoO_x and that the valence of Co has increased. In other words, this oxidized CoO_x was the reaction center that oxidizes water. Furthermore, by using femtosecond TAS, the movement of photoexcited carriers between the photocatalyst material and the cocatalyst can be observed. The results are shown in Figure1.14, and even when 0.5 to 2 wt% of Pt is loaded on $LaTiO_2N$, the electron decay curve at 0 to 1000 ps almost overlaps with the bare $LaTiO_2N$ and cannot be distinguished.

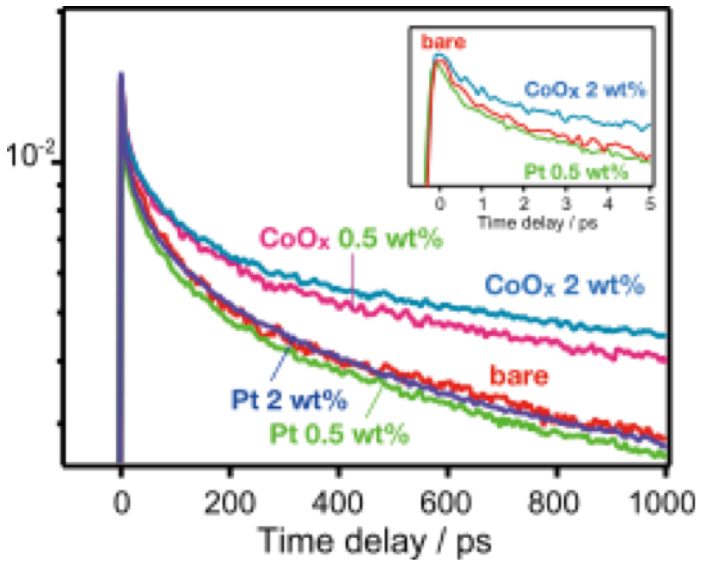

Figure 1.14. Decay of transient absorption at 2000 cm^{-1} on bare, CoO_x, and Pt loaded $LaTiO_2N$ photocatalysts in air. The sample was excited by 500 nm laser pulses.[20]

This result indicates that the electron transfer to Pt occurs in the time domain slower than 1000 ps. In the case of TiO_2, it has been reported that electron transfer to the supported Pt occurs within 10 ps. These results indicate that the rate of electron transfer to Pt depends on the nature of the supported catalyst. In the case of $LaTiO_2N$, the electron transfer is slower than that of TiO_2, which is considered to depend on the energy state of the photoexcited electrons generated in $LaTiO_2N$. This is probably because the electrons generated in $LaTiO_2N$ are trapped at the trap site that absorbs at 6000 cm^{-1}, which reduces the electron reaction activity and hence the slower electron transfer rate to Pt. On the other hand, when CoO_x is loaded, the decay rate of electrons decreases. The absorption intensity of 2000 cm^{-1} at time 0 fs is almost the same as that of the bare $LaTiO_2N$. However, over CoO_x loaded $LaTiO_2N$, the decay rate of electrons becomes slow within a few picoseconds. As the time elapses, the lifetime of electrons increases. These results indicate that hole transfer to CoO_x occurs within a few picoseconds. In other words, it was found that such a very fast hole trapping helps to improve the activity of water oxidation.

Time-resolved X-ray absorption spectroscopy (TR-XAS)

In TR-XAS, a femtosecond (fs) ultraviolet laser pulse is incident on the sample to start the photoreaction. Subsequently, an X-ray laser pulse that emits light in a very short time of femtosecond irradiate onto the sample with the time delay. By measuring X-ray absorption spectra while changing the wavelength of X-rays and time, an absorption spectrum of X-rays can be obtained. The X-ray absorption spectrum reflects the electron distribution and interatomic bond distance around the atom in the sample. By measuring the interval between the ultraviolet light and X-ray laser pulses precisely, it is possible to observe in real time the state of change after the start of the photoreaction. Especially, by using X-ray

as the probe light source, the full information about atomic-scale structural dynamics can be obtained which cannot be observed by ultrafast laser spectroscopy in the ultraviolet (UV), visible, and infrared regions. The conventional TR-XAS can only observe sub-nanoseconds, because X-ray pulsed laser was generated in the synchrotrons storage ring by slicing method. However recent technology such as SPring-8 Angstrom Compact Free Electron Laser (SACLA)[109] allow to shorten measurement time domain to femtoseconds. Obara et al., reported that femtoseconds TR-XAS measurement on anatase TiO_2.[110] The femto-seconds carrier dynamics in TiO_2 has been studied by TAS in the Vis-NIR region. Tamai et al. have studied anatase TiO_2 nanoparticles in an aqueous solution using TAS, and authors reported that 360 nm photoexcitation creates an immediate rise of the transient absorption signal at 520 nm derived from surface trapped holes; the estimated time constant was shorter than 50 fs.[111] On the other hand, absorption at 700 nm was assigned to surface trapped electrons at Ti^{3+} sites, and the trapping time scale was about 260 fs.[111] In similar TAS experiments on nano-crystalline films of TiO_2, Furube et al. have found that 355 nm pump laser created a trapped electron in less than 100 fs, whereas 266 nm excitation increased the electron trapping time to 150~250 fs.[112] These immediate electron traps were assigned as shallow traps near the surface, whereas relaxation to deep (bulk) traps was found to occur in hundreds of picoseconds.[90] It has been argued that the electrons in the conduction band are trapped within a movable distance of several nanometers after photogeneration, while holes can be transferred to the interface very rapidly.

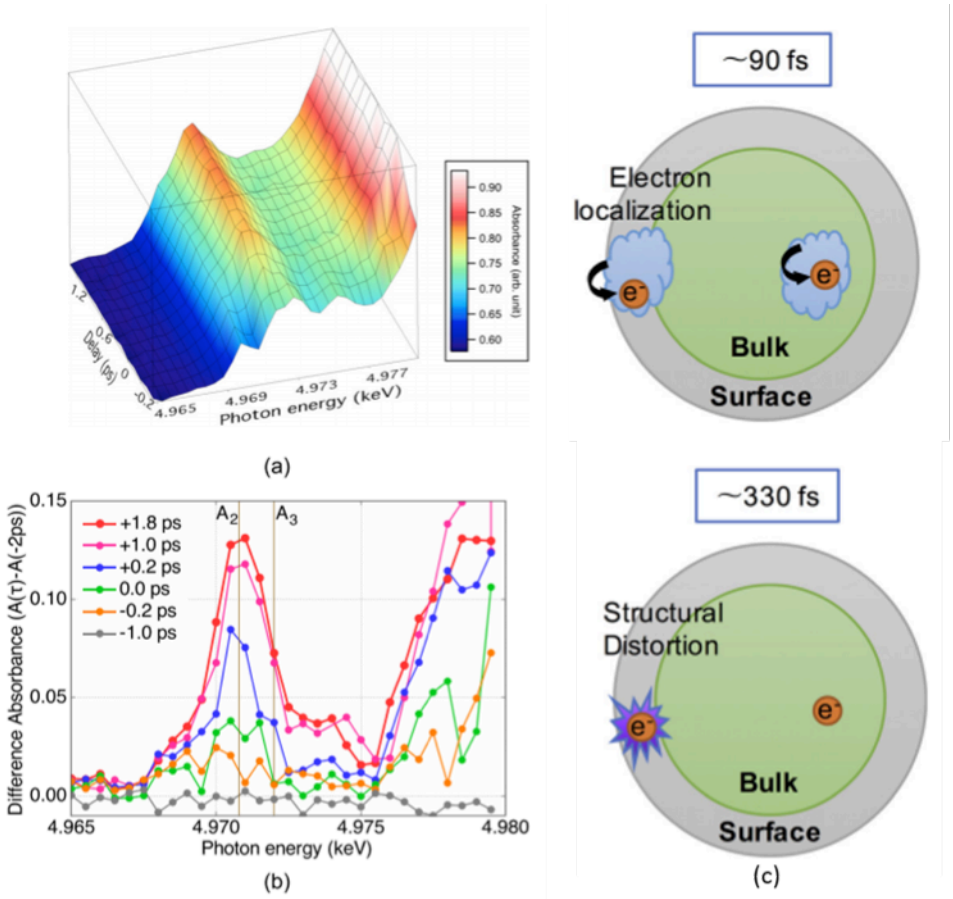

Figure 1.15. (a) Time-resolved X-ray absorption spectra and (b) their corresponding difference spectra of TiO_2 in the pre-edge region. To extract the difference absorbance spectra, subtracted the spectrum at 2.0 ps delay. It gets apparent that the absorbance at around A_2 peak gradually increases after UV irradiation. (c) Schematic illustration of carrier and structural distortion dynamics in an anatase TiO_2 nanoparticle. Electrons in the conduction band generated by the UV photoexcitation are localized at bulk or surface trapping sites within 90 fs. The structural distortions near the surface occur on a different timescale of 330 fs.[110]

The surface achieved hole plays an important role in photocatalytic oxidation activity of TiO_2. Figure 1.15 shows the evolution of the transient absorption intensity as a three-dimensional color-plot of the time-resolved X-ray absorption spectra in (a) and the difference spectra at certain time delays in (b). The difference spectra are obtained by subtracting the spectrum measured at 2 ps from each time-resolved spectra. In Figure 1.15 (b), two distinct features can be seen: The K-edge shift to lower photon energy almost instantaneously around zero delay and a prominent peak rises near the position of A_2 with time goes by. The instantaneous K-edge shift within around 90 fs suggests that electrons in the conduction band are localized very promptly by reducing a Ti^{4+} lattice site to form Ti^{3+}. The edge shift in this study suggests that almost one electron charge is localized around Ti to form Ti^{3+},[113,114] which is consistent

with theoretical prediction that up to 80% of the charge is localized at a single self-trapped Ti site.[115] The structural distortion at the penta-coordinated site near the surface can be assigned to the pre-edge transition.[114,116] The Ti 3d/4p orbital mixing caused by structural distortion from the octahedral symmetry enhance the pre-edge peak. Formation of hexa-coordinated polarons was shown theoretically to leave the pre-edge peak unaffected because distortion around the hexa-coordination does not break the local symmetry.[115] However, the enhancement of the pre-edge peak occurs most likely near the surface, structural distortion where at the penta-coordinated site to break the octahedral symmetry is negligible. Figure. 1.15 (c) explains proposed model of the carrier dynamics and structural distortion in an anatase TiO_2 nanoparticle after excitation of the ultrafast UV laser. The electrons excited into the conduction band of TiO_2 by UV photoexcitation are localized at the trapping sites in the bulk or near the surface within 90 fs, followed by structural deformation at the penta-coordinated sites near the surface within 330 fs. Both the self-trapped polarons and the penta-coordinated species form Ti^{3+}, which appear in the time-resolved X-ray absorption spectra with a similar K-edge shift. Since the subsequent structural distortion does not vary the edge shift, the edge-shift is decoupled from the structural dynamics causing the pre/above-edge signal evolution. Thus, unlike the above-described TAS, it is possible to perform photoexcitation dynamics analysis.

Time-resolved microwave conductivity (TRMC)

Charge mobility, which is an important physical properties governing the characteristics of materials used as semiconductors. The unit $m^2 \cdot V^{-1} s^{-1}$ is obtained by dividing the speed of charge (m s^{-1}) by the electric field (V m^{-1}). It has a very simple meaning: "How fast can an electron or hole move when a certain voltage is applied?" A microwave is an electromagnetic wave having a wavelength of about 1 cm, so that one photon has a small energy and cannot excite an oxide semiconductor, an organic semiconductor, or a complex. However, considering the oscillating electric field of microwaves, which can induce the rotational motion of molecules with electric dipoles like water. Similarly, it is possible to induce reciprocating motion of non-trapped charge carriers that are generated in the photocatalytic material. Since each substance has a specific electrical resistance, the energy of the irradiated microwave is absorbed as the kinetic energy for the movement of charge carriers. This is the principle of transient absorption in the microwave region, which allows to measure the electrical conductivity. Thus, the number and mobility of generated charge carriers can be evaluated from the magnitude of this absorption. This method enables evaluation of photoconductivity even in a sample such as a powder sample, which unable to attache systematically on electrode, and can be applied to the study of photocatalytic reaction. Suzuki et al. reported time-resolved microwave conductivity (TRMC) measurement over bismuth-based layered oxyhalide, which has been attracting attention as a highly efficient photocatalyst for water splitting, was synthesized at each sintering temperature.116 In this research, authors aimed to clarify the correlation between the TRMC results and photocatalytic activity in this bismuth-based layered oxyhalide system. Figure 1.16 (a) shows the decay curves of the TRMC signals over the Bi_4TaO_8Cl powder with different sintering temperatures. The higher the sintering temperature, the higher the crystallinity, and the higher

the microwave signal intensity at time zero ($\Delta\sigma_{max}$). As it turns out, there is a " positive effect " for efficient photocatalytic performance. For more in-depth understanding, the decay curves were fitted by the following the equation (9)

$$\varphi\Sigma\mu(t) = \frac{\varphi\Sigma\mu_0 \cdot k}{((k + \varphi\Sigma\mu_0)e^{kt}) - \varphi\Sigma\mu_0\gamma} + \varphi\Sigma\mu_d \cdot e^{-(k_d t)^{\beta}} \tag{1.14}$$

The first term analytical solution of the differential equation and second term represent the stretched exponential function to fit the extended plateau region, where $\phi\Sigma\mu_0$ is the initial intensity of $\phi\Sigma\mu$, k is the first-order rate constant, and γ is the second-order rate constant (in $V{\cdot}cm^{-2}$ units). $\phi\Sigma\mu_d$, k_d, and β (fixed at 0.3) are the intensity, the rate constant, and a power factor of the delayed component, respectively. The $\phi\Sigma\mu$ maxima ($\phi\Sigma\mu_{max}$) and half-lifetimes ($\tau_{1/2}$) of the TRMC signals are plotted as against to the calcination temperature in Figure 1.16 (b). With the increasing calcination temperature, the $\phi\Sigma\mu_{max}$ increases in a linear tendency, while $\tau_{1/2}$ decreases. The increased $\phi\Sigma\mu_{max}$ is reasonably attributed to improved crystallinity. The decreased $\tau_{1/2}$ can consider when the sintering temperature is high, the number of halogen defects (here, chlorine defects) increases, and the defects act as charge trap sites so that the microwave signal decays quickly (the lifetime is shortened). It turned out that "negative effect" happens at the same time. This trade-off revealed that this material has an appropriate sintering temperature (800 °C), and its activity decreases at both higher and lower temperatures. This tendency of the activity to become a volcano shape concerning temperature was successfully reproduced by plotting the product of microwave signal intensity and lifetime. Figure 1.16 (c) and (d) shows the excitation energy dependence of the $\phi\Sigma\mu_{max}$ and decay constant k. With increasing the excitation intensity, the $\phi\Sigma\mu_{max}$ decreased while the decay constant k is independent. The appearance of trap sites at high calcination temperatures was also examined by the $\phi\Sigma\mu_{max}$ dependence on the incident photon density, as shown in Figure 1.16 (e). The Bi_4TaO_8Cl samples sintered at 700 and 750 °C exhibit a monotonous decrease of $\phi\Sigma\mu_{max}$ with the increasing excitation energy due to accelerated recombination at the end of the pulse.

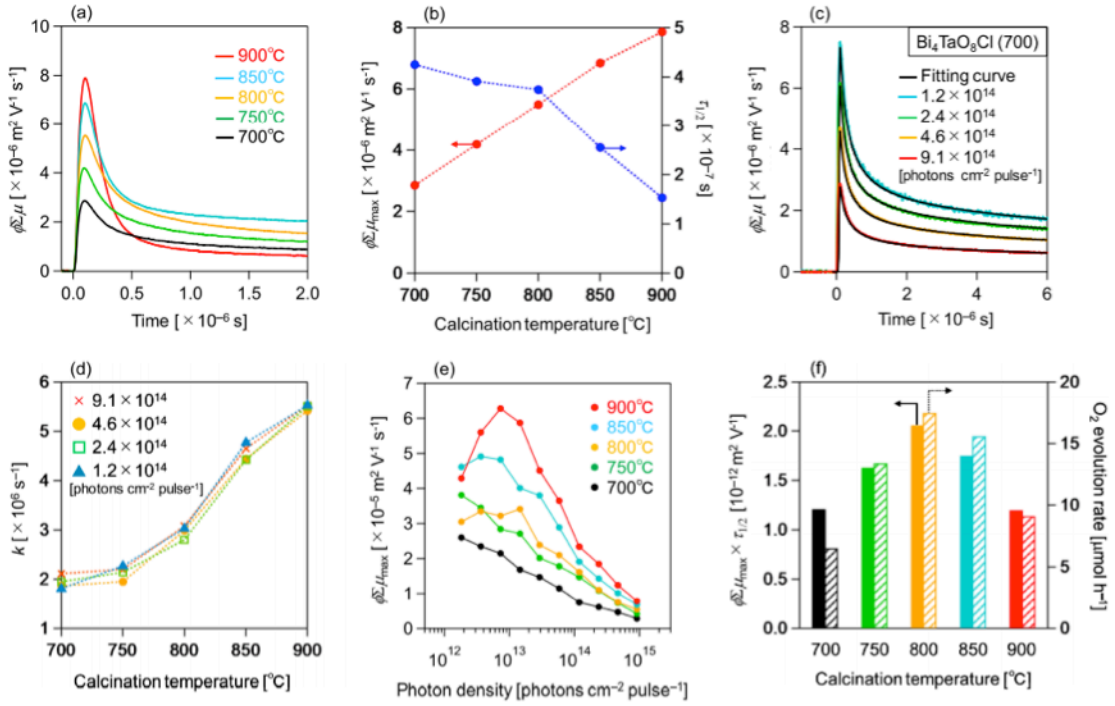

Figure 1.16. (a) TRMC transients of Bi_4TaO_8Cl samples calcined at different temperatures (λ_{ex} = 355 nm, I_0 = 9.1 × 1014 photons cm^{-2} pulse^{-1}). (b) TRMC transient maxima ($\phi\Sigma\mu_{max}$) and half-lifetimes ($\tau_{1/2}$). (c) $\phi\Sigma\mu$ transients of Bi_4TaO_8Cl (700) at varying incident excitation densities of (1.2 — 9.1) × 1014 photons cm^{-2} pulse^{-1}, along with the fitting curves (black lines). (d) First-order rate constants (k) obtained by analyzing the TRMC transients at different I_0 values. (e) $\phi\Sigma\mu_{max}$ dependence on I_0. (f) Correlation between $\phi\Sigma\mu_{max} \times \tau_{1/2}$ (solid bars) and the O_2 evolution rate over Bi_4TaO_8Cl (700 — 900°C) in aqueous $AgNO_3$ solution (striped bars). The O_2 evolution rates were taken from a previous report.[118]

On the other hand, convex curves are observed for the Bi_4TaO_8Cl samples prepared at high temperatures (800-900 °C). This phenomenon is caused by trap-filling effects (increase and saturation of $\phi\Sigma\mu_{max}$ at the high excitation). The efficient photocatalytic reactions correspond to the photogeneration of charge carriers and their transportability to the surface with minimal deactivation energy losses. Therefore, the parameters of $\phi\Sigma\mu_{max}$ and $\tau_{1/2}$ ($\phi\Sigma\mu_{max} \times \tau_{1/2}$), which envelops the charge carrier generation yield, mobility, and lifetime, was anticipated as a possible indicator of the predicting performance of photocatalysts. Figure 1.16 (f) displays the relationship between $\phi\Sigma\mu_{max} \times \tau_{1/2}$ and the O_2 evolution rate over Bi_4TaO_8Cl prepared at different calcination temperatures. Most importantly, the product $\phi\Sigma\mu_{max} \times \tau_{1/2}$ presents its maximum at 800 °C, perfectly corresponding with the O_2 evolution rate trend. The results so far indicated that photocatalytic activity could be diagnosed at high speed by using the product of microwave signal intensity and lifetime as an index. In 2019, Yamada et al. also reported the effects of Sr / Ti stoichiometry of strontium titanate ($SrTiO_3$) photocatalyst on charge trapping and hydrogen generation rate.[119] It has been reported that changing the ratio of Sr and Ti will greatly influence the hydrogen generation rate when

Sr becomes slightly excessive, but the origin of this phenomenon is unknown. The photoconductivity of stoichiometry-varied $SrTiO_3$ (Sr / Ti = 0.9-1.5) was measured by TRMC and analyzed using first- and second-order rate equations. The first-order rate constant (k) of the positive real part of photoconductivity ($\Delta\sigma'$) and the anomalous positive imaginary photoconductivity ($\Delta\sigma''$) correlated with the charge carrier traps progressively decreased with increasing Sr / Ti ratios. Simultaneously, the second-order rate (γ) of $\Delta\sigma'$ slowly decreased, which indicate that increasing Sr / Ti ratios reduce charge recombination probability. H_2 evolution rates of aqueous suspensions of Pt loaded $SrTiO_3$ resulting in stepwise improvement with increasing Sr / Ti from 1.10 to 1.15, related to the decreased trapping revealed by the TRMC evaluation. Thus, excess Sr is concomitant with the formation of Sr-rich Ruddlesden-Popper perovskites (such as Sr_2TiO_4 and $Sr_3Ti_2O_7$), which impedes charge carrier traps and improves overall photocatalytic activity. TRMC photoconductivity with detailed analyzes is a versatile approach for characterizing photocatalytic reaction mechanisms.

Time-resolved THz spectroscopy (TR-THz)

With the emerging of THz technology, THz spectroscopy allows us to observe low frequency intramolecular and intermolecular vibrations because the frequency of these vibrations lies in the THz region. Demanding and broadband THz radiation now can be generated with the source of Ti-sapphire lasers. Time-resolved spectroscopy is a powerful tool allowing us to evaluate the transient response of photocatalytic materials following the photoexcited reaction. Time-resolved attenuated total reflection spectroscopy (TR-ATR) is a suitable technique that enables demarcate excited state dynamics of the sample and solution with high absorption in the THz region. Time-resolved THz-ATR is powerful tool for evaluating molecular interactions in absorbing THz medium because these interactions usually occur in the THz region. Nguyen and Kimura et al. reported the direct observation of the photo-induced relaxation dynamics and reductive quenching process of the photoexcited state of photocatalytic molecule $[Re(CO)_(bpy)(P(OEt)_3)_2]$ (PF_6) (Re complex) in triethanolamine (TEOA) solvent as an electron donor by TR-ATR in the THz region.[120] Photocatalytic Re complex molecules absorb light and reduce CO2 to CO. In this photocatalytic reaction process progress three steps, 1) the Re complex absorbs light and the photogenerated electrons in the Re atom transfer to coordinated ligands. 2) Re complex receives electrons from surrounding an electron donor agent (TEOA). 3) Reducing carbon dioxide (CO_2) to carbon monoxide (CO). The authors focused on the charge transfer process to TEOA solvent and the Re complex and examined how this process occurred. As mentioned above, photocatalytic reactions have been observed mainly using TAS in the Vis-IR region. IR light can observe changes in the bonding force between two adjacent " atoms " in the molecule, i.e., intramolecular vibrations. On the other hand, the THz light we used can see changes in the binding force between two adjacent " molecules ", i.e., intermolecular vibrations. Thus how the TEOA molecules around the Re complex behave after light irradiation and electrons transfer from TEOA to Re complex could be discussed. However, THz light has the property of being easily absorbed by liquids, thus the transmission measurement with the TEOA solution, the THz light has greatly absorbed by TEOA solution. Therefore, a new method called total reflection spectroscopy

and THz spectroscopy was combined to enable THz spectroscopy of solutions. In order to perform ultrafast time-resolved measurement for THz total reflection spectroscopy, the THz pulse irradiates onto the sample with a slight delay after exciting a pulsed laser with a wavelength of 400 nm. The authors successfully observed the photocatalytic reaction mechanism after pulsed laser irradiation for the first time on a picosecond time scale using time-resolved THz total reflection spectroscopy.

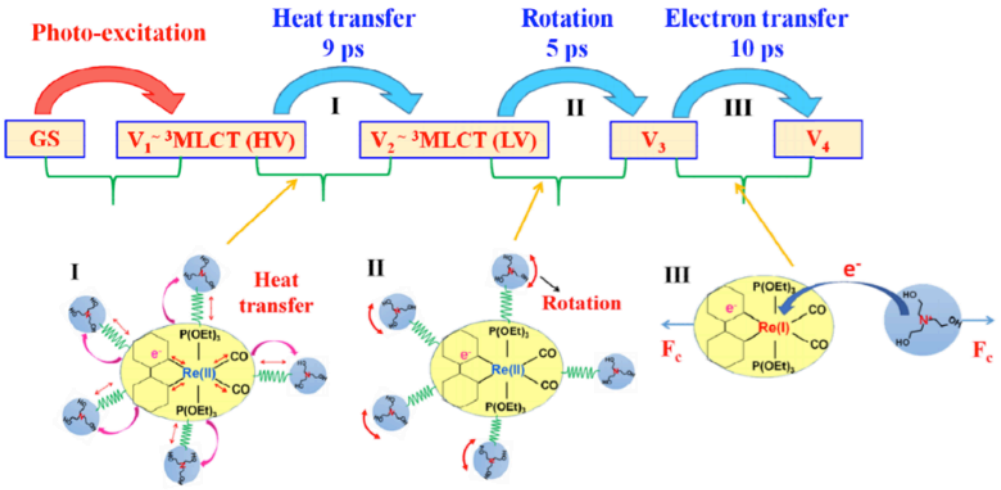

Figure 1.17. Schematic diagram and molecular forms after photoexcitation. The top diagram shows the three-step dynamic from the highest state V_1 through the lowest excited state V_4 of $[Re(CO)_2(bpy)(P(OEt)_3)_2](PF_6)$ in TEOA solvent in the range of 0.3-2.5 THz. The bottom diagram illustrates the interaction between Re complex and TEOA molecules corresponding to each dynamical step I-III.[120]

According to the results of TR-ATR in the THz region, after the excitation light irradiation onto Re complex, the temperature of the Re complex rapidly rises by absorbing light. Within 9 ps, this heat transfer to surrounding TEOA molecules and cooling down Re complex as shown in Figure 1.17 (I). Following the heat transfer process, from 9 to 14 picoseconds, the TEOA molecule rotated, leading to shorten distance to the Re complex, as shown in Figure 1.17 (II). Finally, after 14 picoseconds, as shown in Figure 1.17. (III), charge transfer from the TEOA molecule to the Re atom occurred. The sum of peak area of TR-ATR spectra decreases from 14 ps was interpreted by the repulsive Coulomb force caused by the electron transfer process from nitrogen atoms to Re atoms. The authors have succeeded in observing how the reducing agent moves and electrons move on a swift time scale of picoseconds in a photocatalytic reaction.

Time-resolved photoluminescent spectroscopy (TR-PL)

In addition to pump-probe spectroscopy, time-resolved photoluminescent spectroscopy for observing transient light emission after pulsed laser irradiation is known as ultrafast spectroscopy. Unlike the spec-

troscopy mentioned above, which observes non-radiative charge carriers dynamics, this spectroscopic method can directly observe the radiative recombination process. Yamakata et al. evaluated the charge carriers dynamics over Ni, Ta-codoped $SrTiO_3$ by TAS, and TR-PL to investigate the cause of the significant loss of activity in the ultraviolet light region, while Ni, Ta-codoped $SrTiO_3$ shows visible light response. $SrTiO_3$ exhibits a PL response only when excited by a high-density light source such as laser irradiation. On the other hand, Ni, Ta-codoped $SrTiO_3$ exhibits a PL emission at 1250 nm during the d-d downward transition from $^3T_{2g}$ to $^3A_{2g}$ in the oxygen octahedron within the dopant Ni cation. The authors focused on this physical property to figure out whether the impurity acting as a recombination center that is disadvantageous for the photocatalytic reaction. Comparing the lifetime of free electrons in CB of $SrTiO_3$ observed with TAS and TRPL derived from Ni d-d downwards, PL emission decay was much faster than free electron decay. If Ni dopant sites are a recombination center, the free electrons in CB are intermittently trapped at the Ni dopant site, so the decay time should be the same or a little longer. The decrease in activity concluded that Ni center is not a direct recombination center. (Figure 1.18.)

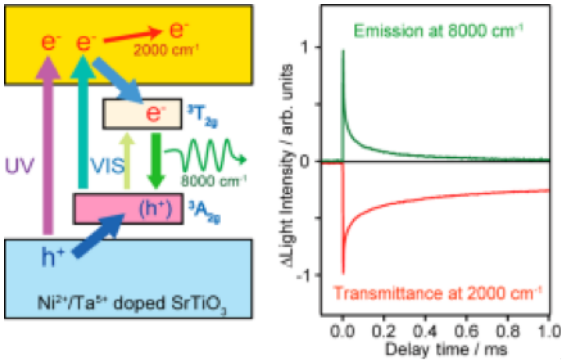

Figure 1.18. schematic diagram of the charge carriers dynamics in Ni, Ta-codoped SrTiO3 (left) and the comparison between the TRPL decay and TAS decay curves.[120]

Bian et al. also reported carrier dynamics using TRPL with single-particle microspectroscopy over the Meso-TiO_2 superstructure.[121] It was found that the light emitted from the center of the surface was much weaker than that of the edge. Also, the decay speed of PL emission from the center was faster than that of the edge. This indicates that the excitons generated near the center of the plane are trapped at the edge and luminescent recombination after the random walk. More importantly, it was found that when Au or Pt is used as cocatalysts and loaded by the photodeposition method, the PL emission is significantly suppressed. Because the photodeposition over the Meso-TiO_2 superstructure is preferentially deposited from the edge, this indicates that the edge has the ability to exchange electrons. As well as steady state PL measurement, in the TRPL measurement, the emission intensity of PL was remarkably suppressed, and the decay was further accelerated. (Figure 1.19) This indicates that the excited electrons are trapped in noble metals cocatalysts such as Au and Pt.[121]

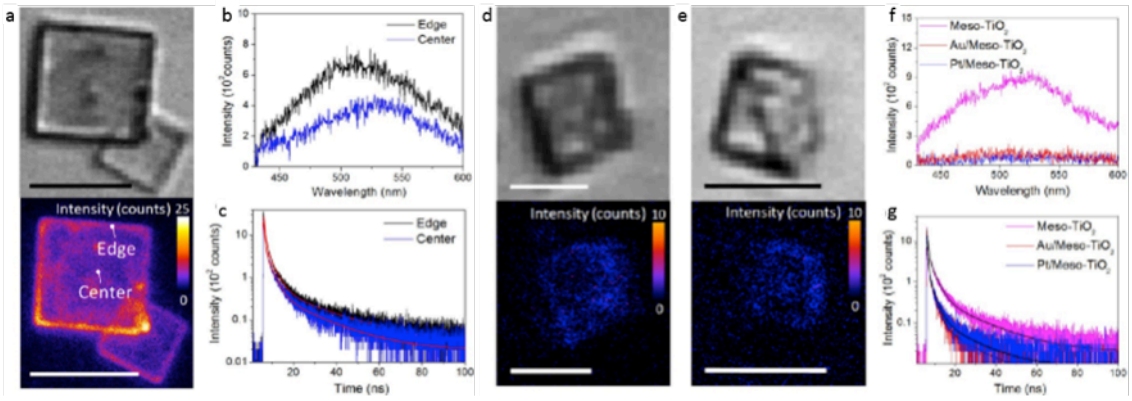

Figure 1.19. schematic diagram of the charge carriers dynamics in Ni, Ta-codoped $SrTiO_3$ (left) and the comparison between the TRPL decay and TAS decay curves.[121]

Similarly, Godin et al. have evaluated carrier dynamics to suggest the necessity for cocatalyst loading in the typical organic semiconductor g-C_3N_4. In this material, the TRPL signal decays faster than TAS. According to the wavelength of PL emission, the radiative recombination process occurs from near CBM to VBM, but the non-emission carriers accumulate at the trapping state located at a deeper position (1 eV lower than CBM), this high concentrated trapped unreactive electrons heavily impede accumulation of holes for multihole reaction. According to the conduction band position of carbon nitride (-1.3 V vs. NHE) and the proton reduction potential of -590 mV vs. NHE at pH = 10, a loss of 600-700 meV in energy stored would result in complete loss of driving force for proton reduction.[122] As mention above, in recent years, with the development of laser technology, ultrafast spectroscopy technology has become a more powerful tool for understanding the most critical carrier dynamics in the photocatalytic reaction mechanism, but there are few reports of research over various photocatalysts. It still takes much effort to elucidate all the carrier dynamics of the photocatalytic reactions. In particular, TAS has recently been applied to various materials, but there have been few reports focusing on the drawbacks of modification associated with a visible light response and on the carrier dynamics in newly developed organic semiconductors.

In my dissertation, $SrTiO_3$ and conjugated polymer photocatalyst were selected as models and their carrier dynamics were evaluated.

1.5 Research motivation

As introduced above, photocatalytic hydrogen production, and CO_2 photoreduction are an ideal solution to global energy and environmental issues and therefore attract enormous interest. Unfortunately, the charge carriers dynamics that govern the photocatalytic reaction performance has not yet been elucidated the mechanism of how the charge carriers take part in photocatalytic reaction completely. Thus, the rational design and developing of a low-cost, sustainable, and efficient visible-light photocatalyst continues

to be a severe challenge in this field. As mentioned in section 1.3.1, perovskite structure materials can be one of the outstanding candidates for stable and highly active photocatalysts by the doping method. However, the adverse effects of the doping method have rarely been addressed and only the positive impact of doping were emphasized. To construct further sophisticated photocatalytic architecture, the charge carrier dynamics in the semiconductors must be solely explained. Also, the relationship between photocatalysts and co-catalysts has a critical impact on the photocatalytic reaction. The loading amount is one of the essential factors for seeking optimized photocatalysts. However, the loading amount of co-catalysts has been discussed only in terms of increasing the photocatalytic activity, the influence of loading amount for the charge carrier dynamics is essential to understand the photocatalytic reaction mechanism. Furthermore, recently, organic conjugated polymer photocatalysts with a complex organometallic compound as co-catalysts have been applied for photocatalytic CO_2 reduction. This kind of CPs and organometallic compound co-catalysts system has high potential towards highly active photocatalysts. However, this new photocatalytic system has a short history, and there are very few reports on the mechanism and the dynamics of electron transfer from conjugated polymer to co-catalysts. The final objective is to propose reasonable conjecture for the charge carriers dynamics in each step of photocatalytic reaction over the inorganic and organic semiconductors. The dissertation contains five chapters, and below are the summaries of the remaining four chapters.

Chapter 2 Transient absorption spectroscopy for analyzing charge carriers dynamics in the photocatalytic reaction

A deeper understanding of transient phenomena in semiconductors is vital for the development of new photocatalysts with improved properties. A higher charge carrier concentration and longer charge carrier lifetime are expected to increase the photocatalytic hydrogen evolution and CO_2 reduction. Transient absorption spectroscopy (TAS) is a feasible technique for the detection of charge carriers, which facilitates a more in-depth insight into the fundamental processes of the photocatalytic reaction. In chapter 2, the principle of TAS is explained.

Chapter 3 Photogenerated charge carriers dynamics on La and/or Cr doped $SrTiO_3$ nanoparticles studied by transient-absorption spectroscopy

As mention in section 1.3.1, one critical problem but rarely addressed is the drastically decreased photocatalytic activity under UV-light despite the increased activity in the visible light region, resulting in a decreased total performance under the full solar spectrum. In order to elucidate the origin of this commonly observed phenomenon, herein, we chose La, Cr-codoped $SrTiO_3$ as a proof-of-concept model to probe the effect of dopants on the behavior of photogenerated charge carriers by TAS. By observing the excitons, it is found that under UV irradiation, the excitation occurring from the Cr impurity bands limits the excitation of $SrTiO_3$ from VB, causing the drastic decrease of the photocatalytic activity overdoped material. The widely proposed recombination at dopant sites, however, was not dominant for declining the UV light-irradiated performance, especially in the presence of reactant gas (methanol vapor).

Chapter 4 Photogenerated charge carriers dynamics on Pt loaded $SrTiO_3$ nanoparticles studied by transient-absorption spectroscopy

In this chapter, to examine the loading effect of Pt cocatalysts, the transient absorption spectra were measured over different amount of Pt and Ni loaded $SrTiO_3$ as a comparison. The transient absorption measurements have carried out in the N_2, O_2, and MeOH vapor, which work as the inert, electron scavenger, and hole scavenger, respectively. With the increase of Pt loading amount, the calculated decay constant was found to linearly increase in the N_2 and O_2 atmospheres. While in the case of Ni loading, the decay constant was almost constant. This linear relationship between Pt loading amount and decay constant suggests that Pt nano-particles on $SrTiO_3$ capture both photogenerated electron and hole in the N_2 and O_2 atmospheres. On the other hand, in the presence of MeOH vapor, interestingly, the decay constants increase rate has been suppressed compared with that observed in the N_2 and O_2 atmospheres. It indicates with the existence of hole scavenger MeOH vapor that Pt would no longer act as recombination center. This also explain why Pt loaded $SrTiO_3$ exhibits excellent photocatalytic HER performance in the MeOH aqueous solution. Therefore, for the cocatalyst, the localized density of state and an appropriate hydrogen absorption/desorption energy property are highly desired for efficient overall water splitting. In this chapter, the effect of Pt loading over the charge carrier dynamics on $SrTiO_3$ will be discussed.

Chapter 5 Direct observation of photogenerated electron transfer process from cascaded π πconjugation polymer to CO_2 molecule for CO_2 photoreduction

The photoreduction of CO_2 to fuels offer a promising strategy for managing the global carbon neutrisation. Nevertheless, the decisive process of oriented photogenerated electron delivery presents a considerable challenge. In chapter 5, we report the construction of intermolecular cascaded π-conjugation channels for CO_2 photoreduction by modifying both intramolecular and intermolecular conjugation of conjugated polymers (CPs). Theoretical simulations and transient spectroscopies were applied to evaluate the charge carriers dynamics in the CPs photocatalysts. TR-MC measurement shows that the alkynyl group between the units molecular of CPs provoke the electrons delocalization, whereas the electron localizes in the CPs composed of C-C direct bonding. This electrons localization dynamics suggests that the ability to tune the localized electrons in a benzen section of the CPs enables control over π-π interactions with an organometallic complexes cocatalyst. Also the electrons transfer from CPs to cocatalysts were observed by pico-seconds TAS measurement. This work devotes to the most critical challenge in the charge dynamics evaluation, especially photogenerated electron delivery, providing new perspectives in the molecular architecture of CPs for CO_2 photoreduction.

Chapter 6 General conclusion

This chapter presents the overall conclusion of this dissertation. Moreover, future prospects based on the research are also given in the chapter.

References

[1] Hoffmann, M. R.; Martin, S. T.; Choi, W.; Bahnemann, D. W., Environmental Applications of Semiconductor Photocatalysis. *Chemical reviews*, **1995**, *95* (1), 69-96.

[2] Domen, K.; Naito, S.; Onishi, T.; Tamaru, K.; Soma, M., Study of the photocatalytic decomposition of water vapor over a nickel(II) oxide-strontium titanate ($SrTiO_3$) catalyst. *The Journal of Physical Chemistry*, **1982**, *86* (18), 3657-3661.

[3] Kanemoto, M.; Shiragami, T.; Pac, C. J.; Yanagida, S., SEMICONDUCTOR PHOTOCATALYSIS - EFFECTIVE PHOTOREDUCTION OF CARBON-DIOXIDE CATALYZED BY ZNS QUANTUM CRYSTALLITES WITH LOW-DENSITY OF SURFACE-DEFECTS. *The Journal of Physical Chemistry*, **1992**, *96* (8), 3521-3526.

[4] Sclafani, A.; Palmisano, L.; Schiavello, M., N_2 PHOTOREDUCTION AND PHENOL AND NITROPHENOL ISOMERS PHOTOOXIDATION AS EXAMPLES OF HETEROGENEOUS PHOTOCATALYTIC REACTIONS. *Research on Chemical Intermediates*, **1992**, *18* (2-3), 211-226.

[5] Chen, X.; Ye, J.; Ouyang, S.; Kako, T.; Li, Z.; Zou, Z., Enhanced Incident Photon-to-Electron Conversion Efficiency of Tungsten Trioxide Photoanodes Based on 3D-Photonic Crystal Design. *ACS Nano*, **2011**, *5* (6), 4310-4318.

[6] Tong, H.; Ouyang, S.; Bi, Y.; Umezawa, N.; Oshikiri, M.; Ye, J., Nano-photocatalytic Materials: Possibilities and Challenges. *Advanced Materials*, **2012**, *24* (2), 229-251.

[7] Fox, M. A.; Dulay, M. T., Heterogeneous photocatalysis. *Chemical reviews*, **1993**, *93* (1), 341-357.

[8] Hagfeldt, A.; Graetzel, M., Light-Induced Redox Reactions in Nanocrystalline Systems. *Chemical reviews*, **1995**, *95* (1), 49-68.

[9] Maeda, K.; Domen, K., New Non-Oxide Photocatalysts Designed for Overall Water Splitting under Visible Light. *The Journal of Physical Chemistry*, **2007**, *111* (22), 7851-7861.

[10] Ouyang, S.; Tong, H.; Umezawa, N.; Cao, J.; Li, P.; Bi, Y.; Zhang, Y.; Ye, J., Surface-alkalinization-induced enhancement of photocatalytic H_2 evolution over $SrTiO_3$-based photocatalysts. *Journal of the American Chemical Society*, **2012**, *134* (4), 1974-7.

[11] Umebayashi, T.; Yamaki, T.; Itoh, H.; Asai, K., Analysis of electronic structures of 3d transition metal-doped TiO_2 based on band calculations. *Journal of Physics and Chemistry of Solids*, **2002**, *63* (10), 1909-1920.

[12] Asahi, R.; Morikawa, T.; Ohwaki, T.; Aoki, K.; Taga, Y., Visible-Light Photocatalysis in Nitrogen-Doped Titanium Oxides. *Science*, **2001**, *293* (5528), 269-271.

[13] Liu, L.; Li, P.; Adisak, B.; Ouyang, S.; Umezawa, N.; Ye, J.; Kodiyath, R.; Tanabe, T.; Ramesh, G. V.; Ueda, S.; Abe, H., Gold photosensitized $SrTiO_3$ for visible-light water oxidation induced by Au interband transitions. *Journal of Materials Chemistry A*, **2014**, *2* (25), 9875.

[14] Chandrasekharan, N.; Kamat, P. V., Improving the photoelectrochemical performance of nanostructured TiO_2 films by adsorption of gold nanoparticles. *The Journal of Physical Chemistry B*, **2000**, *104* (46), 10851-10857.

[15] Tian, Y.; Tatsuma, T., Plasmon-induced photoelectrochemistry at metal nanoparticles supported on nanoporous TiO_2. *Chemical Communications*, **2004**, (16), 1810-1811.

[16] Youngblood, W. J.; Lee, S.-H. A.; Maeda, K.; Mallouk, T. E., Visible Light Water Splitting Using Dye-Sensitized Oxide Semiconductors. *Accounts of Chemical Research*, **2009**, *42* (12), 1966-1973.

[17] Hirano, K.; Suzuki, E.; Ishikawa, A.; Moroi, T.; Shiroishi, H.; Kaneko, M., Sensitization of TiO_2 particles by dyes to achieve H_2 evolution by visible light. *Journal of Photochemistry and Photobiology A: Chemistry*, **2000**, *136* (3), 157-161.

[18] Takahashi, M.; Mita, K.; Toyuki, H.; Kume, M., PT-TIO_2 THIN-FILMS ON GLASS SUBSTRATES AS EFFICIENT PHOTOCATALYSTS. *Journal of Materials. Science*, **1989**, *24* (1), 243-246.

[19] Kaise, M.; Nagai, H.; Tokuhashi, K.; Kondo, S.; Nimura, S.; Kikuchi, O., ELECTRON-SPIN-RESONANCE STUDIES OF PHOTOCATALYTIC INTERFACE REACTIONS OF SUSPENDED M/TIO(2) (M=PT, PD, IR, RH, OS, OR RU) WITH ALCOHOL AND ACETIC-ACID IN AQUEOUS-MEDIA. *Langmuir*, **1994**, *10* (5), 1345-1347.

[20] Yamakata, A.; Kawaguchi, M.; Nishimura, N.; Minegishi, T.; Kubota, J.; Domen, K., Behavior and Energy States of Photogenerated Charge Carriers on Pt- or CoO_x-Loaded $LaTiO_2N$ Photocatalysts: Time-Resolved Visible to Mid-Infrared Absorption Study. *The Journal of Physical Chemistry C*, 2014, *118* (41), 23897-23906.

[21] Sayama, K.; Arakawa, H., EFFECT OF NA2CO3 ADDITION ON PHOTOCATALYTIC DECOMPOSITION OF LIQUID WATER OVER VARIOUS SEMICONDUCTOR CATALYSTS. *Journal of Photochemistry and Photobiology A: Chemistry*, **1994**, *77* (2-3), 243-247.

[22] Jia, H.; Xu, H.; Hu, Y.; Tang, Y.; Zhang, L., TiO_2@CdS coreshell nanorods films: Fabrication and dramatically enhanced photoelectrochemical properties. *Electrochemistry Communications*, **2007**, *9* (3), 354-360.

[23] Chang, K.; Hai, X.; Pang, H.; Zhang, H.; Shi, L.; Liu, G.; Liu, H.; Zhao, G.; Li, M.; Ye, J., Targeted Synthesis of 2H- and 1T-Phase MoS_2 Monolayers for Catalytic Hydrogen Evolution. *Advanced Materials*, **2016**, *28* (45), 10033-10041.

[24] Hai, X.; Chang, K.; Pang, H.; Li, M.; Li, P.; Liu, H.; Shi, L.; Ye, J., Engineering the Edges of MoS_2 (WS_2) Crystals for Direct Exfoliation into Monolayers in Polar Micromolecular Solvents. *Journal of the American Chemical Society*, **2016**, *138* (45), 14962-14969.

[25] Wang, Q.; Hisatomi, T.; Jia, Q.; Tokudome, H.; Zhong, M.; Wang, C.; Pan, Z.; Takata, T.; Nakabayashi, M.; Shibata, N.; Li, Y.; Sharp, I. D.; Kudo, A.; Yamada, T.; Domen, K., Scalable water splitting on particulate photocatalyst sheets with a solar-to-hydrogen energy conversion efficiency exceeding 1%. *Nature Materials*, **2016**, *15*, 611.

[26] Hirai, T.; Shiojiri, S.; Komasawa, I., PREPARATION OF METAL SULFIDE COMPOSITE ULTRAFINE PARTICLES IN REVERSE MICELLAR SYSTEMS AND THEIR PHOTOCATALYTIC PROPERTY. *Journal Chemical Engineering Japan*, **1994**, *27* (5), 590-597.

[27] Fujishima, A.; Honda, K., Electrochemical Photolysis of Water at a Semiconductor Electrode. *Nature*, **1972**, *238* (5358), 37-38.

[28] Inoue, T.; Fujishima, A.; Konishi, S.; Honda, K., Photoelectrocatalytic reduction of carbon dioxide in aqueous suspensions of semiconductor powders. *Nature*, **1979**, *277* (5698), 637-638.

[29] Momirlan, M.; Veziroglu, T. N., The properties of hydrogen as fuel tomorrow in sustainable energy system for a cleaner planet. International. *Journal of Hydrogen Energy*, **2005**, *30* (7), 795-802.

[30] Badwal, S. P. S.; Giddey, S.; Munnings, C., Hydrogen production via solid electrolytic routes. *Wiley Interdisciplinary Reviews: Energy and Environment*, **2013**, *2* (5), 473-487.

[31] Chen, X.; Shen, S.; Guo, L.; Mao, S. S., Semiconductor-based Photocatalytic Hydrogen Generation. *Chemical reviews*, **2010**, *110* (11), 6503-6570.

[32] Tu, W.; Zhou, Y.; Zou, Z., Photocatalytic Conversion of CO_2 into Renewable Hydrocarbon Fuels: State-of-the-Art Accomplishment, Challenges, and Prospects. *Advanced Materials*, **2014**, *26* (27), 4607-4626.

[33] Fujita, E., Photochemical carbon dioxide reduction with metal complexes. *Coordination Chemistry Reviews*, **1999**, 185-186, 373-384.

[34] Iizuka, K.; Wato, T.; Miseki, Y.; Saito, K.; Kudo, A., Photocatalytic Reduction of Carbon Dioxide over Ag Cocatalyst-Loaded $ALa_4Ti_4O_{15}$ (A = Ca, Sr, and Ba) Using Water as a Reducing Reagent. *Journal of the American Chemical Society*, **2011**, *133* (51), 20863-20868.

[35] Bhalla, A. S.; Guo, R.; Roy, R., The perovskite structure a review of its role in ceramic science and technology. *Material Research Innovations*, **1999**, *4* (1), 3-26.

[36] Kudo, A.; Miseki, Y., Heterogeneous Photocatalyst Materials for Water Splitting. *Chemical Society Reviews*, **2008**, *38*, 253-278

[37] Goldschmidt, V. M., Die Gesetze der Krystallochemie. *Naturwissenschaften*, **1926**, *14* (21), 477-485.

[38] Liu, Y.; Yang, Z.; Liu, S., Recent Progress in Single-Crystalline Perovskite Research Including Crystal Preparation, Property Evaluation, and Applications. *Advanced Science*, **2018**, *5* (1), 1700471.

[39] Wang, D.; Kako, T.; Ye, J., Efficient Photocatalytic Decomposition of Acetaldehyde over a Solid-Solution Perovskite $(Ag_{0.75}Sr_{0.25})(Nb_{0.75}Ti_{0.25})O_3$ under Visible-Light Irradiation. *Journal of the American Chemical Society*, **2008**, *130* (9), 2724-2725.

[40] Maeda, K., Photocatalytic water splitting using semiconductor particles: History and recent developments. *Journal of Photochemistry and Photobiology C: Photochemistry Reviews*, **2011**, *12* (4), 237-268.

[41] Kavan, L.; Grätzel, M.; Gilbert, S. E.; Klemenz, C.; Scheel, H. J., Electrochemical and Photoelectrochemical Investigation of Single-Crystal Anatase. *Journal of the American Chemical Society*, **1996**, *118* (28), 6716-6723.

[42] Kato, H.; Kudo, A., Visible-Light-Response and Photocatalytic Activities of TiO_2 and $SrTiO_3$ Photocatalysts Codoped with Antimony and Chromium. *The Journal of Physical Chemistry B*, **2002**, *106* (19), 5029-5034.

[43] Cardona, M., Optical Properties and Band Structure of $SrTiO_3$ and $BaTiO_3$. *Physical Review*, **1965**, *140* (2A), A651-A655.

[44] Wagner, F. T.; Somorjai, G. A., Photocatalytic hydrogen production from water on Pt-free $SrTiO_3$ in alkali hydroxide solutions. *Nature*, **1980**, 285 (5766), 559-560.

[45] Wagner, F. T.; Somorjai, G. A., Photocatalytic and photoelectrochemical hydrogen production on strontium titanate single crystals. *Journal of the American Chemical Society*, **1980**, *102* (17), 5494-5502.

[46] Domen, K.; Naito, S.; Soma, M.; Onishi, T.; Tamaru, K., Photocatalytic decomposition of water vapour on an NiO-$SrTiO_3$ catalyst. *Journal of the Chemical Society, Chemical Communications*, **1980**, (12), 543-544.

[47] Domen, K.; Kudo, A.; Onishi, T.; Kosugi, N.; Kuroda, H., Photocatalytic decomposition of water into hydrogen and oxygen over nickel(II) oxide-strontium titanate ($SrTiO_3$) powder. 1. Structure of the catalysts. *The Journal of Physical Chemistry*, **1986**, *90* (2), 292-295.

[48] Domen, K.; Naito, S.; Onishi, T.; Tamaru, K., Photocatalytic decomposition of liquid water on a NiO/$SrTiO_3$ catalyst. *Chemical Physics Letters*, **1982**, *92* (4), 433-434.

[49] Kato, H.; Asakura, K.; Kudo, A., Highly Efficient Water Splitting into H_2 and O_2 over Lanthanum-Doped $NaTaO_3$ Photocatalysts with High Crystallinity and Surface Nanostructure. *Journal of the American Chemical Society*, **2003**, *125* (10), 3082-3089.

[50] Meng, X.; Zuo, G.; Zong, P.; Pang, H.; Ren, J.; Zeng, X.; Liu, S.; Shen, Y.; Zhou, W.; Ye, J., A rapidly room-temperature-synthesized Cd/ZnS:Cu nanocrystal photocatalyst for highly efficient solar-light-powered CO_2 reduction. *Applied Catalysis B: Environmental*, **2018**, *237*, 68-73.

[51] Wang, D.; Ye, J.; Kako, T.; Kimura, T., Photophysical and Photocatalytic Properties of $SrTiO_3$ Doped with Cr Cations on Different Sites. *The Journal of Physical Chemistry B*, **2006**, *110* (32), 15824-15830.

[52] Yu, H.; Ouyang, S.; Yan, S.; Li, Z.; Yu, T.; Zou, Z., Solgel hydrothermal synthesis of visible-light-driven Cr-doped $SrTiO_3$ for efficient hydrogen production. *Journal of Materials Chemistry*, **2011**, *21* (30), 11347-11351.

[53] Xie, T.-H.; Sun, X.; Lin, J., Enhanced Photocatalytic Degradation of RhB Driven by Visible Light-Induced MMCT of Ti(IV)-O-Fe(II) Formed in Fe-Doped $SrTiO_3$. *The Journal of Physical Chemistry C*, **2008**, *112* (26), 9753-9759.

[54] Piskunov, S.; Lisovski, O.; Begens, J.; Bocharov, D.; Zhukovskii, Y. F.; Wessel, M.; Spohr, E., C-, N-, S-, and Fe-Doped TiO_2 and $SrTiO_3$ Nanotubes for Visible-Light-Driven Photocatalytic Water Splitting: Prediction from First Principles. *The Journal of Physical Chemistry C*, **2015**, *119* (32), 18686-18696.

[55] Konta, R.; Ishii, T.; Kato, H.; Kudo, A., Photocatalytic Activities of Noble Metal Ion Doped $SrTiO_3$ under Visible Light Irradiation. *The Journal of Physical Chemistry B*, **2004**, *108* (26), 8992-8995.

[56] Xie, K.; Umezawa, N.; Zhang, N.; Reunchan, P.; Zhang, Y.; Ye, J., Self-doped $SrTiO_{3-\delta}$ photocatalyst with enhanced activity for artificial photosynthesis under visible light. *Energy & Environmental Science*, **2011**, *4* (10), 4211-4219.

[57] Nishioka, S.; Hyodo, J.; Vequizo, J. J. M.; Yamashita, S.; Kumagai, H.; Kimoto, K.; Yamakata, A.; Yamazaki, Y.; Maeda, K., Homogeneous Electron Doping into Nonstoichiometric Strontium Titanate Improves Its Photocatalytic Activity for Hydrogen and Oxygen Evolution. *ACS Catalysis*, **2018**, *8* (8), 7190-7200.

[58] Zou, F.; Jiang, Z.; Qin, X.; Zhao, Y.; Jiang, L.; Zhi, J.; Xiao, T.; Edwards, P. P., Template-free synthesis of mesoporous N-doped $SrTiO_3$ perovskite with high visible-light-driven photocatalytic activity. *Chem. Commun*, **2012**, *48* (68), 8514-8516.

[59] Yamakata, A.; Kawaguchi, M.; Murachi, R.; Okawa, M.; Kamiya, I., Dynamics of Photogenerated Charge Carriers on Ni- and Ta-Doped $SrTiO_3$ Photocatalysts Studied by Time-Resolved Absorption and Emission Spectroscopy. *The Journal of Physical Chemistry C*, **2016**, *120* (15), 7997-8004.

[60] Fan, X.; Chen, X.; Zhu, S.; Li, Z.; Yu, T.; Ye, J.; Zou, Z., The structural, physical and photocatalytic properties of the mesoporous Cr-doped TiO_2. *Journal of Molecular Catalysis A: Chemical*, **2008**, *284* (1-2), 155-160.

[61] Niishiro, R.; Kato, H.; Kudo, A., Nickel and either tantalum or niobium-codoped TiO_2 and $SrTiO_3$ photocatalysts with visible-light response for H_2 or O_2 evolution from aqueous solutions. *Physical Chemistry Chemical Physics*, **2005**, *7* (10), 2241-2245.

[62] Takata, T.; Domen, K., Defect Engineering of Photocatalysts by Doping of Aliovalent Metal Cations for Efficient Water Splitting. *The Journal of Physical Chemistry C*, **2009**, *113* (45), 19386-19388.

[63] Schneider, J.; Matsuoka, M.; Takeuchi, M.; Zhang, J.; Horiuchi, Y.; Anpo, M.; Bahnemann, D. W., Understanding TiO_2 Photocatalysis: Mechanisms and Materials. *Chemical reviews*, **2014**, *114* (19), 9919-9986.

[64] Wang, X.; Maeda, K.; Thomas, A.; Takanabe, K.; Xin, G.; Carlsson, J. M.; Domen, K.; Antonietti, M., A metal-free polymeric photocatalyst for hydrogen production from water under visible light. *Nature Materials*, **2009**, *8* (1), 76-80.

[65] Cao, S.; Low, J.; Yu, J.; Jaroniec, M., Polymeric Photocatalysts Based on Graphitic Carbon Nitride. *Advanced Materials*, **2015**, *27* (13), 2150-2176.

[66] Hong, J.; Xia, X.; Wang, Y.; Xu, R., Mesoporous carbon nitride with in situ sulfur doping for enhanced photocatalytic hydrogen evolution from water under visible light. *Journal of Materials Chemistry*, **2012**, *22* (30), 15006-15012.

[67] Ding, Z.; Chen, X.; Antonietti, M.; Wang, X., Synthesis of Transition Metal-Modified Carbon Nitride Polymers for Selective Hydrocarbon Oxidation. *ChemSusChem*, **2011**, *4* (2), 274-281.

[68] Yanagida, S.; Kabumoto, A.; Mizumoto, K.; Pac, C.; Yoshino, K., Poly(p-phenylene)-catalysed photoreduction of water to hydrogen. *Journal of the Chemical Society, Chemical Communications*, **1985**, (8), 474-475.

[69] Okemoto, A.; Kishishita, K.; Maeda, S.; Gohda, S.; Misaki, M.; Koshiba, Y.; Ishida, K.; Horie, T.; Taniya, K.; Ichihashi, Y.; Nishiyama, S., Application of picene thin-film semiconductor as a photocatalyst for photocatalytic hydrogen formation from water. *Applied Catalysis B: Environmental*, **2016**, *192*, 88-92.

[70] Sprick, R. S.; Jiang, J.-X.; Bonillo, B.; Ren, S.; Ratvijitvech, T.; Guiglion, P.; Zwijnenburg, M. A.; Adams, D. J.; Cooper, A. I., Tunable Organic Photocatalysts for Visible-Light-Driven Hydrogen Evolution. *Journal of the American Chemical Society*, **2015**, *137* (9), 3265-3270.

[71] Yang, C.; Ma, B. C.; Zhang, L.; Lin, S.; Ghasimi, S.; Landfester, K.; Zhang, K. A. I.; Wang, X., Molecular Engineering of Conjugated Polybenzothiadiazoles for Enhanced Hydrogen Production by Photosynthesis. *Angewandte Chemie International Edition*, **2016**, *55* (32), 9202-9206.

[72] Lin, S.; Diercks, C. S.; Zhang, Y.-B.; Kornienko, N.; Nichols, E. M.; Zhao, Y.; Paris, A. R.; Kim, D.; Yang, P.; Yaghi, O. M.; Chang, C. J., Covalent organic frameworks comprising cobalt porphyrins for catalytic CO_2 reduction in water. *Science*, **2015**, *349* (6253), 1208.

[73] Ran, J.; Jaroniec, M.; Qiao, S.-Z., Cocatalysts in Semiconductor-based Photocatalytic CO_2 Reduction: Achievements, Challenges, and Opportunities. *Advanced Materials*, **2018**, *30* (7), 1704649.

[74] Hori, H.; Johnson, F. P. A.; Koike, K.; Ishitani, O.; Ibusuki, T., Efficient photocatalytic CO_2 reduction using $[Re(bpy)(CO)_3P(OEt)_3]^+$. *Journal of Photochemistry and Photobiology A: Chemistry*, **1996**, *96* (1), 171-174.

[75] Cometto, C.; Kuriki, R.; Chen, L.; Maeda, K.; Lau, T.-C.; Ishitani, O.; Robert, M., A Carbon Nitride/Fe Quaterpyridine Catalytic System for Photostimulated CO_2-to-CO Conversion with Visible Light. *Journal of the American Chemical Society* , **2018**, *140* (24), 7437-7440.

[76] Kuramochi, Y.; Ishitani, O., An Ir(III) Complex Photosensitizer With Strong Visible Light Absorption for Photocatalytic CO_2 Reduction. *Frontiers in Chemistry*, **2019**, *7* (259).

[77] Sato, S.; Morikawa, T.; Saeki, S.; Kajino, T.; Motohiro, T., Visible-Light-Induced Selective CO_2 Reduction Utilizing a Ruthenium Complex Electrocatalyst Linked to a p-Type Nitrogen-Doped Ta_2O_5 Semiconductor. *Angewandte Chemie International Edition*, **2010**, *49* (30), 5101-5105.

[78] Kuehnel, M. F.; Orchard, K. L.; Dalle, K. E.; Reisner, E., Selective Photocatalytic CO_2 Reduction in Water through Anchoring of a Molecular Ni Catalyst on CdS Nanocrystals. *Journal of the American Chemical Society*, **2017**, *139* (21), 7217-7223.

[79] Takeda, H.; Koike, K.; Inoue, H.; Ishitani, O., Development of an Efficient Photocatalytic System for CO_2 Reduction Using Rhenium(I) Complexes Based on Mechanistic Studies. *Journal of the American Chemical Society*, **2008**, *130* (6), 2023-2031.

[80] Wang, S.; Guan, B. Y.; Lou, X. W. D., Construction of $ZnIn_2S_4In_2O_3$ Hierarchical Tubular Heterostructures for Efficient CO_2 Photoreduction. *Journal of the American Chemical Society*, **2018**, *140* (15), 5037-5040.

[81] Zhao, G.; Zhou, W.; Sun, Y.; Wang, X.; Liu, H.; Meng, X.; Chang, K.; Ye, J., Efficient photocatalytic CO_2 reduction over Co(II) species modified CdS in aqueous solution. *Applied Catalysis B: Environmental*, **2018**, *226* 252-257.

[82] Yang, C.; Huang, W.; da Silva, L. C.; Zhang, K. A. I.; Wang, X., Functional Conjugated Polymers for CO_2 Reduction Using Visible Light. *Chemistry A European Journal*, **2018**, *24* (66), 17454-17458.

[83] Zhang, H.; Wei, J.; Dong, J.; Liu, G.; Shi, L.; An, P.; Zhao, G.; Kong, J.; Wang, X.; Meng, X.; Zhang, J.; Ye, J., Efficient Visible-Light-Driven Carbon Dioxide Reduction by a Single-Atom Implanted MetalOrganic Framework. *Angewandte Chemie International Edition*, **2016**, *55* (46), 14310-14314.

[84] Fu, M.-C.; Shang, R.; Zhao, B.; Wang, B.; Fu, Y., Photocatalytic decarboxylative alkylations mediated by triphenylphosphine and sodium iodide. *Science*, **2019**, *363* (6434), 1429.

[85] Rao, H.; Schmidt, L. C.; Bonin, J.; Robert, M., Visible-light-driven methane formation from CO_2 with a molecular iron catalyst. *Nature*, **2017**, *548* (7665), 74-77.

[86] Costentin, C.; Robert, M.; Savéant, J.-M., Current Issues in Molecular Catalysis Illustrated by Iron Porphyrins as Catalysts of the CO_2-to-CO Electrochemical Conversion. *Accounts of Chemical Research*, **2015**, *48* (12), 2996-3006.

[87] Li, X.; Yu, J.; Jaroniec, M.; Chen, X., Cocatalysts for Selective Photoreduction of CO_2 into Solar Fuels. *Chemical reviews*, **2019**, *119* (6), 3962-4179.

[88] Liu, B.; Zhao, X., A kinetic model for evaluating the dependence of the quantum yield of nano-TiO_2 based photocatalysis on light intensity, grain size, carrier lifetime, and minority carrier diffusion coefficient: Indirect interfacial charge transfer. *Electrochimica Acta*, **2010**, *55* (12), 4062-4070.

[89] Reynal, A.; Lakadamyali, F.; Gross, M. A.; Reisner, E.; Durrant, J. R., Parameters affecting electron transfer dynamics from semiconductors to molecular catalysts for the photochemical reduction of protons. *Energy & Environmental Science*, **2013**, *6* (11), 3291-3300.

[90] Tamaki, Y.; Furube, A.; Murai, M.; Hara, K.; Katoh, R.; Tachiya, M., Dynamics of efficient electronhole separation in TiO_2 nanoparticles revealed by femtosecond transient absorption spectroscopy under the weak-excitation condition. *Physical Chemistry Chemical Physics*, **2007**, *9* (12), 1453-1460.

[91] Hoch, L. B.; Szymanski, P.; Ghuman, K. K.; He, L.; Liao, K.; Qiao, Q.; Reyes, L. M.; Zhu, Y.; El-Sayed, M. A.; Singh, C. V.; Ozin, G. A., Carrier dynamics and the role of surface defects: Designing a photocatalyst for gas-phase CO_2 reduction. *Proceedings of the National Academy of Sciences*, **2016**, *113* (50), E8011.

[92] Ohko, Y.; Hashimoto, K.; Fujishima, A., Kinetics of Photocatalytic Reactions under Extremely Low-Intensity UV Illumination on Titanium Dioxide Thin Films. *The Journal of Physical Chemistry A*, **1997**, *101* (43), 8057-8062.

[93] Yamakata, A.; Yeilin, H.; Kawaguchi, M.; Hisatomi, T.; Kubota, J.; Sakata, Y.; Domen, K., Morphology-sensitive trapping states of photogenerated charge carriers on $SrTiO_3$ particles studied by time-resolved visible to Mid-IR absorption spectroscopy: The effects of molten salt flux treatments. *Journal of Photochemistry and Photobiology A: Chemistry*, **2015**, *313*, 168-175.

[94] Yamakata, A.; Ishibashi, T.-a.; Onishi, H., Electron- and Hole-Capture Reactions on Pt/TiO_2 Photocatalyst Exposed to Methanol Vapor Studied with Time-Resolved Infrared Absorption Spectroscopy. *The Journal of Physical Chemistry B*, **2002**, *106* (35), 9122-9125.

[95] Murakami, Y.; Nishino, J.; Mesaki, T.; Nosaka, Y., Femtosecond Diffuse-Reflectance Spectroscopy of Various Commercially Available TiO_2 Powders. *Spectroscopy Letters*, **2011**, *44* (2), 88-94.

[96] Serpone, N.; Lawless, D.; Khairutdinov, R.; Pelizzetti, E., Subnanosecond Relaxation Dynamics in TiO_2 Colloidal Sols (Particle Sizes R_p = 1.0-13.4 nm). Relevance to Heterogeneous Photocatalysis. *The Journal of Physical Chemistry*, **1995**, *99* (45), 16655-16661.

[97] Ohtani, B., Titania Photocatalysis beyond Recombination: *A Critical Review. Catalysts*, **2013**, *3* (4).

[98] Tachikawa, T.; Tojo, S.; Fujitsuka, M.; Majima, T., Influence of Metal Ions on the Charge Recombination Processes during TiO_2 Photocatalytic One-Electron Oxidation Reactions. *The Journal of Physical Chemistry B*, **2004**, *108* (30), 11054-11061.

[99] Yamakata, A.; Vequizo, J. J. M.; Kawaguchi, M., Behavior and Energy State of Photogenerated Charge Carriers in Single-Crystalline and Polycrystalline Powder $SrTiO_3$ Studied by Time-Resolved Absorption Spectroscopy in the Visible to Mid-Infrared Region. *The Journal of Physical Chemistry C*, **2015**, *119* (4), 1880-1885.

[100] Bahnemann, D. W.; Hilgendorff, M.; Memming, R., Charge Carrier Dynamics at TiO_2 Particles: Reactivity of Free and Trapped Holes. *The Journal of Physical Chemistry B*, **1997**, *101* (21), 4265-4275.

[101] Fujishima, A.; Rao, T. N.; Tryk, D. A., Titanium dioxide photocatalysis. *Journal of Photochemistry and Photobiology C: Photochemistry Reviews*, **2000**, *1* (1), 1-21.

[102] Pelaez, M.; Nolan, N. T.; Pillai, S. C.; Seery, M. K.; Falaras, P.; Kontos, A. G.; Dunlop, P. S. M.; Hamilton, J. W. J.; Byrne, J. A.; O'Shea, K.; Entezari, M. H.; Dionysiou, D. D., A review on the visible light active titanium dioxide photocatalysts for environmental applications. *Applied Catalysis B: Environmental*, **2012**, *125*, 331-349.

[103] Katsuhiro Ajito, J.-Y. K., Yuko Ueno, and Ho-Jin Song, Terahertz Spectroscopic Identification of Pharmaceutical Crystals: Cocrystals and Polymorphic Forms. *NTT Technical Review*, **2014**, *12* (4).

[104] Yamakata, A.; Ishibashi, T.; Onishi, H., Water- and Oxygen-Induced Decay Kinetics of Photogenerated Electrons in TiO_2 and Pt/TiO_2: A Time-Resolved Infrared Absorption Study. *The Journal of Physical Chemistry B*, **2001**, *105* (30), 7258-7262.

[105] Katoh, R.; Murai, M.; Furube, A., Electronhole recombination in the bulk of a rutile TiO_2 single crystal studied by sub-nanosecond transient absorption spectroscopy. *Chemical Physics Letters*, **2008**, *461* (4), 238-241.

[106] Yoshida, M.; Yamakata, A.; Takanabe, K.; Kubota, J.; Osawa, M.; Domen, K., ATR-SEIRAS Investigation of the Fermi Level of Pt Cocatalyst on a GaN Photocatalyst for Hydrogen Evolution under Irradiation. *Journal of the American Chemical Society*, **2009**, *131* (37), 13218-13219.

[107] Barroso, M.; Cowan, A. J.; Pendlebury, S. R.; Grätzel, M.; Klug, D. R.; Durrant, J. R., The Role of Cobalt Phosphate in Enhancing the Photocatalytic Activity of α-Fe_2O_3 toward Water Oxidation. *Journal of the American Chemical Society***2011**, *133* (38), 14868-14871.

[108] Barroso, M.; Mesa, C. A.; Pendlebury, S. R.; Cowan, A. J.; Hisatomi, T.; Sivula, K.; Grätzel, M.; Klug, D. R.; Durrant, J. R., Dynamics of photogenerated holes in surface modified α-Fe_2O_3 photoanodes for solar water splitting. Proceedings of the National Academy of *Sciences*, **2012**, *109* (39), 15640.

[109] Tono, K.; Togashi, T.; Inubushi, Y.; Sato, T.; Katayama, T.; Ogawa, K.; Ohashi, H.; Kimura, H.; Takahashi, S.; Takeshita, K.; Tomizawa, H.; Goto, S.; Ishikawa, T.; Yabashi, M., Beamline, experimental stations and photon beam diagnostics for the hard x-ray free electron laser of SACLA. *New Journal of Physics*, **2013**, *15* (8), 083035.

[110] Obara, Y.; Ito, H.; Ito, T.; Kurahashi, N.; Thrmer, S.; Tanaka, H.; Katayama, T.; Togashi, T.; Owada, S.; Yamamoto, Y.-i.; Karashima, S.; Nishitani, J.; Yabashi, M.; Suzuki, T.; Misawa, K., Femtosecond time-resolved X-ray absorption spectroscopy of anatase TiO_2 nanoparticles using XFEL. *Structural Dynamics*, **2017**, *4* (4), 044033.

[111] Yang, X.; Tamai, N., How fast is interfacial hole transfer? In situ monitoring of carrier dynamics in anatase TiO_2 nanoparticles by femtosecond laser spectroscopy. *Physical Chemistry Chemical Physics*, **2001**, *3* (16), 3393-3398.

[112] Furube, A.; Tamaki, Y.; Murai, M.; Hara, K.; Katoh, R.; Tachiya, M., Femtosecond visible-to-IR spectroscopy of TiO_2 nanocrystalline films: dynamics of UV-generated charge carrier relaxation at different excitation wavelengths. *SPIE*, **2007**, Vol. 6643.

[113] Rittmann-Frank, M. H.; Milne, C. J.; Rittmann, J.; Reinhard, M.; Penfold, T. J.; Chergui, M., Mapping of the Photoinduced Electron Traps in TiO_2 by Picosecond X-ray Absorption Spectroscopy. *Angewandte Chemie International Edition*, **2014**, *53* (23), 5858-5862.

[114] Santomauro, F. G.; Lübcke, A.; Rittmann, J.; Baldini, E.; Ferrer, A.; Silatani, M.; Zimmermann, P.; Grübel, S.; Johnson, J. A.; Mariager, S. O.; Beaud, P.; Grolimund, D.; Borca, C.; Ingold, G.; Johnson, S. L.; Chergui, M., Femtosecond X-ray absorption study of electron localization in photoexcited anatase TiO_2. *Scientific Reports*, **2015**, *5* (1), 14834.

[115] Di Valentin, C.; Selloni, A., Bulk and Surface Polarons in Photoexcited Anatase TiO_2. *The Journal of Physical Chemistry Letters*, **2011**, *2* (17), 2223-2228.

[116] Luca, V.; Djajanti, S.; Howe, R. F., Structural and Electronic Properties of Sol — Gel Titanium Oxides Studied by X-ray Absorption Spectroscopy. *The Journal of Physical Chemistry B*, **1998**, *102* (52), 10650-10657.

[117] Suzuki, H.; Higashi, M.; Kunioku, H.; Abe, R.; Saeki, A., PhotoconductivityLifetime Product Correlates Well with the Photocatalytic Activity of Oxyhalides Bi_4TaO_8Cl and $PbBiO_2Cl$: An Approach to Boost Their O_2 Evolution Rates. *ACS Energy Letters*, **2019**, *4* (7), 1572-1578.

[118] Kunioku, H.; Nakada, A.; Higashi, M.; Tomita, O.; Kageyama, H.; Abe, R., Improved water oxidation under visible light on oxyhalide Bi_4MO_8X (M = Nb, Ta; X = Cl, Br) photocatalysts prepared using excess halogen precursors. *Sustainable Energy & Fuels*, **2018**, *2* (7), 1474-1480.

[119] Yamada, K.; Suzuki, H.; Abe, R.; Saeki, A., Complex Photoconductivity Reveals How the Nonstoichiometric Sr/Ti Affects the Charge Dynamics of a $SrTiO_3$ Photocatalyst. *The Journal of Physical Chemistry Letters*, **2019**, *10* (8), 1986-1991.

[120] Nguyen, P. N.; Watanabe, H.; Tamaki, Y.; Ishitani, O.; Kimura, S.-i., Relaxation dynamics of $[Re(CO)_2(bpy)P(OEt)_{32}](PF_6)$ in TEOA solvent measured by time-resolved attenuated total reflection terahertz spectroscopy. *Scientific Reports*, **2019**, *9* (1), 11772.

[121] Bian, Z.; Tachikawa, T.; Kim, W.; Choi, W.; Majima, T., Superior Electron Transport and Photocatalytic Abilities of Metal-Nanoparticle-Loaded TiO_2 Superstructures. *The Journal of Physical Chemistry C*, **2012**, *116* (48), 25444-25453.

[122] Godin, R.; Wang, Y.; Zwijnenburg, M. A.; Tang, J.; Durrant, J. R., Time-Resolved Spectroscopic Investigation of Charge Trapping in Carbon Nitrides Photocatalysts for Hydrogen Generation. *Journal of the American Chemical Society*, **2017**, *139* (14), 5216-5224.

Chapter 2 . Transient absorption spectroscopy

2.1 Transient absorption spectroscopy

As mentioned in Chapter1, the photocatalytic reaction undergoes various transient reactions. A deep understanding of these transient phenomena will help to design more sophisticated photocatalytic materials. Prolonged lifetime of photoexcited carriers and efficient and rapid carrier movement are expected to improve photocatalytic activity. Transient Absorption Spectroscopy (TAS) is the most suitable spectroscopic method, and it can observe carriers generated in semiconductors, so it can gain deep knowledge on the basic process of photocatalysis.[1,2] Light irradiation generates transient species in the semiconductor and changes the optical characteristics of the semiconductor. TAS is a spectroscopic method to detect this change in optical properties, which firstly used by Wilkinson in 1981 for measuring the optical density of powder samples.(Figure 2.1)[3] This technique enables time-resolved observation of photoinduced reactions induced on the powder surface. In other words, time-resolved observation of photocatalytic reactions that occur on the surface of powders such as TiO_2 and $SrTiO_3$ is possible. Furthermore, as a practical technique, research on carrier dynamics in many semiconductors in the range from femto-second to second has been conducted.[2,4,5]

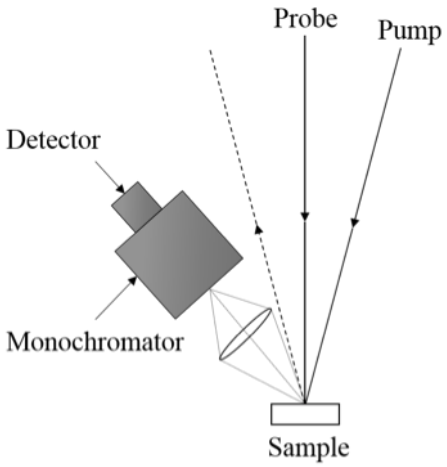

Figure 2.1. Schematic diagram of the diffuse reflectance TAS setup.[3]

The TAS concept has been applied not only to carrier kinetic analysis but also recently to time-resolved

PL emission spectroscopy,[6–8] microwave conductivity,[9–13] etc. PL emission occurs in the process of radiative band to band recombination of photoexcited carriers, or occurs when trapped electrons move to VB.[6] Usually, PL signals from band to band and shallowly trapped electrons state to VB are observed in the visible light range.[6] On the other hand, time-resolved microwave conductivity (TRMC) can detect the mobility of the photogenerated free charge carrier in the material after light excitation.[10] However, unlike optical TAS, direct observation of trapped carriers is not possible.

In the most case, there is not enough physical relationship between the paremeters obtained from fitting functions, like charge carrier concentration or lifetime of excited carriers and the physical property of the samples, such as crystallinity, surface morphology and particle size. Oftentimes, the characterization of transient signals are carried out by comparing transient signal height under different experimental conditions without the utilization of a fit function.[2,14] In the future, measuring transient signal in the different reactive atmosphere with an appropriate fit function should be applied by a detailed kinetic analysis of the decaying charge carrier signals, which would facilitate a deeper understanding of the underlying processes. The typical fitting functions which most widely applied to analyze will be discussed in the following sections.

2.2 The system setup of transient absorption spectroscopy for nano-micro seconds regime.

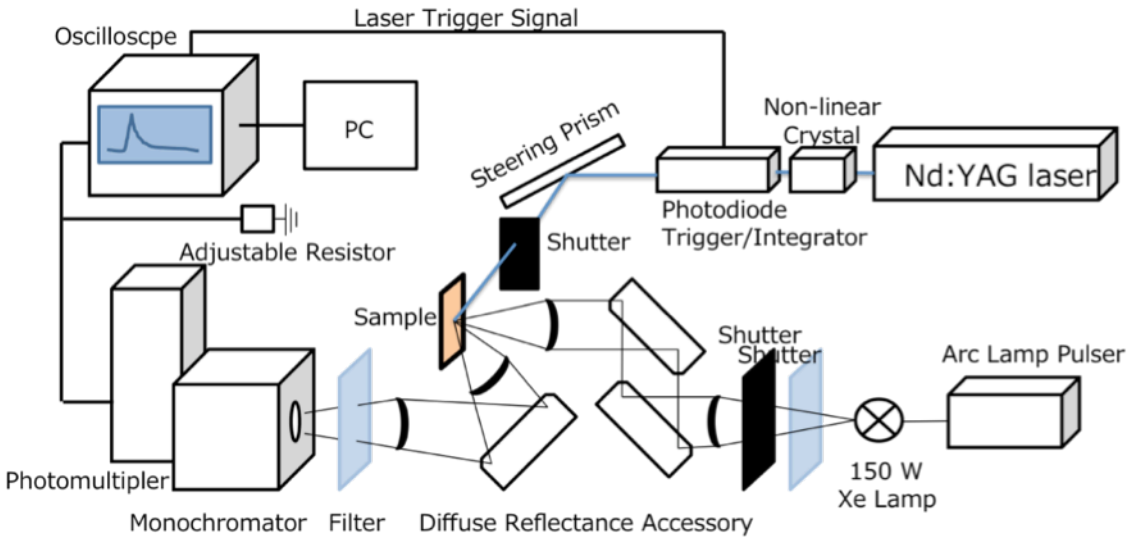

Figure 2.2. The system set-up for the nano-micro seconds regime transient absorption spectroscopy.

In the setup of nano-micro seconds TAS, a pulsed Xe lamp (Osram XBO; 150 W) was focused onto the solid samples surface and the defuse reflected light was guided into the monochromator and detector

Table 2.1. The experimental conditions of transient absorption spectroscopy for nano-micro seconds regime.

Time range	1 ms	100 μs
Laser frequency	10 Hz	1 Hz
Terminal resistance	5 kΩ	50 Ω
Xenon lamp	Non-pulsed	Pulsed
Laser energy	1.3 mJ/cm^2	1.3 mJ/cm^2
Averaging time	500	25
Excitation wavelength	355 nm	355 nm

(Hamamatsu photonics PMT R928) by using two plane folding mirrors and lens. Transient reflectance signals were detected between 850 nm and 400 nm (1 nm step-size). The samples were analyzed in two different time domains (100 μs and 1 ms) and excited at $t = 0$ by the UV-laser (355 nm) with the 6 ns full width of half maximum. To enhance transient signal intensity, the probe light was pulsed to gain a high light intensity for the optical analysis of the samples. The pulsed probe light can generate approximately 200 μs. stable light level. Therefore, the transient absorption measurement for longer than 200 μs required non-pulsed Xe lamp irradiation. The energy of light intensity in the non-pulsed Xe lamp operation was amplified with the tunable signal terminator and increasing the number of averages lead to the reduced signal/noise-ratio. The measurements parameters employed for the different time-scales are summarized in Table 2.1.

In every transient measurement, 1000000 data points with a time resolution of 0.1 ps/point and 1 ps /point were acquired. Generally, data points were collected by the employed photomultiplier as a current depending of the number of photons hitting the detector which enable to convert optical signals into electrical signals. These signals were subjected into the distal oscilloscope via tunable signal terminator. The oscilloscope recorded the data points as voltage changes, this voltage changes were recalculated to the transient absorbance values based on the ratio of the diffusely reflected light signals before the laser excitation I0 and the diffusely reflected light signals after the laser excitation I by instrument 's software. (Equation 2.1).

$$Abs = logI_0/I \tag{2.1}$$

This correlation includes the assumption that the scattering properties of the sample are constant during laser excitation. The set of acquired data points was reduced to 1000 points by averaging the 1000 reflections into one data point, allowing for simpler processing and mathematical fitting of the transient signal. Additionally, the change in reflectance of the powder samples was calculated from the absorbance value (Equation 2.2):

$$\Delta J = 1 - 10^{-(Abs)} = \frac{J_0/I_0 - J_x/I_0}{J_0/I_0} = \frac{J_0 - J_x}{J_0} \tag{2.2}$$

The change in reflectance represents the fraction of the light that is absorbed by the transient species. Lin and Kan demonstrated in 1970 that the optical change in reflectance depends linearly on the concentration of the transient species, as long as the changes in reflectance are considerably small (J<15%).[15] In this method, every sample was at first flushed with nitrogen gas for at least 30 min, after that further flushed with O_2 or methanol vapor if necessary, prior to the transient reflectance measurements.

2.3 The system setup of transient absorption spectroscopy for pico-nano seconds regime.

Figure 2.3 shows a scheme of an ultrafast transient absorption setup. The light source of 1 kHz Ti:sapphire regenerative amplifier (Solstice, Spectra-Physics.) generates pulses of 100 fs duration with a wavelength of 800 nm, a bandwidth of 20 nm. In order to perform transient absorption spectroscopy with a Ti:sapphire laser alone, the laser beam is split into two parts, one is restricted to a wavelength region for the excitation pulse around 800 nm, the other is further split into two beams. In order to shift the wavelength to the visible and near-IR spectra, optical parametric amplifiers (OPAs) is typically used. In an OPA, non-linear birefringent crystals such as beta barium borate (BBO) are pumped by the direct output of the amplified laser system at 800 nm or frequency-doubled pulses at 400 nm. The pump is timely and spatially overlapped in the crystal, and depending on the angle between the laser beam and the symmetry axis of the crystal, two particular wavelengths of the white-light continuum called ‘‘ signal ’’ and ‘‘ idler ’’ are amplified through the second-order nonlinear polarizability of the crystal. On this crystal, the signal has the shortest wavelength and is routinely selected for further use. Since signal and idler beams have different polarizations, the group velocity, signal, and idler beams can be made equal by varying the angle between the laser beam and the symmetry axis of the birefringent crystal locate in the TOPAS. This allows energy from the light source beam to be converted to the signal and idler beams over a large conversion length up to millimeters. This is the so-called phase-matching condition. To maintain the energy of the light requires that the sum of the frequencies of signal and idler add up to the frequency of the pump beam. Thus, when 800 nm light source was applied as pump, the OPA can generate in the range of near-InfraRed (IR) (1,1001,600 nm for the signal) while OPA generate in the range of visible (475750 nm for the signal) spectrum by 400 nm pump. Using the output of an OPA as a fundamental, logically all wavelengths from the UltraViolet (UV) to mid-IR can be generated at relatively high pulse energies by applying non-linear mixing processes such as frequency-doubling and sum-frequency generation in suitable non-linear crystals. Obviously, UV to mid-IR light are the most useful wavelengths for the study of photocatalytic systems. In order to initiate the time delay between the excitation and probe pulses, the excitation pulse generated by the OPA go through an optical delay line, which consists of a two mirrors mounted on a punctual motorized computer-controlled moveable stage. The optical delay

line employed in our experiments has an accuracy and reproducibility of 0.1 μm, which corresponds to a timing accuracy of 0.5 fs. The delay line is able to move over 200 mm at maximum, indicating that time delays up to 1.25 ns can be generated between pump and probe beams. At last, both excitation light and probe lights were focused and overlapped on the surface of the photocatalysts. The transmitted probe light was focused into the Si or InGaAs photodetectors with a detection range of 500-1000 and 1000-2600 nm. A long wave pass filter placed in front of the photodetectors blocked scattered excitation light. The intensity of the transmitted probe light T is detected by the amplification of the signal from the probe light by a lock in amplifier synchronized with the 1 kHz repetition of the probe light pulsed. The change of the intensity of the transmitted probe light caused by the excitation light $\Delta T(t)$ was detected by the differential amplification of the signal from probe light and that from the reference light using a lock-in amplifier synchronized with the frequency of the optical chopper, where t is the time delay between pump and probe pulses generated by optical delay line. For the measurement of transient absorption spectra, the wavelength of the probe light was measured over the range from 500 to 2600 nm, while the measurement for the signal decay of the transient absorption was performed by scanning the delay time to about 1 ns as maximum using optical delay line.

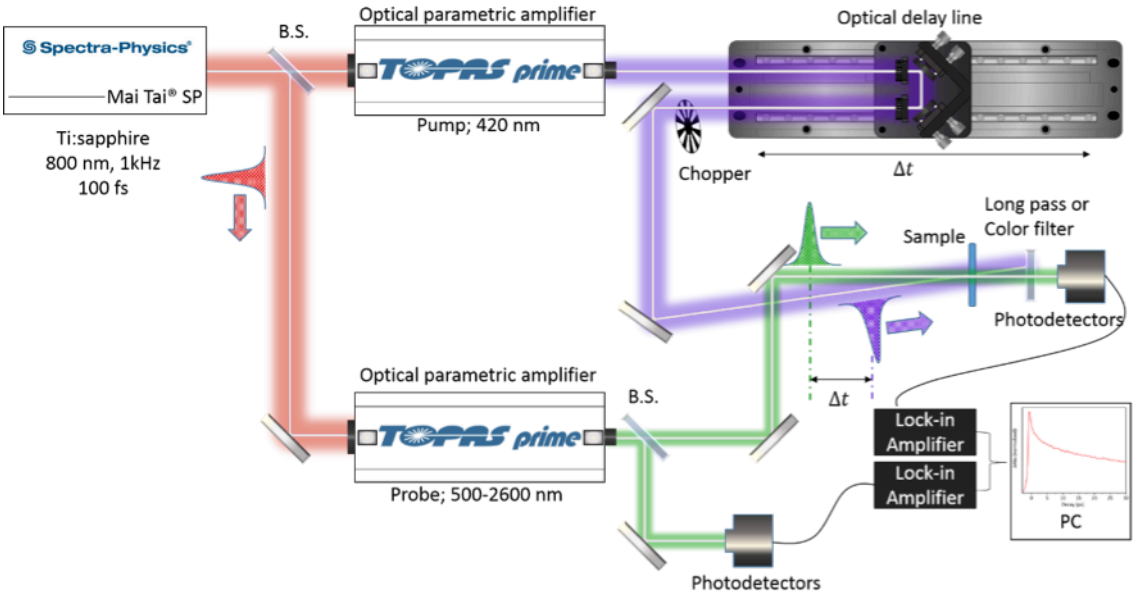

Figure 2.3. The system set-up for the pico-nano seconds transient absorption spectroscopy.

2.4 The fitting function for transient absorption spectroscopy

2.4.1 Second-order kinetics

Monoexponential,[16] double-exponential,[5] and second order[2,17,18] fitting functions have already been used to explain the recombination rate of charge carriers in TAS measurements. Although expo-

nential functions have been used mainly for exciton recombination, double-exponential and second order functions have also been used to explain the recombination rate of trapped charge species in a material.[19] In this section, I focus on second-order processes because the complex recombination of charge carriers obtained by TAS does not usually correlate with a single exponential decay.[2,20,21] Furthermore, multi-exponential fit functions have the inherent disadvantage that the physical meaning of the modeled constants is uncertain.[22]

On the other hand, the second-order fit function is based on the bimolecular reaction of two species A and B, such as photogenerated electrons and photogenerated holes.[23]

$$A + B \rightarrow C \tag{2.3}$$

The second order reaction rate is defined as the change in the concentration of the reactants over the course of time.

$$Rate = \frac{-d[A]}{dt} = \frac{-d[B]}{dt} \tag{2.4}$$

When photogenerated electrons and holes pairs are formed, it can be assumed that the concentrations of both species are always the same. ($[A] = [B]$). Furthermore, the reaction rate is determined by the rate constant k_2.

$$Rate = \frac{-d[A]}{dt} = k_2[A][B] = k_2[A]^2 \tag{2.5}$$

The integration of rate equation results in:

$$\frac{1}{[A]} = k_2 t + \frac{1}{[A_0]} \tag{2.6}$$

$$[A] = \frac{[A]_0}{[1 + [A_0]k_2 t} \tag{2.7}$$

The linearization presented in Equation 2.6 can be used to evaluate the fit of the second-order fit function. Therefore, when the experimental data were plotted at inverse concentrations against time t, there was a linear trend with the slope representing the second-order rate constant k_2 when a simple second-order reaction kinetics was observed. In 2008, Katoh et al. analyzed the transient absorption signal of a rutile single crystal after excitation at 2.8 mJ/cm^2 in the time range of 0 to 25 ns (Figure 2.4).[20]

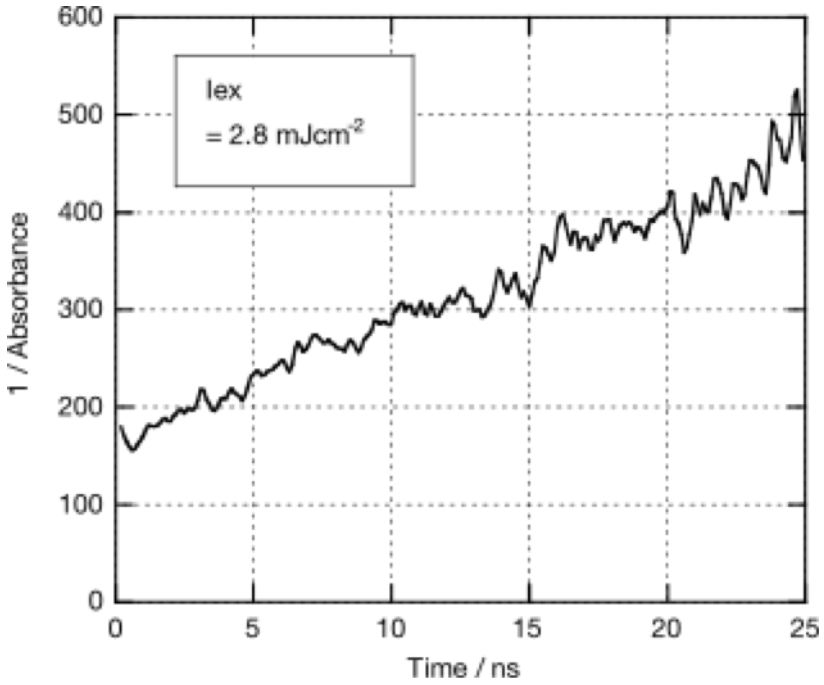

Figure 2.4. Reciprocal absorbance at 850 nm of rutile after excitation with 2.8 mJ/cm^2.[20]

Unfortunately, a second-order kinetic fit with an arbitrarily selected baseline is commonly employed for the analysis of charge carrier recombination, because there is no alternative.[2, 24] In 1995, Serpone et al. have applied second-order fit function with baceline over a long-lived charge carriers transitent signal in TiO_2.[24] The authors assumed that the deeply trapped electrons give this long-lasting transient signal. Recently, Schneider et al. discussed whether transient absorption spectroscopy is a nondestructive spectroscopy by using TiO_2 as a standerd photocatalyst, and reported that a permanent change in optical properties was observed in TiO_2.[25] This irreversible damage to the sample due to the energy intensity of 7-60 mJ/cm^2 may explain the long-lived signal observed in the TAS. This baseline is used to hide the long-lived component of the signal, which differs from pure second order kinetics and exhibits a more complex behavior.[26] However, Grela and Colussi reported that charge carrier recombination in colloidal TiO_2 samples cannot be expressed in terms of second-order kinetics on all time scales.[26] The obtained second-order rate constants were found to depend on both the selected time window and the laser intensity. Therefore, second-order fitting with baselines is not an ideal model to apply to charge carrier recombination in TiO_2, provided accurate and comparable results are obtained.

2.4.2 Power law decays

In 1990, a different approach has been proposed by Schindler and Kunst apart from the fit function that has been discussed.[21] Power law recombination kinetics in a specific electron tunneling process is reported, and the power law is fitted to the transient radiative conductivity (TRMC) decay observed

in TiO_2, as observed by Tatsutani and Mozumder.[21,27] It was also reported that multiple trapping and detrapping processes of photogenerated electrons were involved in the power law decay rate in dye-sensitized TiO_2 nanoparticles.[28] The linearisation of the power law kinetics can be obtained by means of a double logarithmic plot. Figure 2.5 shows a double logarithmic plot of power law kinetics for untreated TiO_2 and Pt loaded TiO_2.

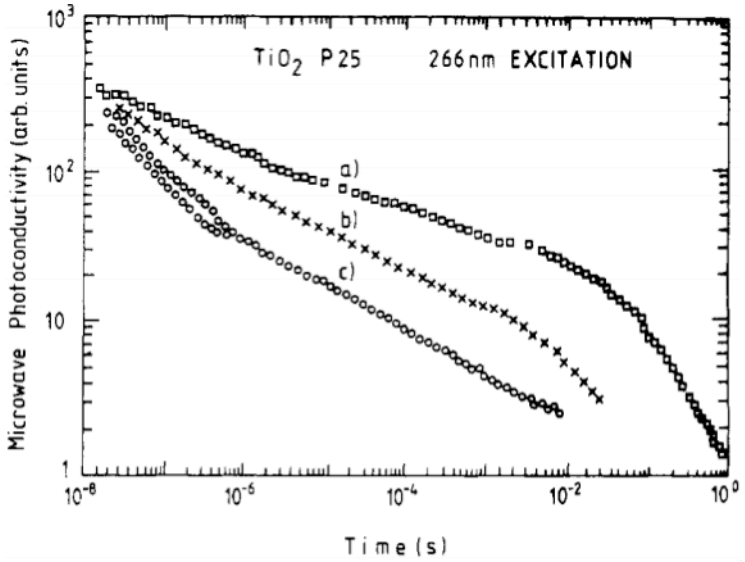

Figure 2.5. Transient photoconductivity of TiO_2 powder (P25) after laser excitation (λ_{ex}= 266 nm ; 0.5-1 mJ/cm^2). (a) untreated P25; (b) platinized P25 treated with 2-propanol; (c) platinized P25.[21]

However, the physical background of the fundamental processes observed in photoconductivity measurements and transient absorption spectroscopy are different. A model resulting in a power-law decay in transient absorption signals of charge carriers was reported by Shuttle *et.al.* in 2010.[29] This result was derived from the exponential distribution of states trapped in the band gap.[30] Furthermore, it is assumed that the trapped hole species are immobile and that the mobility of the effective charge carriers depends on the charge density.[28,29,31] The power law model further assumes that at a very long time after excitation, the decay dynamics of charge carrier recombination is only affected by the energy distribution of the trapping state. This model is mostly applied to studies using very low laser intensities and to the study of charge carrier signals from microseconds to a few seconds after laser excitation.[16,31,32] Using a combination of power law decay and an exponential decay curve, Wang *et.al.* reported that they were able to achieve a fitting of the entire transient photoluminescence signal.[33] In 2008, Tang *et.al.* reported that hole-decay dynamics at reasonably high excitation intensities were shown to exhibit mono-exponential recombination kinetics in TiO_2.[31]

2.4.3 Fractal kinetics

Fractal models for kinetic analysis are based on the concept of fractal geometry. This fractal model is already often used in the analysis of experimental observations and has been applied to the decay of trapped electrons in the form of $O^{2\bullet-}$ on the TiO_2 surface and the dielectric response of TiO_2.[34,35] In addition, The analysis of reactions at the TiO_2 surface, such as dehydrogenation of methanol[36,37] and optical desorption of O_2, has also been reported using a fractal model.[38] In 1983, Mandelbrot first proposed fractals in natural science.Mandelbrot proposed that natural phenomena such as shorelines and Brownian motion can be explained by employing fractal geometry. The application of fractal theory to heterogeneous surfaces was also discussed by Pfeifer and Avnir in 1983.[39] In general, a fractal is an object that has a proper ”fractal” dimension that is not the same as the first, second or third dimension of Euclidean space. Because reactants need to diffuse into each other, the underlying structure and geometry have a significant impact on catalytic reactions on heterogeneous surfaces. In this case, similar bimolecular chemical reactions show different kinetics when they take place on a heterogeneous surface and when they take place in solution. The cause of the observed phenomenon is due to geometric diffusion limitation causing charge carrier segregation.[40] Because of the inability to diffuse reagents into the liquid/gas environment and the bulk of the semiconductor particles, the reaction takes place on a structured two-dimensional surface rather than in a free three-dimensional space. Figure 2.6 shows this restricted diffusion for a random walk on a fractal surface. The limited geometric diffusion can result in apparent one-dimensional reaction kinetics within some nanostructured surfaces and pores.[23] The heterogeneous TiO_2 powder surface has different parts with various characteristic structures, such as catalytic active sites and irregularly distributed trap sites.[41] Therefore, the surface of the powder sample has both a nanostructure, which is composed by the particle size and morphological shape, and a secondary particle-specific microstructure, which is produced by the aggregation of the particles.

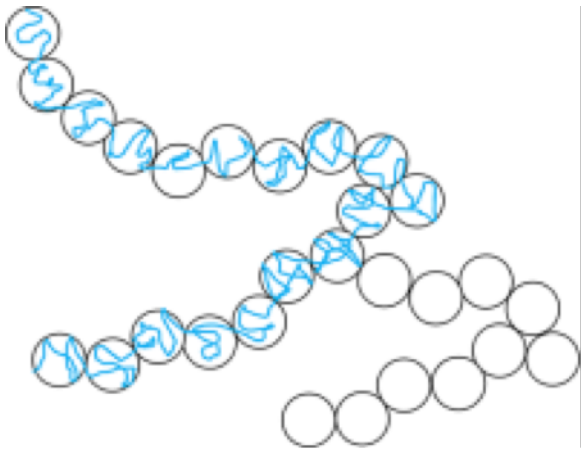

Figure 2.6. Schematic view of a fractal surface (black circles) and random pathway of a charge carrier (blue line)[14]

The relationship between fractal structure and reaction kinetics was reported by Kopelman in 1988.[23] Batch reactions on fractal surfaces require the replacement of rate constants with fractal rate coefficients, as reported by Kopelman et al. The fractal rate coefficient can be defined by the product of the fractal recombination constant multiplied by the time to the power of fractal parameter (Equation 2.8).[14,23]

$$k_f = k_{2,f} t^{-h} \tag{2.8}$$

where, h represents the fractal parameter, which is a measure of the fractal dimension of the surface and limits the observed diffusion of the species. This fractal parameter is zero in the homogeneous reaction systems, such as in solution or in the gas phase, where classical time-dependent kinetics are observed ($h = 0$).[23] However, the exponent differs from zero ($h > 0$) because the reactions that take place on the fractal plane do not exhibit the classical time dependence, and a fractal-specific kinetics is observed. Typical values for of fractal surfaces are between $h = 1/3$ and $h = 1/2$.[23]

As mentioned above, fractal models are very useful for studying the dynamics, such as recombination of charge carriers that occur in powder samples but there are few reports on their application to analysis. Grela and Colussi demonstrated that stochastic calculations of the recombination of photogenerated electrons and holes in a two-dimensional lattice modeling reveal a second-order rate coefficient change that can be explained by fractal kinetics.[42] Grela and Colussi's kinetic model shows that the initial uniform distribution of charge carriers follows the segregation process described above, leading to a non-classical kinetic behavior. Therefore, the recombination dynamics of the photogenerated charge carriers could be closely related to the stochastic surface reactions.

Fabian et al. developed power law decays with combining above mentioned the time dominant rate coefficient(Equation. 2.8).[14] The mathematical description of the fractal-like kinetics from Equation.2.8 was included in the second order fit function according to Equation 2.7, the result is shown in Equation 2.9.

$$\Delta J = \frac{A(1-h)}{((1-h) + Ak_{2,f} t^{1-h})} \tag{2.9}$$

Where A represents the intensity of transient signals, and the exponent h represents the fractal dimension of the surface; the decay constant $k_{2,f}$ is related to charge carriers trapping and recombination. The authors confirmed the accuracy of fitting function (Equation. 2.9) over TiO_2 nano-particles in nanoseconds to microseconds is close to well established second order processes in the short time scale (picoseconds to nanoseconds) and power law model for the long time scale (milliseconds to seconds), when the employing excitation energies is relatively weak (1-5 mJ/cm^2). Additionally, this fractal kinetic explained that characteristic charge carriers signals can be simulated by a mathematical model based on segregation, a phenomenon strongly related to fractal surface. In this dissertation, we applied this fractal kinetics to fit the decay curves, because in the transient absorption spectra measured sample particles were packed in the quartz cuvette.

References

[1] Bahnemann, D.; Henglein, A.; Lilie, J.; Spanhel, L., Flash photolysis observation of the absorption spectra of trapped positive holes and electrons in colloidal titanium dioxide. *The Journal of Physical Chemistry 1984*, **88** (4), 709-711.

[2] Furube, A.; Asahi, T.; Masuhara, H.; Yamashita, H.; Anpo, M., Charge Carrier Dynamics of Standard TiO_2 Catalysts Revealed by Femtosecond Diffuse Reflectance Spectroscopy. *The Journal of Physical Chemistry B*, **1999**, *103* (16), 3120-3127.

[3] Wilkinson, F., Diffuse reflectance flash photolysis. Journal of the Chemical Society, *Faraday Transactions 2: Molecular and Chemical Physics*, **1986**, *82* (12), 2073-2081.

[4] Cowan, A. J.; Leng, W.; Barnes, P. R. F.; Klug, D. R.; Durrant, J. R., Charge carrier separation in nanostructured TiO_2 photoelectrodes for water splitting. *Physical Chemistry Chemical Physics*, **2013**, *15* (22), 8772-8778.

[5] Murakami, Y.; Nishino, J.; Mesaki, T.; Nosaka, Y., Femtosecond Diffuse-Reflectance Spectroscopy of Various Commercially Available TiO_2 Powders. *Spectroscopy Letters*, **2011**, *44* (2), 88-94.

[6] Serpone, N.; Lawless, D.; Khairutdinov, R., Size Effects on the Photophysical Properties of Colloidal Anatase TiO_2 Particles: Size Quantization versus Direct Transitions in This Indirect Semiconductor? *The Journal of Physical Chemistry*, **1995**, *99* (45), 16646-16654.

[7] Yamada, Y.; Sato, H. K.; Hikita, Y.; Hwang, H. Y.; Kanemitsu, Y., Spatial density profile of electrons near the $LaAlO_3/SrTiO_3$ heterointerface revealed by time-resolved photoluminescence spectroscopy. *Applied Physics Letters*, **2014**, *104* (15), 151907.

[8] Yamada, Y.; Yasuda, H.; Tayagaki, T.; Kanemitsu, Y., Photocarrier recombination dynamics in highly excited $SrTiO_3$ studied by transient absorption and photoluminescence spectroscopy. *Applied Physics Letters*, **2009**, *95* (12), 121112.

[9] Katoh, R.; Tamaki, Y.; Furube, A., Primary photocatalytic reactions in TiO_2 nanoparticles studied by time-resolved laser spectroscopy. *SPIE*, **2011**; Vol. 8109.

[10] Martin, S. T.; Herrmann, H.; Choi, W.; Hoffmann, M. R., Time-resolved microwave conductivity. Part 1.—TiO_2 photoreactivity and size quantization. Journal of the Chemical Society, *Faraday Transactions*, **1994**, *90* (21), 3315-3322.

[11] Suzuki, H.; Higashi, M.; Kunioku, H.; Abe, R.; Saeki, A., PhotoconductivityLifetime Product Correlates Well with the Photocatalytic Activity of Oxyhalides Bi_4TaO_8Cl and $PbBiO_2Cl$: An Approach to Boost Their O_2 Evolution Rates. *ACS Energy Letters*, **2019**, *4* (7), 1572-1578.

[12] Tahiri Alaoui, O.; Herissan, A.; Le Quoc, C.; Zekri, M. e. M.; Sorgues, S.; Remita, H.; Colbeau-Justin, C., Elaboration, charge-carrier lifetimes and activity of Pd-TiO_2 photocatalysts obtained by gamma radiolysis. *Journal of Photochemistry and Photobiology A: Chemistry*, **2012**, *242*, 34-43.

[13] Yamada, K.; Suzuki, H.; Abe, R.; Saeki, A., Complex Photoconductivity Reveals How the Nonstoichiometric Sr/Ti Affects the Charge Dynamics of a $SrTiO_3$ Photocatalyst. *The Journal of Physical Chemistry Letters*, **2019**, *10* (8), 1986-1991.

[14] Sieland, F.; Schneider, J.; Bahnemann, D. W., Fractal Charge Carrier Kinetics in $TiO0_2$. *The Journal of Physical Chemistry C*, **2017**, *121* (43), 24282-24291.

[15] Lin, T.-P.; Kan, H. K. A., Calculation of Reflectance of a Light Diffuser with Nonuniform Absorption*. *J. Opt. Soc. Am.*, **1970**, *60* (9), 1252-1256.

[16] Barroso, M.; Pendlebury, S. R.; Cowan, A. J.; Durrant, J. R., Charge carrier trapping, recombination and transfer in hematite (α-Fe_2O_3) water splitting photoanodes. *Chemical Science*, **2013**, *4* (7), 2724-2734.

[17] Draper, R. B.; Fox, M. A., Titanium dioxide photosensitized reactions studied by diffuse reflectance flash photolysis in aqueous suspensions of TiO_2 powder. *Langmuir*, **1990**, *6* (8), 1396-1402.

[18] Hoffmann, M. R.; Martin, S. T.; Choi, W.; Bahnemann, D. W., Environmental Applications of Semiconductor Photocatalysis. *Chemical reviews*, **1995**, *95* (1), 69-96.

[19] Bao, J.; Yu, Z.; Gundlach, L.; Benedict, J. B.; Coppens, P.; Chen, H. C.; Miller, J. R.; Piotrowiak, P., Excitons and Excess Electrons in Nanometer Size Molecular Polyoxotitanate Clusters: Electronic Spectra, Exciton Dynamics, and Surface States. *The Journal of Physical Chemistry B*, **2013**, *117* (16), 4422-4430.

[20] Katoh, R.; Murai, M.; Furube, A., Electronhole recombination in the bulk of a rutile TiO_2 single crystal studied by sub-nanosecond transient absorption spectroscopy. *Chemical Physics Letters*, **2008**, *461* (4), 238-241.

[21] Schindler, K. M.; Kunst, M., Charge-carrier dynamics in titania powders. *The Journal of Physical Chemistry*, **1990**, *94* (21), 8222-8226.

[22] Yang, X.; Tamai, N., How fast is interfacial hole transfer? In situ monitoring of carrier dynamics in anatase TiO_2 nanoparticles by femtosecond laser spectroscopy. *Physical Chemistry Chemical Physics*, **2001**, *3* (16), 3393-3398.

[23] Kopelman, R., Fractal Reaction Kinetics. *Science*, **1988**, *241* (4873), 1620.

[24] Serpone, N.; Lawless, D.; Khairutdinov, R.; Pelizzetti, E., Subnanosecond Relaxation Dynamics in TiO_2 Colloidal Sols (Particle Sizes R_p = 1.0-13.4 nm). Relevance to Heterogeneous Photocatalysis. *The Journal of Physical Chemistry*, **1995**, *99* (45), 16655-16661.

[25] Schneider, J.; Nikitin, K.; Dillert, R.; Bahnemann, D. W., Laser-flash-photolysis-spectroscopy: a nondestructive method? *Faraday discussions*, **2017**, *197*, 505-516.

[26] Grela, M. A.; Coronel, M. E. J.; Colussi, A. J., Quantitative Spin-Trapping Studies of Weakly Illuminated Titanium Dioxide Sols. Implications for the Mechanism of Photocatalysis. *The Journal of Physical Chemistry*, **1996**, *100* (42), 16940-16946.

[27] Tachiya, M.; Mozumder, A., Kinetics of geminate-ion recombination by electron tunnelling. *Chemical Physics Letters*, **1975**, *34* (1), 77-79.

[28] Barzykin, A. V.; Tachiya, M., Mechanism of Charge Recombination in Dye-Sensitized Nanocrystalline Semiconductors: Random Flight Model. *The Journal of Physical Chemistry B*, **2002**, *106* (17), 4356-4363.

[29] Shuttle, C. G.; Hamilton, R.; Nelson, J.; O'Regan, B. C.; Durrant, J. R., Measurement of Charge-Density Dependence of Carrier Mobility in an Organic Semiconductor Blend. *Advanced Functional Materials*, **2010**, *20* (5), 698-702.

[30] Nelson, J.; Haque, S. A.; Klug, D. R.; Durrant, J. R., Trap-limited recombination in dye-sensitized nanocrystalline metal oxide electrodes. *Physical Review B*, **2001**, *63* (20), 205321.

[31] Tang, J.; Durrant, J. R.; Klug, D. R., Mechanism of Photocatalytic Water Splitting in TiO_2. Reaction of Water with Photoholes, Importance of Charge Carrier Dynamics, and Evidence for Four-Hole Chemistry. *Journal of the American Chemical Society*, **2008**, *130* (42), 13885-13891.

[32] Pendlebury, S. R.; Barroso, M.; Cowan, A. J.; Sivula, K.; Tang, J.; Grätzel, M.; Klug, D.; Durrant, J. R., Dynamics of photogenerated holes in nanocrystalline α-Fe_2O_3 electrodes for water oxidation probed by transient absorption spectroscopy. *Chem. Commun.*, **2011**, *47* (2), 716-718.

[33] Wang, X.; Feng, Z.; Shi, J.; Jia, G.; Shen, S.; Zhou, J.; Li, C., Trap states and carrier dynamics of TiO_2 studied by photoluminescence spectroscopy under weak excitation condition. *Physical Chemistry Chemical Physics*, **2010**, *12* (26), 7083-7090.

[34] Niklasson, G. A., Fractal aspects of the dielectric response of charge carriers in disordered materials. *Journal of Applied Physics*, **1987**, *62* (7), R1-R14.

[35] Hirakawa, T.; Nosaka, Y., Properties of $O^{2\bullet-}$ and $OH^{\bullet}$ Formed in TiO_2 Aqueous Suspensions by Photocatalytic Reaction and the Influence of H_2O_2 and Some Ions. *Langmuir*, **2002**, *18* (8), 3247-3254.

[36] Feng, H.; Tan, S.; Tang, H.; Zheng, Q.; Shi, Y.; Cui, X.; Shao, X.; Zhao, A.; Zhao, J.; Wang, B., Temperature- and Coverage-Dependent Kinetics of Photocatalytic Reaction of Methanol on TiO_2 (110)-(1×1) Surface. *The Journal of Physical Chemistry C*, **2016**, *120* (10), 5503-5514.

[37] Zhou, C.; Ma, Z.; Ren, Z.; Mao, X.; Dai, D.; Yang, X., Effect of defects on photocatalytic dissociation of methanol on TiO_2(110). *Chemical Science*, **2011**, *2* (10), 1980-1983.

[38] Thompson, T. L.; Yates, J. T., Control of a Surface Photochemical Process by Fractal Electron Transport Across the Surface: O_2 Photodesorption from TiO_2(110). *The Journal of Physical Chemistry B*, **2006**, *110* (14), 7431-7435.

[39] Pfeifer, P.; Avnir, D., Chemistry in noninteger dimensions between two and three. I. Fractal theory of heterogeneous surfaces. *The Journal of Chemical Physics*, **1983**, *79* (7), 3558-3565.

[40] Le Mehaute, A.; Crepy, G., Introduction to transfer and motion in fractal media: The geometry of kinetics. *Solid State Ionics*, **1983**, 9-10, 17-30.

[41] Arabatzis, I. M.; Antonaraki, S.; Stergiopoulos, T.; Hiskia, A.; Papaconstantinou, E.; Bernard, M. C.; Falaras, P., Preparation, characterization and photocatalytic activity of nanocrystalline thin film TiO_2 catalysts towards 3,5-dichlorophenol degradation. *Journal of Photochemistry and Photobiology A: Chemistry*, **2002**, *149* (1), 237-245.

[42] Grela, M. A.; Colussi, A. J., Kinetics of Stochastic Charge Transfer and Recombination Events in Semiconductor Colloids. Relevance to Photocatalysis Efficiency. *The Journal of Physical Chemistry*, **1996**, *100* (46), 18214-18221.

Chapter 3 . Photogenerated charge carriers dynamics on La and/or Cr doped $SrTiO_3$ nanoparticles studied by transient-absorption spectroscopy

3.1 Introduction

Photocatalytic production of solar fuels from water splitting,[1–5] CO_2 reduction,[6–10] and nitrogen fixation[11,12] has become a major research topic in solar energy conversion. New photocatalysts are continually being designed to demonstrate their capabilities for effective light absorption and conversion. In most reports, taking into consideration that the ultraviolet light only accounts for 4 % of the solar spectrum,[1,13] the extended light absorption into visible light over the developed photocatalysts were emphasized. Among the strategies including photosensitization,[14,15] doping,[2,16] localized surface plasmon resonance,[6,17] etc., extrinsic elemental doping into the semiconductor-based photocatalysts to narrow the bandgap is a conventional and useful method widely engaged by the researchers. Taking TiO_2 and $SrTiO_3$ as examples, doping of transition metals,[18–21] nitrogen[22,23] and sulfur[24] have been extensively carried out. It is reported that by doping, impurity bands are created which enable the absorption of visible-light to excite electrons. However, one of the critical problems but rarely addressed is the change of the light absorption and photocatalytic activity under UV-light region. In fact, the photocatalytic activity under UV-light is drastically decreased after doping even though their performance under visible-light could be enhanced, resulting in a lower total photocatalytic activity under the full spectrum of solar-light irradiation.[25–27] The only exception is that doping of lanthanides and alkali earth metals into $SrTiO_3$ and TiO_2 seems to enhance the photocatalytic activities under UV light irradiation, leading to the improved total photocatalytic activity under full solar spectrum.[16,28] It is widely believed that the unoccupied d-orbital of transition metals may form some mid-gap states which can capture electrons and holes together, acting as a recombination center.[29,30] But the actual role of dopants and how they affect the charge carriers dynamics has not yet been fully elucidated. To restrain the negative drawbacks of the lattice mismatching or valence state unbalance by monodoping, codoping is often used beyond monodoping, which makes the charge carriers dynamics more complicated. In this regard, to investigate the function of dopants for regulating the photocatalytic activity is imperative to design and fabricate

a UV and visible light active photocatalyst. Transient absorption spectroscopy (TAS) is a well-known powerful technique to monitor the photo-excited charge carrier trapping and lifetime in the semiconductors.[31,32] In TAS measurements, the transient changes in absorption are tracked after irradiation of pulse light for excitation. By monitoring this absorption, the decay kinetics of photo-generated charge carrier trapping as well as recombination process can be studied. The time resolved absorption has been applied to elucidate the charge carriers dynamics in TiO_2,[30,33] $NaTaO_3$,[34] $SrTiO_3$,[35,36] $LaTiO_2N$[37] and $Ba_5Ta_4O_{15}$.[31] However to our knowledge, there are only few reports on the doped materials. As one of the reports, Yamakata et al. assumed that the recombination occurring on Ni might be the reason which caused the decreased photocatalytic activity over Ni, Ta-codoped $SrTiO_3$.[25] But later they found that Ni is not the main recombination center via TAS observation of the charge carrier dynamics. Onishi et al. also applied TAS measurements over Rh, Sb-codoped $SrTiO_3$. Even though monodoped Rh^{4+} was demonstrated to be the recombination center, after charge compensation by Sb^{5+} codoping, the recombination on Rh^{3+} was suppressed. And the suppressed recombination could not trigger the photocatalytic HER performance. Instead the photocatalytic HER activity decreased to less than one third.[38] Why the photocatalytic activity of the codoped $SrTiO_3$ reduced under UV light still remains a pending question. In our previous effort to extending light absorption of $SrTiO_3$ to visible light region,[18] we found that Cr doping is an effective way to red-shift the light absorption because of the Cr^{3+} energy state located at 2.2 eV lower than the bottom of conduction band of $SrTiO_3$.[39] However, Cr^{6+} state often occurs in the Cr mono-doped $SrTiO_3$, which diminishes the photocatalytic activity due to the unoccupied Cr^{6+} state with a potential lower than that for H_2 evolution reaction (HER). To restrain the formation of Cr^{6+}, codoping with Sb, Ta, Nb and W was proposed to suppress the formation of defects and to maintain the charge neutralization.[2,4,40,41] Later, we demonstrated that codoping with lanthanum (La) is more promising compared with other elements to stabilize the Cr^{3+} for HER under visible-light irradiation,[42] from a systematic study combining experiments and theoretical calculation. Herein, we chose the La and/or Cr doped $SrTiO_3$ as a proof-of-concept model to examine the effects of doping on the carrier dynamics within nano-micro seconds regime. By using the TAS measurements, the trapped charge carriers were probed in the visible-light range in the presence of the electrons and holes scavengers. The effects of dopants on velocity of the carriers in the photocatalytic reaction and the recombination were investigated. This chapter provides a unique perspective of the codoped photocatalyst and a deep understanding of the doping effect. The fresh inspiration on charge dynamics to the design of photocatalysts are also expected to apply for other photocatalysts.

Characterization

3.2 Experimental section

3.2.1 Materials and synthesis

$SrTiO_3$ nanoparticles were synthesized by a polymerizable complex (PC) method.[13] In brief, $Ti(OC_4H_9)_4$ (Sigma-Aldrich, 99.9%) was dissolved into ethylene glycol and continuously stirred for 30 minutes un-

der nitrogen atmosphere. Afterwards, $Sr(NO_3)_3$ (Sigma-Aldrich, 99.9%) and citric monohydrate (Carl Roth, 99.5%) were added; the stirring was continued until the solution became entirely transparent (denoted as solution A). For doping of lanthanum and chromium, $La(NO_3)_36H_2O$ (Sigma-Aldrich, 99.9%) and $Cr(NO_3)_39H_2O$ (Sigma-Aldrich, 98%) were separately dissolved into 2-methoxymethnol (Sigma-Aldrich, 98%). The required stoichiometric amount of these solutions with the concentration of 0.05 mol/L were added into solution A. The reaction mixture was subsequently stirred for 15 minutes to achieve the dissolution of reagents, and then heated at around 120 °C for 5 h to promote polymerization. During the heating process, the solvent was evaporated and the suspension turned into a transparent brownish resin. The resin was further heated at 350 °C for 3 h with slow heating rate (1 °C/min). Subsequently, the resulted cinders were grinded to obtain fine nanoparticles, and further calcined at 750 °C for 6 hours. It should be stated here that in La, Cr-codoped $SrTiO_3$, the doping amounts were ca. 3%. For investigation of monodoped effect of either La or Cr on $SrTiO_3$, a higher doping amount (12%) was applied to magnify the effects of dopants.

3.2.2 Characterization

The transient absorption system set-up used in this work is described in the literature.[31] In brief, Q-switched Nd:YAG laser (Quantel; Brilliant B, third harmonics, 355 nm, 10 Hz) was used as an excitation light with the duration time of 20 ns. After the sample was irradiated by the excitation light, 150 W Xe lamp (Osram XBO; 150 W) was applied as the probe light source for analyzing the absorption of transient species. Probe light was focused onto solid samples surface by using two plane folding mirrors and lens. The diffusely reflected probe light was collected by a different set of lens and plane folding mirror leading to a monochromator. Then, the dispersed light from the monochromator fell into photomultiplier detector (Hamamatsu R928 photomultiplier), which would convert the optical signals to electric signals; these signals were subjected into the distal oscilloscope via tunable signal terminator. The oscilloscope recorded the data points as voltage changes, which can be recalculated to transient absorption, ΔJ, according to following equation: (Equation 3.1)

$$\Delta J = \frac{J_0/I_0 - J_x/I_0}{J_0/I_0} = \frac{J_0 - J_x}{J_0} \tag{3.1}$$

where I_0 is the light intensity of probe light, J_0 is the signal intensity of diffusely reflected probe light without the excitation, and J_x is the signal of diffusely reflected probe light with irradiation of the excitation laser pulse. The recorded decay signal ΔJ was fitted to a fractal fit function[39] (Equation 3.2)

$$\Delta J = \frac{A(1-h)}{((1-h) + Ak_{2,f}t^{1-h})} \tag{3.2}$$

, where A represents the intensity of transient signals, and the exponent h represents the fractal dimension of the surface; the decay constant $k_{2,f}$ is related to charge carriers trapping and recombination.

For the transient absorption experiments, the powder photocatalysts was packed in the quartz cuvette

which allowed the introduction of reactant gases. Here O_2 gas and MeOH vapor were applied as electrons and holes scavengers, respectively. The optical properties of powders were recorded by the diffuse reflectance spectroscopy in the range of 270-850 nm over V-570 UV/Vis Spectrophotometer (JASCO Corp, Japan) equipped with an integrating sphere and a $BaSO_4$ reference. The measured reflectance data were converted to absorbance via the Kubelka-Munk function. The X-ray powder diffraction (XRD) measurements were performed on an X-ray diffractometer (X'pert powder, PANalytical B.V., Netherlands) with a Bragg Brentano geometry using Cu Kα radiation. High-resolution transmission electron microscopy (HR-TEM) measurements were performed using JEM-2010 with an acceleration voltage of 200 kV. The core level photoelectron spectra were recorded by X-ray photoelectron spectroscopy (XPS; VG-ESCA Mark II), in which Mg Kα radiation (1253.6 eV) and a pass energy were employed at 200 W and 100 eV, respectively. The charge-up of the binding energy values was referenced to the C-C bond of adventitious carbon contamination in the C 1s peak at 284.8 eV as the internal standard. Quantitative analyses were performed by comparing relative area taking into consideration of the atomic sensitivity factor for the corresponding elements.

3.2.3 Photocatalytic H_2 reduction reaction

The photocatalytic H_2 reductions over the samples in 10 vol% methanol aqueous solution were carried out in a Pyrex glass reaction cell linked to a gas-closed circulation system connected to a gas chromatography (GC) (GC-8A, Shimadzu Co., Japan, Carrier gas: Ar) with a thermal conductivity detector (TCD) for online analysis of the H_2 production.

3.3 Results and discussion

3.3.1 Steady state characterization of the La and/or Cr doped $SrTiO_3$

Figure 3.1a shows the powder XRD patterns of synthesized catalysts. The XRD patterns exhibited that all samples reflect cubic perovskite symmetry. In perovskite (ABO_3) structure, cations with larger ionic radius generally occupy A site and the smaller one occupy B site. Thus, it is considered that Sr and La cations have 12 coordination to oxygen atoms, while Ti and Cr cations have octahedral coordination with 6 oxygen atoms. Figure 3.1b shows the magnified 110 diffraction peak of the doped and undoped $SrTiO_3$. In this case, the ionic radius of La (1.36 Å) is smaller than that of Sr (1.44 Å), while the ionic radius of Cr (0.615 Å) is bigger than that of Ti (0.605 Å), the corresponding peak position of the La, Cr-codoped $SrTiO_3$ is found to be close to that of the undoped $SrTiO_3$. Goldschmidt[43] has introduced a tolerance factor (t), defined by the equation:

$$t = \frac{(r_A + r_O)}{\sqrt{2}(r_B + r_O)} \tag{3.3}$$

(r_A, r_B, and r_O are the empirical ionic radii at room temperature), to evaluate the deviation of $SrTiO_3$ from the ideal structure. The t values of $SrTiO_3$, La-doped $SrTiO_3$, Cr-doped $SrTiO_3$ and La, Cr-codoped

$SrTiO_3$ were calculated to be 0.9986, 0.9958, 0.9981 and 0.9983, respectively, all of which are within the allowed t values (0.75 to 1.0).[44] So, it is further confirmed that there is no significant distortion in the $SrTiO_3$ crystal structure by doping.

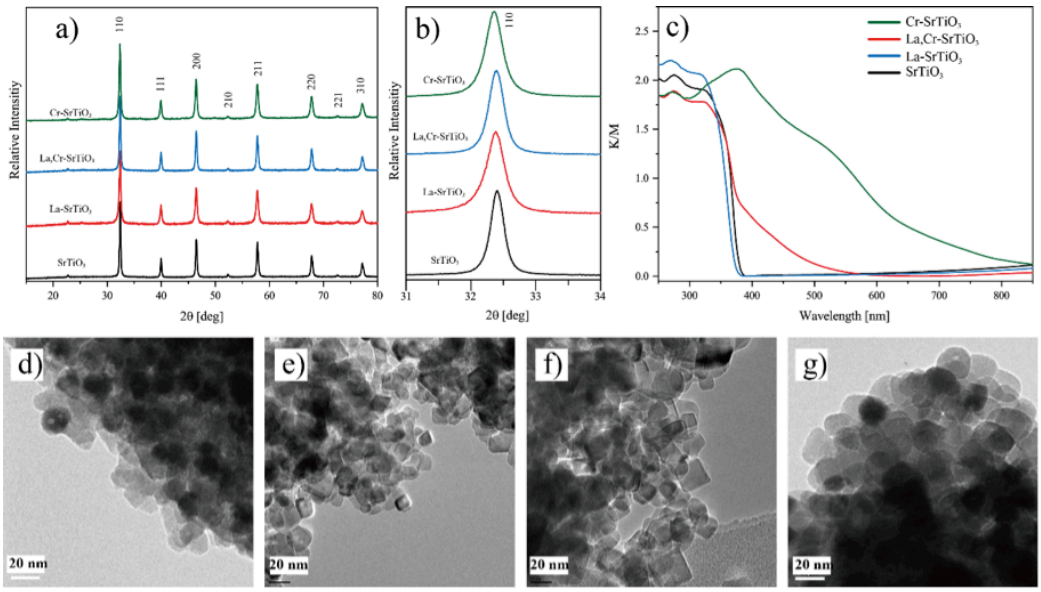

Figure 3.1. (a) XRD patterns and (b) (110) facet (c) UV-vis spectra of doped and pure $SrTiO_3$. TEM images of $SrTiO_3$ (d), La-doped-(e), Cr-doped- (f) and La, Cr-codoped-(g) $SrTiO_3$.

Figure 3.1c shows the absorption spectra of the La and/or Cr doped $SrTiO_3$ powders. The undoped and La-doped $SrTiO_3$ can only absorb UV light with wavelength less than 400 nm. However, La, Cr-codoped $SrTiO_3$ and Cr-doped $SrTiO_3$ exhibited strong absorption in the visible light region (400-580 nm for La, Cr-codoped $SrTiO_3$ and 400-850 nm for Cr-doped $SrTiO_3$). A broad absorption band at 400-600 nm can be assigned to the charge transfer absorption from Cr^{3+} to Ti^{4+}, while the absorption at 580-750 nm can be assigned to the upward d-d transition of $^4A_2 \rightarrow {}^4T_2$ in Cr^{3+} cations in octahedral units, indicating that a part of Cr cations would form tri-valence state in $SrTiO_3$.[45,46] In contrast, Cr-doped $SrTiO_3$ exhibited an additional absorption band over 700 nm, due to the presence of incorporated vacancy by Cr^{6+}.[3,19] It is reported that Cr^{3+} state is beneficial for photocatalytic HER.[2,18] The doped Cr cations will induce an absorption band over 400 nm, which is caused by electrons excitation from d-orbital of Cr cations to the conduction band of $SrTiO_3$. This optical transition is necessary for the photocatalytic activity under visible light irradiation.

As it is known that the transient absorption spectra in the visible region are very sensitive to the morphology of the $SrTiO_3$ powders, surface defects and the surface treatment,[47] the morphology of the synthesized samples were confirmed by TEM observation. As shown in Figure 3.1d-g, all the particles presented similar shapes with fairly smooth surfaces, suggesting that a comparative study by TAS is rational. The doping of La and Cr seems to have no obviously change on the morphology of $SrTiO_3$ nanoparticles if compared with the TEM image of the undoped $SrTiO_3$ (Figure 3.1d).

Cr 2p XPS for 3%, 10% La, Cr-$SrTiO_3$, and Cr-doped $SrTiO_3$ are shown in Figure 3.2. The Cr 2p spectra allow us to tentatively assign the oxidation states of the Cr dopants. The binding energies and the multiplet splitting of the $2p_{3/2}$ peak at 575-577 eV in the 3%, 10% La, Cr-$SrTiO_3$ suggests that the majority of Cr dopants are in the Cr^{3+} state. However, Cr-doped $SrTiO_3$ shows nearly equivalent intensity in the binding energy range characteristic of higher oxidation states Cr^{6+} (578-580 eV) with the Cr^{3+} state.

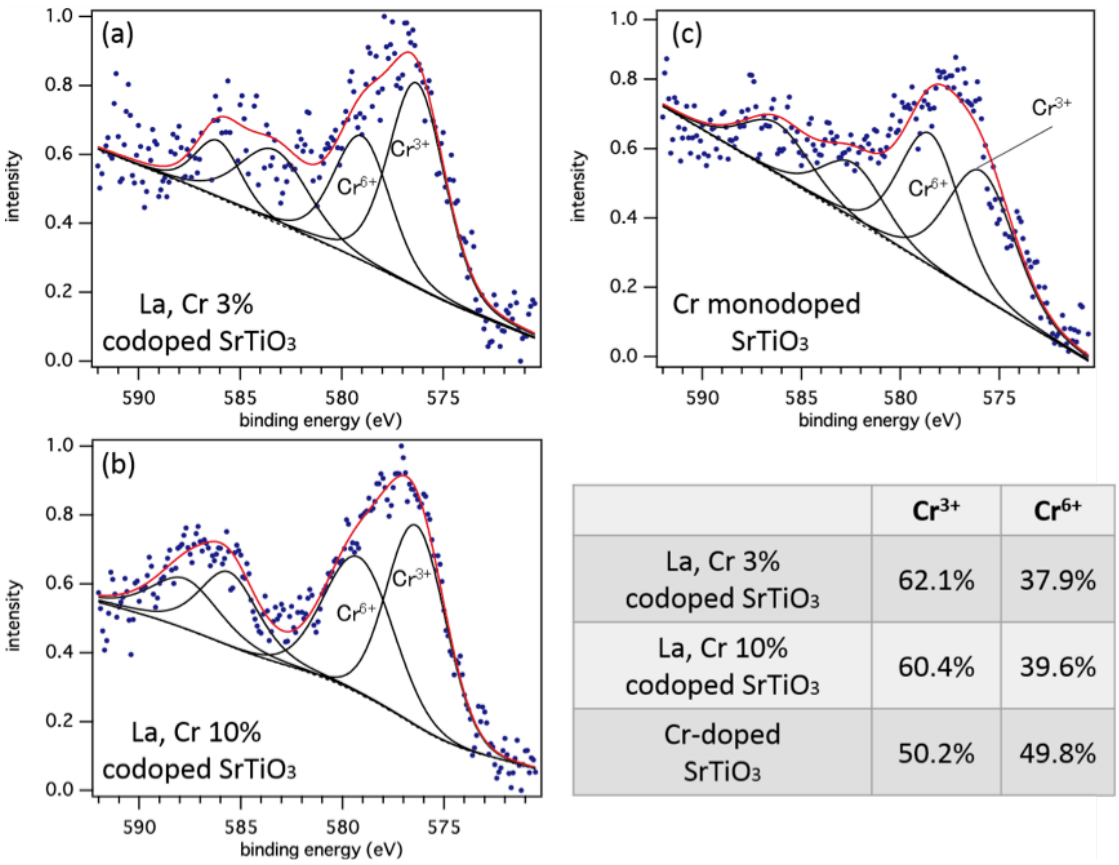

	Cr^{3+}	Cr^{6+}
La, Cr 3% codoped $SrTiO_3$	62.1%	37.9%
La, Cr 10% codoped $SrTiO_3$	60.4%	39.6%
Cr-doped $SrTiO_3$	50.2%	49.8%

Figure 3.2. XPS spectra of Cr $2p_{3/2}$ in the Cr-doped $SrTiO_3$ and La,Cr-codoped $SrTiO_3$.

XPS measurements were also performed to investigate the oxidation states of Cr cations in La, Cr-codoped $SrTiO_3$ and Cr-doped $SrTiO_3$. Figure 3.2 shows Cr $2p_{3/2}$ in those samples. The peaks at around 576.3 eV and 579.2 eV are attributed to Cr^{3+} and Cr^{6+} state, respectively. La, Cr-codoped $SrTiO_3$ showed a relatively strong peak intensity of Cr^{3+} due to charge compensation by La cations. In contrast, the Cr-doped $SrTiO_3$ sample showed a peak intensity of Cr^{6+}, and a small shoulder peak of Cr^{3+}.

3.3.2 Photocatalytic activity of the samples

The photocatalytic HER activity was evaluated by suspending the synthesized catalysts (loaded by 1.0 wt% Pt cocatalyst) in 10 vol% methanol aqueous solution. Figure 3.3 shows the hydrogen evolution over the synthesized catalysts under visible (420 nm cut off filter) and full-arc (UV+Vis) light irradiation, re-

spectively. Under visible light irradiation, only negligible amount of H_2 evolved over the undoped $SrTiO_3$ (< 1 μmol/h) as expected from its wide band gap. However, the rate of HER of La, Cr-codoped $SrTiO_3$ increased to 7.97 μmol/h, in a good accordance with those previously reported for doped $SrTiO_3$.[25,38] In contrast, under the UV + Vis light irradiation, La, Cr-codoped (15.9 μmol/h) and Cr-doped (2.69 μmol/h) $SrTiO_3$ showed much lower activity compared to La-doped $SrTiO_3$ (550.4 μmol/h) and the undoped $SrTiO_3$ (379.2 μmol/h).

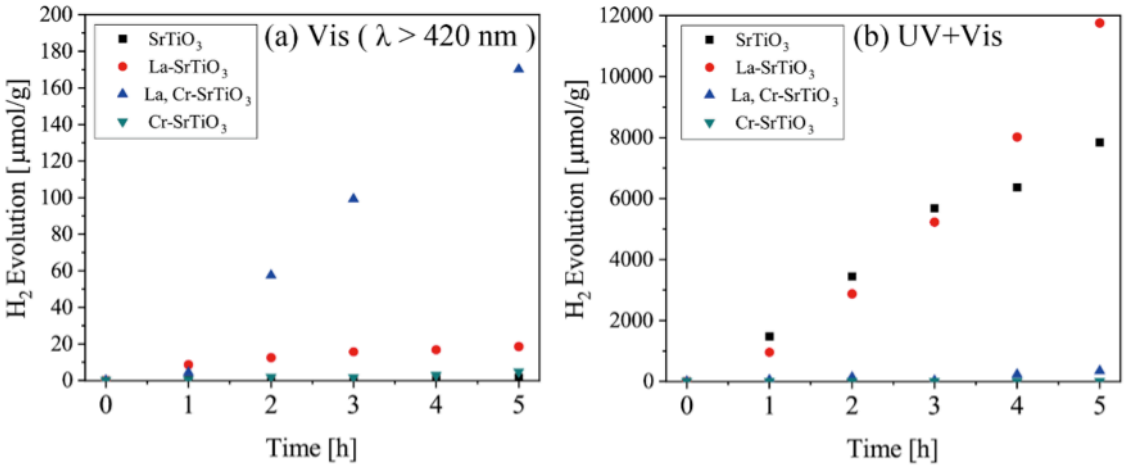

Figure 3.3. (a) Photocatalytic HER under Visible light irradiation (b) UV+Vis light irradiation.

3.3.3 Behavior of photogenerated charge carriers in undoped $SrTiO_3$

In order to determine the effects of doping on the photocatalytic activity, transient absorption spectra of the undoped $SrTiO_3$ were firstly measured upon UV pulsed laser (355 nm) irradiation in N_2 atmosphere. The measurement was performed in the wavelength range of 400-850 nm whereby the transient absorption signal of trapped electrons and holes are usually generated. In this kind of measurement, the intensity of the signal which corresponds to trapped electrons will decrease drastically when electron scavenger is applied. Meanwhile, in the situation where hole scavenger is utilized, slow kinetics of trapped electrons will be observed (preservation of the signal), since the electrons cannot recombine with the photogenerated holes. In contrast, the signal for trapped holes will last longer after the addition of electron scavenger, indicating prolonged life time of holes due to the deceleration of recombination process. Besides, the transient absorption decay curve will display a fast decay characteristic of the holes signal in the presence of hole scavenger.

As shown in Figure 3.4a, at least two broad absorption bands can be observed at 825 nm and 765 nm, which can be assigned to the charge carries that were gravitated towards the trapping states in the band gap. The detailed decay processes ΔJ of the transient absorption bands recorded at 825 and 765 nm were further investigated in the presence of O_2 gas and methanol (MeOH) vapor, which work as

the electron and hole scavengers, respectively.[48,49] As shown in Figure 3.5a, the transient absorption intensity decay curves at 765 nm were fitted in 0-400 μs scale by equation.3.2 In the presence of hole scavenger MeOH, the signal intensity A drastically decreased to 0.68 from 7.70 in N_2 atomosphere. Meanwhile, the decay constant $k_{2,f}$ increased to 0.06, about 5 times higher than those in the N_2 and O_2 environment (0.012 and 0.013, respectively) due to hole-consuming reaction by MeOH. In contrast, in the presence of electron scavenger O_2, the signal intensity increased to 8.08, and the $k_{2,f}$ became slightly lower by electron-consuming reaction of O_2. Thus, the transient absorption signal at 765 nm can be assigned to the population of photogenerated holes. As the absorption band at 825 nm also shows similar trend in the presence of MeOH vapor and O_2 gas, the transient absorption at 825 nm was also assigned to the signal of holes (See Figure 3.6). These highly reactive photogenareted holes in the undoped $SrTiO_3$ contribute to the photocatalytic activity under UV light irradiation.

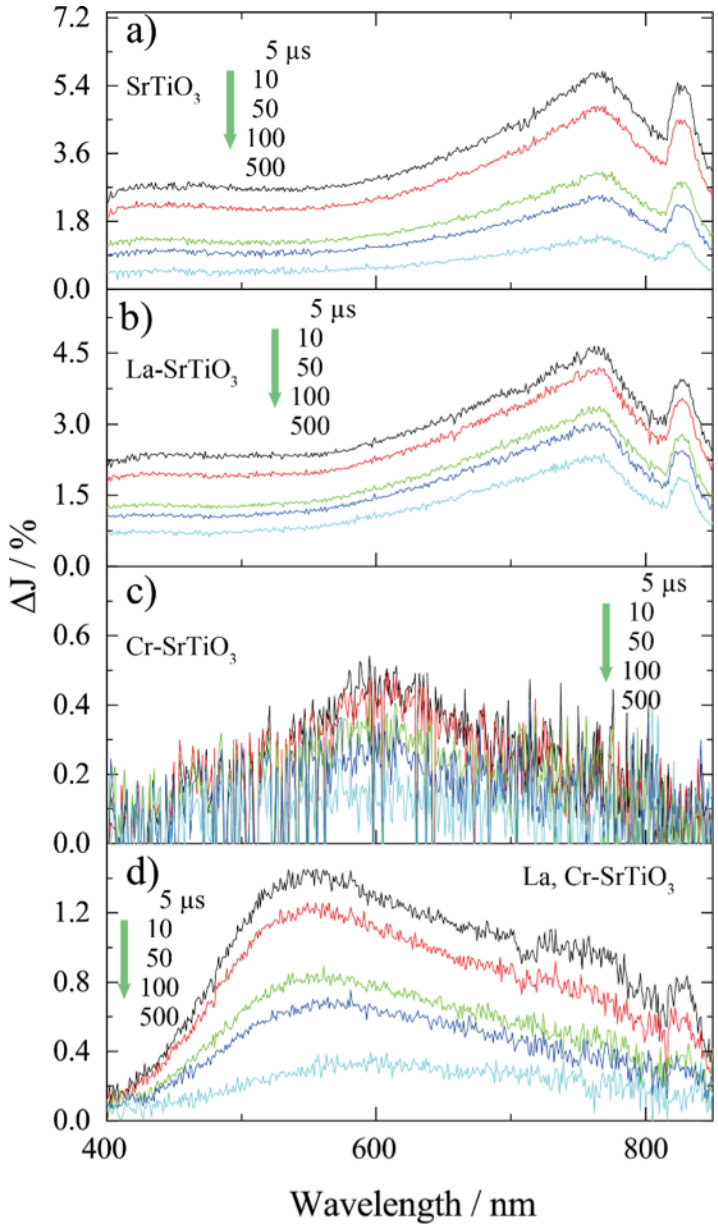

Figure 3.4. (a) Transient absorption spectra of $SrTiO_3$ (a), La- $SrTiO_3$ (b), Cr- $SrTiO_3$ (c), La, Cr- $SrTiO_3$ (d) particles irradiated by UV(355 nm) pulsed laser under N_2 gas. The pump energy was 1.0 mJ/pulse, and the repetition rate was 10 Hz.

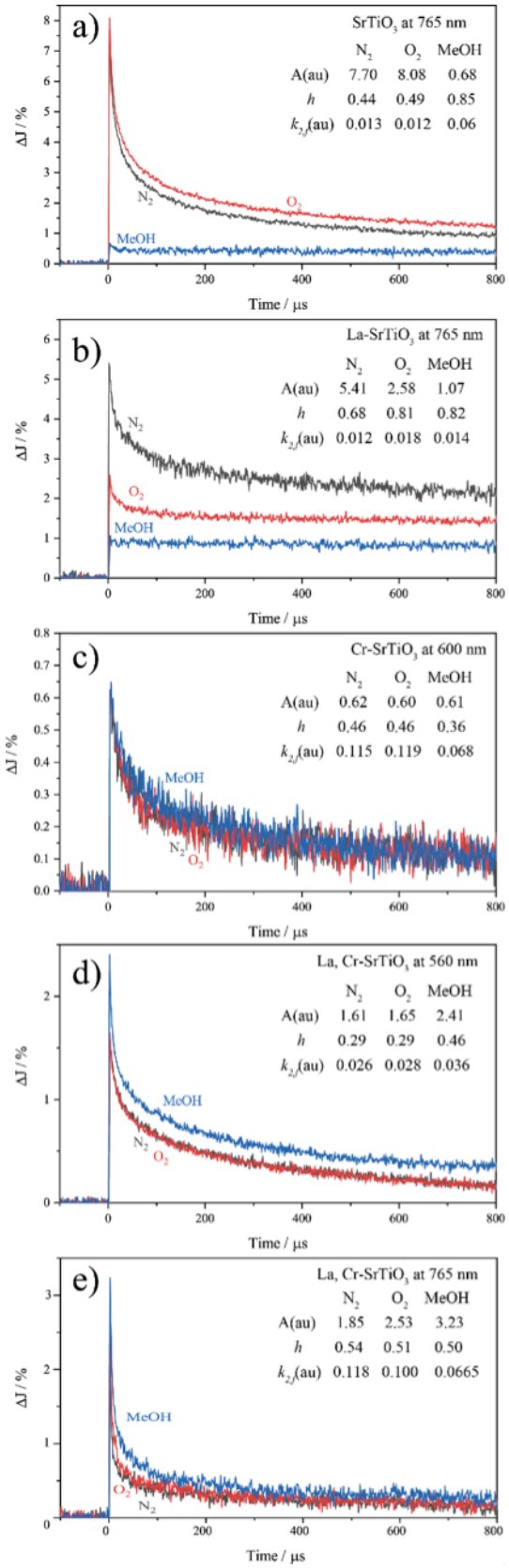

Figure 3.5. Decay curves of transient absorption of the $SrTiO_3$ at 765 nm (a) , La- $SrTiO_3$ at 765 nm(b), Cr- $SrTiO_3$ at 600 nm(c), La, Cr- $SrTiO_3$ at 560 nm(d) and 765 nm(e).

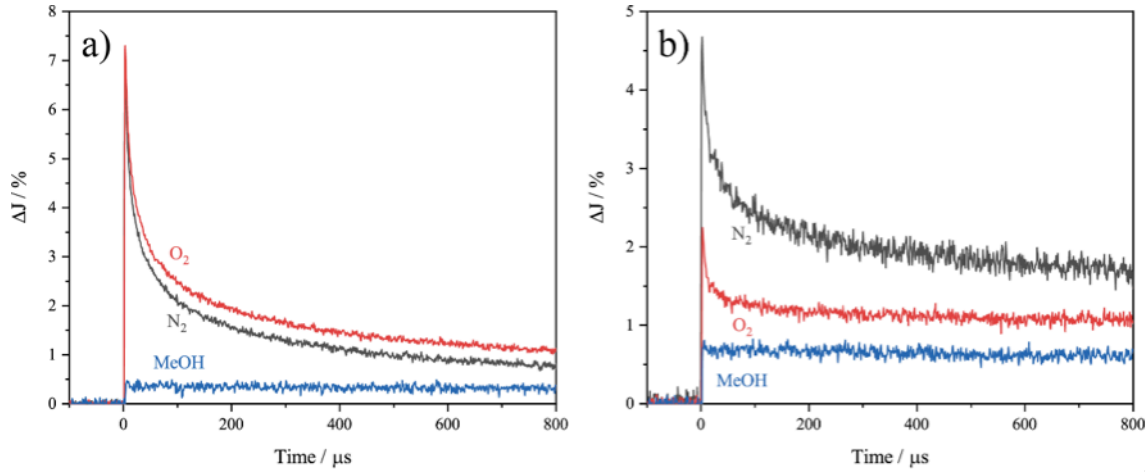

Figure 3.6. Transient decay curves of the undoped $SrTiO_3$ (a) and La-doped $SrTiO_3$ (b) at 825 nm

The transient absorption spectral shape of La-doped $SrTiO_3$ (Figure 3.4b) was in resemblance to that of $SrTiO_3$. However, La-doped $SrTiO_3$ exhibited different decay processes of the transient absorption bands at 825 and 765 nm compared to those of the undoped $SrTiO_3$ where the signal reflects the population of photogenerated holes. As shown in Figure 3.5b, in the presence of hole scavenger MeOH, vapor the signal intensity of transient absorption exhibited fastest decrease, similar to those observed in the undoped $SrTiO_3$. Interestingly, the signal observed in the presence of O_2 gas also showed faster decrease compared with that in N_2 gas. The above results suggest that transient absorption of La-doped $SrTiO_3$ in the visible light region reflects the quantity of both photogenerated electrons and holes. Why the transient species at 765 nm and 825 nm have been changed to both trapped electrons and holes, different with only holes in the undoped $SrTiO_3$? It is suggested that the trapped electrons could absorb the probe light (765 nm and 825 nm), and hence be excited to La 5d bands which are associated with Ti 3d orbital when La is doped at the Sr site of $SrTiO_3$.[50] To prove the effect of La doping on recombination kinetics, the normalized decay processes of the undoped $SrTiO_3$ and La-doped $SrTiO_3$ at 765 nm in the presence of N_2 gas were compared as shown in Figure 3.7. Since there is no molecules that photogenerated charge carriers can react with, the decay processes should reflect the intrinsic recombination kinetics within the undoped $SrTiO_3$ and La-doped $SrTiO_3$. According to the fitting results of the decay curves, La doping can improve the decay constant $k_{2,f}$ value which is implicated in prolonging the carriers lifetime in each arbitrary time scale (0 to 50 μs, 50 to 100 μs and 100 to 400 μs), owing to its ability to secure the photogenerated charge carriers.[50–52] As the longer lifetime carriers have higher probability of taking part in the photocatalytic reaction than the shorter lifetime carriers, it is understandable that the photocatalytic activity of the La-doped $SrTiO_3$ increased under UV+Vis light irradiation (Figure 3.3b).

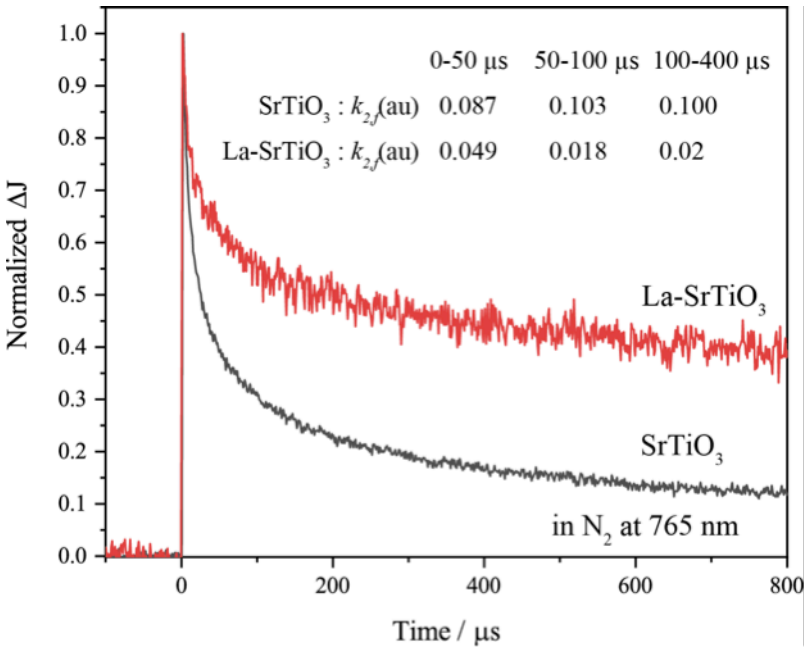

Figure 3.7. Comparison of the normalized decay curves of the undoped $SrTiO_3$ and La-$SrTiO_3$ in N_2 ambient at 765 nm.

The above results imply that those dopants which can form and hybridize the impurity level with the conduction band of the semiconductor, will be beneficial for securing the carriers and prolonging the lifetime of the photogenerated carriers, rather than acting as recombination center.

3.3.4 Effect of Cr doping

Since Cr doping can significantly affect the band structure of $SrTiO_3$, the corresponding transient absorption spectra have a drastic change compared to the original one as seen from Figure 3.4c. It is found that the absorption bands at 825 nm and 765 nm are dumped since the Cr impurity levels are located in the band gap of the $SrTiO_3$ and may overlap with the trapping states of holes. Instead, a new broad absorption band with the peak at around 600 nm can be observed. XPS spectra (Figure 3.8) indicate that Cr with two different valence states (Cr^{3+} and Cr^{6+}) coexisted in Cr-doped $SrTiO_3$ in a nearly equivalent amount. This newly emerged absorption band can be therefore attributed to the inserted Cr^{3+} and Cr^{6+} impurity level between valence band top and conduction band bottom.

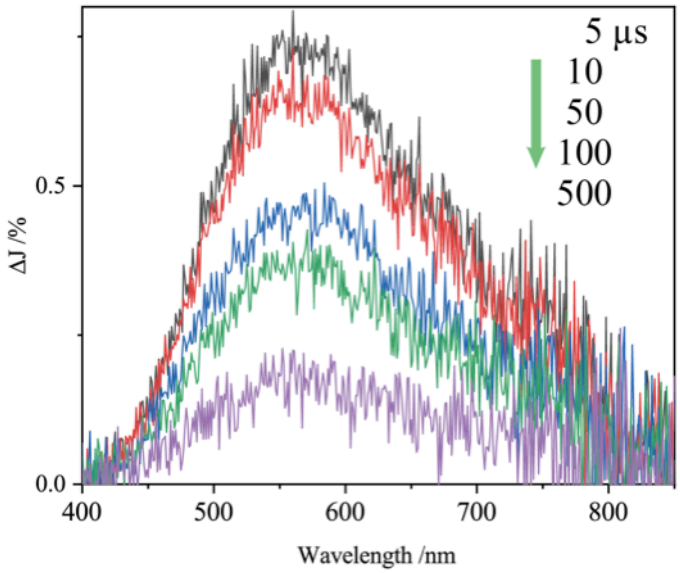

Figure 3.8. Transient absorption spectra of 10% La, Cr-codoped $SrTiO_3$.

As shown in Figure 3.5c, in the presence of hole scavenger MeOH, the decay constant $k_{2,f}$ decreased to half of the value in N_2 and O_2, indicating that the decay process of the absorption maxima at 600 nm was decelerated. According to what we mentioned above in section 3.3.3, this transient absorption signal mainly reflected the population of photogenerated electrons. But when exposed to electron scavenger O_2 gas, the decay process seldom changed, suggesting that the photogenerated electrons have no reactivity compared with charge carriers in $SrTiO_3$ and those in La-doped $SrTiO_3$. This lost reactivity is possibly the main reason for the drastic decrease in photocatalytic HER activity over Cr-doped $SrTiO_3$.

3.3.5 Effect of La and Cr co-doping

The 3% La, Cr-codoped $SrTiO_3$ was then measured by TAS. As shown in Figure 3.4d, the transient absorption spectra exhibited intermediary shape between the undoped $SrTiO_3$ (Figure 3.4a) and Cr-doped $SrTiO_3$ (Figure 3.4c). Interestingly, the peak of transient absorption signal appeared at 560 nm initially (3 μs), but shifted to 600 nm (500 μs) gradually along with the time proceeded, approaching to the shape of Cr-doped $SrTiO_3$ finally. This kind of decay kinetic of La, Cr- codoped $SrTiO_3$ obviously disobeyed the thermal equilibrium. Considering the fact that Cr^{6+} co-existed with Cr^{3+} equivalently in the Cr doped $SrTiO_3$, but was much suppressed by La doping in either 3% and 10% La, Cr-codoped $SrTiO_3$ (Figure 3.8), the peak shift in transient absorption signal from 560 to 600 nm might be attributed to the valence change of Cr^{3+} to Cr^{6+} by trapping three holes.[13] To confirm if the transient absorption peak position at 560 nm is assigned to the Cr^{3+} impurity level, we further conducted TAS measurement by using a sample

with higher doping amount (10% La, Cr-codoped $SrTiO_3$). The shape of the transient absorption spectra (See Figure 3.6) resembled with Cr-doped $SrTiO_3$ (Figure 3.4c), however, the apex blue-shifted from 600 nm to 560 nm, indicating that the trapping state of Cr^{3+} impurity levels are located deeper than Cr^{6+} level. The peak shift of transient absorption along with time was not obvious in this case, probably because a part of Cr^{3+} cations in 10% La, Cr-codoped $SrTiO_3$ still remains tri-valence state due to much increased Cr doping amount. To understand the role of Cr in La, Cr-codoped $SrTiO_3$, the decay curves of transient absorption at 560 nm and 600 nm were investigated in N_2 gas and MeOH vapor, respectively. As shown in Figure 3.9a, in the inert N_2 gas, the signal at 560 nm derived from Cr^{3+} decays faster than the signal of Cr^{6+} (at 600 nm). This suggests that Cr^{3+} doped into $SrTiO_3$ would trap 3 holes and hence change to Cr^{6+}. However, the reverse phenomenon where Cr^{6+} trapped three photoexcited electrons and reverted to Cr^{3+} again couldn't be observed within the range up to 800 μs. On the other hand, while MeOH vapor existed in the measurement environment (as hole scavengers), the decay curves were almost the same for both 560 nm and 600 nm wavelength (Figure 3.9b). Since the photogenerated holes by laser irradiation were instantaneously captured by MeOH vapor, consequently the Cr^{3+} cations were not able to trap the photogenerated holes. Thus in this situation, the decay curve at 560 nm derived from Cr^{3+} mainly follows the thermal equilibrium, similar to the one at 600 nm derived from Cr^{6+}. This suggests that in the photocatalytic HER evaluation with methanol as sacrificial agent, the Cr^{3+} would not act as the recombination center and therefore couldn't be considered as the main reason for the decrease in photocatalytic activity under UV light irradiation.

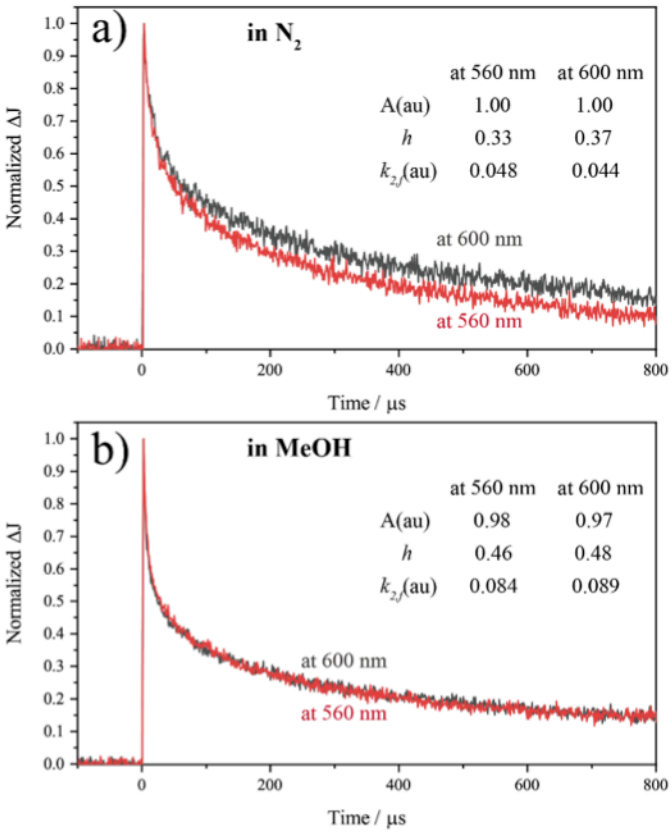

Figure 3.9. The comparison of La, Cr-$SrTiO_3$ at 600 and 560 nm in N_2 ambient (a) and MeOH vapor (b).

To evaluate the effects of La and Cr codoping on the carriers property of $SrTiO_3$, the decay curves at 765 nm (where $SrTiO_3$ exhibits the absorption maxima on transient absorption spectra) are essential for analyzing the recombination kinetics. As shown in Figure 3.4d, the transient absorption spectra around 765 nm preserve part of the feature of the undoped $SrTiO_3$, hence similar reactivity might be expected from La, Cr-codoped $SrTiO_3$. However, the decay processes shown in Figre 3.5e reveal that the reactivity of the corresponding charge carriers was quite different from that of the undoped $SrTiO_3$ (Figure 3.5a) and La-doped $SrTiO_3$ (Figure 4b). In MeOH, the signal intensity relatively increases compared with that in N_2 and displays trapped electrons tendency, while the undoped $SrTiO_3$ displays holes tendency. This implies that $SrTiO_3$ was not sufficiently excited by UV laser irradiation and the majority of excitation originated from the Cr impurity band in La, Cr-codoped $SrTO_3$. This is probably because Cr cations occupy oxygen octahedral coordination center, and the electronic structure of the predominantly O 2p-derived valence band has been affected by Cr doping. Correspondingly, UV-Vis spectra (Figure 3.1c) also show that the absorption intensity in the UV light region decreases after Cr doping and La, Cr codoping. Furthermore, in oxygen environment, the decay curve of La, Cr-codoped $SrTiO_3$ slightly increases compared to the one

in N2 environment, in contrast to the decay curve of La-doped $SrTiO_3$ which experiences a significant decrease (see Figure 3.5b), indicating the disappearance of electrons reactivity by La, Cr codoping. On the other hand, the signal intensity for the undoped $SrTiO_3$ increases noticeably, which might be attributed to the electron scavenging by O_2 (see Figure 3.5a), suggesting the exiguous holes feature in La, Cr-codoped $SrTiO_3$. In the presence of N_2 gas, the decay curves of both La-doped $SrTiO_3$ and La, Cr-codoped $SrTiO_3$ represents the population of electrons and holes. Based on the fitting results at 765 nm in 0-400 μs timescale, the decay constant of La, Cr-codoped $SrTiO_3$ is calculated to be 0.118 (see Figure 3.5e), which is much higher than that of La-doped $SrTiO_3$ ($k_{2,f}$ = 0.012), indicating that La, Cr-codoped $SrTiO_3$ exhibited relatively shorter lifetime of photogenerated electrons. The above results clarify that the recombination at Cr impurity level was not the main reason for the decrease in photocatalytic activity; since the Cr impurity level would absorb UV light and therefore inhibited the excitation of $SrTiO_3$, the activity under UV light was largely suppressed.

3.3.6 Charge carriers dynamics

According to the study using TAS, the charge carriers dynamics of the La-doped $SrTiO_3$ and La, Cr-codoped $SrTiO_3$ are proposed (Figure 3.10a and 10b). After La doping, the TAS displays the distinctive feature of holes and electrons which cannot be observed on the undoped $SrTiO_3$. This distinction indicates that upon the illumination of probe light, the electrons were further excited to La 5d band which hybridized with the conduction band of $SrTiO_3$. As discussed above, the charge carriers lifetime of La-doped $SrTiO_3$ was relatively longer than the undoped $SrTiO_3$, implying that the La 5d orbital could contribute to prolonging lifetime of the charge carries, thus extending the interval for relaxation (see Figure 3.7 and Figure 3.10a). After the codoping of La and Cr, the transient absorption spectra mainly exhibit the feature of electrons due to impurity level formed by Cr within the bandgap of $SrTiO_3$, but not excited from the valence band of $SrTiO_3$. We experimentally observed that Cr d-orbital would act as such a recombination center through the oxidation of Cr^{3+} to Cr^{6+} by trapping 3 holes from the valence band of $SrTiO_3$. The reformation feature of Cr^{6+} to Cr^{3+} could not be observed in the micro second regime. However, stable photocatalytic activity of the material could be observed (as shown in Figure 3.3a), suggesting the reformation of Cr^{6+} to Cr^{3+} in longer time regime (and thus complete the recombination process, see Figure 3.10b).

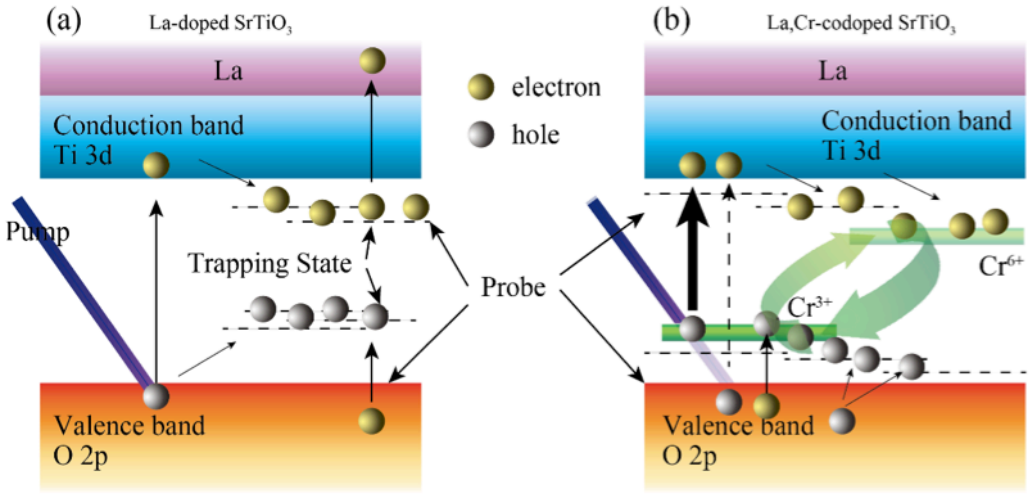

Figure 3.10. The proposed carrier dynamics from the transient absorption spectra.

3.4 Conclusion

Based on the results of TAS, it can be inferred that La doping would extend the lifetime of photogenerated charge carriers due to the hybridization of La 5d band with conduction band of $SrTiO_3$ which could contribute to secure the excited electrons and thus increased total photocatalytic HER performance. After codoping of La and Cr, it was experimentally observed that on inert condition, Cr d-orbital would act as a recombination center through the oxidation state alteration. However, in the photocatalytic reaction environment where MeOH is existing as hole scavenger, the holes had the great tendency to be consumed by MeOH. Hence, the aforementioned recombination process could be avoided and should not be the main reason for the drastic decline in the photocatalytic activity. Interestingly, the majority of the electron excitation occurred from Cr impurity levels under UV light irradiation, which displayed less reactivity and lifetime, could account for decreasing the photocatalytic activity. Accordingly, in order to design a superior photocatalyst for effective solar energy harvesting, one should strive for enhancing the electron reactivity as well as retaining the excitation state of $SrTiO_3$.

References

[1] Zou, Z.; Ye, J.; Sayama, K.; Arakawa, H. Direct Splitting of Water under Visible Light Irradiation with an Oxide Semiconductor Photocatalyst. *Nature*, **2001**, *414*, 625-627.

[2] Kato, H.; Kudo, A. Visible-Light-Response and Photocatalytic Activities of TiO_2 and $SrTiO_3$ Photocatalysts Codoped with Antimony and Chromium. *The Journal of Physical Chemistry B*, **2002**, 106, 5029-5034.

[3] Liu, J. W.; Chen, G.; Li, Z. H.; Zhang, Z. G., Electronic structure and visible light photocatalysis water splitting property of chromium-doped $SrTiO_3$. *Journal of Solid State Chemistry*, **2006**, *179* (12), 3704-3708.

[4] Ouyang, S.; Tong, H.; Umezawa, N.; Cao, J.; Li, P.; Bi, Y.; Zhang, Y.; Ye, J., Surface-alkalinization-induced enhancement of photocatalytic H_2 evolution over $SrTiO_3$-based photocatalysts. *Journal of the American Chemical Society*, **2012**, *134* (4), 1974-7.

[5] Tong, H.; Ouyang, S.; Bi, Y.; Umezawa, N.; Oshikiri, M.; Ye, J., Nano-photocatalytic Materials: Possibilities and Challenges. *Advanced Materials*, **2012**, *24* (2), 229-251.

[6] Meng, X.; Zuo, G.; Zong, P.; Pang, H.; Ren, J.; Zeng, X.; Liu, S.; Shen, Y.; Zhou, W.; Ye, J. A Rapidly Room-Temperature-Synthesized Cd/ZnS:Cu Nanocrystal Photocatalyst for Highly Efficient Solar-Light-Powered CO_2 Reduction. *Applied Catalysis B: Environmental*, **2018**, *237*, 68-73.

[7] Li, P.; Ouyang, S.; Xi, G.; Kako, T.; Ye, J., The Effects of Crystal Structure and Electronic Structure on Photocatalytic H_2 Evolution and CO_2 Reduction over Two Phases of Perovskite-Structured $NaNbO_3$. *The Journal of Physical Chemistry C 2012*, **116**(14), 7621-7628.

[8] Kang, Q.; Wang, T.; Li, P.; Liu, L.; Chang, K.; Li, M.; Ye, J., Photocatalytic Reduction of Carbon Dioxide by Hydrous Hydrazine over AuCu Alloy Nanoparticles Supported on $SrTiO_3/TiO_2$ Coaxial Nanotube Arrays. *Angewandte Chemie*, **2015**, *127* (3), 855-859.

[9] Yan, S. C.; Ouyang, S. X.; Gao, J.; Yang, M.; Feng, J. Y.; Fan, X. X.; Wan, L. J.; Li, Z. S.; Ye, J. H.; Zhou, Y.; Zou, Z. G., A Room-Temperature Reactive-Template Route to Mesoporous $ZnGa_2O_4$ with Improved Photocatalytic Activity in Reduction of CO_2. *Angewandte Chemie International Edition*, **2010**, *49* (36), 6400-6404.

[10] Xie, K.; Umezawa, N.; Zhang, N.; Reunchan, P.; Zhang, Y.; Ye, J. Self-Doped $SrTiO_{3-\delta}$ Photocatalyst with Enhanced Activity for Artificial Photosynthesis under Visible Light. *Energy & Environmental Science*, **2011**, *4*

[11] Li, H.; Shang, J.; Ai, Z.; Zhang, L. Efficient Visible Light Nitrogen Fixation with BiOBr Nanosheets of Oxygen Vacancies on the Exposed 001 Facets. *Journal of the American Chemical Society*, **2015**, *137*, 6393-6399.

[12] Wang, S.; Hai, X.; Ding, X.; Chang, K.; Xiang, Y.; Meng, X.; Yang, Z.; Chen, H.; Ye, J. Light-Switchable Oxygen Vacancies in Ultrafine Bi_5O_7Br Nanotubes for Boosting Solar-Driven Nitrogen Fixation in Pure Water. *Advanced Materials*, **2017**, *29*, 1701774.

[13] Tonda, S.; Kumar, S.; Anjaneyulu, O.; Shanker, V. Synthesis of Cr and La-Codoped $SrTiO_3$ Nanoparticles for Enhanced Photocatalytic Performance under Sunlight Irradiation. *Physical Chemistry Chemical Physics*, **2014**, *16*, 23819-28.

[14] Hirano, K.; Suzuki, E.; Ishikawa, A.; Moroi, T.; Shiroishi, H.; Kaneko, M. Sensitization of TiO_2 Particles by Dyes to Achieve H_2 Evolution by Visible Light. *Journal of Photochemistry and Photobiology A: Chemistry*, **2000**, *136*, 157-161.

[15] Youngblood, W. J.; Lee, S.-H. A.; Maeda, K.; Mallouk, T. E. Visible Light Water Splitting Using Dye-Sensitized Oxide Semiconductors. *Accounts of Chemical Research*, **2009**, *42*, 1966-1973.

[16] Kato, H.; Asakura, K.; Kudo, A. Highly Efficient Water Splitting into H_2 and O_2 over Lanthanum-Doped $NaTaO_3$ Photocatalysts with High Crystallinity and Surface Nanostructure. *Journal of the American Chemical Society*, **2003**, *125*, 3082-3089.

[17] Liu, L.; Li, P.; Adisak, B.; Ouyang, S.; Umezawa, N.; Ye, J.; Kodiyath, R.; Tanabe, T.; Ramesh, G. V.; Ueda, S.; Abe, H. Gold Photosensitized $SrTiO_3$ for Visible-Light Water Oxidation Induced by Au Interband Transitions. *Journal of Materials Chemistry A*, **2014**, *2*, 9875.

[18] Wang, D.; Ye, J.; Kako, T.; Kimura, T. Photophysical and Photocatalytic Properties of $SrTiO_3$ Doped with Cr Cations on Different Sites.*The Journal of Physical Chemistry B*, **2006**, *110*, 15824-15830.

[19] Serpone, N.; Lawless, D.; Disdier, J.; Herrmann, J.-M. Spectroscopic, Photoconductivity, and Photocatalytic Studies of TiO_2 Colloids: Naked and with the Lattice Doped with Cr^{3+}, Fe^{3+}, and V^{5+} Cations. *Langmuir*, **1994**, *10*, 643-652.

[20] Xie, T.; Sun, X.; Lin, J. Enhanced Photocatalytic Degradation of RhB Driven by Visible Light-Induced MMCT of Ti(IV)-O-Fe(II) Formed in Fe-Doped $SrTiO_3$. *The Journal of Physical Chemistry C*, **2008**, *112*, 9753-9759.

[21] Wu, G.; Li, P.; Xu, D.; Luo, B.; Hong, Y.; Shi, W.; Liu, C. Hydrothermal Synthesis and Visible-Light-Driven Photocatalytic Degradation for Tetracycline of Mn-Doped $SrTiO_3$ Nanocubes. *Applied Surface Science*, **2015**, *333*, 39-47.

[22] Asahi, R.; Morikawa, T.; Ohwaki, T.; Aoki, K.; Taga, Y. Visible-Light Photocatalysis in Nitrogen-Doped Titanium Oxides. *Science***2001**, *293*, 269-271.

[23] Maeda, K.; Domen, K. New Non-Oxide Photocatalysts Designed for Overall Water Splitting under Visible Light. *The Journal of Physical Chemistry C*, **2007**, *111*, 7851-7861.

[24] Teruhisa, O.; Takahiro, M.; Michio, M. Photocatalytic Activity of S-Doped TiO_2 Photocatalyst under Visible Light. *Chemical Letters*, **2003**, *32*, 364-365.

[25] Yamakata, A.; Kawaguchi, M.; Murachi, R.; Okawa, M.; Kamiya, I. Dynamics of Photogenerated Charge Carriers on Ni- and Ta-Doped $SrTiO_3$ Photocatalysts Studied by TimeResolved Absorption and Emission Spectroscopy. *The Journal of Physical Chemistry C*, **2016**, *120*, 7997-8004.

[26] Fan, X.; Chen, X.; Zhu, S.; Li, Z.; Yu, T.; Ye, J.; Zou, Z. The Structural, Physical and Photocatalytic Properties of the Mesoporous Cr-Doped TiO_2. *Journal Molecular Catalysis A: Chemical*, **2008**, *284*, 155-160.

[27] Niishiro, R.; Kato, H.; Kudo, A. Nickel and Either Tantalum or Niobium-Codoped TiO_2 and $SrTiO_3$ Photocatalysts with Visible-Light Response for H_2 or O_2 Evolution from Aqueous Solutions. *Physical Chemistry Chemical Physics*, **2005**, *7*, 2241-2245.

[28] Takata, T.; Domen, K. Defect Engineering of Photocatalysts by Doping of Aliovalent Metal Cations for Efficient Water Splitting. *The Journal of Physical Chemistry C*, **2009**, *113*, 19386-19388.

[29] Hoffmann, M. R.; Martin, S. T.; Choi, W.; Bahnemann, D. W. Environmental Applications of Semiconductor Photocatalysis. *Chemical reviews*, **1995**, *95*, 69-96.

[30] Schneider, J.; Matsuoka, M.; Takeuchi, M.; Zhang, J.; Horiuchi, Y.; Anpo, M.; Bahnemann, D. W. Understanding TiO_2 Photocatalysis: Mechanisms and Materials. *Chemical reviews*, **2014**, *114*, 9919-9986.

[31] Schneider, J.; Nikitin, K.; Wark, M.; Bahnemann, D. W.; Marschall, R. Improved Charge Carrier Separation in Barium Tantalate Composites Investigated by Laser Flash Photolysis. *Physical Chemistry Chemical Physics*, **2016**, *18*, 10719-26.

[32] Yamakata, A.; Vequizo, J. J. M.; Matsunaga, H. Distinctive Behavior of Photogenerated Electrons and Holes in Anatase and Rutile TiO_2 Powders. *The Journal of Physical Chemistry C*, **2015**, *119*, 24538 24545.

[33] Sieland, F.; Schneider, J.; Bahnemann, D. W. Fractal Charge Carrier Kinetics in TiO_2. *The Journal of Physical Chemistry C*, **2017**, *121*, 24282-24291.

[34] Yamakata, A.; Ishibashi, T.; Kato, H.; Kudo, A.; Onishi, H. Photodynamics of $NaTaO_3$ Catalysts for Efficient Water Splitting. *The Journal of Physical Chemistry B*, **2003**, *107*, 14383-14387.

[35] Nishioka, S.; Hyodo, J.; Vequizo, J. J. M.; Yamashita, S.; Kumagai, H.; Kimoto, K.; Yamakata, A.; Yamazaki, Y.; Maeda, K. Homogeneous Electron Doping into Nonstoichiometric Strontium Titanate Improves Its Photocatalytic Activity for Hydrogen and Oxygen Evolution. *ACS Catalysis*.**2018**, *8*, 7190-7200.

[36] Yamakata, A.; Vequizo, J. J. M.; Kawaguchi, M. Behavior and Energy State of Photogenerated Charge Carriers in Single-Crystalline and Polycrystalline Powder $SrTiO_3$ Studied by Time-Resolved Absorption Spectroscopy in the Visible to Mid-Infrared Region. *The Journal of Physical Chemistry C*, **2015**, *119*, 1880-1885.

[37] Yamakata, A.; Kawaguchi, M.; Nishimura, N.; Minegishi, T.; Kubota, J.; Domen, K. Behavior and Energy States of Photogenerated Charge Carriers on Pt- or CoO_x-Loaded $LaTiO_2N$ Photocatalysts: Time-Resolved Visible to Mid-Infrared Absorption Study. *The Journal of Physical Chemistry C*, **2014**, *118*, 23897-23906.

[38] Furuhashi, K.; Jia, Q.; Kudo, A.; Onishi, H. Time-Resolved Infrared Absorption Study of $SrTiO_3$ Photocatalysts Codoped with Rhodium and Antimony. *The Journal of Physical Chemistry C*, **2013**, *117*, 19101-19106.

[39] Umebayashi, T.; Yamaki, T.; Itoh, H.; Asai, K. Analysis of Electronic Structures of 3d Transition Metal-Doped TiO_2 Based on Band Calculations. *Journal of Physics and Chemistry of Solids*, **2002**, *63*, 1909-1920.

[40] Jia, Y.; Shen, S.; Wang, D.; Wang, X.; Shi, J.; Zhang, F.; Han, H.; Li, C. Composite $Sr_2TiO_4/SrTiO_3$(La, Cr) Heterojunction Based Photocatalyst for Hydrogen Production under Visible Light Irradiation. *Journal of Materials Chemistry A*, **2013**, *1*, 7905-7912.

[41] Ishii, T.; Kato, H.; Kudo, A. H_2 Evolution from an Aqueous Methanol Solution on $SrTiO_3$ Photocatalysts Codoped with Chromium and Tantalum Ions under Visible Light Irradiation. *Journal of Photochemistry and Photobiology A: Chemistry*, **2004**, *163*, 181-186.

[42] Reunchan, P.; Ouyang, S.; Umezawa, N.; Xu, H.; Zhang, Y.; Ye, J. Theoretical Design of Highly Active $SrTiO_3$-Based Photocatalysts by a Codoping Scheme towards Solar Energy Utilization for Hydrogen Production.*Journal of Materials Chemistry A*, **2013**, *1*, 4221-4227.

[43] Goldschmidt, V. M. Die Gesetze der Krystallochemie. *Naturwissenschaften***1926**, 14, 477-485.

[44] Peña, M. A.; Fierro, J. L. G. Chemical Structures and Performance of Perovskite Oxides. *Chemical reviews*, **2001**, *101*, 1981-2018.

[45] Borgarello, E.; Kiwi, J.; Grätzel, M.; Pelizzetti, E.; Visca, M. Visible Light Induced Water Cleavage in Colloidal Solutions of Chromium-Doped Titanium Dioxide Particles. *Journal of the American Chemical Society*, **1982**, *104*, 2996-3002.

[46] Mackor, A.; Blasse, G. Visible-Light Induced Photocurrents in $SrTiO_3$-$LaCrO_3$ SingleCrystalline Electrodes. *Chemical Physics. Letters*, **1981**, *77*, 6-8.

[47] Yamakata, A.; Yeilin, H.; Kawaguchi, M.; Hisatomi, T.; Kubota, J.; Sakata, Y.; Domen, K. Morphology-Sensitive Trapping States of Photogenerated Charge Carriers on $SrTiO_3$ Particles Stud-

ied by Time-Resolved Visible to Mid-IR Absorption Spectroscopy: The Effects of Molten Salt Flux Treatments. *Journal of Photochemistry and Photobiology A: Chemistry*, **2015**, *313*, 168-175.

[48] Yamakata, A.; Ishibashi, T.; Onishi, H. Water- and Oxygen-Induced Decay Kinetics of Photogenerated Electrons in TiO_2 and Pt/TiO_2: A Time-Resolved Infrared Absorption Study. *The Journal of Physical Chemistry B*, **2001**, 105, 7258-7262.

[49] Yamakata, A.; Ishibashi, T.; Onishi, H. Electron- and Hole-Capture Reactions on Pt/TiO_2 Photocatalyst Exposed to Methanol Vapor Studied with Time-Resolved Infrared Absorption Spectroscopy. *The Journal of Physical Chemistry B*, **2002**, *106*, 9122-9125.

[50] Shanthi, N.; Sarma, D. D. Electronic structure of electron doped $SrTiO_3$: $SrTiO_{3-\delta}$ and $Sr_{1-x}La_xTiO_3$. *Physical Review B*, **1998**, *57*, 2153-2158.

[51] El-Mellouhi, F.; Brothers, E. N.; Lucero, M. J.; Bulik, I. W.; Scuseria, G. E. Structural phase transitions of the metal oxide perovskites $SrTiO_3$, $LaAlO_3$, and $LaTiO_3$ studied with a screened hybrid functional. *Physical Review B*, **2013**, *87*, 035107.

[52] Biswas, A.; Li, N.; Jung, M. H.; Lee, Y. W.; Kim, J. S.; Jeong, Y. H. La doped $SrTiO_3$ thin films on $SrLaAlO_4$ (001) as transparent conductor. *Journal Applied Physics***2013**, *113*, 183711.

Chapter 4 . Photogenerated charge carriers dynamics on Pt loaded $SrTiO_3$ nanoparticles studied by transient-absorption spectroscopy

4.1 Introduction

Photocatalysis has attracted much attention as a green technology since it can use sunlight to convert water and carbon dioxide into chemical energy such as hydrogen[1–5] and hydrocarbons.[6–10] Despite a lot of effort, its efficiency is still far from industrial demands and has not yet reached practical use. One method of increasing the photocatalytic efficiency is loading "cocatalysts" on photocatalysts. Some cocatalysts are known as rectifiers for efficient photocatalytic hydrogen-oxygen evolution reactions. For example, Pt,[11,12] Ni, NiO[13–16] and CrO_x / Rh[17] are well known as cocatalysts for hydrogen generation reaction, and IrO_2,[18,19] RuO_2,[18][20] CoPi (cobalt phosphate)[21–24] and CoO_x[12,25,26] are well known as cocatalysts for oxygen generation reaction. There are two main purposes for loading cocatalysts: 1) to reduce the overpotential for corresponding redox process and 2) to restrain the photogenerated charge carriers recombination by securing and storing electrons or holes. The former has been confirmed by electrochemical measurements. However, there is little experimental evidence to confirm the latter; i.e. carrier collection behaivior. In the field of theoretical calculations, cocatalysts loading is expected to act as a recombination center.[27] When Pt is loaded on TiO_2, the broad density of states of Pt overlaps the conduction band minimum and valence band maximum of TiO_2, thus it is expected that both photo-generated electrons and holes are collected by Pt cocatalysts. Consequently, the recombination is promoted. Furthermore, although Pt is an excellent hydrogen generation cocatalyst, Pt cocatalyst is not suitable for complete decomposition of water due to backward reaction in which hydrogen and oxygen generated are recombined and returned to water again.[28] On the other hand, in the case of transition metals such as Ni and Co, localized 3d orbitals do not serve as a bridge between conduction band and valence band.[29,30] It is therefore expected that loading a transition metal can contribute to relatively low recombination. As described above, the cocatalyst loading is very important but complicated in the photocatalyst design, and it is extremely important to obtain experimental knowledge on the change in carrier dynamics caused by the loading. Transient absorption spectroscopy is a very useful technique for mea-

suring and evaluating such recombination in semiconductors and reactions proceeding on the surface of a photocatalytic material.[31–36] By this measurement method, non-emission carrier dynamics in a semiconductor after photoexcitation can be observed. This method has already been applied to evaluate carrier dynamics of Pt-TiO_2,[31] Ru- Rh and La: $SrTiO_3$, NiO-$NaTaO_3$,[37] Pt-$LaTiO_2N$,[12] Co-Pi-Fe_2O_3,[38,39] Pt, Au-CdS,[40,41] Ni-CdS,[42] MoS_2-CdS.[43] However, in many cases, since the measurement is performed with a focus on the carrier expected to move, the discussion as a recombination center is not sufficiently performed. For instance in case of Pt-TiO_2, electrons is highly expected to migrate to Pt cocatalysts, thus the migration behavior of the photogenerated holes is rarely addressed. In this study, the interaction between photo-excited holes and broad density of state of Pt and localized density of state of Ni cocatalyst loaded on $SrTiO_3$ was observed using transient absorption spectroscopy. By comparing the carrier dynamics after Pt and Ni loading, this study aims to investigate which kind differences favor the photocatalytic reaction and to gain insight into the photocatalytic reaction mechanism and the search for new cocatalysts.

4.2 Experimental methods

4.2.1 Materials and synthesis

$SrTiO_3$ nanoparticles were synthesized by a polymerizable complex (PC) method.[44] In brief, $Ti(OC_4H_9)_4$ (Sigma-Aldrich, 99.9%) was dissolved into ethylene glycol and continuously stirred for 30 minutes under nitrogen atmosphere. Afterwards, $Sr(NO_3)_3$ (Sigma-Aldrich, 99.9%) and citric monohydrate (Carl Roth, 99.5%) were added; the stirring was continued until the solution became entirely transparent. The reaction mixture was subsequently stirred for 15 minutes to achieve the dissolution of reagents, and then heated at around 120 °C for 5 h to promote polymerization. During the heating process, the solvent was evaporated and the suspension turned into a transparent brownish resin. The resin was further heated at 350 °C for 3 h with slow heating rate (1 °C/min). Subsequently, the resulted cinders were grinded to obtain fine nanoparticles, and further calcined at 750 °C for 6 hours. Pt and Ni photo-deposition has carried out in the 300 ml of 10vol% methanol aqueous solution. 50 mg $SrTiO_3$ powder was placed in a Pyrex glass reactor and subjected to some ultrasonic treatment for 30 minutes, then $H_2PtCl_66H_2O$ or $Ni(NO_3)_2$ aqueous solution was added while vigorously stirring for Pt and Ni photo-deposition respectively. The Pyrex glass reactor and solution were degassed by linking to a gas-closed circulation system connected to a rotary pump. The solution was irradiated for 3 h with the full arc of 300 W Xe lump for photo-deposition.

4.2.2 Characterization

The transient absorption system set-up used in this work is described in the literature.[31] In brief, Q-switched Nd:YAG laser (Quantel; Brilliant B, third harmonics, 355 nm, 10 Hz) was used as an excitation light with the duration time of 20 ns. After the sample was irradiated by the excitation light, 150 W Xe

lamp (Osram XBO; 150 W) was applied as the probe light source for analyzing the absorption of transient species. Probe light was focused onto solid samples surface by using two plane folding mirrors and lens. The diffusely reflected probe light was collected by a different set of lens and plane folding mirror leading to a monochromator. Then, the dispersed light from the monochromator fell into photomultiplier detector (Hamamatsu R928 photomultiplier), which would convert the optical signals to electric signals; these signals were subjected into the distal oscilloscope via tunable signal terminator. The oscilloscope recorded the data points as voltage changes, which can be recalculated to transient absorption, ΔJ, according to following equation: (Equation 3.1)

$$\Delta J = \frac{J_0/I_0 - J_x/I_0}{J_0/I_0} = \frac{J_0 - J_x}{J_0} \tag{4.1}$$

where I_0 is the light intensity of probe light, J_0 is the signal intensity of diffusely reflected probe light without the excitation, and J_x is the signal of diffusely reflected probe light with irradiation of the excitation laser pulse. The recorded decay signal ΔJ was fitted to a fractal fit function[39] (Equation 3.2)

$$\Delta J = \frac{A(1-h)}{((1-h) + Ak_{2,f}t^{1-h})} \tag{4.2}$$

, where A represents the intensity of transient signals, and the exponent h represents the fractal dimension of the surface; the decay constant $k_{2,f}$ is related to charge carriers trapping and recombination.

For the transient absorption experiments, the powder photocatalysts was packed in the quartz cuvette which allowed the introduction of reactant gases. Here O_2 gas and MeOH vapor were applied as electrons and holes scavengers, respectively.[31,32] Figure 4.1 shows a scheme of an ultrafast transient absorption setup. The light source of 1 kHz Ti:sapphire regenerative amplifier (Solstice, Spectra-Physics.) generates pulses of ~100 fs duration with a wavelength of 800 nm, a bandwidth of 20 nm. In order to perform transient absorption spectroscopy with a Ti:sapphire laser alone, the laser beam is split into two parts. One beam is restricted to a wavelength region for the excitation pulse around 800 nm, the other is further split into two beams. In order to shift the wavelength to other parts of the visible and near-IR spectra, optical parametric amplifiers (OPAs) is typically used. In an OPA, non-linear birefringent crystals such as beta barium borate (BBO) are pumped by the direct output of the amplified laser system at 800 nm or frequency-doubled pulses at 400 nm. The pump is timely and spatially overlapped in the crystal, and depending on the angle between the laser beam and the symmetry axis of the crystal, two particular wavelengths of the white-light continuum called ‘‘ signal ’’ and ‘‘ idler ’’ are amplified through the second-order nonlinear polarizability of the crystal. On this crystal, the signal has the shortest wavelength and is routinely selected for further use. Since signal and idler beams have different polarizations, the group velocity, signal, and idler beams can be made equal by varying the angle between the laser beam and the symmetry axis of the birefringent crystal locate in the OPA (TOPAS prime, Light Conversion Ltd.). This allows energy from the light source beam to be converted to the signal and idler beams over a large conversion length up to millimeters. This is the so-called phase-matching condition. In this case, by changing the phase-matching condition, the signal frequency and idler frequency can be tuned in order to

maintain the light energy. Thus, when 800 nm light source was applied as pump, the OPA can generate in the range of near-InfraRed (IR) (1,1001,600 nm for the signal) while visible (475750 nm for the signal) spectrum can be generated by 400 nm pump. Using the output of an OPA as a fundamental, logically all wavelengths from the UltraViolet (UV) to mid-IR can be generated at relatively high pulse energies by applying non-linear mixing processes such as frequency-doubling and sum-frequency generation in suitable non-linear crystals. Obviously, UV to mid-IR light are the most useful wavelengths for the study of photocatalytic systems. In order to initiate the time delay between the excitation and probe pulses, the excitation pulse generated by the OPA go through an optical delay line, which consists of two mirrors mounted on a punctual motorized computer-controlled moveable stage. The optical delay line employed in our experiments has an accuracy and reproducibility of 0.1 μm, which corresponds to a timing accuracy of 0.5 fs. The delay line is able to move over 200 mm at maximum, suggesting that time delays up to 1.25 ns can be generated between pump and probe beams. At last, both excitation light and probe lights were focused and overlapped on the surface of the photocatalysts. The transmitted probe light was focused into the Si or InGaAs photodetectors with a detection range of 500-1000 and 1000-2600 nm. Scattered excitation light was blocked by a long wave pass filter placed in front of the photodetectors. The intensity of the transmitted probe light T is detected by the amplification of the signal from the probe light by a lock in amplifier synchronized with the 1 kHz repetition of the probe light pulsed. The change of the intensity of the transmitted probe light caused by the excitation light $\Delta T(t)$ was detected by the differential amplification of the signal from probe light and that from the reference light using a lock-in amplifier synchronized with the frequency of the optical chopper, where t is the time delay between pump and probe pulses generated by optical delay line. For the measurement of transient absorption spectra, the wavelength of the probe light was measured over the range from 500 to 2600 nm, while the measurement for the signal decay of the transient absorption was performed by scanning the delay time to about 1 ns as maximum using optical delay line.

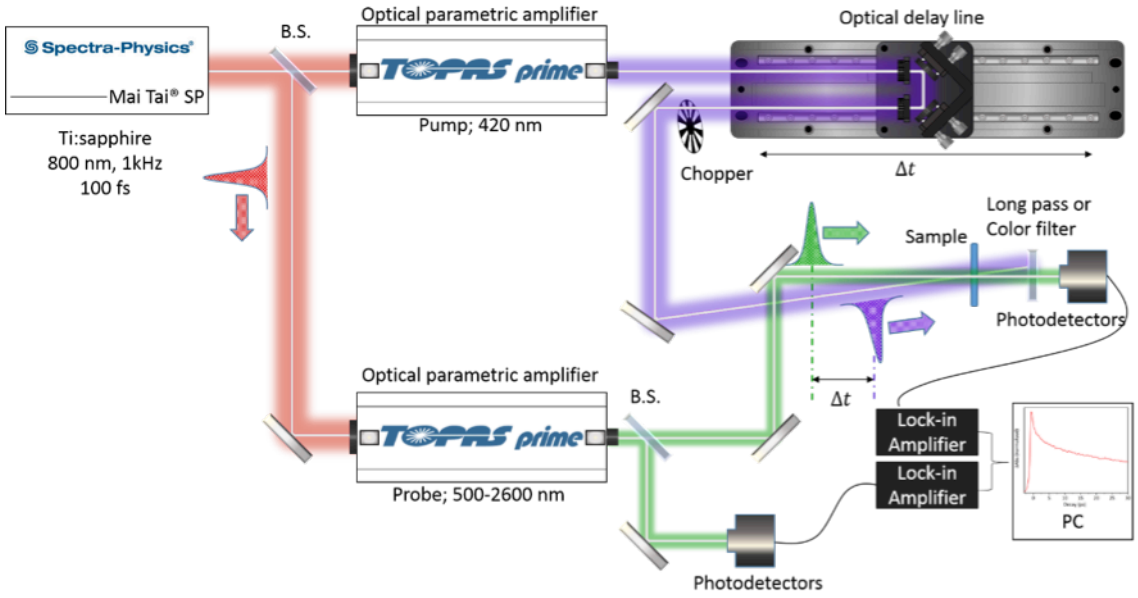

Figure 4.1. The system set-up for the pico-nano seconds transient absorption spectroscopy.

4.3 Results and Discussion

4.3.1 The effects of Pt, Ni loading over $SrTiO_3$

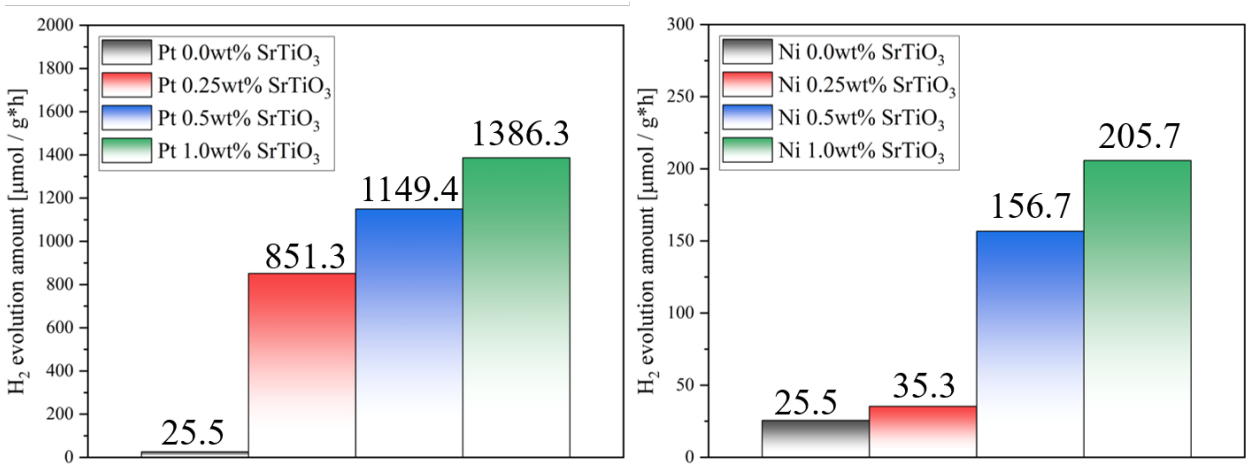

Figure 4.2. Effect of the loaded platinum weight percent on the photocatalytic activity of $SrTiO_3$ nanoparticles for photocatalytic hydrogen evolution.

Figure 4.2(a) shows the effect of the loaded Pt weight percent on the photocatalytic activities of $SrTiO_3$ nanoparticles for photocatalytic hydrogen evolution. The results showed that the photocatalytic activity was significantly enhanced from 25.5 μmol/g·h to 851.3, 1149.4, 1386.3 μmol/g·h with the increase of doped Pt weight percent from 0.0 to 0.25, 0.5, and 1.0 wt%; respectively. This is reasonable because the loading with noble metal such as Pt is expected to create active site for hydrogen evolution reaction. Moreover, the photocatalytic activity is getting saturation with further increase of the platinum loading weight percent on the photocatalytic activity of $SrTiO_3$ nanoparticles. Therefore, the loaded metallic Pt weight percent affect the electron-hole recombination rate of $SrTiO_3$ nanoparticles. Figure 4.2(b) shows the photocatalytic hydrogen evolution with respect to the amount of Ni loaded. A similar tendency was observed in the case of Ni up to 1 wt%, but at 1 wt% the activity was as low as 205 μmol/g·h, only about one-seventh of the activity of Pt.

4.3.2 Transient absorption of photogenerated charge carriers in $SrTiO_3$

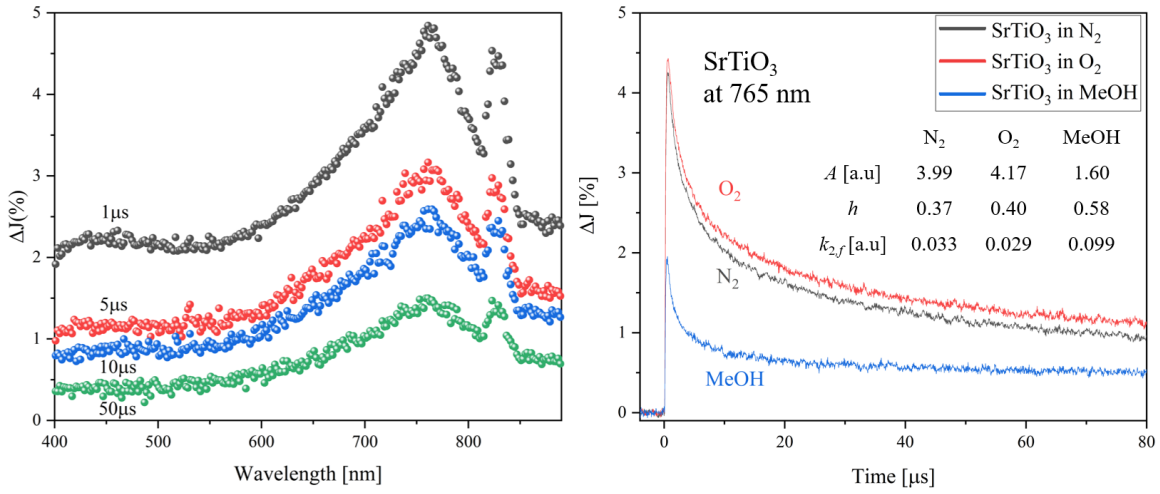

Figure 4.3. Transient absorption spectra of $SrTiO_3$ particles irradiated by UV (355 nm) pulsed laser under N_2 gas. The pump energy was 1.3 mJ/cm^2, and the repetition rate was 10 Hz. (b) Decay curves of transient absorption of the $SrTiO_3$ at 765 nm.

Figure 4.3(a) shows the transient absorption spectrum after 355 nm Nd: YAG laser irradiation over $SrTiO_3$. A broad absorption band was observed around 765 nm, and a relatively narrow absorption band was observed around 825 nm. To identify the observed carriers, TAS measurements were taken at 765 nm with the presence of an electron scavenger (O_2 gas) and a hole scavenger (MeOH vapor) (Figure 4.3(b)). As a reference TAS measurement was also performed in the N_2 gas atmosphere. In this case, there is no reactant existing, the results simply means a process of recombination of electrons and holes. In the

measurement in the oxygen atmosphere, the decay began to slow down slightly after 1 μs. This is because the electrons which tend to recombine with holes are captured by O_2;[47]

$$O_2(g) + e^- \rightarrow O_2^-(a) \tag{4.3}$$

Where (g) and (a) represent gas phase and adsorbed phase, respectively. On the contrary, the decay was dramatically accelerated when measuring in MeOH. This is because the holes were collected by methanol-derived adsorbate:

$$CH_3O^-(a) + h^+ \rightarrow CH_3O^\bullet(a) \tag{4.4}$$

From the above results, it can be concluded that the photoexcited carriers at 765 nm are absorption bands derived from holes.

4.3.3 Transient absorption of photogenerated charge carriers over Pt, Ni loaded $SrTiO_3$

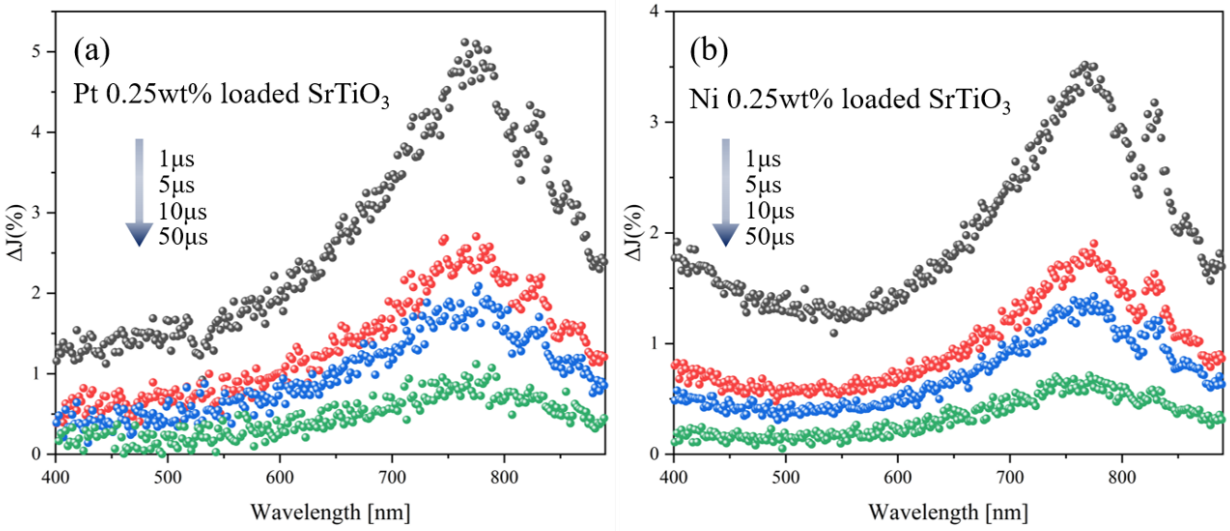

Figure 4.4. (a) Transient absorption spectra of Pt 0.25wt% $SrTiO_3$ particles and (b) Ni 0.25wt% $SrTiO_3$ particles irradiated by UV (355 nm) pulsed laser under N_2 gas. The pump energy was 1.3 mJ/cm^2, and the repetition rate was 10 Hz.

Figure 4.4(a) and (b) shows the transient absorption spectra of Pt and Ni $SrTiO_3$, respectively. Both transient absorption spectra of Pt and Ni loaded $SrTiO_3$ show broad absorption peak around 765 nm and 825 nm, similar to that of the pure $SrTiO_3$.This suggests that even after loading of cocatalyst, transient absorption signal mainly reflect the transient feature of $SrTiO_3$. To further investigate the interaction between the cocatalysts loading and trapping behavior of photogenerated holes generated in $SrTiO_3$, the

relationship between the amount of cocatalyst loading and the decay constant in the inert N_2 atmosphere is examined. (Figure 4.5) The linear increase in $k_{2,f}$, which indicates the rate of decay, with respect to the amount of cocatalyst loading, indicates that the unwilling transfer of holes to the cocatalyst is occurring. The increase in the decay constant with Pt loading is much stronger than that with Ni, suggesting that the broad density of state of Pt acts as a recombination center.

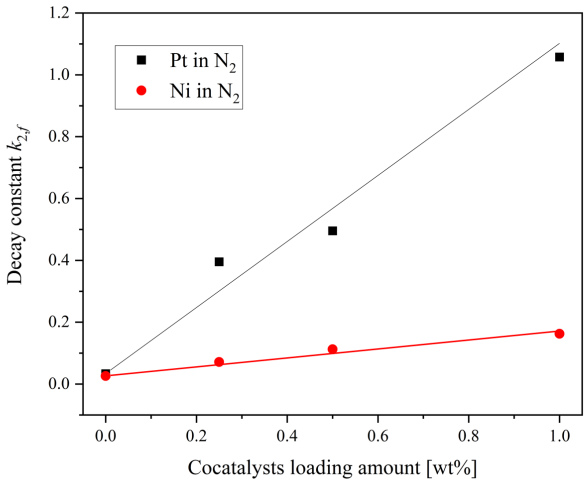

Figure 4.5. The relationship between the loading amount of Pt and Ni cocatalysts and decay constant $k_{2,f}$.

In addition, Figure 4.6(a) shows the relationship between the amount of cocatalyst loading and the decay constant of Pt loaded $SrTiO_3$ in different atmospheres. As described in Figure 4.5, the increasing decay constant in N_2 atmosphere with increase the Pt loading amount have been observed, this increasing decay constant was found to be further promoted in the presence of O_2 gas but suppressed in MeOH vapor. This suggests that the adsorption of O_2 and MeOH molecule might affect the decay dynamics. However, unlike Pt loaded $SrTiO_3$, Ni loaded $SrTiO_3$, shown in Figure 4.6(b), had only a limited effect on the decay constant against to the increase in loading amount in various atmospheres, and no significant difference was observed.

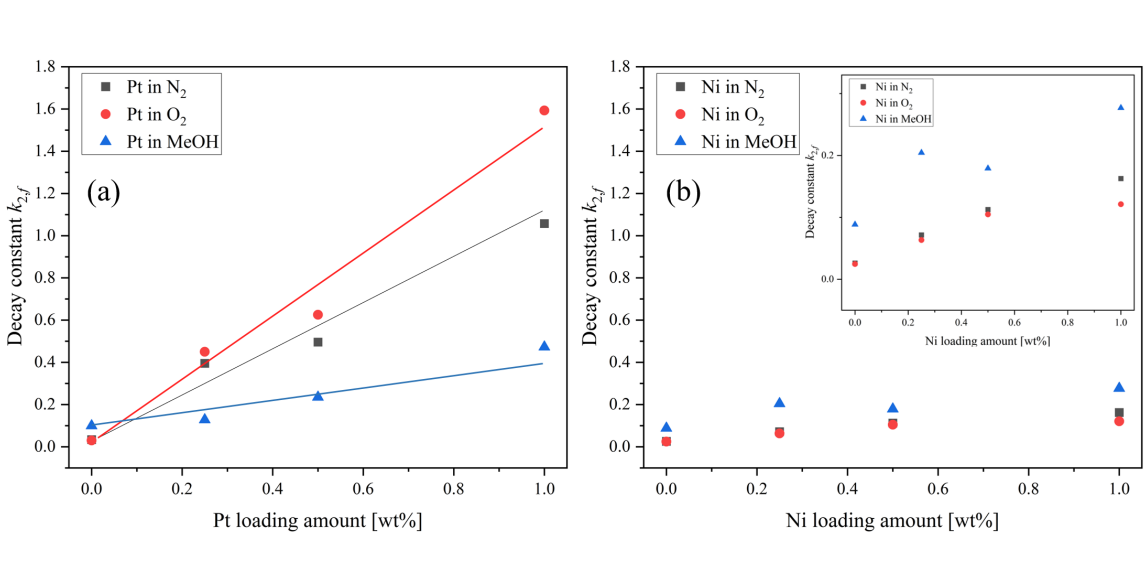

Figure 4.6. The relationship between the loading amount of Pt cocatalysts, (b) Ni cocatalyst and decay constant $k_{2,f}$ in the different atmosphere. Inset figure shows enlarged vertical axis of (b).

To further understand the effect of the molecules adsorbed on Pt cocatalyst, the decay curves of Pt loaded $SrTiO_3$ at 765 nm in N_2, O_2 and MeOH atmospheres are compared as shown in Figure4.7 (a). As described in Figure 4.6(a), the decay accelerates in the O_2 atmosphere and decelerates in MeOH vapor compared to that of N_2 atmosphere. Unlike $SrTiO_3$ (Figure 4.3(b)), after Pt loading, the transient decay was most decelerated in MeOH vapor. Besides in O_2 atmosphere, the decay was slightly accelerated as the decay constant $k_{2,f}$ increases from 0.395 to 0.449 compared with N_2 atmospheres. Moreover, as shown in Figure 4.8, the decay curves of Pt loaded $SrTiO_3$ at 765 nm in N2 and MeOH atmospheres show that Pt loading dramatically decreases the signal intensity and increases the decay constant in N_2 atmosphere (Figure 4.8(a)), while in MeOH atmosphere, the decrease in signal intensity and increase in decay constant are not as significant as those observed in N_2 atmosphere (Figure 4.8(b)). This limited changes in MeOH indicates that MeOH scavenge the photogenerated holes in $SrTiO_3$. Thus the decay curves was not strongly affected by Pt cocatalyst loading. On the other hand, Ni loaded $SrTiO_3$ decelerated in an oxygen atmosphere and accelerated in a MeOH atmosphere compared with N_2 atmosphere, similar to that of $SrTiO_3$, confirming that Ni cocatalyst loading has a small effect on the carrier dynamics of $SrTiO_3$ and would not act as recombination center.

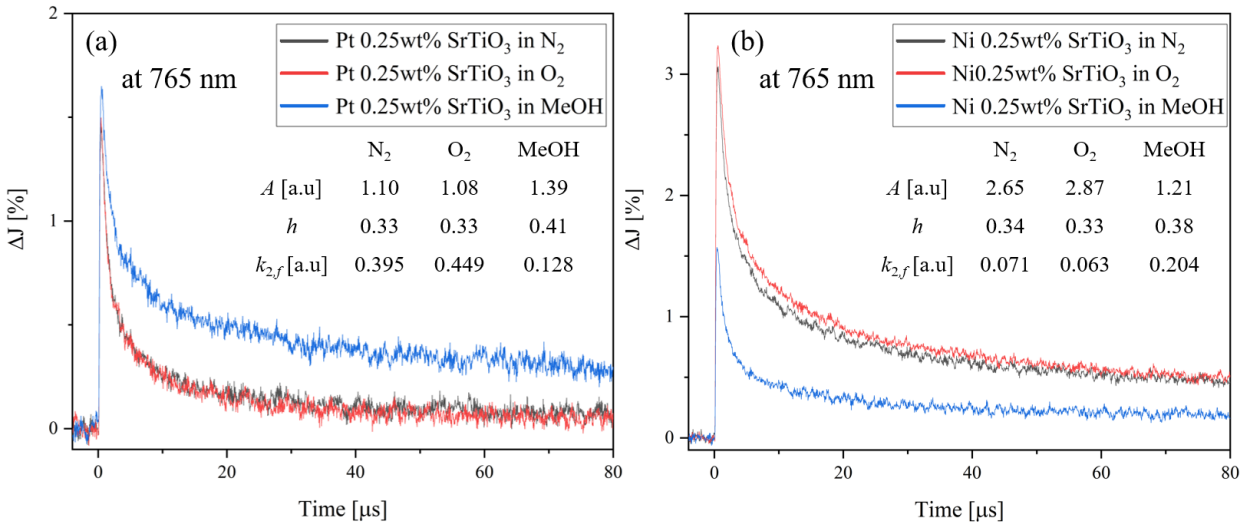

Figure 4.7. Decay curves of transient absorption of the (a) Pt 0.25wt% loaded $SrTiO_3$ and (b) Ni 0.25wt% loaded $SrTiO_3$ in the different atmospheres at 765 nm.

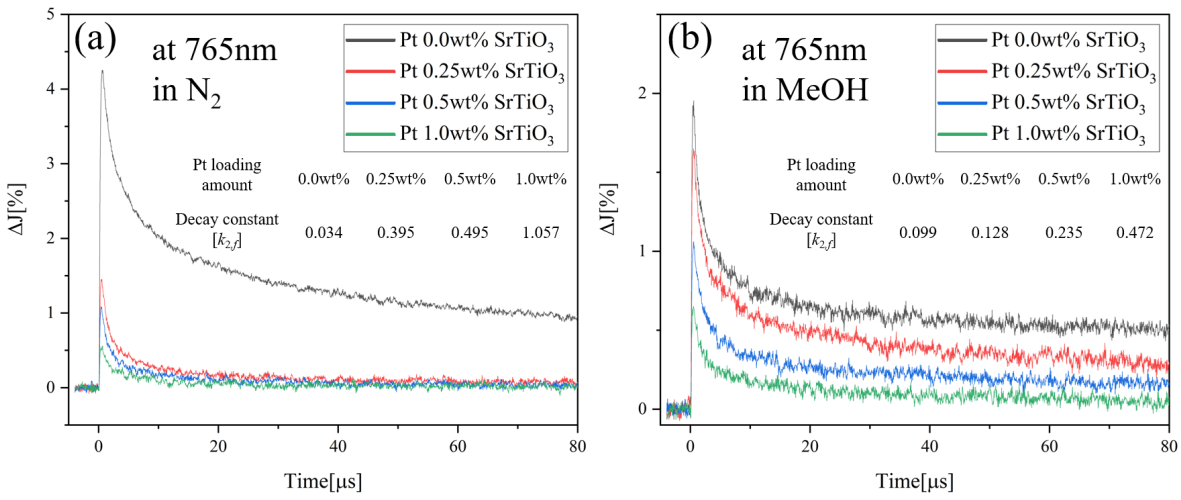

Figure 4.8. Decay curves of transient absorption of the Pt loaded $SrTiO_3$ in (a) N_2 atmospheres and (b) MeOH vapor at 765 nm.

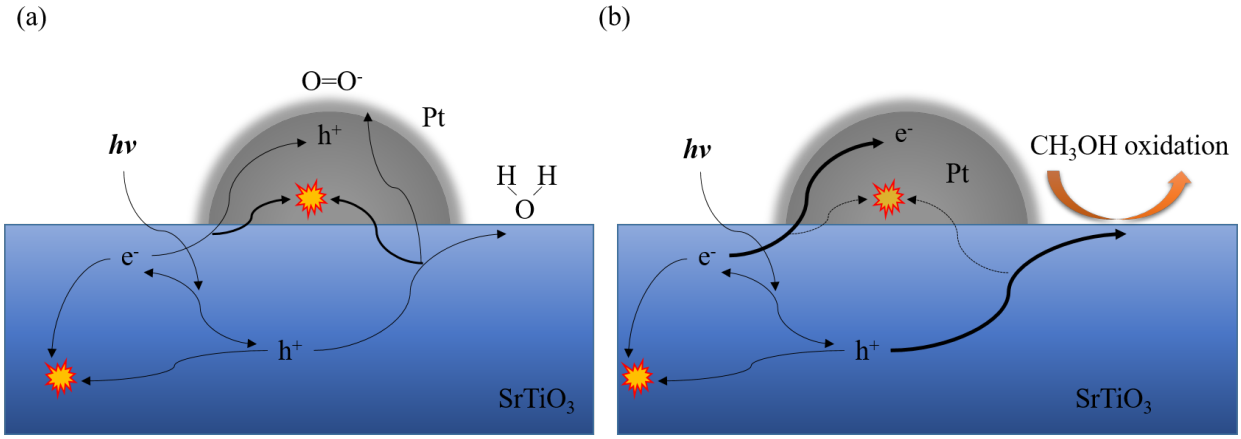

Figure 4.9. Schematic representation of the photoexcited electron and hole path over Pt loaded $SrTiO_3$ in the presence of (a) O_2 gas and (b) MeOH vapor.

From the results discussed above, the dynamics shown in Figure 4.9 can be considered as follows: in an O_2 atmosphere, oxygen molecules adsorbed on Pt scavenge the electron of the Pt cocatalyst to form charged oxygen species and produce holes.[27,48] These charged oxygen species and the holes generated at the Pt cocatalyst is expected to trap the electron-hole pairs generated in $SrTiO_3$, accelerating the consumption of charge carriers in the oxygen atmosphere compared to the N_2 atmosphere. In the case of MeOH vapor, MeOH molecules tend to scavenge the photogenerated holes in $SrTiO_3$. Thus, there is no large effect over the carrier dynamics by loading different amount of Pt cocatalyst. Therefore, the recombination at Pt cocatalyst has been suppressed in the presence of hole sacrificial reagents.

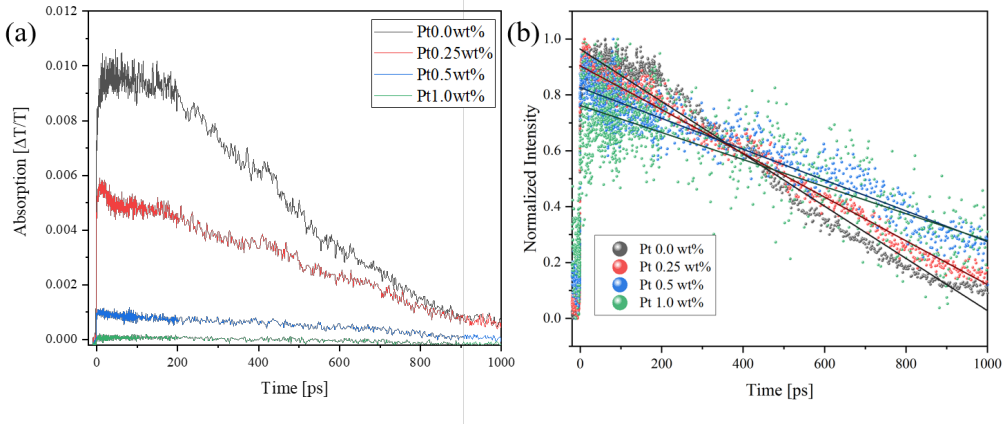

Figure 4.10. Pico-second transient absorption spectra of Pt loaded $SrTiO_3$ nanoparticles irradiated by UV (355 nm) pulsed laser under ambient condition at 765 nm.

The photocatalytic reaction takes place in three steps, i.e., carrier generation, charge transfer, and

surface reaction. In order to investigate in detail which time scale the photo-generated holes transfer, we measured the transient absorption spectrum at 765 nm on the femto-second scale. Figure 4.10 (a) shows the measurement results. When Pt is loaded, the sample itself absorbed 765 nm, and the signal intensity decreased with the increase in the loading amount. Comparing the spectra after normalization (Figure 4.10 (b)), it was observed that the photoexcitation showed a faster decay than pure $SrTiO_3$ with the increase in the amount of Pt loading up to about 400 ps, but after 400 ps, the lifetime was extended. This phenomena indicate that within 400 ps, photoexcited holes near the surface were trapped by the Pt cocatalysts, but subsequently holes trapping behavior from the bulk could not occur within the time range of pico-nano second TAS measurement. However, as described above, in the μs range, most likely the holes were attracted and recombined in Pt cocatalysts.

4.4 Conclusion

The samples loaded with Pt and Ni cocatalysts on $SrTiO_3$ by photodeposition were evaluated using ns-μs transient absorption spectroscopy. Focusing on the transient absorption signal derived from holes instead of the normally focused electron signal, it is found that with increasing loading amount of co-catalysts the decay constant which represent speed of decay increased linearly. When loading with Pt cocatalyst, this increase in decay constant was more significant than Ni cocatalyst loading, indicating that the broad density of state of Pt might act as recombination center as suggested by theoretical calculation. Moreover, in MeOH vapor, this increasing recombination tendency has been suppressed compared with that of N_2 and O_2 atmosphere, indicating Pt cocatalyst would not act as recombination center with the presence of hole sacrificial agents. On the other hand, in the case of the transition metal Ni, it was observed that the recombination was not accelerated. Therefore, it is desired to design the cocatalyst with localized density of state and an appropriate hydrogen absorption/desorption feature for efficient overall water splitting. Furthermore by measuring ps-ns, it is found that the photo-generated holes near the surface transferred to Pt cocatalysts within 400 ps after photoexcitation.

References

[1] Zou, Z.; Ye, J.; Sayama, K.; Arakawa, H., Direct splitting of water under visible light irradiation with an oxide semiconductor photocatalyst. *Nature*, **2001**, *414* (6864), 625-627.

[2] Kato, H.; Kudo, A., Visible-Light-Response and Photocatalytic Activities of TiO_2 and $SrTiO_3$ Photocatalysts Codoped with Antimony and Chromium. *The Journal of Physical Chemistry B*, **2002**, *106* (19), 5029-5034.

[3] Liu, J. W.; Chen, G.; Li, Z. H.; Zhang, Z. G., Electronic structure and visible light photocatalysis water splitting property of chromium-doped $SrTiO_3$. *Journal of Solid State Chemistry*, **2006**, *179* (12), 3704-3708.

[4] Ouyang, S.; Tong, H.; Umezawa, N.; Cao, J.; Li, P.; Bi, Y.; Zhang, Y.; Ye, J., Surface-alkalinization-induced enhancement of photocatalytic H_2 evolution over $SrTiO_3$-based photocatalysts. *Journal of the American Chemical Society*, **2012**, *134* (4), 1974-7.

[5] Tong, H.; Ouyang, S.; Bi, Y.; Umezawa, N.; Oshikiri, M.; Ye, J., Nano-photocatalytic Materials: Possibilities and Challenges. *Advanced Materials*, **2012**, *24* (2), 229-251.

[6] Meng, X.; Zuo, G.; Zong, P.; Pang, H.; Ren, J.; Zeng, X.; Liu, S.; Shen, Y.; Zhou, W.; Ye, J., A rapidly room-temperature-synthesized Cd/ZnS:Cu nanocrystal photocatalyst for highly efficient solar-light-powered CO_2 reduction. *Applied Catalysis B: Environmental*, **2018**, *237*, 68-73.

[7] Li, P.; Ouyang, S.; Xi, G.; Kako, T.; Ye, J., The Effects of Crystal Structure and Electronic Structure on Photocatalytic H_2 Evolution and CO_2 Reduction over Two Phases of Perovskite-Structured $NaNbO_3$. *The Journal of Physical Chemistry C 2012*, **116**(14), 7621-7628.

[8] Kang, Q.; Wang, T.; Li, P.; Liu, L.; Chang, K.; Li, M.; Ye, J., Photocatalytic Reduction of Carbon Dioxide by Hydrous Hydrazine over Au-Cu Alloy Nanoparticles Supported on $SrTiO_3/TiO_2$ Coaxial Nanotube Arrays. *Angewandte Chemie*, **2015**, *127* (3), 855-859.

[9] Yan, S. C.; Ouyang, S. X.; Gao, J.; Yang, M.; Feng, J. Y.; Fan, X. X.; Wan, L. J.; Li, Z. S.; Ye, J. H.; Zhou, Y.; Zou, Z. G., A Room-Temperature Reactive-Template Route to Mesoporous $ZnGa_2O_4$ with Improved Photocatalytic Activity in Reduction of CO_2. *Angewandte Chemie International Edition*, **2010**, *49* (36), 6400-6404.

[10] Xie, K.; Umezawa, N.; Zhang, N.; Reunchan, P.; Zhang, Y.; Ye, J., Self-doped $SrTiO_{3-\delta}$ photocatalyst with enhanced activity for artificial photosynthesis under visible light. *Energy & Environmental Science*, **2011**, *4* (10), 4211-4219.

[11] Kudo, A.; Miseki, Y., Heterogeneous photocatalyst materials for water splitting. *Chemical Society Reviews*, **2009**, *38* (1), 253-278.

[12] Yamakata, A.; Kawaguchi, M.; Nishimura, N.; Minegishi, T.; Kubota, J.; Domen, K., Behavior and Energy States of Photogenerated Charge Carriers on Pt- or CoO_x-Loaded $LaTiO_2N$ Photocatalysts: Time-Resolved Visible to Mid-Infrared Absorption Study. *The Journal of Physical Chemistry C*, **2014**, *118* (41), 23897-23906.

[13] Domen, K.; Naito, S.; Soma, M.; Onishi, T.; Tamaru, K., Photocatalytic decomposition of water vapour on an $NiOSrTiO_3$ catalyst. *Journal of the Chemical Society, Chemical Communications*, **1980**, (12), 543-544.

[14] Domen, K.; Naito, S.; Onishi, T.; Tamaru, K., Photocatalytic decomposition of liquid water on a $NiO@SrTiO_3$ catalyst. *Chemical Physics Letters*, **1982**, *92* (4), 433-434.

[15] Domen, K.; Naito, S.; Onishi, T.; Tamaru, K.; Soma, M., Study of the photocatalytic decomposition of water vapor over a nickel(II) oxide-strontium titanate ($SrTiO_3$) catalyst. *The Journal of Physical Chemistry*, **1982**, *86* (18), 3657-3661.

[16] Domen, K.; Kudo, A.; Onishi, T.; Kosugi, N.; Kuroda, H., Photocatalytic decomposition of water into hydrogen and oxygen over nickel(II) oxide-strontium titanate ($SrTiO_3$) powder. 1. Structure of the catalysts. *The Journal of Physical Chemistry*, **1986**, *90* (2), 292-295.

[17] Maeda, K.; Teramura, K.; Lu, D.; Takata, T.; Saito, N.; Inoue, Y.; Domen, K., Photocatalyst releasing hydrogen from water. *Nature*, **2006**, *440* (7082), 295-295.

[18] Harriman, A.; Pickering, I. J.; Thomas, J. M.; Christensen, P. A., Metal oxides as heterogeneous catalysts for oxygen evolution under photochemical conditions. *Journal of the Chemical Society, Faraday Transactions 1: Physical Chemistry in Condensed Phases*, **1988**, *84* (8), 2795-2806.

[19] Meekins, B. H.; Kamat, P. V., Role of Water Oxidation Catalyst IrO_2 in Shuttling Photogenerated Holes Across TiO_2Interface. *The Journal of Physical Chemistry Letters*, **2011**, *2* (18), 2304-2310.

[20] Inoue, Y., Photocatalytic water splitting by RuO_2-loaded metal oxides and nitrides with d^0- and d^{10} -related electronic configurations. *Energy & Environmental Science*, **2009**, *2* (4), 364-386.

[21] Barroso, M.; Mesa, C. A.; Pendlebury, S. R.; Cowan, A. J.; Hisatomi, T.; Sivula, K.; Grätzel, M.; Klug, D. R.; Durrant, J. R., Dynamics of photogenerated holes in surface modified α-Fe_2O_3 photoanodes for solar water splitting. *Proceedings of the National Academy of Sciences*, **2012**, *109* (39), 15640.

[22] Ma, S. S. K.; Hisatomi, T.; Maeda, K.; Moriya, Y.; Domen, K., Enhanced Water Oxidation on Ta_3N_5 Photocatalysts by Modification with Alkaline Metal Salts. *Journal of the American Chemical Society*, **2012**, *134* (49), 19993-19996.

[23] Kanan, M. W.; Nocera, D. G., In Situ Formation of an Oxygen-Evolving Catalyst in Neutral Water Containing Phosphate and Co^{2+}. *Science*, **2008**, *321* (5892), 1072.

[24] Seabold, J. A.; Choi, K.-S., Effect of a Cobalt-Based Oxygen Evolution Catalyst on the Stability and the Selectivity of Photo-Oxidation Reactions of a WO_3 Photoanode. *Chemistry of Materials*, **2011**, *23* (5), 1105-1112.

[25] Zhang, F.; Yamakata, A.; Maeda, K.; Moriya, Y.; Takata, T.; Kubota, J.; Teshima, K.; Oishi, S.; Domen, K., Cobalt-Modified Porous Single-Crystalline $LaTiO_2N$ for Highly Efficient Water Oxidation under Visible Light. *Journal of the American Chemical Society*, **2012**, *134* (20), 8348-8351.

[26] Higashi, M.; Domen, K.; Abe, R., Highly Stable Water Splitting on Oxynitride TaON Photoanode System under Visible Light Irradiation. *Journal of the American Chemical Society*, **2012**, *134* (16), 6968-6971.

[27] Muhich, C. L.; Zhou, Y.; Holder, A. M.; Weimer, A. W.; Musgrave, C. B., Effect of Surface Deposited Pt on the Photoactivity of TiO_2. *The Journal of Physical Chemistry C*, **2012**, *116* (18), 10138-10149.

[28] Abe, R.; Sayama, K.; Arakawa, H., Significant effect of iodide addition on water splitting into H_2 and O_2 over Pt-loaded TiO_2 photocatalyst: suppression of backward reaction. *Chemical Physics Letters*, **2003**, *371* (3), 360-364.

[29] Peng, H.; Li, J.; Li, S.-S.; Xia, J.-B., First-principles study of the electronic structures and magnetic properties of 3d transition metal-doped anatase TiO_2. Journal of Physics: *Condensed Matter*, **2008**, *20*, 125207.

[30] Tosoni, S.; Chen, H.-Y. T.; Pacchioni, G., A DFT study of Ni clusters deposition on titania and zirconia (101) surfaces. *Surface Science*, **2016**, *646*, 230-238.

[31] Yamakata, A.; Ishibashi, T.-a.; Onishi, H., Water- and Oxygen-Induced Decay Kinetics of Photogenerated Electrons in TiO_2 and Pt/TiO_2: A Time-Resolved Infrared Absorption Study. *The Journal of Physical Chemistry B*, **2001**, *105* (30), 7258-7262.

[32] Yamakata, A.; Ishibashi, T.-a.; Onishi, H., Electron- and Hole-Capture Reactions on Pt/TiO_2 Photocatalyst Exposed to Methanol Vapor Studied with Time-Resolved Infrared Absorption Spectroscopy. *The Journal of Physical Chemistry B*, **2002**, *106* (35), 9122-9125.

[33] Yamakata, A.; Vequizo, J. J. M.; Matsunaga, H., Distinctive Behavior of Photogenerated Electrons and Holes in Anatase and Rutile TiO_2 Powders. *The Journal of Physical Chemistry C*, **2015**, *119* (43), 24538-24545.

[34] Yamakata, A.; Vequizo, J. J. M.; Kawaguchi, M., Behavior and Energy State of Photogenerated Charge Carriers in Single-Crystalline and Polycrystalline Powder $SrTiO_3$ Stud-

ied by Time-Resolved Absorption Spectroscopy in the Visible to Mid-Infrared Region. *The Journal of Physical Chemistry C*, **2015**, *119* (4), 1880-1885.

[35] Cowan, A. J.; Leng, W.; Barnes, P. R. F.; Klug, D. R.; Durrant, J. R., Charge carrier separation in nanostructured TiO_2 photoelectrodes for water splitting. *Physical Chemistry Chemical Physics*, **2013**, *15* (22), 8772-8778.

[36] Tang, J.; Durrant, J. R.; Klug, D. R., Mechanism of Photocatalytic Water Splitting in TiO_2. Reaction of Water with Photoholes, Importance of Charge Carrier Dynamics, and Evidence for Four-Hole Chemistry. *Journal of the American Chemical Society*, **2008**, *130* (42), 13885-13891.

[37] Yamakata, A.; Ishibashi, T.-a.; Kato, H.; Kudo, A.; Onishi, H., Photodynamics of $NaTaO_3$ Catalysts for Efficient Water Splitting. *The Journal of Physical Chemistry B*, **2003**, *107* (51), 14383-14387.

[38] Pendlebury, S. R.; Barroso, M.; Cowan, A. J.; Sivula, K.; Tang, J.; Grtzel, M.; Klug, D.; Durrant, J. R., Dynamics of photogenerated holes in nanocrystalline α-Fe_2O_3 electrodes for water oxidation probed by transient absorption spectroscopy. *Chemical Communication*, **2011**, *47* (2), 716-718.

[39] Barroso, M.; Cowan, A. J.; Pendlebury, S. R.; Grtzel, M.; Klug, D. R.; Durrant, J. R., The Role of Cobalt Phosphate in Enhancing the Photocatalytic Activity of α-Fe_2O_3 toward Water Oxidation. *Journal of the American Chemical Society*, **2011**, *133* (38), 14868-14871.

[40] Wu, K.; Chen, Z.; Lv, H.; Zhu, H.; Hill, C. L.; Lian, T., Hole Removal Rate Limits Photodriven H_2 Generation Efficiency in CdS-Pt and CdSe/CdS-Pt Semiconductor NanorodMetal Tip Heterostructures. *Journal of the American Chemical Society*, **2014**, *136* (21), 7708-7716.

[41] Wu, K.; Rodríguez-Córdoba, W. E.; Yang, Y.; Lian, T., Plasmon-Induced Hot Electron Transfer from the Au Tip to CdS Rod in CdS-Au Nanoheterostructures. *Nano Letters*, **2013**, *13* (11), 5255-5263.

[42] Nakibli, Y.; Mazal, Y.; Dubi, Y.; Wächtler, M.; Amirav, L., Size Matters: Cocatalyst Size Effect on Charge Transfer and Photocatalytic Activity. *Nano Letters*, **2018**, *18* (1), 357-364.

[43] Yan, Z.; Du, L.; Lee Phillips, D., Multilayer coreshell MoS_2/CdS nanorods with very high photocatalytic activity for hydrogen production under visible-light excitation and investigation of the photocatalytic mechanism by femtosecond transient absorption spectroscopy. *RSC Advances*, **2017**, *7* (88), 55993-55999.

[44] Tonda, S.; Kumar, S.; Anjaneyulu, O.; Shanker, V., Synthesis of Cr and La-codoped $SrTiO_3$ nanoparticles for enhanced photocatalytic performance under sunlight irradiation. *Physical chemistry chemical physics : PCCP*, **2014**, *16* (43), 23819-28.

[45] Schneider, J.; Nikitin, K.; Wark, M.; Bahnemann, D. W.; Marschall, R., Improved charge carrier separation in barium tantalate composites investigated by laser flash photolysis. *Physical chemistry chemical physics : PCCP*, **2016**, *18* (16), 10719-26.

[46] Ichihara, F.; Sieland, F.; Pang, H.; Philo, D.; Duong, A.-T.; Chang, K.; Kako, T.; Bahnemann, D. W.; Ye, J., Photogenerated Charge Carriers Dynamics on La- and/or Cr-Doped $SrTiO_3$ Nanoparticles Studied by Transient Absorption Spectroscopy. *The Journal of Physical Chemistry C*, **2020**, *124* (2), 1292-1302.

[47] Schneider, J.; Matsuoka, M.; Takeuchi, M.; Zhang, J.; Horiuchi, Y.; Anpo, M.; Bahnemann, D. W., Understanding TiO_2 Photocatalysis: Mechanisms and Materials. *Chemical reviews*, **2014**, *114* (19), 9919-9986.

[48] Pepin, P. A.; Lee, J. D.; Murray, C. B.; Vohs, J. M., Thermal and Photocatalytic Reactions of Methanol and Acetaldehyde on Pt-Modified Brookite TiO_2 Nanorods. *ACS Catalysis*, **2018**, *8* (12), 11834-11846.

Chapter 5 . Direct observation of photogenerated electron transfer process from cascaded π-conjugation polymer to CO_2 molecule for CO_2 photoreduction

5.1 Introduction

Global carbon dioxide (CO_2) emissions from burning fossil fuels reached 33 gigatons in 2017, twice the natural rate at which CO_2 is adsorbed back into land and ocean sinks. Harnessing solar radiation holds the answer to reducing our dependence on fossil fuels and reducing greenhouse gas emissions. The utilization of photoexcited high-energy photoelectrons with the help of semiconductors to drive the energy conversion of CO_2 to valued-added green fuels is believed to be an effective strategy for promoting sustainable development in society.[1–5] Beyond conventional semiconductors, conjugated polymers (CPs), as a new class of organic semiconductors, is expected to be the next generation of multifunctional photocatalyst because of their versatile photophysical properties, intriguing electronic properties, and especially the adjustable monomer structure, endowing it with manageable light absorption and controllable electronic localization ability. Therefore, numerous studies on developing various strategies for capable of photocatalytic energy conversion over CPs have been carried out.[6–8] Since Cooper 's group first found a series of pyrene-based CPs active in hydrogen (H_2) evolution under visible light irradiation with platinum as cocatalyst,[9] researchers have tried to anticipate to the application of such materials in CO_2 photoreduction.[10] For CPs in photocatalytic CO_2 reduction, the light conversion efficiency is rate-determined by the photoexcited electrons delivery from CPs to the surface loaded cocatalyst (adsorb and active CO_2 molecule). However, a limitation still exists in finding an appropriate way to promote the delivery of photoexcited electrons to cocatalyst due to a higher energy barrier of the out-of-plane Ohm or Schottky contact than the intramolecular cascade between cocatalyst and CPs.[11,12] Photoinduced intermolecular charge transfer through molecules by non-covalent interactions is a well-known efficient process in photochemistry.[13] To achieve kinetically favorable electron transfer from CPs to cocatalyst and make a breakthrough in CO_2 photoreduction, an intermolecular cascaded channel between the CPs

and cocatalyst is desirable to be established for oriented delivery of photoexcited electrons to overcome a lower energy barrier and a less carrier.[14–17] Transition metal bipyridine compounds with a π-conjugated structure, such as Co (II) bipyridine complexes has recognized as one of the most active centers for adsorbing and activating CO_2 molecular and even achieving photocatalytic CO_2 reduction in the presence of some photosensitizer.[18–21] However, the photocatalytic CO_2 reduction process is severely hampered due to the instability of the light-absorbing material and the obstruction of interface electron transport.[15] When analyzing the spatial structure of π-conjugated Co (II) bipyridine complexes cocatalyst appeared in the large π-conjugated pyrene-based CPs, the most striking feature is that the strong π-π interactions will self-assemble them into an intermolecular π-π stacking structure.[22–25] Inspired by this, we speculated that an electronic transmission channel could be built *via* the enhanced π-electronic cloud interactions to ensure the photoexcited electrons freely deliver from CPs to cocatalysts.[26] Furthermore, for CPs, removing the unsaturated bond between two adjacent aromatic rings through eliminating the alkynyl can not only reduce the steric repulsion (reducing the twist angle of adjacent aromatic rings) but also weaken the intramolecular conjugate interaction.[27,28] The weakened conjugate interaction between adjacent aromatic rings of CPs is expected to result in free-π-electrons localized that could improve its intermolecular cascading ability with Co (II) bipyridine complexes.[29] To validate the above strategy, four goal-oriented materials including linear and net-like CPs with simple structure but different π-conjugation were built by using Suzuki-Miyaura coupling instead of Sonogashira-Hagihara coupling in synthesis. From DFT calculation and experimental data, we proved that the CPs without alkynyl groups strictly block the delocalization of photoexcited electrons due to the lack of intramolecular charge-transfer bridges, which in turn deliver the photoexcited electrons faster to Co (II) bipyridine complexes through the intermolecular cascaded channels, leading to a state-of-the-art CO_2 photoreduction activity. This new strategy constructs an efficient system of CO_2 photoreduction over Co (II) bipyridine complexes and pyrene-based CPs with modification of both intramolecular and intermolecular conjugations. Our results also provide evidence and mechanism of enhanced charge transfer via the new pathway of non-covalent interactions. The built-in intermolecular cascaded channels worked out the most critical challenge in the electron delivery from CPs to cocatalyst, providing a new point of view in the nanoarchitecture of CPs for CO_2 photoreduction.

5.2 Methods

5.2.1 Synthesis of CP-A series (L-CP-A and N-CP-A).

All reagents were purchased from Sigma-Aldrich or Tokyo Chemical Industry without further purification. The CP-A series were synthesized according to Sonogashira-Hagihara cross-coupling polycondensation. In details, a dry 250 mL round-bottom flask was charged with two monomer reactants, $Pd(PPh_3)Cl_2$ and CuI, and mixed solvent of dimethyl formamide/triethylamine (DMF/TEA). The mixture was degassed by bubbling with Ar for 30 min, and then the resulting mixture was stirred at 80 °C for 24 h under Ar condition. After that, the precipitate was collected by filtration, and the solid was washed with methanol and CH_2Cl_2 in the Soxhlet for 48 hours. The final product was dried at 60 °C overnight.

For synthesis of L-CP-A, 1,4-diethynylbenzene (189 mg, 1.5 mmol), 1,6-dibromopyrene (540 mg, 1.5 mmol) $Pd(PPh_3)Cl_2$ (27 mg), CuI (5 mg), DMF (60 mL), and TEA (60 mL) were used. For N-CP-A, 1,4-diethynylbenzene (189 mg, 1.5 mmol), 1,3,6,8-Tetrabromopyrene (388 mg, 0.75 mmol), $Pd(PPh_3)Cl_2$ (27 mg), CuI (5 mg), DMF (60 mL), and TEA (60 mL) were used.

5.2.2 Synthesis of CP-D series (L-CP-D and N-CP-D).

All reagents were purchased from Sigma-Aldrich or Tokyo Chemical Industry without further purification. The CP-D series were synthesized according to Suzuki-Miyaura cross-coupling polycondensation. In details, a dry 250 mL round-bottom flask was charged with two monomer reactants, $Pd(PPh_3)_4$, K_2CO_3, and mixed solvent of dimethyl formamide/water (DMF/H_2O). The mixture was degassed by bubbling with Ar for 30 min and then the resulting mixture was stirred at 150 °C for 24 h under Ar condition. After that, the precipitate was collected by filtration, and the solid was washed with methanol and CH_2Cl_2 in the Soxhlet for 48 hours. The final product was dried at 60 °C overnight. For synthesis of L-CP-D, 1,4-phenylenediboronic acid (248 mg, 1.5 mmol), 1,6-dibromopyrene (540 mg, 1.5 mmol), $Pd(PPh_3)_4$ (10 mg), K_2CO_3 (2.0 g) DMF (60 mL), and H_2O (8 mL) were used. For N-CP-D, 1,4-phenylenediboronic acid (248 mg, 1.5 mmol), 1,3,6,8-Tetrabromopyrene (388 mg, 0.75 mmol), $Pd(PPh_3)_4$ (10 mg), K_2CO_3 (2.0 g) DMF (60 mL), and H_2O (8 mL) were used.

5.2.3 FP-TRMC measurement.

FP-TRMC measurements were carried out at room temperature under a N_2 atmosphere, using different CPs powder on poly(methylmethacrylate) (PMMA) films. The films were cast onto quartz substrates. The microwave power and frequency were set at 50 mW and ~9.1 GHz, respectively. Charge carriers were generated in the films by direct excitation of CPs using third-harmonic generation (λ = 355 nm) light pulses from a Nd: YAG laser (Spectra Physics, INDI-HG). The excitation density was tuned at $9.1 times 10^{15}$ photons cm^{-2}. The TRMC signal from a diode was recorded on a digital oscilloscope (Tektronix, TDS 3032B). Comparison of the integrated photocurrents with the polymer standard (poly-9,9'-dioctylfluorene, ϕ ~2.3×10^{-4}) allowed determination of the quantum efficiency of charge carrier generation for the CPs samples. The local-scale charge carrier mobility μ_{tot} was estimated by the quotient of ($\phi\Gamma\mu$) max by ϕ.

5.2.4 Photocatalytic activities measurement.

The photoreduction CO_2 activities of all CPs were carried out in gas-closed system with a gas-circulated pump. The setup of the photocatalytic system is illustrated in Figure 5.1. In detail, the 5 mg catalyst, 50 mL of solution (acetonitrile/water = 7:3), 5 mL of triethanolamine and the Co (II) bipyridine complexes cocatalyst synthesized according to the previous publications[43] were added in a Pyrex glass reaction cell which was connected to the CO_2 reduction system. After complete evacuation of the reaction system

(no O_2 or N_2 could be detected by gas chromatography), ~80 kPa of pure CO_2 gas was injected into the airtight system. After adsorption equilibrium, a 300 W xenon lamp (~100 mW/cm^2) with a UV-cut filter (L42), to remove light with wavelengths lower than 420 nm (λ > 420 nm) was used as the light source. The produced H_2 and CO was analyzed by two gas chromatographs (GC-8A and GC-2014, Shimadzu Corp., Japan) equipped with different chromatographic column.[12,25]

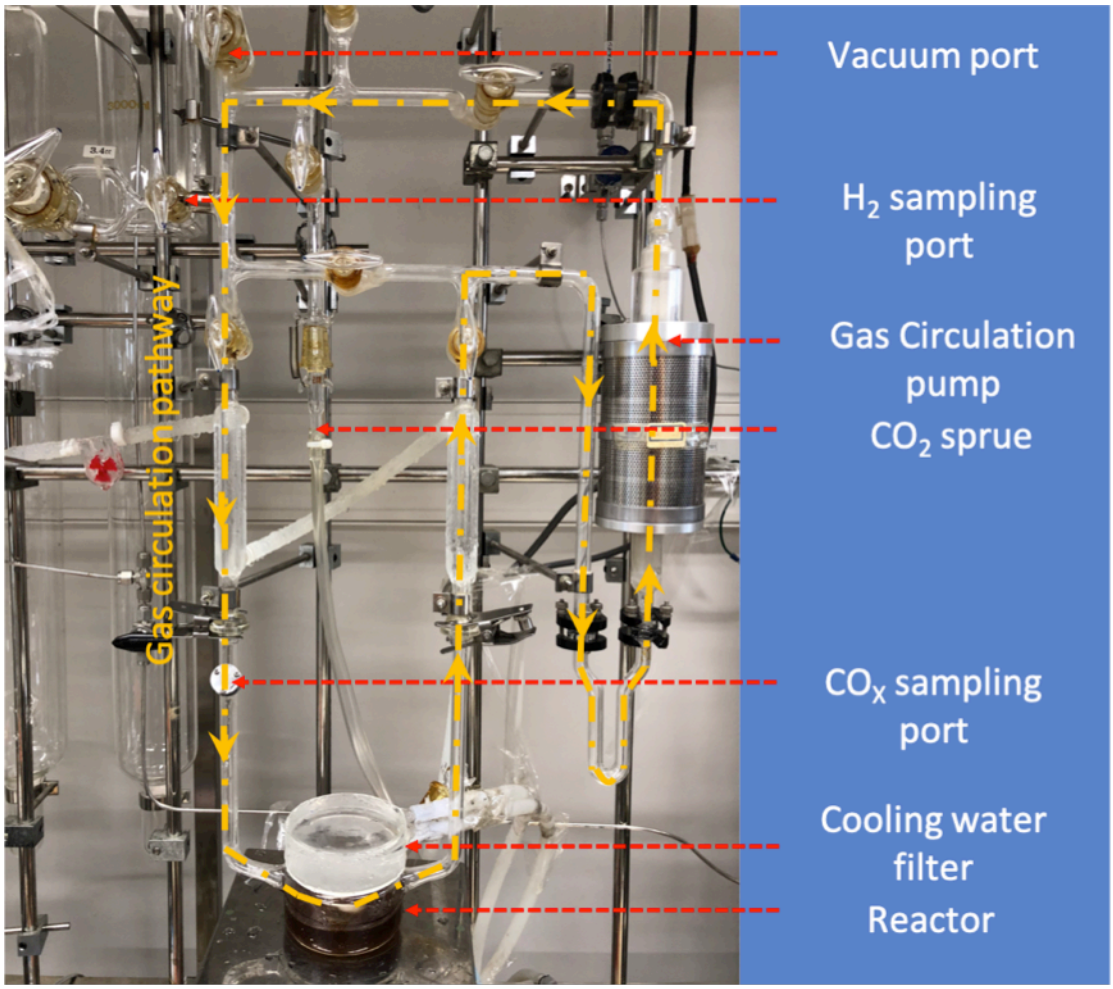

Figure 5.1. The closed gas circulation system for visible light photocatalytic CO_2 reduction.

5.2.5 Isotope labelling measurement.

The isotope labelling measurement was carried out by using $^{13}CO_2$ gas (Isotope purity, 99% and chemical purity, 99.9%, Tokyo Gas Chemicals Co., Ltd.) instead of pure $^{12}CO_2$ gas (Chemical purity, 99.999%, Showa Denko Gas Products Co., Ltd.) as the carbon source with the same reaction set as mentioned above and the gas products were analyzed by gas chromatography-mass spectrometry (JMS-K9, JEOL-GCQMS, Japan and 6890N Network GC system, Agilent Technologies, USA) equipped with two different kinds of column for detecting the products of ^{13}CO (HP-MOLESIEVE, 30 m × 0.32 mm × 25

μm, Agilent Technologies, USA) and source of $^{13}CO_2$ (HP-PLOT/Q, 30 m × 0.32 mm × 20 μm, Agilent Technologies, USA), respectively.[12,25]

5.2.6 TA measurement.

The output pulses of a 1kHz Ti: sapphire regenerative amplifier (Solstice, Spectra-Physics) were split into two beams. One of the beams was used as an excitation light source of an optical parametric amplifier (OPA) (TOPAS prime, NIR-UV-Vis. LIGHT CONVERSION Inc.). The 420 nm output of the OPA was as the excitation light source. The excitation light was chopped at 500Hz by an optical chopper. The other beam was used as an excitation light source of another OPA. The output of the OPA was used as the wavelength-tunable probe and reference light source (500-2600 nm). Si photodetectors and InGaAs photodetectors were used to detect the probe and reference light depending on probe light wavelength (500-1000 nm and1000-2600 nm respectively). (Figure 5.2)

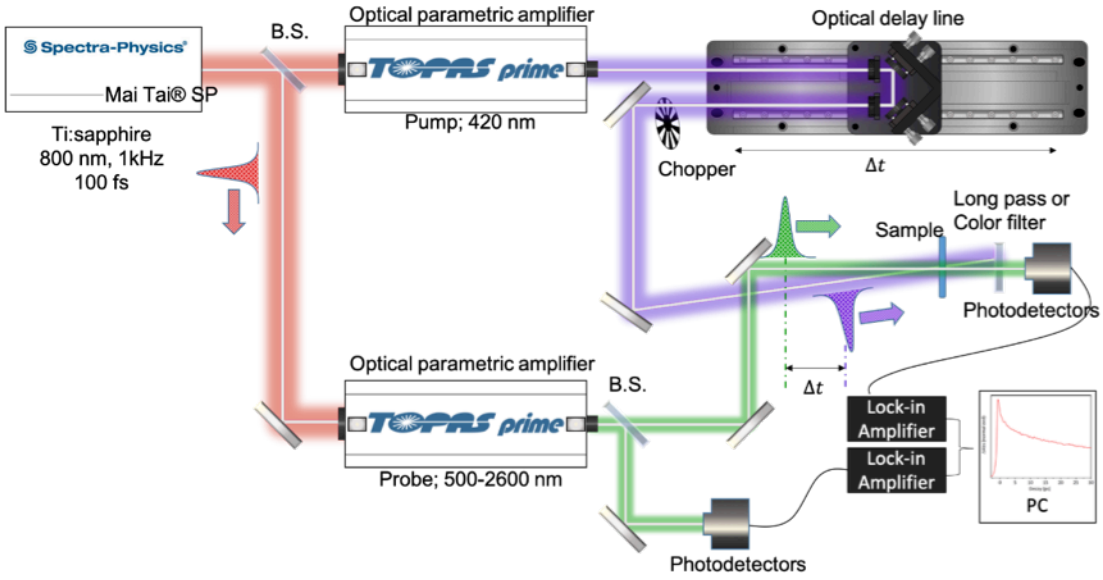

Figure 5.2. The illustration diagram of transient adsorption measurement.

As shown in Figure 5.2, both excitation light and probe lights were focused and overlapped on the surface of the photocatalysts. The transmitted probe light was focused into the Si or InGaAs photodetectors with a detection range of 500-1000 and 1000-2600 nm. Scattered excitation light was blocked by a long wave pass filter placed in front of the photodetectors. The intensity of the transmitted probe light T is detected by the amplification of the signal from the probe light by a lock in amplifier synchronized with the 1 kHz repetition of the probe light pulsed. The change of the intensity of the transmitted probe light caused by the excitation light $\Delta T(t)$ was detected by the differential amplification of the signal from probe light and that from the reference light using a lock-in amplifier synchronized with the frequency of the optical chopper, where t is the time delay between pump and probe pulses generated by optical delay line.

For the measurement of transient absorption spectra, the wavelength of the probe light was measured over the range from 500 to 2600 nm, while the measurement for the signal decay of the transient absorption was performed by scanning the delay time to about 1 ns as maximum using optical delay line.

5.2.7 Computational methods.

All the computations were performed with the Vienna ab initio simulation package (VASP 5.4.4 version),[30,31] patched to include the implicit solvent VASPsol.[32,33] The electron exchange and correlation were handled with generalized gradient approximation using PBE functional and HSE06,[34,35] and which were applied for structure optimization and electronic structures computations, respectively. The Grimme PBE-D3 and HSE06-D3 methods were used for the dispersion correction.[36] The plane wave cut-off energy was set to 400 eV, the electronic self-convergence was 10^{-6} eV, and the core electrons were replaced by the projector augmented wave pseudopotential.[37,38] The geometries are converged to a residual force smaller than 0.03 eV/Å using PBE-D3. The L-CP-D, L-CP-A, N-CP-D, and N-CP-A were modeled in a monolayer structure, with a vacuum thickness of 25 Å. The atomic position and lattice parameters are fully relaxed during the slab mode optimized. The optimized lattice parameters were, a = b = 11.44 Å, γ = 100.65 degree for N-CP-D, a = b = 16.03 Å, γ = 79.77 degree for N-CP-A, respectively. And the value was a = 16.14 Å, b = 21.27 Å, γ = 90.22 degree and a = 11.96 Å, b = 22.10 Å, γ = 89.60 degree for L-CP-A and L-CP-D, respectively. The optimization structures were shown in Figure 5.3. The Brillouin zone was integrated by 3×1×1, 3×1×1, 3×3×1, and 3×3×1 Monkhorst-Pack grid for optimization for L-CP-D, L-CP-A, N-CP-D, and N-CP-A, respectively. There existed a dihedral angle around 50 degrees between benzene and pyrene rings, due to the steric effect for L-CP-D and N-CP-D, as shown in Figure 5.3a and 5.3c, which was reported in similar structures.[39] And the optimized L-CP-A and N-CP-A were flat structures. In addition, the band structures were calculated along the high symmetry lines G (0.0, 0.0, 0.0)-F (0.0, 0.5, 0.0)-Z (0.0, 0.0, 0.5)-B (0.5, 0.0, 0.0) using HSE06-D3. The calculated bandgaps were 2.62 eV, 1.84 eV, 2.45 eV and 1.29 eV for L-CP-D, L-CP-A, N-CP-D, and N-CP-A, respectively. The adsorption energies of the Co (II) bipyridine complexes on L-CP-D or L-CP-A surface were calculated via ΔE_{bind} = E(Co(bpy)$_2^{2+}$/surf) - E(Co(bpy)$_2^{2+}$)- E(surf), where E(Co(bpy)$_2^{2+}$/surf) denoted the energies of Co(bpy)$_2^{2+}$/L-CP-D or Co(bpy)$_2^{2+}$/L-CP-A, E(Co(bpy)$_2^{2+}$) represented the energies of Co(bpy)$_2^{2+}$ and E(surf) stood for the energy of L-CP-D and L-CP-A surface.The interlayer interaction energies of L-CP-D, L-CP-A, N-CP-D and N-CP-A were calculated via, ΔE_i =(E(bilayer) -2×E(monolayer))/A, where E was the computational total energy of L-CP-D, L-CP-A, N-CP-D and N-CP-A, and A was the surface area of N-CP-A and N-CP-A, and A was the length of L-CP-A and L-CP-D, which was the lattice parameter a.

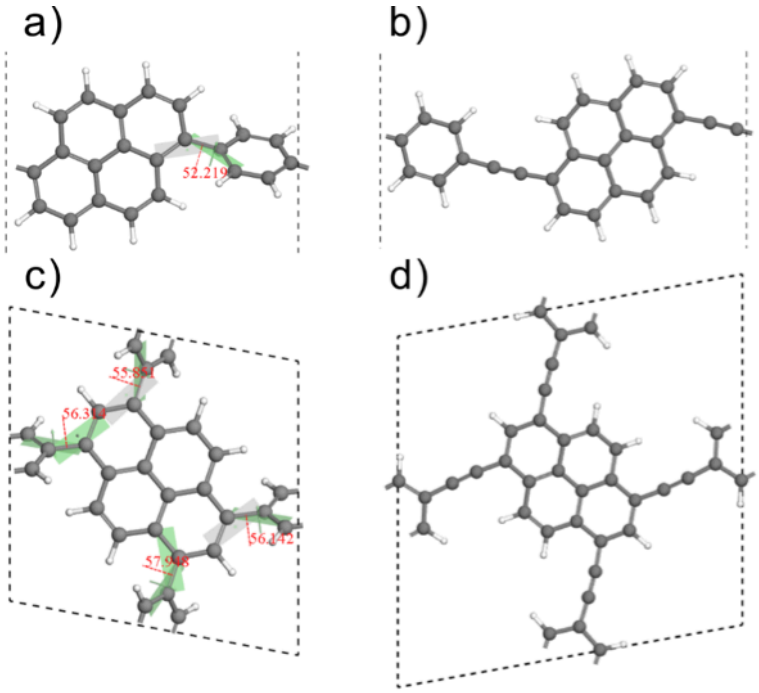

Figure 5.3. The top view of L-CP-D (a), L-CP-A (b), N-CP-D (c) and N-CP-A (d). The dark grey and white balls represent C and H atoms, respectively. The dihedral angle was listed (red) for L-CP-D and N-CP-D, while the grey and light green plane represented the corresponding plane.

5.2.8 Characterization.

Transmission electron microscopy (TEM, Tecnai G2 F20, FEI, Holland) and scanning electron microscope (SEM, SU8010, Hitachi, Japan) were used to analyze the morphologies of polymers. The diffractometer (D8 advance, Bruker, Germany) with Cu Kα radiation was used to record the Powder X-ray diffraction (PXRD). The solid-state ^{13}C cross polarization magic angle spinning (^{13}C-CP/MAS) NMR spectra (Avance III HD 400 MHz spectrometer, Bruker, Germany) were measured to analyze the structure of polymers. The infrared spectra were recorded using a Fourier transform-infrared (FT-IR) spectrometer (Nicolet 6700, Thermo Scientific, USA). Raman spectra were collected using a Raman spectrometer (DXR, Thermo Scientific, USA). The low-pressure gas adsorption measurements were investigated with a gas adsorption analyzer (ASAP 2040, Micrometrics, USA) using nitrogen/carbon dioxide as the adsorbate at 77 K. UV-Vis diffused reflectance spectra (DRS) were measured on a spectrometer (UV-3100, Shimadzu, Japan). The thermal stability was evaluated by thermal gravity analysis (TGA, TG 209 F3 Tarsus, Netzsch, Germany) with the temperature increased at 10 °C/min^{-1} under air atmosphere. Metal content was determined by inductively coupled plasma mass spectrometry (ICP-MS, 7800, Agilent Technologies, USA), where the sample was first digested by H_2SO_4/HNO_3 (0.8 mL/0.2 mL) solvent at 60 °C. The surface electronic states of polymers were analyzed via X-ray photoelectron spectroscopy (XPS,

ESCALAB 250Xi, Thermo Scientific, USA). Cyclic voltammetry (CV) measurements, electrochemistry impedance spectroscopy (EIS) and photocurrent intensity response measurements were performed in a typical three-electrode cell system. Electrochemical measurements were carried out in a conventional three-electrode system using an Ag/Ag^+ as reference electrode, platinum plate as the counter electrode, and the sample modified glassy carbon as the working electrode. The electrochemical workstation was a CHI 660E potentiostat (Shanghai Chenhua Co.) and CVs were collected at a scan rate of 50 mV s^{-1} with the protection of nitrogen. A solution of 0.1 M $TBAPF_6$ in CH_3CN was used as the electrolyte. All of these have been performed as described in our previous report.[40]

5.2.9 Photocatalytic cyclic testing experiment and AQY Evaluation.

For cyclic testing experiment, the 25 mL of fresh solution (acetonitrile/water = 7:3) and 5 mL of triethanolamine were added into the Pyrex glass reaction cell. After complete evacuation of the reaction system, ~80 kPa of pure CO_2 gas was injected into the airtight system. The subsequent photoirradiation and sampling analysis processes are consistent with the previous photocatalytic measurement process. The apparent quantum efficiency (AQY) was measured under similar conditions as described above except for the light intensity and the wavelength regions of the irradiation light. A series of band-pass filters were adopted to control the wavelength regions of incident light. A water filer was also used together with the band-pass filter to avoid the possible damage caused by heating effect of Xe lamp. The average intensity of irradiation was determined by using a spectroradiometer (AvaSolar - 1, Avantes, America). The AQY at each monochromatic wavelength was calculated by following the equation below:

$$\mathrm{AQY for CO evolution} = \mathrm{N(CO)} \times 2/\mathrm{N(photons)} \times 100\% \tag{5.1}$$

5.2.10 In situ DRIFTS measurement

In situ DRIFTS measurement were carried out by FT-IR spectrometer (Nicolet iS50 Thermo Scientific, USA) with a designed reaction cell simulated in Figure 5.4. The substrate lying in the center of the designed reaction cell and a thin layer of N-CP-D mixture with or without cocatalyst as the model sample was placed uniformly on the substrate. An ultra-high vacuum pump was used to pump out all the gases in the reaction cell and adsorbed on the photocatalyst surface. Then the large amount of carbon dioxide or carbon monoxide was pumped in to construct a CO_2 or CO atmosphere for CO_2 photoreduction or CO adsorption, respectively. At last, visible light was turned on and the IR signal was in situ collected through MCT detector along with the reaction.[41,42]

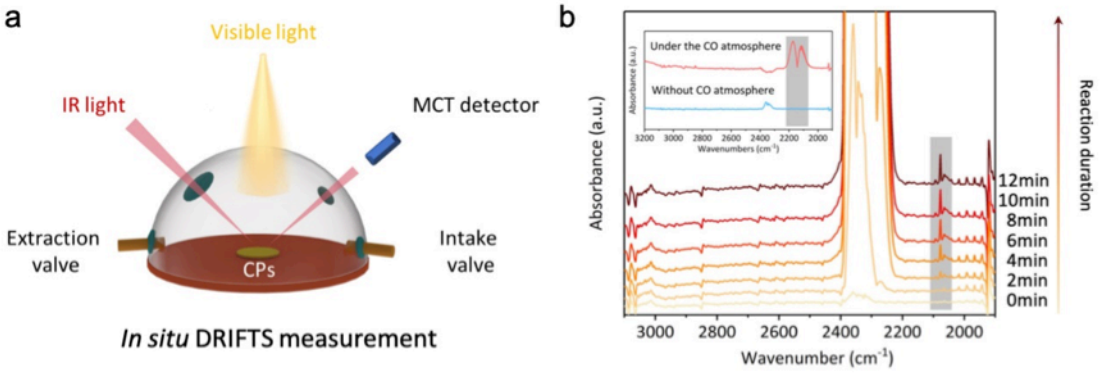

Figure 5.4. The designed reaction cell for the in situ diffuse reflectance infrared Fourier transform spectroscopy (DRIFTS) (a) and the CO_2 photoreduction process over N-CP-D according to the DRIFTS measurement (b) inset: N-CP-D with (red line) or without (blue line) absorbed CO in DRIFTS.

5.3 Results and discussion

5.3.1 Synthesis, structure, and spectroscopic properties of CPs

The four kinds of pyrene-based CPs with or without alkynyl groups were designed based on classic Sonogashira-Hagihara and Suzuki-Miyaura coupling processes, and linear or net-like structures were modified by changing the building blocks (see Methods for experimental details), as outlined in Figure5.5a.[9,43] Linear (L-CP-A) and net-like (N-CP-A) alkynyl-connected CPs can be obtained by using the Sonogashira blocks (1,4-diethynylbenzene) polymerized with the linear blocks (1,6-dibromopyrene) and net-like blocks (1,3,6,8-tetrabromopyrene), respectively. As a comparison, Suzuki blocks (1,4-phenylenediboronic acid) were employed as substitutes for Sonogashira blocks and successfully construct the corresponding linear (L-CP-D) and net-like (N-CP-D) directly connected CPs without alkynyl groups.

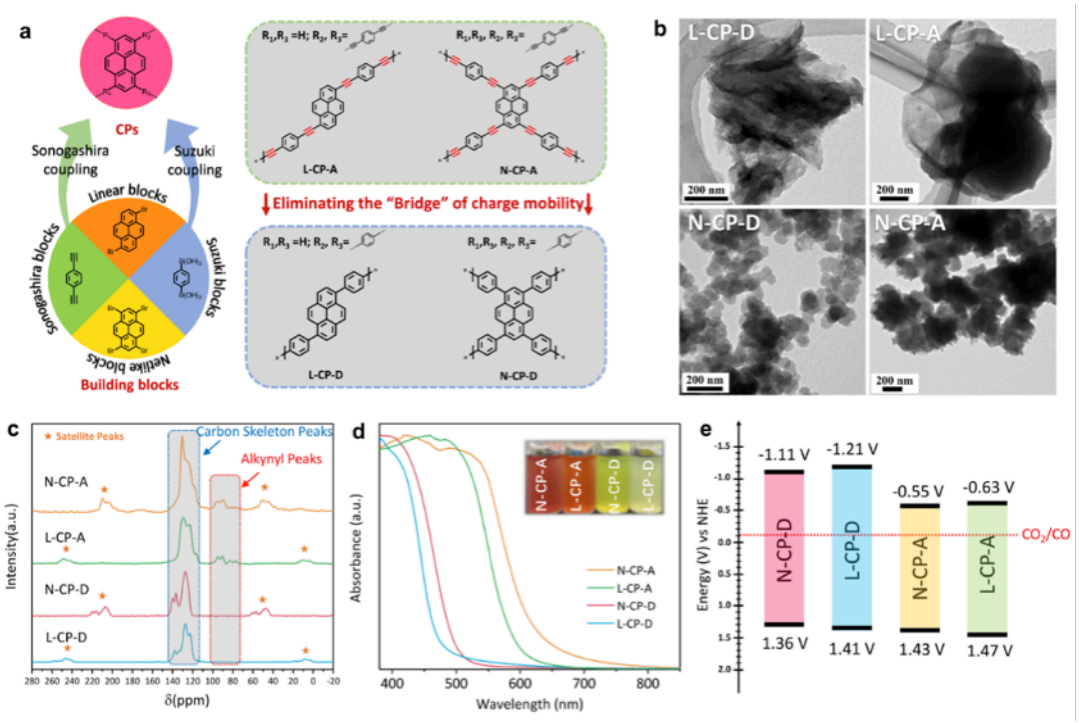

Figure 5.5. Preparation and characterization of the CPs. a, Illustration of synthesis and the strategy of eliminating the charge-transfer bridge. b, TEM images of CPs. c, Solid-state ^{13}C CP/MAS NMR spectroscopy of CPs. d, Solid-state UV/Vis DRS spectra of CPs. Inset: CPs dispersed in an acetonitrile/water (7:3) mixture. e, HOMO and LUMO band position diagram for CPs.

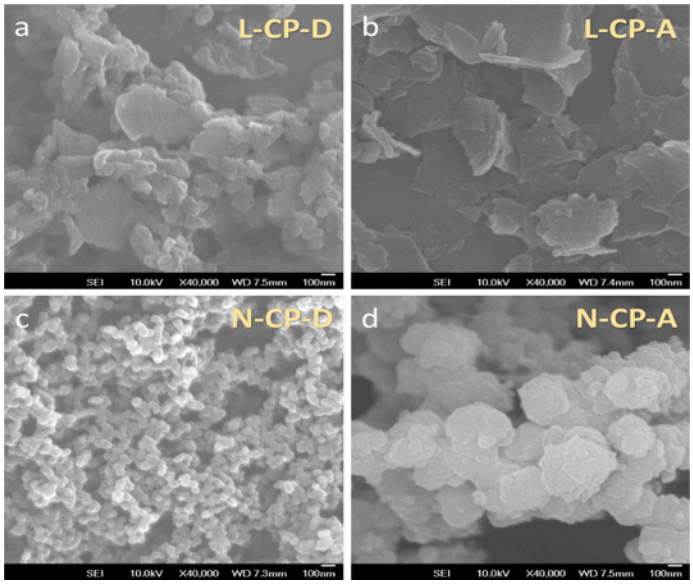

Figure 5.6. Representative scanning electron microscopy (SEM) images of L-CP-D (a), L-CP-A (b), N-CP-D (c) and N-CP-A (d).

The transmission electron microscopy (TEM) and scanning electron microscopy (SEM) revealed that the CP-A series (L-CP-A and N-CP-A) exhibited a more agglomerated state than did the CP-D series (D-CP-A and D-CP-A) because of the higher π conjugation. (Figure 5.5b and Figure 5.6). Although the CPs presented different agglomeration states at low resolution, the high-resolution transmission electron microscopy (HR-TEM) and the powder X-ray diffraction profile (PXRD) revealed that each CPs exhibits the basic characteristics of amorphous carbon, which means similar structure of CPs were constructed during the synthesis process (Figure 5.7 and Figure 5.8).[44]

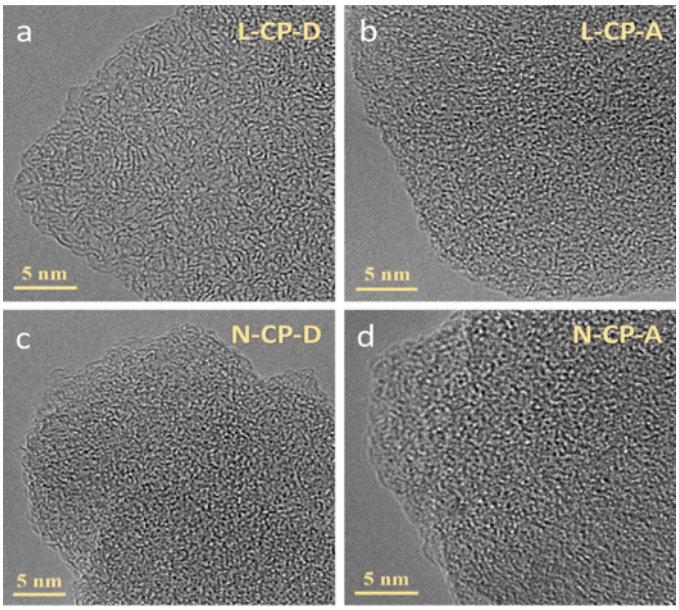

Figure 5.7. Representative high-resolution transmission electron microscopy (HR-TEM) images of L-CP-D (a), L-CP-A (b), N-CP-D (c) and N-CP-A (d).

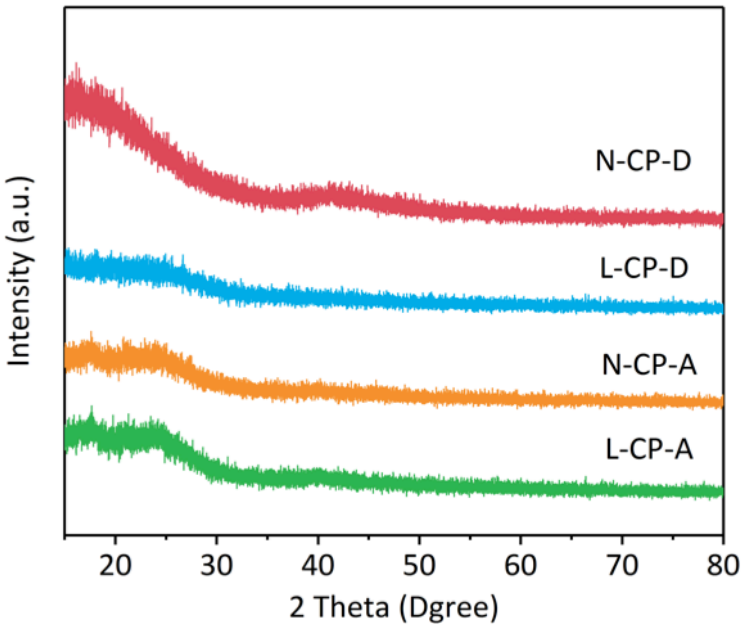

Figure 5.8. Powder X-ray diffraction (PXRD) patterns of L-CP-D, L-CP-A, N-CP-D and N-CP-A.

For a more in-depth comparison of the structural differences in CPs, we utilized solid-state ^{13}C cross-polarization/magic angle spinning nuclear magnetic resonance (^{13}C CP/MAS NMR) spectroscopy to demonstrate the exact structure (Figure 5.5c).[45] Referencing the estimated chemical shifts of different carbons in CPs (Figure 5.9), the similar chemical shifts of all these CPs between 110 and 130 parts per million (ppm) can be assigned to the aromatic carbons of the phenyl and pyrenyl units.[46] The peaks at approximately 140 ppm, which only existed in the CP-D series, were ascribed to the mutually substituted aromatic carbon. For the CP-A series, there are some signals at approximately 90 ppm can be indexed to the characteristic peak of alkynyl.[47] Notably, the locations of the satellite peaks attribute to spinning sidebands in N-CP-A were consistent with those in N-CP-D. A similar phenomenon was also found for L-CP-A and L-CP-D, which may be attributed to the structural difference between linear and net-liked CPs.

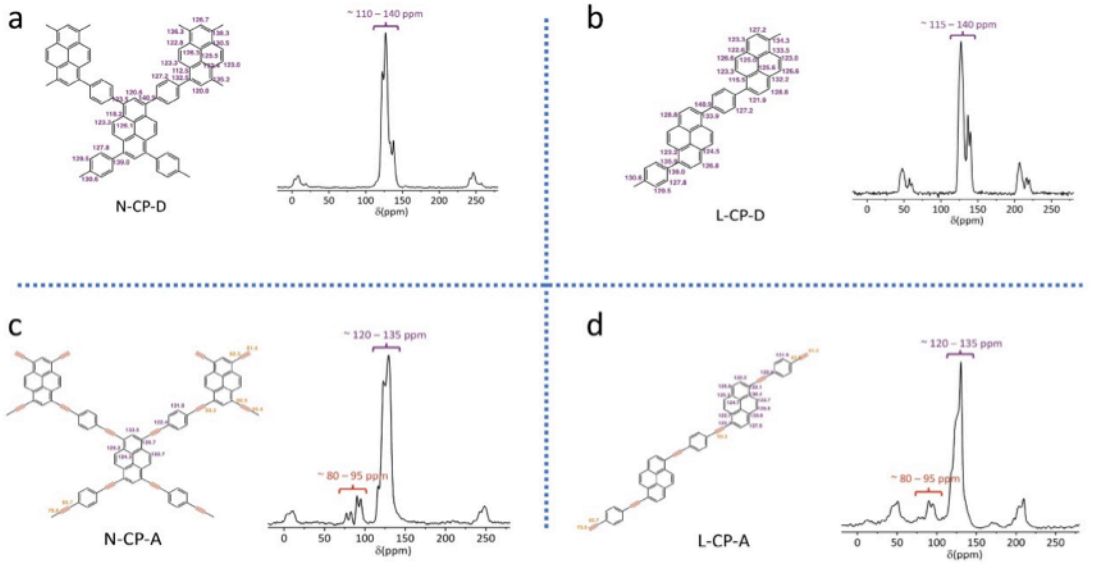

Figure 5.9. The estimated chemical shifts and the corresponding solid-state ^{13}C cross-polarization/magic angle spinning nuclear magnetic resonance of N-CP-D (a), L-CP-D (b), N-CP-A (c) and L-CP-A (d).

Besides, the CPs with or without alkynyl was also confirmed by Raman spectroscopy, X-ray photoelectron spectroscopy (XPS) and Fourier transform infrared (FT-IR) spectroscopy (Figure 5.10-12).[39,48]

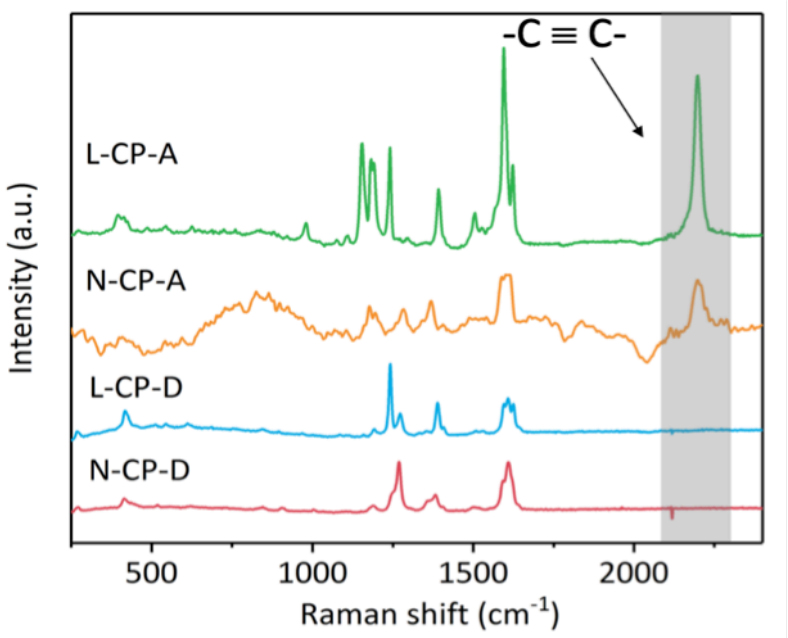

Figure 5.10. Raman spectroscopy of L-CP-D, L-CP-A, N-CP-D and N-CP-A.

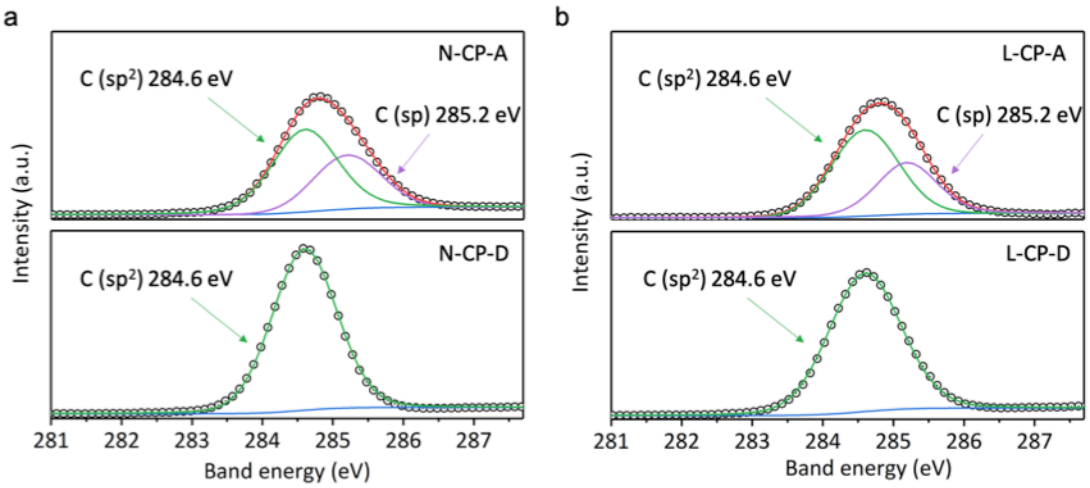

Figure 5.11. Comparison of X-ray photoelectron (XPS) spectroscopy (XPS) between N-CP-A and N-CP-D (a), L-CP-A and L-CP-D (b).

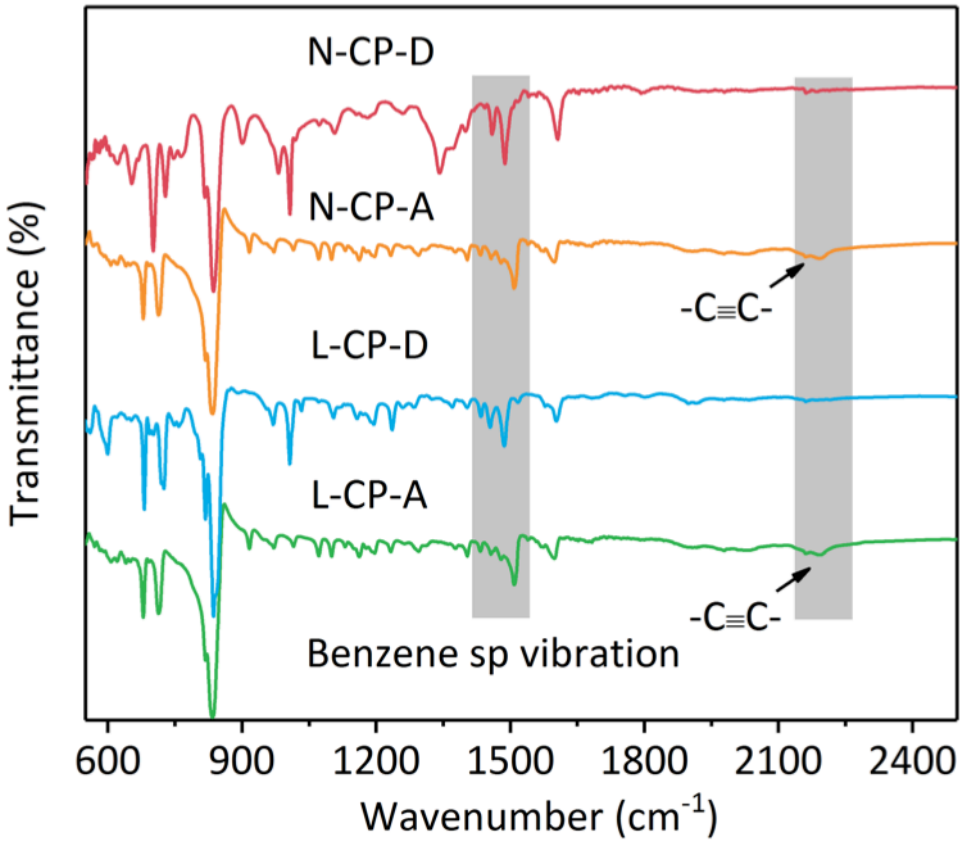

Figure 5.12. Fourier transform infrared (FT-IR) spectroscopy of L-CP-D, L-CP-A, N-CP-D and N-CP-A.

After fully identifying the structure of CPs, we employed UV-Visible diffuse reflectance (DRS) spectra to monitor the light absorption of CPs.[49] As shown in Figure 5.5d, the absorption band edges of CPs were located in the visible region ranging from 470 to 620 nm, which was consistent with the color of the CPs (inset of Figure 5.5d). According to the Kubelka-Munk equation, the absorption band edges of L-CP-A and N-CP-A correspond to bandgaps of 2.10 and 1.98 eV, respectively. While the bandgaps of L-CP-D and N-CP-D were estimated to be 2.62 and 2.47 eV, respectively, which is larger than CP-A series due to the decreased conjugation (Figure 5.13).[50] Cyclic voltammetry (CV) measurements were also conducted, the different position of the irreversibility of the oxidation peaks due to the irreversible oxidation process of the CPs at the impressed voltage (Figure 5.14) revealed different energy levels within the CPs (Table 5.2).[40] Although the CP-D series exhibited higher LUMO levels than the CP-A series, all of these CPs had enough negative potentials to carry out the reduction of CO_2 to CO (Figure 5.5e).

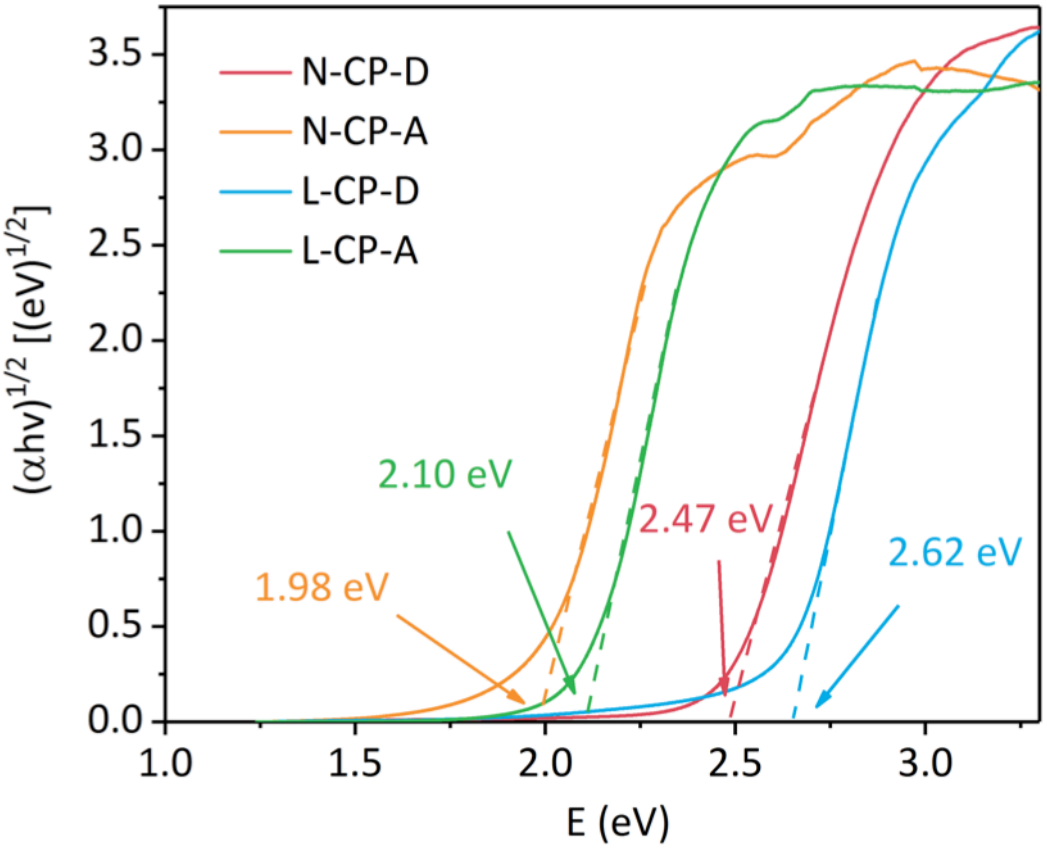

Figure 5.13. Bandgap energies of L-CP-D, L-CP-A, N-CP-D and N-CP-A according to the Kubelka-Munk Function.

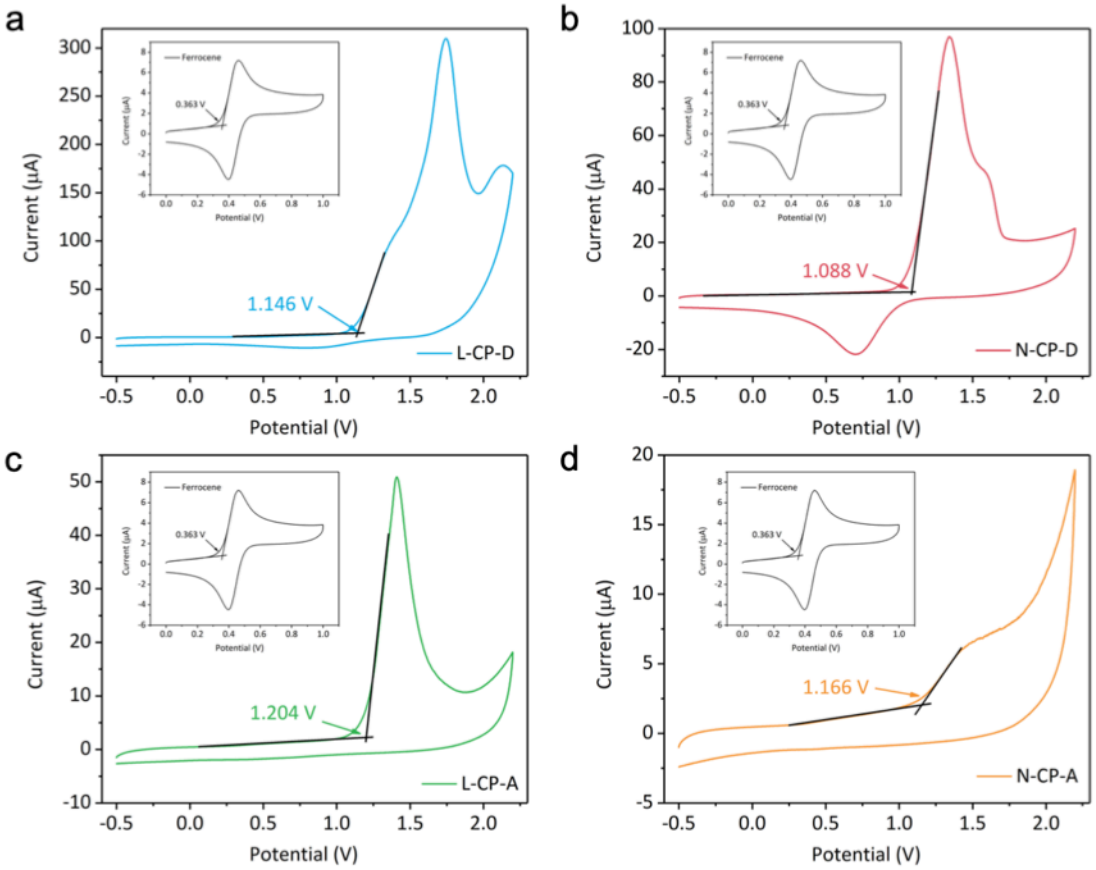

Figure 5.14. Cyclic voltammograms of L-CP-D (a), N-CP-D (b), L-CP-A (c) and N-CP-A (d), Inset: the ferrocene/ferrocenium (Fc/Fc^+) couple was provided for an internal reference.

Table 5.1. The energy levels within the L-CP-D, L-CP-A, N-CP-D and N-CP-A.

	L-CP-D	L-CP-A	N-CP-D	N-CP-A
Band gap	2.62 eV	2.47eV	2.10 eV	1.98 eV
HOMO	1.41 V	1.36 V	1.47 V	1.43 V
LUMO	-1.21 V	-1.11 V	-0.63 V	-0.55 V

5.3.2 Charge mobility and intermolecular cascaded channel of CP

Based on the conjugation of CPs, we can speculate the electron localization of CPs could be increased by eliminating the alkynyl group. For further confirmation of the weakened conjugate interaction and free-π-electrons localization of these CPs without the alkynyl group, the electrodeless flash-photolysis time-resolved microwave conductivity (FP-TRMC) was employed to evaluate photoexcited electrons transport in CPs. Unlike the conventional techniques that are highly affected by the influence of factors such as impurities, chemical or physical defects, and organic/electrode interfaces, FP-TRMC allows

for probing the motion of the charge carrier before complete deactivation by trapping sites.[51,52] The conductivity transients and calculated charge mobilities for CPs are displayed in Figure 5.15a, in which the L-CP-A, with a linear structure and alkynyl group, exhibits charge mobility (μ_{tot}) of 0.32 cm^2 V^{-1} s^{-1} ($\phi\Delta\mu$= 7.4×10^{-5} V^{-1} s^{-1}). As expected, the charge mobility of L-CP-D in the absence of alkynyl decreased to a much lower value of 0.15 cm^2 V^{-1} s^{-1}($\phi\Delta\mu$= 3.4×10^{-5} V^{-1} s^{-1}). For N-CP-A CPs, the network structure provided two additional pathways than that of linear structured L-CP-A for electronic delocalization due to the two more connections of the alkynyl group to each pyrenyl units, thus resulting in the maximum value of 0.35 cm^2 V^{-1} s^{-1} ($\phi\Delta\mu$= 7.6×10-5 V^{-1} s^{-1}) among all CPs. In comparison, the N-CP-D possesses relative lower charge mobility of 0.25 cm^2 V^{-1} s^{-1} ($\phi\Delta\mu$= 5.5×10-5 V^{-1} s^{-1}) as a result of the weak intramolecular conjugate interaction. Moreover, the CPs were subjected to additional electrochemical analyses, such as photocurrent measurement and the electrochemical impedance spectroscopy (EIS) Nyquist plots, which further validated that, consistent with the FP-TRMC results, the elimination of the alkynyl group in CPs greatly enhanced localization of free-π-electrons (Figure 5.15a and b).

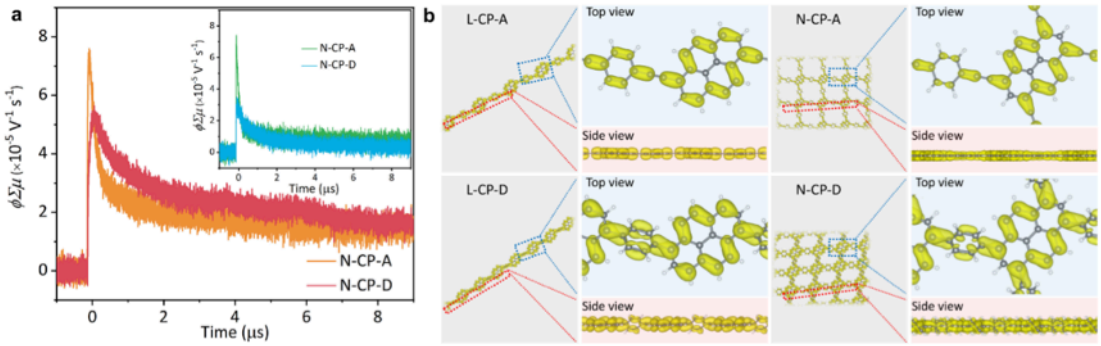

Figure 5.15. Characterization of Electronic Delocalization in CPs. a, Conductivity transients observed by flash-photolysis time-resolved microwave spectroscopy upon excitation at 355nm laser pulses at 9.1 × 10^{15} photons cm^{-2} for CPs. b, Top and side views of the charge distribution of LUMO at the Γ*k*-point of CPs.

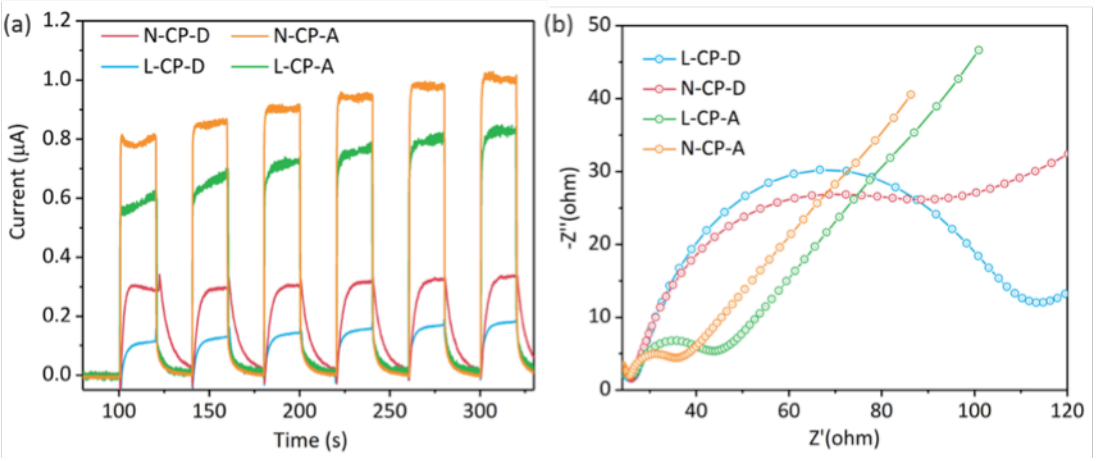

Figure 5.16. Photocurrent measurement of L-CP-D, L-CP-A, N-CP-D and N-CP-A.(a) And electrochemical impedance spectroscopy (EIS) Nyquist plots of L-CP-D, L-CP-A, N-CP-D and N-CP-A.(b)

To gain insight into the effect of the alkynyl group on the localization of free-π-electrons, hybrid density-functional-theory-based first-principles calculations were subsequently performed to compare the electronic localization of the CPs (see Methods for experimental details).[39] As shown, the lowest unoccupied molecular orbital (LUMO) and highest occupied molecular orbital (HOMO) changes (Figure 5.15b and Figure 5.17) at the Γk-point distribution unambiguously demonstrated the apparent difference in the localization of free-π-electrons in CP-D series and CP-A series, respectively. From the top view of the charge distribution profiles of the two linear CPs (L-CP-A and L-CP-D), both LUMO and HOMO of L-CP-D exhibited stronger electron distribution asymmetry than those of L-CP-A as the conjugation changed. This means that L-CP-D could concentrate more electrons in a particular section under the light irradiation. Moreover, a similar phenomenon can also be observed from the comparison of two net-like CPs (N-CP-A and N-CP-D). In the light of the above results and comparison of backbone architecture with or without alkynyl based on Becke-Lee-Yang-Parr (BLYP) function (Figure 5.18), the energy gap between unoccupied and occupied orbital at the edge and corner of the pyrenyl is smaller than that at central area, the pyrenyl could play a role of a kind of antenna to collect the excited carriers at around the edge and corner. This is an advantage to achieve charge separation and harvest a wide range of photon energy.

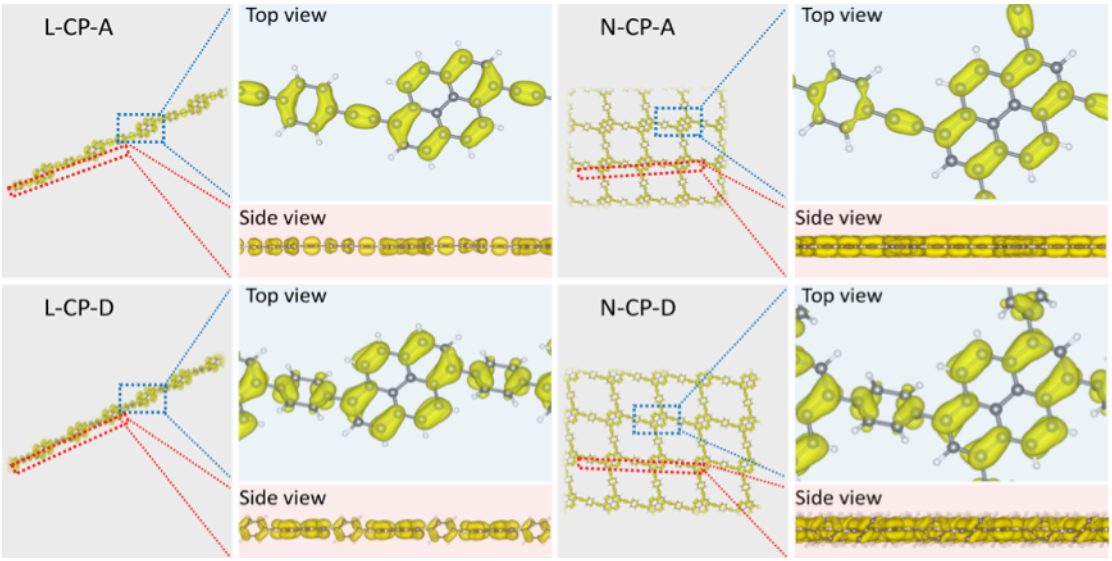

Figure 5.17. Top and side views of the charge distribution of HOMO at the Γk-point of L-CP-D, L-CP-A, N-CP-D and N-CP-A.

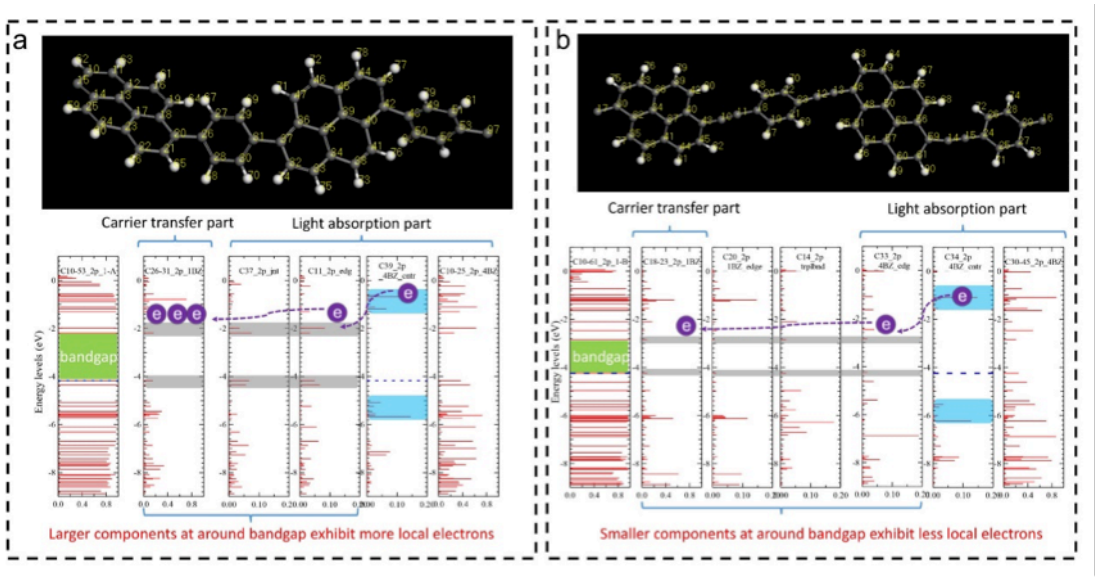

Figure 5.18. Electronic structure comparison of backbone architecture between with and without alkynyl based on Becke-Lee-Yang-Parr (BLYP) functionals.

Though the comparative analysis of computed interlayer interaction energies, it was consistency with what we expected (Figure 5.19 and Table 5.2). The existence of alkyne in CP-A series favors the electrons transfer in intramolecular. However, the CP-D series without alkynyl as a connector could possess more local photoelectrons, thus the interlayer interaction energy of bilayer CP-D series was much strong than that of CP-A series. This might indicate electron transfer along intermolecular of bilayer CP-D

series more easily than that of bilayer CP-A series. Thus, we could propose the following situation on different CPs. For the CP-A series, photoelectrons were generated on the central light-responsive part of pyrenyl and then transferred to the other parts with alkynyl as a bridge, which results homogeneously charge density of CP-A series. In contrast, the absence of alkynyl in CP-D series led to a retardation of intramolecular electron delocalization. Moreover, it also gave rise to the increased charge density in some parts of CP-D series under light irradiation, which is favorable for improving the electronic delivery over the built-in intermolecular cascaded channels via π-π interactions between CPs and cocatalyst.

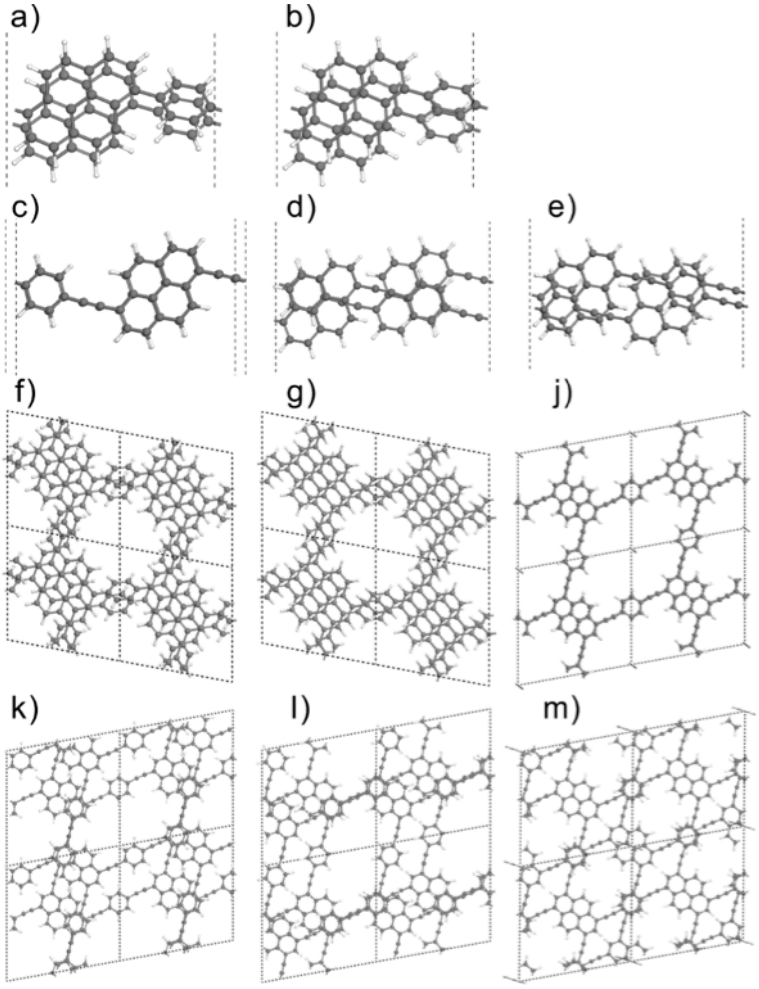

Figure 5.19. Top view of optimized bilayer structures of L-CP-D with (a) AB stacking and (b) AB' stacking, L-CP-A with (c) AA stacking, (d) AB stacking and (e)AB' stacking, N-CP-D with (f) AB stacking and (g) AB' stacking, and N-CP-A with (j) AA stacking, (k) AB stacking and (l) AB' stacking and (m) AC stacking. The dark gray and white balls represent C and H atoms, respectively.

Table 5.2. The computed interlayer interaction energies (ΔE_i, J/m, and J/m^2) and distances ($D_{interlayer}$, Å) of interlayer for L-CP-D, L-CP-A, N-CP-D and N-CP-A.

Stacking		AA	AB	AB'	AC
ΔE_i (10^{-10} J·m^{-1})	L-CP-D	-	-0.934	-0.925	-
	L-CP-A	-0.63	-0.713	-0.756	-
ΔE_i (J·m^{-2})	N-CP-D	-	-0.116	-0.114	-
	N-CP-A	-0.058	-0.063	-0.063	-0.043
$D_{interlayer}$	L-CP-D	-	3.53	3.53	-
	L-CP-A	3.82	3.59	3.51	-
	N-CP-D	-	3.35	3.6	-
	N-CP-A	3.84	3.73	3.74	3.62

5.3.3 CO_2 Photoreduction activity over CPs.

To study the built-in intermolecular cascaded channel for electron delivery from CPs to cocatalyst has effects on CO_2 photoreduction properties, the evaluation of CO_2 photoreduction activities (see Methods for experimental details) was carried out in a closed gas circulation system with CPs as the catalyst and Co (II) bipyridine complexes as cocatalyst. (Figure 5.1).[53,54] The Co (I) bipyridine complexes produced by reduction of Co (II) bipyridine complexes are very powerful reducing agents which could be excellent candidates cocatalyst for photoreduction reaction based on the previous report.[53] We also demonstrated that electrons on the LUMO of CPs in the present work do have the ability to produce Co (I) bipyridine complexes from Co (II) bipyridine complexes the via the cyclic-voltammetry method (Figure 5.20) and EPR measurement (Figure 5.21).[25] In some recent researches, the Co (II) bipyridine complexes were selected as the model cocatalyst to study the CO_2 photoreduction activity of the materials.[15,54] Therefore, we speculate that after optimizing the π-conjugation of CPs, the system consist of CPs and Co (II) bipyridine complexes will exhibit good potential for CO_2 photoreduction. As displayed in Figure 5.22a, after 5 h of visible light (> 420 nm) irradiation, the N-CP-D generated a maximum amount of carbon monoxide (CO) of 56.8 μmol (11.37 μmol h^{-1}), while the L-CP-D generated 20.2 μmol (4.03 μmol h^{-1}) of CO. In contrast, only 0.3 and 0.4 μmol of CO was detected when L-CP-A and N-CP-A were used as the catalyst, respectively. The CO evolution rates of N-CP-D and L-CP-D were almost 138 times and 81 times higher than those of N-CP-A and L-CP-A, respectively. These CO_2 photoreduction rates and enhancements are comparable to that of many similar systems containing photocatalyst and cobalt-complexes cocatalyst, especially π-conjugated Co (II) bipyridine complexes. It can be found that, although the addition of Co (II) bipyridine complexes significantly improved the photocatalytic CO_2 reduction activity of the original photocatalyst, the photocatalytic CO_2 reduction activity severely hampered by the obstruction of interface electron transport caused a relative lower multiple of increases (Table 5.3). Owing to the solution of the oriented electron delivery, the activity of CO_2 reduction reaction over the CPs with optimized conjugation showed a most considerable enhancement.

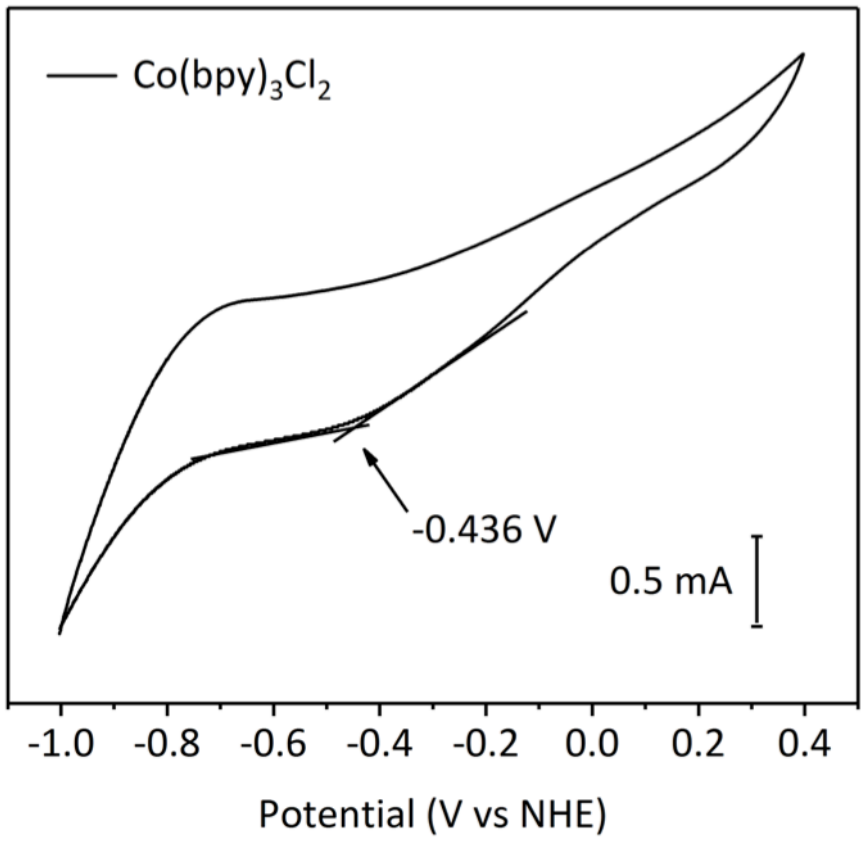

Figure 5.20. Cyclic voltammograms of Co (II) bipyridine complexes in mixture of acetonitrile/water (7:3) and the redox potential can be assigned to the recycle of Co (II)/Co (I).[55]

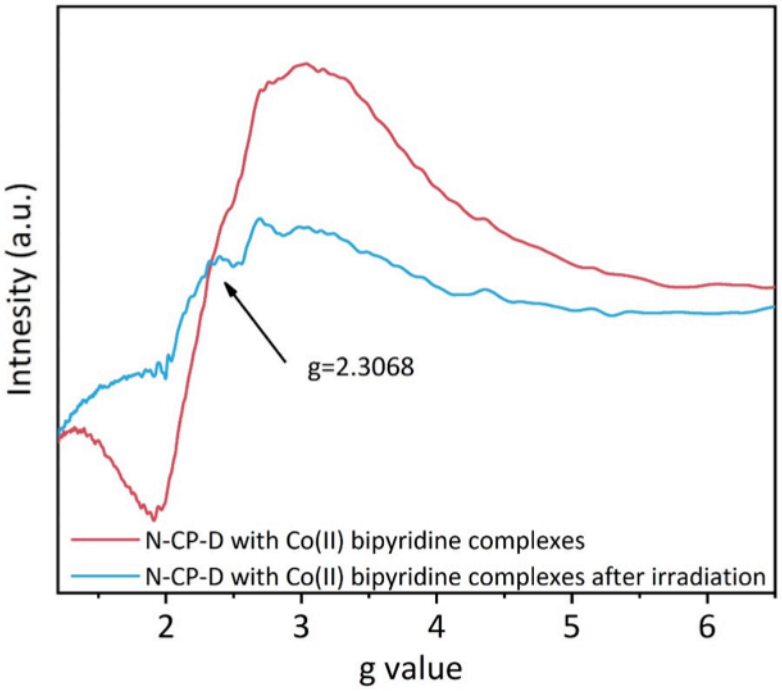

Figure 5.21. The ESR spectra of N-CP-D with Co (II) bipyridine complexes under irradiation and dark condition.

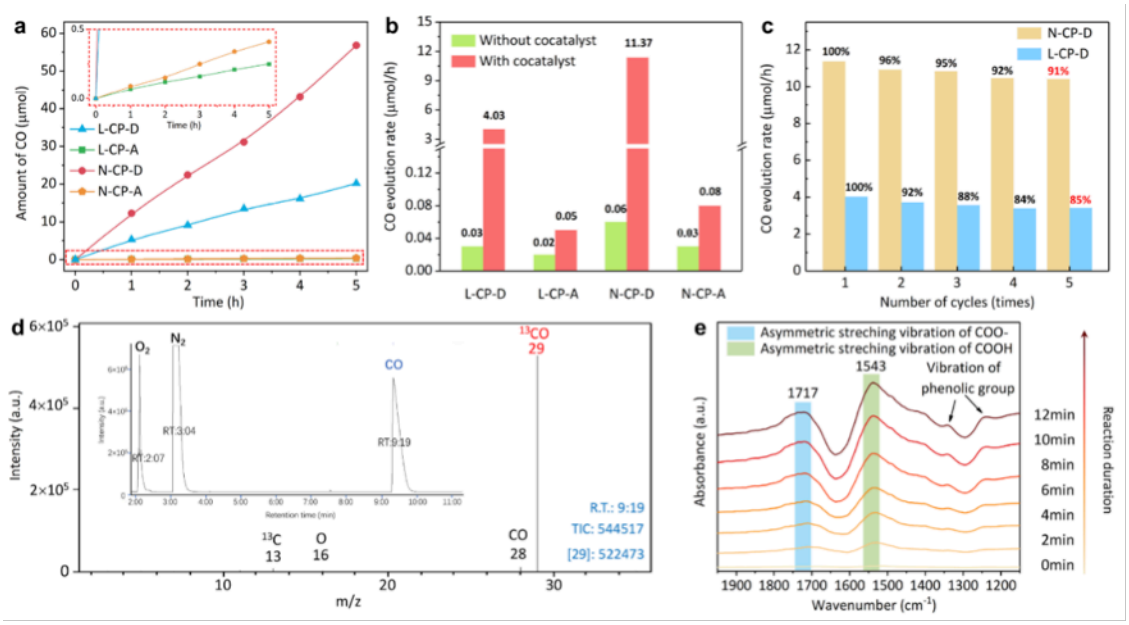

Figure 5.22. CO_2 photoreduction performance of the CPs. a, Time course of the produced CO for CPs during 5 h experiment performed under visible light (420 nm cut-off filter) in an acetonitrile/water (7:3) mixture using triethanolamine (TEOA) as sacrificial agent and Co (II) bipyridine complexes as a cocatalyst over 5 mg CPs. inset: X-axis enlarged performance of CO evolution. b, Average CO evolution rates for CPs with (red bar) or without (green bar) cocatalyst. c, Recyclability of N-CPD (yellow bar) and L-CP-D (blue bar) in the photocatalytic CO_2 reduction within five cycles. d, Mass spectra of ^{13}CO and total ion chromatography (inset) over N-CP-D in the photocatalytic reduction of $^{13}CO_2$. e, In-situ diffuse reflectance infrared Fourier transform spectroscopy (DRIFTS) for the photocatalytic reduction of CO_2 over N-CP-D.

To further uncover the underlying reasons for the substantial difference that we obtained between the CP-D series and the CP-A series, we applied CPs in the CO_2 photoreduction without a cocatalyst (Figure 5.22b). All CPs showed quite low activity in the absence of cocatalyst. After the addition of Co (II) bipyridine complexes as a cocatalyst, although all of CPs exhibit enough negative potential to transfer the photoelectrons to cocatalyst, only an approximately 2.5-fold increase was found for L-CP-A and N-CP-A. However, for L-CP-D and N-CP-D, the CO evolution rate increased by 134 times and 190 times, respectively (Figure 5.23 and 24). With the addition of enough cocatalyst, the CO evolution selectivity of L-CP-D and N-CP-D obtained through our experiment reached 86% and 82% and achieved an apparent quantum yield (AQY) of 3.39 % and 1.23 % at 400 nm, respectively (Figure 5.25). Moreover, the cyclic testing over L-CP-D and N-CP-D indicated that after 5 cycles, the CO evolution was still high compared to the initial values (Figure 5.22c), suggesting the adequate stability of CPs (Figure 5.26). Therefore, we speculate that upon eliminating the alkynyl group in the structure of CPs, the weakened intramolecular conjugation of CP-D series blocks the delocalization of photoexcited electron. Stacked electrons on CP-D

Table 5.3. Comparison of CO_2 photoreduction performance of the reported catalysts in the system similar to this work.

Cataslyst	Cocatalyst	Sacrificial agent	Major products evaluation rate	Enhancement after modification	Selectivity	Ref.
L-CP-D	$Co(bpy)_3Cl_2$	TEOA	CO:806 $\mu molg^{-1}h^{-1}$	81-times	86%	This work
N-CP-D	$Co(bpy)_3Cl_2$	TEOA	CO:2274 $\mu molg^{-1}h^{-1}$	138-times	82.00%	This work
$ZnIn_2S_4$-In_2O_3	$Co(bpy)_3Cl_2$	TEOA	CO:3075 $\mu molg^{-1}h^{-1}$	3.5-times	79.40%	20
In_2S_3-$CdIn_2S_4$	$Co(bpy)_3Cl_2$	TEOA	CO:825 $\mu molg^{-1}h^{-1}$	12.0-times	73.30%	54
CPs-BT	$Co(bpy)_3Cl_2$	TEOA	CO:1213 $\mu molg^{-1}h^{-1}$	4.6-times	81.60%	62
CdS-BCN	$Co(bpy)_3Cl_2$	TEOA	CO:250 $\mu molg^{-1}h^{-1}$	10.3-times	81.10%	63
BCN	$Co(bpy)_3Cl_2$	TEOA	CO:94 $\mu molg^{-1}h^{-1}$	-	76.20%	64
HR-CN	$Co(bpy)_3Cl_2$	TEOA	CO:297 $\mu molg^{-1}h^{-1}$	22.3-times	96.70%	21
MCN/CoOx	$Co(bpy)_3Cl_2$	TEOA	CO:204 $\mu molg^{-1}h^{-1}$	2.76-times	78.50%	65
CNU-BA	$Co(bpy)_3Cl_2$	TEOA	CO:1036 $\mu molg^{-1}h^{-1}$	15.0-times	81.80%	66
MOF-525-Co	$Co(bpy)_3Cl_2$	TEOA	CO:201 $\mu molg^{-1}h^{-1}$	3.13-times	-	12

series were not well dispersed and thus tended to be fast delivered to cocatalyst through the intermolecular cascaded channels, leading to the CP-D series performed far better activity than did the CP-A series. Besides, the net-like CPs (N-CP-A and N-CP-D) possess more cocatalyst absorption sites of phenyl in the units, thus resulting in enhanced performance of net-like CPs (N-CP-A and N-CP-D) than those of linear CPs (L-CP-A and L-CP-D).

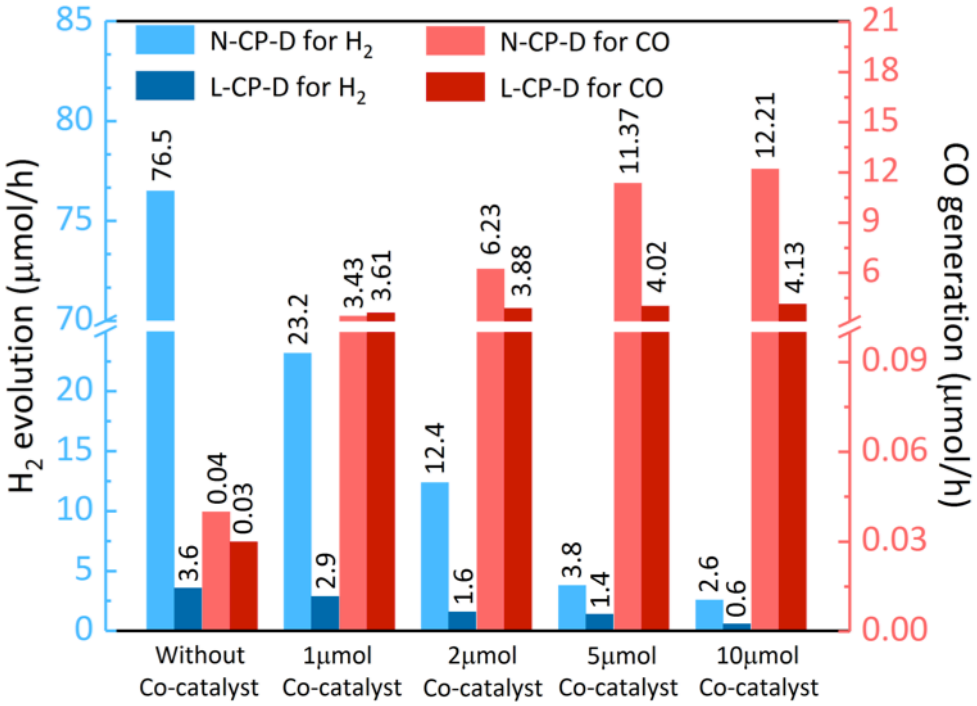

Figure 5.23. The selectivity of the amount of cocatalyst to the catalytic products of CO (red bars) and H_2 (blue bars) formed over L-CP-D (dark bars) and N-CP-D (light bars).

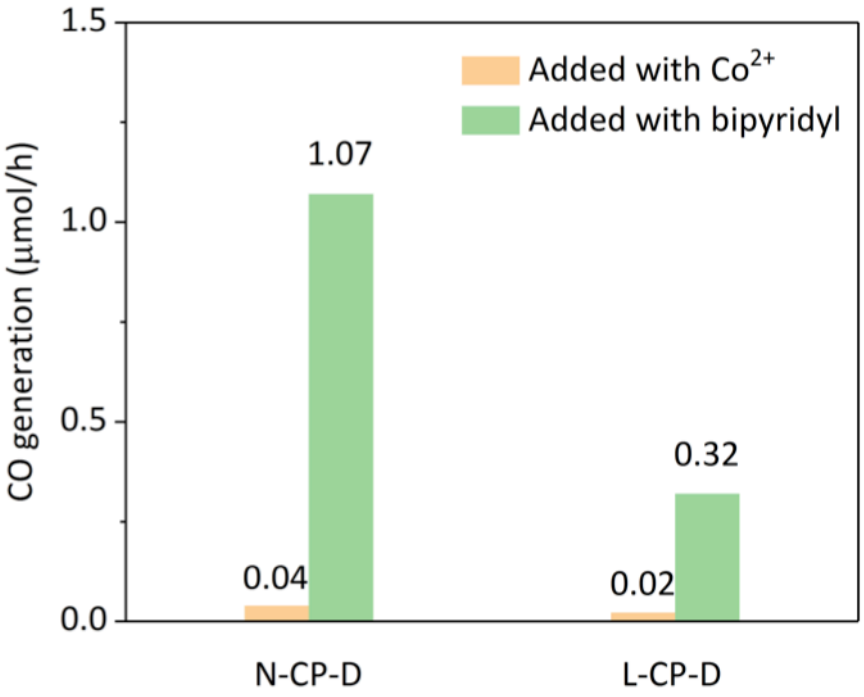

Figure 5.24. CO generation of N-CP-D or L-CP-D under the condition of using the same 5 μmol of isolated cobalt chloride or dipyridyl as the cocatalyst.

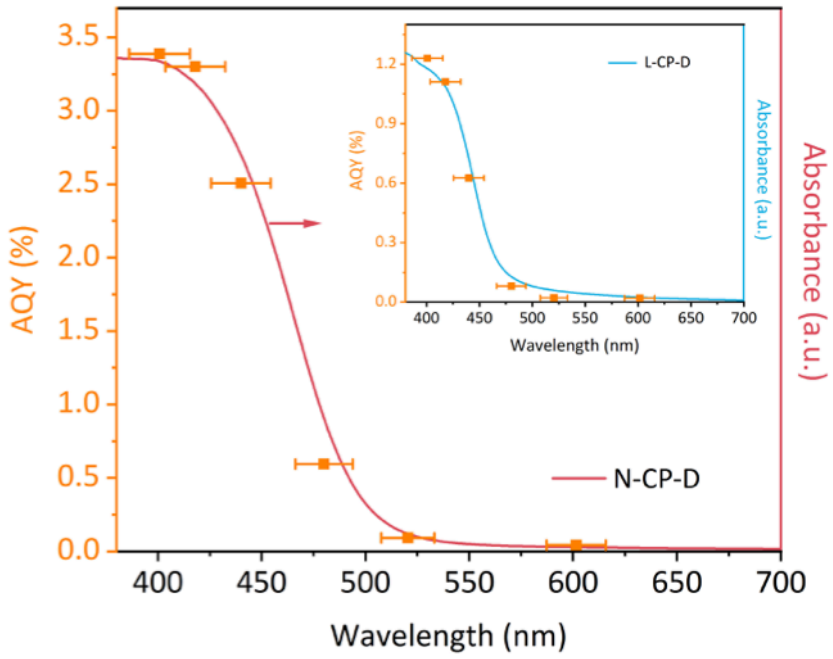

Figure 5.25. Wavelength-dependent apparent quantum yield (AQY) of CO generation from L-CP-D and N-CP-D.

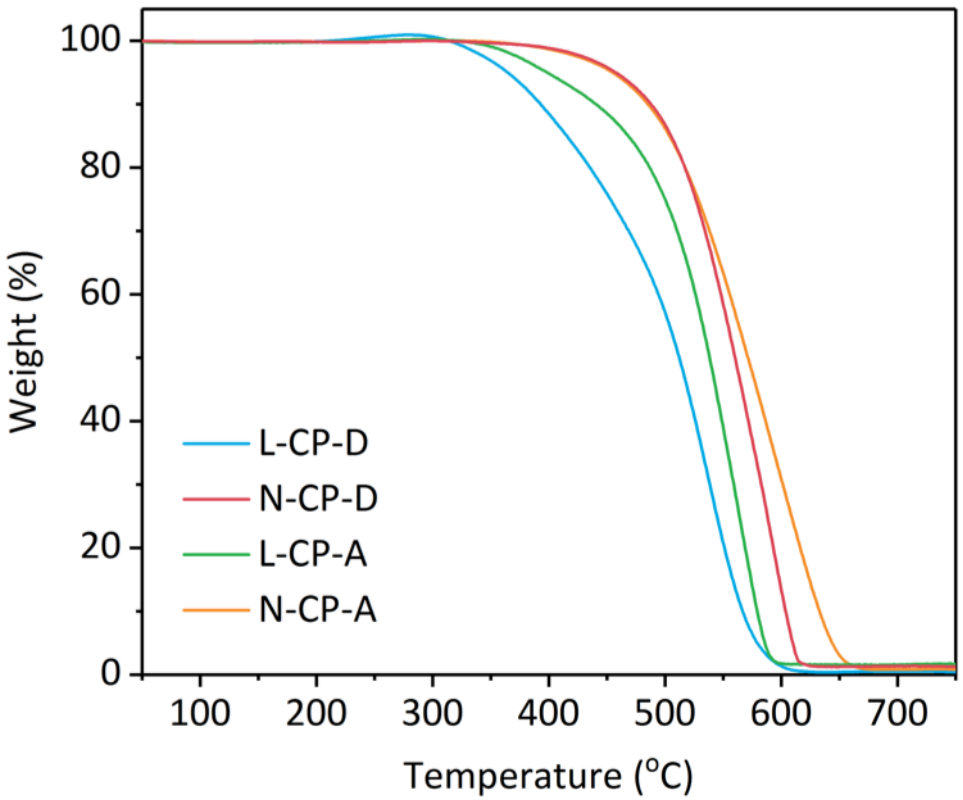

Figure 5.26. Thermal gravimetric of L-CP-D, L-CP-A, N-CP-D and N-CP-A.

To validate the generation of CO originated from the catalytic splitting of CO_2, we employed isotope-labeled carbon dioxide ($^{13}CO_2$) as a substitute source gas with the N-CP-D (Figure 5.22d) or L-CP-D (Figure 5.27) to complete the evaluation experiment (see Methods for experimental details).[56] As shown in Figure 5.22d, the total ion chromatographic peak around 9.3 minutes can be assigned to the CO (inset of Figure 5.22d). Moreover, the main peak at m/z = 29 achieved a high abundance, and the fragments produced from this peak (^{13}C at m/z = 29 and O at m/z = 16) in the mass spectra indicated that the produced ^{13}CO indeed originated from $^{13}CO_2$ in the CO_2 photoreduction over N-CP-D. A similar phenomenon can also be observed in using L-CP-D as catalyst and intensity of ^{13}CO is one-third of using N-CP-D (Figure 5.27), which is highly consistent with the above activity measurement. Subsequently, we also used the in situ diffuse reflectance infrared fourier transform spectroscopy (DRIFTS) to unveil the process of CO_2 photoreduction occurring on N-CP-D with a cocatalyst (see Methods for experimental details). Based on the spectra collected for the N-CP-D with or without absorbed CO, the in situ generated CO increased with the illumination time (Figure 5.4) and the main intermediates of this process were assigned to the asymmetric stretching vibrations of COO- and COOH species in Figure 5.22e,[57] which is solidly in accordance with the mechanism of CO_2 conversion to CO in the previous report.[58,59]

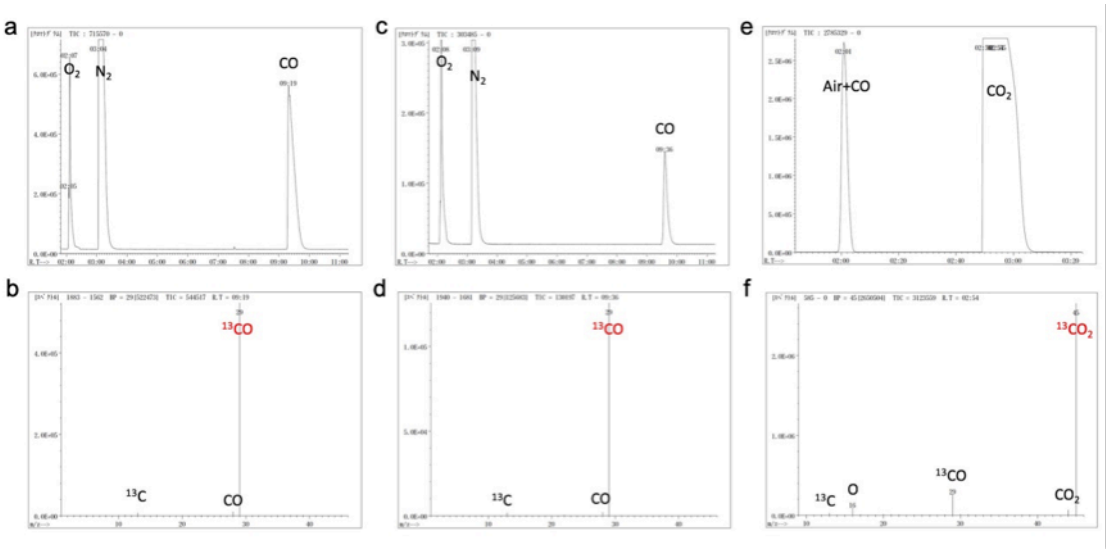

Figure 5.27. The total ion chromatograph and mass spectra for the sample of N-CP-D (a, b) and L-CP-D (c, d) by using the column of HP-MOLESIEVE and total ion chromatograph and mass spectra for the sample of N-CP-D (e, f) by using the column of HP-PLOT/Q.

5.3.4 Electron delivery from CPs to cocatalyst for efficient CO_2 photoreduction.

By discovering and scrutinizing the CO_2 photoreduction of CPs, we hope to verify our conjecture that the localized free-π-electrons of CPs could improve its intermolecular cascading ability with cocatalyst for CO_2 photoreduction. The adsorption of CO_2 is a prerequisite for CO_2 photoreduction. Nevertheless, although the CP-D series has a larger specific surface area (Figure 5.28 and Table 5.4) due to a shorter skeleton length,[60] the CP-A series exhibited greater CO_2 adsorption than the CPs-D series (Figure 5.29a), attributing to the high conjugation from bifunctionalization with pyrenyl and alkynyl group.[61] It means that the capacity for CO_2 adsorption was not the determining factor for the CO_2 photoreduction. Femtosecond transient absorption (TA) spectroscopy is a useful technique for studying ultrafast charge transfer in interfaces. We thus employed this method (see Methods for experimental details) to verify the different kinetics in intermolecular electron delivery for the solid evidence of built-in intermolecular cascade channel. From the TA spectra dependence on the wavelength, the main state of trapped electrons can be assigned to the wavelength of 2500 nm and 2200 nm, while the corresponding state of holes at 550 nm and 525 nm for N-CP-A and N-CP-D, respectively. Considering these results, we measured the kinetics of electrons over N-CP-D with or without cocatalyst under a probe wavelength of 2200 nm. In Figure 5.29b, compared to the initial one, the decay of N-CP-D with cocatalyst showed a noticeable decrease, while N-CP-A showed no difference with or without cocatalyst (inset of Figure 5.29b). Combining the results for the corresponding holes (Figure 5.30 (a) and (b)), the enhanced electron delivery over N-CP-D was determined. Moreover, we employed time-resolved photoluminescence (TR-PL) spectroscopy to gain insight into the subsequent process of electrons transfer from the cocatalyst to CO_2 (see Methods for

experimental details). For both N-CP-D (Figure 5.29c) and L-CP-D (inset of Figure 5.29c), the average lifetime of electrons (Table 5.4) in a CO_2 atmosphere was significantly shortened compared to that in an argon atmosphere, which can be attributed to the fact that electrons with a relatively long lifetime (τ_2) can be fast delivered to CO_2 via the cocatalyst (Figure 5.31). However, both N-CP-A and L-CP-A in TR-PL measurements showed no difference between the atmosphere of CO_2 and argon due to the weak delivery (Figure 5.32).

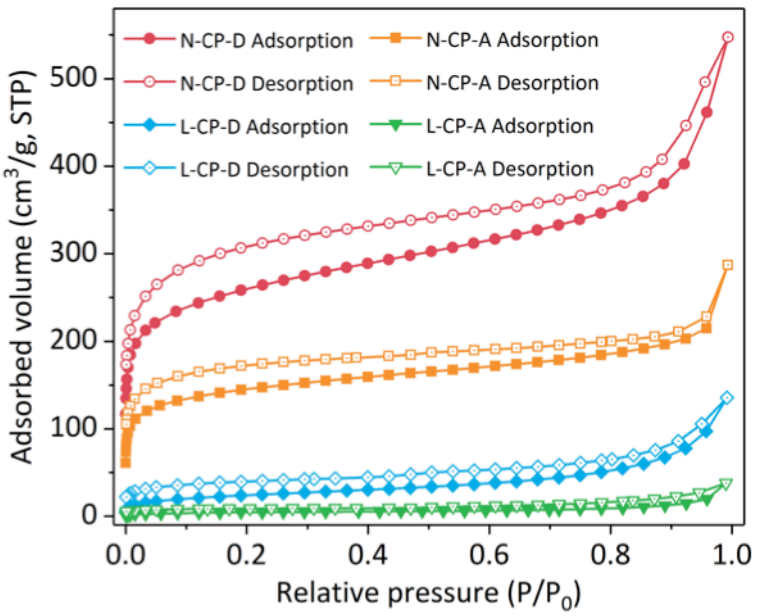

Figure 5.28. Nitrogen adsorption and desorption isotherms of L-CP-D, L-CP-A, N-CP-D and N-CP-A at 77.3 K (filled symbols: adsorption, open symbols: desorption, STP= standard temperature pressure).

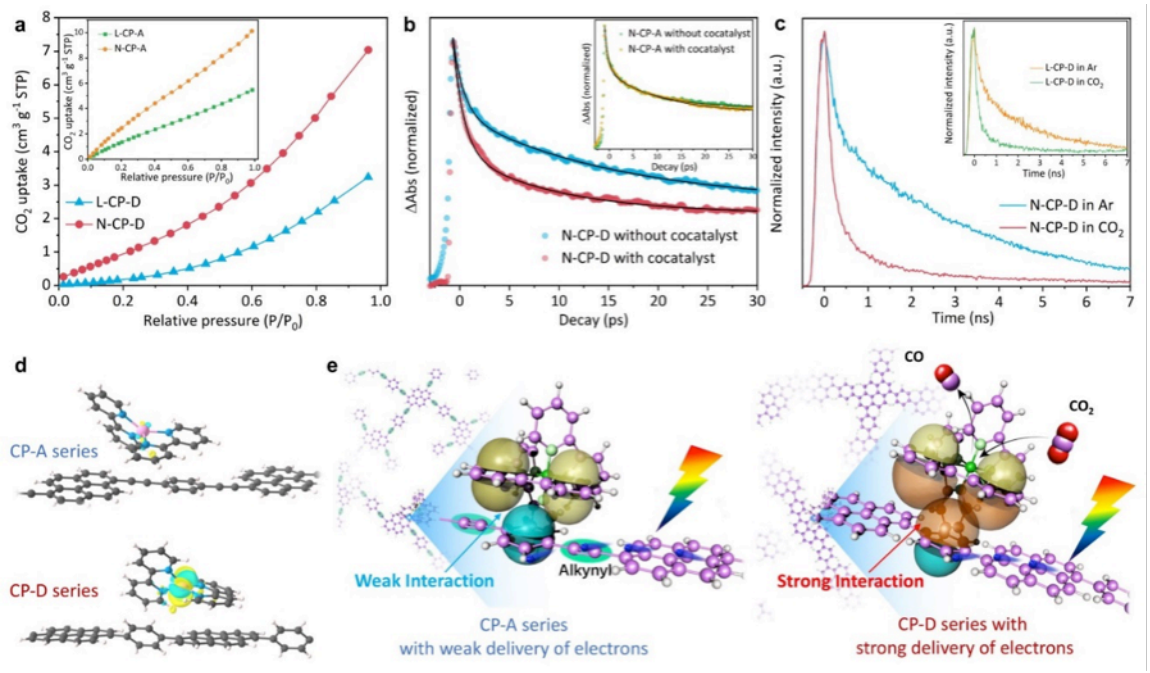

Figure 5.29. Electron delivery from CPs to cocatalyst for CO_2 photoreduction. a, CO_2 adsorption capacities of the CP-D series and CP-A series (inset) at 273.15 K. b, Kinetics of electrons in transient absorption over N-CP-D with or without cocatalyst under a probe wavelength of 2200 nm. Inset: Kinetics of electrons in transient absorption over N-CP-A with or without cocatalyst under a probe wavelength of 2500 nm. c, Time-resolved photoluminescence decay of L-CP-D and N-CP-D (inset) under a CO_2 or argon atmosphere. d, Charge density difference of CPs in present and absent of Co (II) bipyridine complexes with the isosurfaces value of 0.001 e/Å3. yellow and cyan represent charge accumulation and charge depletion, respectively. The pink, indigo, dark gray and white pink balls represent Co, N, C and H atoms, respectively. e, Proposed process of electron transfer over the CP-A series and CP-D series for the CO_2 photoreduction reaction.

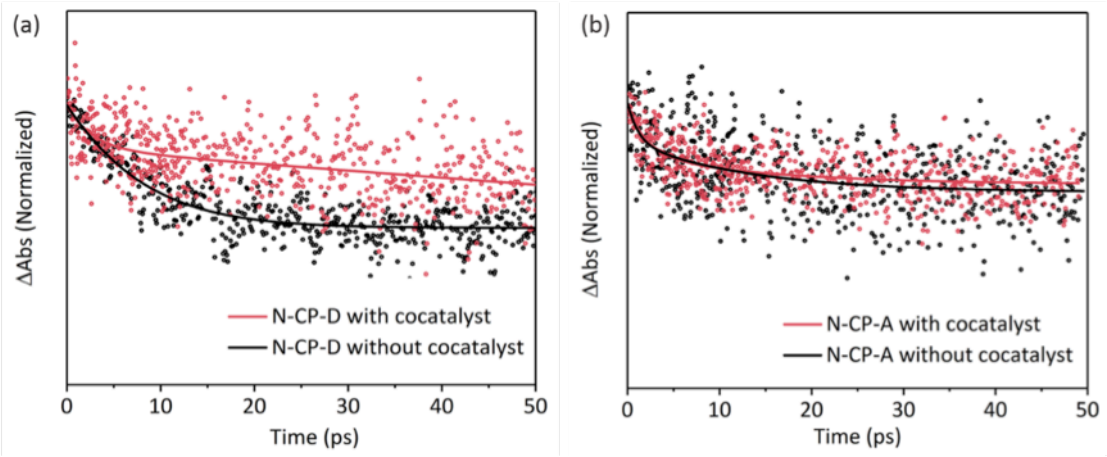

Figure 5.30. Kinetics of electrons in transient absorption over N-CP-D with or without cocatalyst under a probe wavelength of 525 nm.(a) And kinetics of electrons in transient absorption over N-CP-A with or without cocatalyst under a probe wavelength of 550 nm.(b)

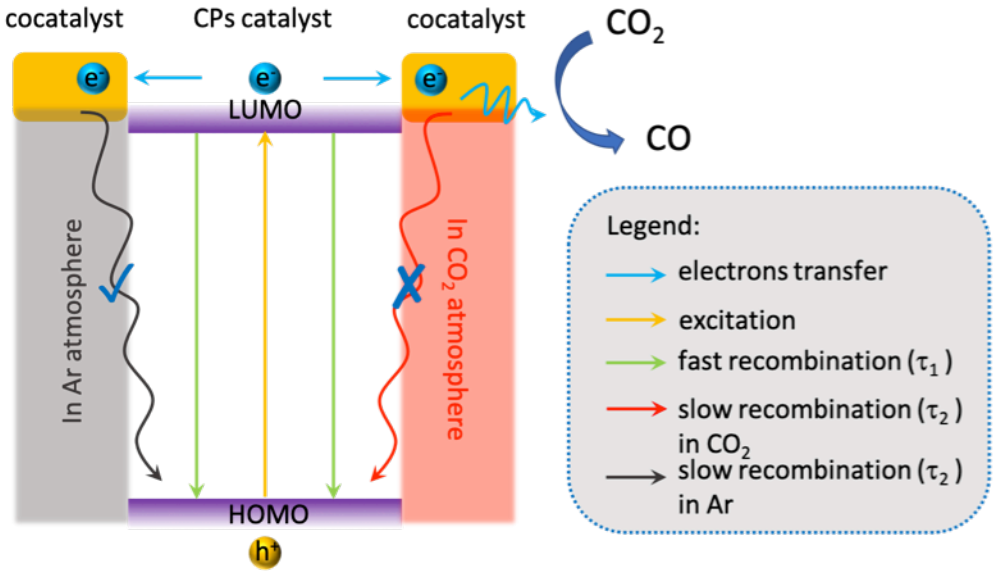

Figure 5.31. Explanation for the difference in measurement of time-resolved photoluminescence (TR-PL) in CO_2 or Ar over CPs-D series.

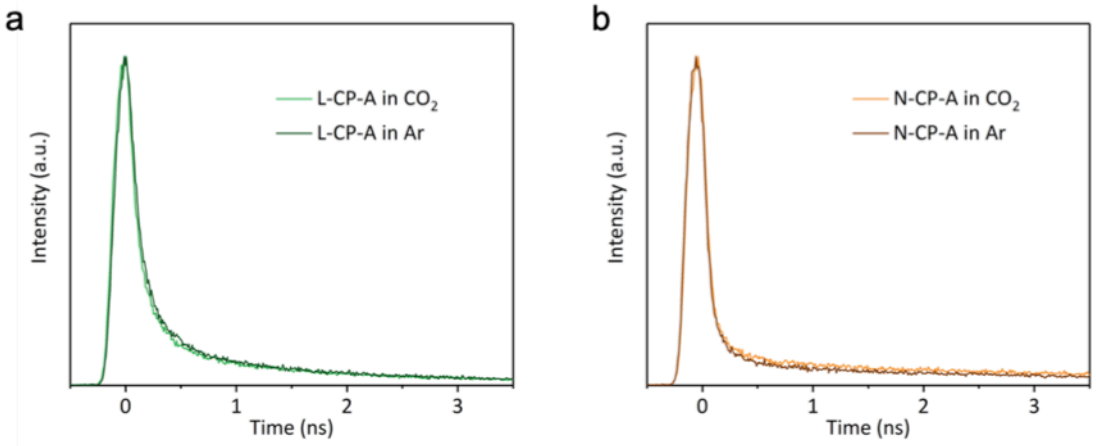

Figure 5.32. Time-resolved photoluminescence (TR-PL) decay of L-CP-A (a) and N-CP-A (b) under a CO_2 or argon atmosphere.

In order to gain a deeper insight into the built-in intermolecular cascaded channels between CPs and Co (II) bipyridine complexes, the charge distribution analysis and charge density difference (Figure 5.29d and Figure 5.33 and 5.34) of before and after adsorption of Co (II) bipyridine complexes over L-CP-D (0.12 e) and L-CP-A (0.07 e) were used to figure out that more charges were delivered from the CP-D series to the adsorbed Co (II) bipyridine complexes than that of CP-A series. It indicates that the CP-A series in presence of alkynyl facilitate its intramolecular charge mobility, while the CP-D series in absence of promote its intermolecular cascading ability with the Co (II) bipyridine complexes. Therefore, we can rationally propose that the CO_2 photoreduction over CPs was promoted by the built-in intermolecular cascaded channels, as shown in Figure 5.29e. When using the CP-A series, the photoelectrons were generated and quickly transferred to the other part of the CPs in the presence of alkynyl groups as the bridge. Since the electrons were distributed throughout the CPs, it was difficult to be delivered to the cocatalyst through the weak intermolecular π-π interactions in CP-A series. In contrast, by eliminating the alkynyl group, the CP-D series could prevent photoexcited electrons from transferring to other parts of CPs due to lack of intramolecular charge-transfer bridges. An intermolecular cascaded channel could be built via the enhanced π-electronic cloud interactions between CPs and cocatalyst to ensure the delivery of photoexcited electrons. As a result, a cascaded electron supply though the above intermolecular channel were fast delivered to the metal center of the cocatalyst, working out the most critical challenge in the oriented electron delivery from CPs to cocatalyst and achieves the efficient π-conjugation system for CO_2 photoreduction (Figure 5.35).[12]

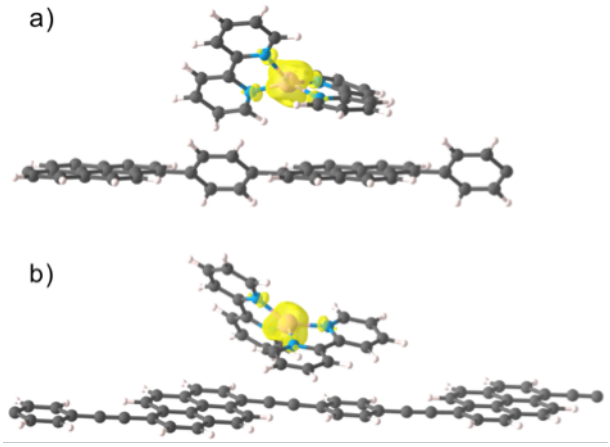

Figure 5.33. Spin density of (a) $Co(bpy)_2^{2+}$/L-CP-D and (b) $Co(bpy)_2^{2+}$/L-CP-A, with isosurfaces value of 0.005 e/Å3. yellow and cyan represent spin up and spin down, respectively. The pink, indigo, dark gray and white pink balls represent Co, N, C and H atoms, respectively.

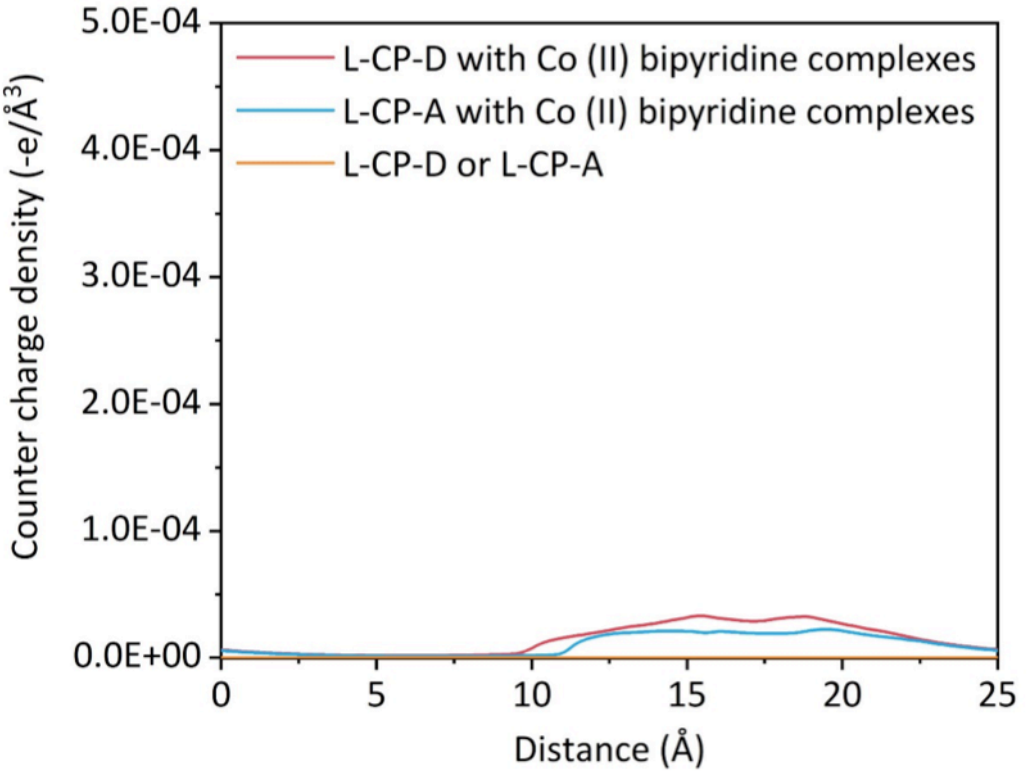

Figure 5.34. Countercharge density distribution in Co (II) bipyridine complexes/L-CP-D and Co (II) bipyridine complexes /L-CP-A, before and after Co (II) bipyridine complexes.

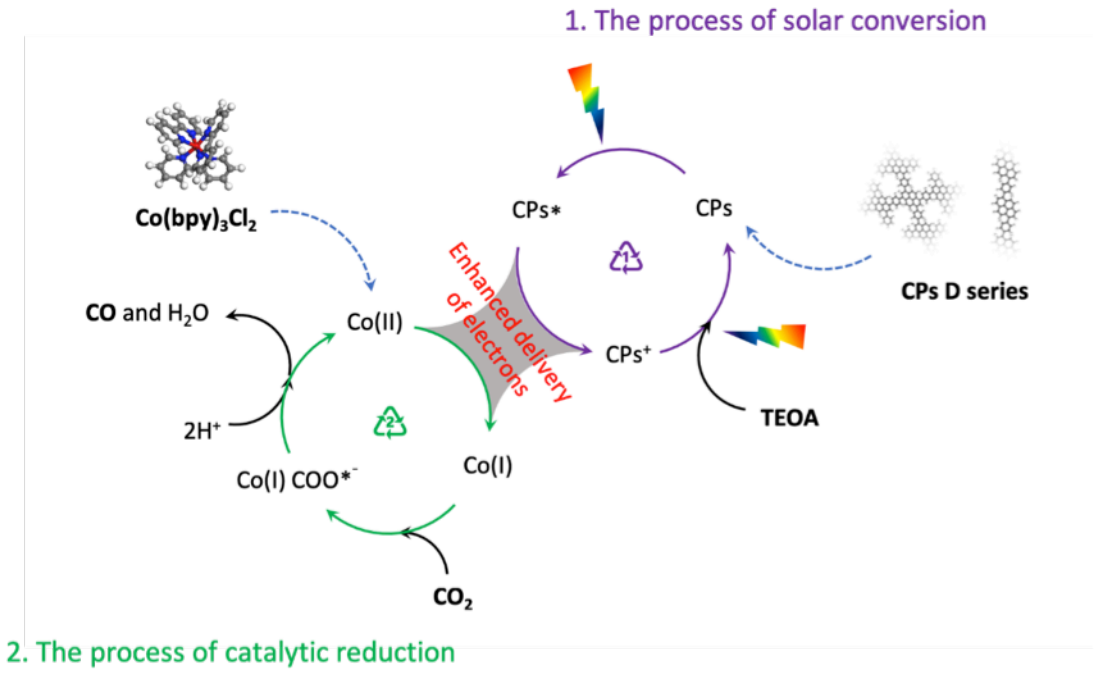

Figure 5.35. Mechanism of two-step CO_2 photoreduction depended on enhanced delivery of electrons in CPs D series system.

5.4 Conclusion

The efficient CO_2 photoreduction reaction eagerly relies on the construction of intermolecular cascaded channels, which maintains the photoelectrons flow through the active site to the CO_2 molecule. The pathway towards engendering the electron delivery to catalytic sites remains a challenging endeavor. Here, we found that an intermolecular cascaded channel for the electron delivery can be stablished through the modification of intramolecular and intermolecular π-π conjugation. Encouragingly, with the strategy of utilizing the Suzuki-Miyaura coupling instead of Sonogashira-Hagihara coupling to modify both intramolecular conjugation and intermolecular interaction of CPs, the photoelectrons generated from the pyrene part were localized on the benzene part of CPs, which in turn deliver the photoelectrons faster to Co (II) bipyridine complexes through the intermolecular cascaded channel. The current work reported directly connected net-like CPs systems exhibits highest CO evolution activity of 2247 $\mu molg^{-1}h^{-1}$ with an apparent quantum efficiency exceeds 3.39% among all reported CPs and most considerable enhancement of 138-times compared to unmodified CPs (N-CP-A) in CO_2 photoreduction with adding Co (II) bipyridine complexes as cocatalyst. From the theoretical calculations and transient spectroscopy techniques, this high efficiency could be attribute to the intermolecular cascaded channels built by modification of π-conjugation in CPs. In addition, this strategy constructs a reliable system of CO_2 photoreduction over CPs via smart engineering in molecular level, which figures out the most critical challenge in the ori-

ented electron delivery as well as providing a viable route for designing high-efficiency polymers-based systems of CO_2 photoreduction.

References

[1] Diercks, C. S.; Liu, Y.; Cordova, K. E.; Yaghi, O. M., The role of reticular chemistry in the design of CO_2 reduction catalysts. *Nature Materials*, **2018**, *17* (4), 301-307.

[2] Li, J.; Chen, G.; Zhu, Y.; Liang, Z.; Pei, A.; Wu, C.-L.; Wang, H.; Lee, H. R.; Liu, K.; Chu, S.; Cui, Y., Efficient electrocatalytic CO_2 reduction on a three-phase interface. *Nature Catalysis*, **2018**, *1* (8), 592-600.

[3] Niu, K.; Xu, Y.; Wang, H.; Ye, R.; Xin, H. L.; Lin, F.; Tian, C.; Lum, Y.; Bustillo, K. C.; Doeff, M. M.; Koper, M. T. M.; Ager, J.; Xu, R.; Zheng, H., A spongy nickel-organic CO_2 reduction photocatalyst for nearly 100% selective CO production. *Science Advances*, **2017**, *3* (7), e1700921.

[4] Schreier, M.; Hroguel, F.; Steier, L.; Ahmad, S.; Luterbacher, J. S.; Mayer, M. T.; Luo, J.; Grätzel, M., Solar conversion of CO_2 to CO using Earth-abundant electrocatalysts prepared by atomic layer modification of CuO. *Nature Energy*, **2017**, *2* (7), 17087.

[5] Studt, F.; Sharafutdinov, I.; Abild-Pedersen, F.; Elkjœr, C. F.; Hummelshøj, J. S.; Dahl, S.; Chorkendorff, I.; Nrskov, J. K., Discovery of a Ni-Ga catalyst for carbon dioxide reduction to methanol. *Nature Chemistry*, **2014**, *6* (4), 320-324.

[6] Kim, J.; Swager, T. M., Control of conformational and interpolymer effects in conjugated polymers. *Nature*, **2001**, *411* (6841), 1030-1034.

[7] Wang, X.; Maeda, K.; Thomas, A.; Takanabe, K.; Xin, G.; Carlsson, J. M.; Domen, K.; Antonietti, M., A metal-free polymeric photocatalyst for hydrogen production from water under visible light. *Nature Materials*, **2009**, *8* (1), 76-80.

[8] Yu, J.; Hu, D.; Barbara, P. F., Unmasking Electronic Energy Transfer of Conjugated Polymers by Suppression of O_2 Quenching. *Science*, **2000**, *289* (5483), 1327.

[9] Sprick, R. S.; Jiang, J.-X.; Bonillo, B.; Ren, S.; Ratvijitvech, T.; Guiglion, P.; Zwijnenburg, M. A.; Adams, D. J.; Cooper, A. I., Tunable Organic Photocatalysts for Visible-Light-Driven Hydrogen Evolution. *Journal of the American Chemical Society*, **2015**, *137* (9), 3265-3270.

[10] Yang, C.; Ma, B. C.; Zhang, L.; Lin, S.; Ghasimi, S.; Landfester, K.; Zhang, K. A. I.; Wang, X., Molecular Engineering of Conjugated Polybenzothiadiazoles for Enhanced Hydrogen Production by Photosynthesis. *Angewandte Chemie International Edition*, **2016**, *55* (32), 9202-9206.

[11] Lin, S.; Diercks, C. S.; Zhang, Y.-B.; Kornienko, N.; Nichols, E. M.; Zhao, Y.; Paris, A. R.; Kim, D.; Yang, P.; Yaghi, O. M.; Chang, C. J., Covalent organic frameworks comprising cobalt porphyrins for catalytic CO_2 reduction in water. *Science*, **2015**, *349* (6253), 1208.

[12] Zhang, H.; Wei, J.; Dong, J.; Liu, G.; Shi, L.; An, P.; Zhao, G.; Kong, J.; Wang, X.; Meng, X.; Zhang, J.; Ye, J., Efficient Visible-Light-Driven Carbon Dioxide Reduction by a Single-Atom Implanted Metal-Organic Framework. *Angewandte Chemie International Edition*, **2016**, *55* (46), 14310-14314.

[13] Fu, M.-C.; Shang, R.; Zhao, B.; Wang, B.; Fu, Y., Photocatalytic decarboxylative alkylations mediated by triphenylphosphine and sodium iodide. *Science*, **2019**, *363* (6434), 1429.

[14] Costentin, C.; Robert, M.; Savéant, J.-M., Current Issues in Molecular Catalysis Illustrated by Iron Porphyrins as Catalysts of the CO_2-to-CO Electrochemical Conversion. *Accounts of Chemical Research*, **2015**, *48* (12), 2996-3006.

[15] Li, X.; Yu, J.; Jaroniec, M.; Chen, X., Cocatalysts for Selective Photoreduction of CO_2 into Solar Fuels. *Chemical reviews*, **2019**, *119* (6), 3962-4179.

[16] Ran, J.; Jaroniec, M.; Qiao, S.-Z., Cocatalysts in Semiconductor-based Photocatalytic CO_2 Reduction: Achievements, Challenges, and Opportunities. *Advanced Materials*, **2018**, *30* (7), 1704649.

[17] Rao, H.; Schmidt, L. C.; Bonin, J.; Robert, M., Visible-light-driven methane formation from CO_2 with a molecular iron catalyst. *Nature*, **2017**, *548* (7665), 74-77.

[18] Huang, C.; Chen, C.; Zhang, M.; Lin, L.; Ye, X.; Lin, S.; Antonietti, M.; Wang, X., Carbon-doped BN nanosheets for metal-free photoredox catalysis. *Nature Communications*, **2015**, *6* (1), 7698.

[19] Kuehnel, M. F.; Orchard, K. L.; Dalle, K. E.; Reisner, E., Selective Photocatalytic CO_2 Reduction in Water through Anchoring of a Molecular Ni Catalyst on CdS Nanocrystals. *Journal of the American Chemical Society*, **2017**, *139* (21), 7217-7223.

[20] Wang, S.; Guan, B. Y.; Lou, X. W. D., Construction of $ZnIn_2S_4$-In_2O_3 Hierarchical Tubular Heterostructures for Efficient CO_2 Photoreduction. *Journal of the American Chemical Society*, **2018**, *140* (15), 5037-5040.

[21] Zheng, Y.; Lin, L.; Ye, X.; Guo, F.; Wang, X., Helical Graphitic Carbon Nitrides with Photocatalytic and Optical Activities. *Angewandte Chemie International Edition*, **2014**, *53* (44), 11926-11930.

[22] Cooper, A. I., Conjugated Microporous Polymers. *Advanced Materials*, **2009**, *21* (12), 1291-1295.

[23] Kuriki, R.; Sekizawa, K.; Ishitani, O.; Maeda, K., Visible-Light-Driven CO_2 Reduction with Carbon Nitride: Enhancing the Activity of Ruthenium Catalysts. *Angewandte Chemie International Edition*, **2015**, *54* (8), 2406-2409.

[24] Xu, Y.; Jin, S.; Xu, H.; Nagai, A.; Jiang, D., Conjugated microporous polymers: design, synthesis and application. *Chemical Society Reviews*, **2013**, *42* (20), 8012-8031.

[25] Zhao, G.; Zhou, W.; Sun, Y.; Wang, X.; Liu, H.; Meng, X.; Chang, K.; Ye, J., Efficient photocatalytic CO_2 reduction over Co(II) species modified CdS in aqueous solution. *Applied Catalysis B: Environmental Vol 226*, **2018**, 252-257.

[26] Maurin, A.; Robert, M., Noncovalent Immobilization of a Molecular Iron-Based Electrocatalyst on Carbon Electrodes for Selective, Efficient CO_2-to-CO Conversion in Water. *Journal of the American Chemical Society*, **2016**, *138* (8), 2492-2495.

[27] Liu, W.; Luo, X.; Bao, Y.; Liu, Y. P.; Ning, G.-H.; Abdelwahab, I.; Li, L.; Nai, C. T.; Hu, Z. G.; Zhao, D.; Liu, B.; Quek, S. Y.; Loh, K. P., A two-dimensional conjugated aromatic polymer via CC coupling reaction. *Nature Chemistry*, **2017**, *9* (6), 563-570.

[28] Noriega, R.; Rivnay, J.; Vandewal, K.; Koch, F. P. V.; Stingelin, N.; Smith, P.; Toney, M. F.; Salleo, A., A general relationship between disorder, aggregation and charge transport in conjugated polymers. *Nature Materials*, **2013**, *12*, 1038.

[29] Leung, J. J.; Warnan, J.; Ly, K. H.; Heidary, N.; Nam, D. H.; Kuehnel, M. F.; Reisner, E., Solar-driven reduction of aqueous CO_2 with a cobalt bis(terpyridine)-based photocathode. *Nature Catalysis*, **2019**, *2* (4), 354-365.

[30] Kresse, G.; Furthmüller, J., Efficient iterative schemes for ab initio total-energy calculations using a plane-wave basis set. *Physical Review B*, **1996**, *54* (16), 11169-11186.

[31] Kresse, G.; Hafner, J., Ab initio molecular dynamics for liquid metals. *Physical Review B*, **1993**, *47* (1), 558-561.

[32] Mathew, K.; Chaitanya Kolluru, V. S.; Mula, S.; Steinmann, S. N.; Hennig, R. G. Implicit self-consistent electrolyte model in plane-wave density-functional theory arXiv e-prints [Online], 2016. https://ui.adsabs.harvard.edu/abs/2016arXiv160103346M (accessed January 01, 2016).

[33] Mathew, K.; Sundararaman, R.; Letchworth-Weaver, K.; Arias, T. A.; Hennig, R. G., Implicit solvation model for density-functional study of nanocrystal surfaces and reaction pathways. *The Journal of Chemical Physics*, **2014**, *140* (8), 084106.

[34] Heyd, J.; Scuseria, G. E.; Ernzerhof, M., Hybrid functionals based on a screened Coulomb potential. *The Journal of Chemical Physics*, **2003**, *118* (18), 8207-8215.

[35] Perdew, J. P.; Burke, K.; Ernzerhof, M., Generalized Gradient Approximation Made Simple. *Physical Review Letters*, **1996**, *77* (18), 3865-3868.

[36] Grimme, S., Semiempirical GGA-type density functional constructed with a long-range dispersion correction. *Journal of Computational Chemistry*, **2006**, *27* (15), 1787-1799.

[37] Blöchl, P. E., Projector augmented-wave method. *Physical Review B*, **1994**, *50* (24), 17953-17979.

[38] Kresse, G.; Joubert, D., From ultrasoft pseudopotentials to the projector augmented-wave method. *Physical Review B*, **1999**, *59* (3), 1758-1775.

[39] Wang, L.; Wan, Y.; Ding, Y.; Wu, S.; Zhang, Y.; Zhang, X.; Zhang, G.; Xiong, Y.; Wu, X.; Yang, J.; Xu, H., Conjugated Microporous Polymer Nanosheets for Overall Water Splitting Using Visible Light. *Advanced Materials*, **2017**, *29* (38), 1702428.

[40] Xiang, Y.; Wang, X.; Rao, L.; Wang, P.; Huang, D.; Ding, X.; Zhang, X.; Wang, S.; Chen, H.; Zhu, Y., Conjugated Polymers with Sequential Fluorination for Enhanced Photocatalytic H2 Evolution via Proton-Coupled Electron Transfer. *ACS Energy Letters*, **2018**, *3* (10), 2544-2549.

[41] Li, H.; Shang, J.; Ai, Z.; Zhang, L., Efficient Visible Light Nitrogen Fixation with BiOBr Nanosheets of Oxygen Vacancies on the Exposed 001 Facets. *Journal of the American Chemical Society*, **2015**, *137* (19), 6393-6399.

[42] Song, H.; Meng, X.; Dao, T. D.; Zhou, W.; Liu, H.; Shi, L.; Zhang, H.; Nagao, T.; Kako, T.; Ye, J., Light-Enhanced Carbon Dioxide Activation and Conversion by Effective Plasmonic Coupling Effect of Pt and Au Nanoparticles. *ACS Applied Materials & Interfaces*, **2018**, *10* (1), 408-416.

[43] Zhang, X.-H.; Wang, X.-P.; Xiao, J.; Wang, S.-Y.; Huang, D.-K.; Ding, X.; Xiang, Y.-G.; Chen, H., Synthesis of 1,4-diethynylbenzene-based conjugated polymer photocatalysts and their enhanced visible/near-infrared-light-driven hydrogen production activity. *Journal of Catalysis*, **2017**, *350*, 64-71.

[44] Wang, K.; Yang, L.-M.; Wang, X.; Guo, L.; Cheng, G.; Zhang, C.; Jin, S.; Tan, B.; Cooper, A., Covalent Triazine Frameworks via a Low-Temperature Polycondensation Approach. *Angewandte Chemie International Edition*, **2017**, *56* (45), 14149-14153.

[45] Byun, J.; Huang, W.; Wang, D.; Li, R.; Zhang, K. A. I., CO_2-Triggered Switchable Hydrophilicity of a Heterogeneous Conjugated Polymer Photocatalyst for Enhanced Catalytic Activity in Water. *Angewandte Chemie International Edition*, **2018**, *57* (11), 2967-2971.

[46] Jiang, J.-X.; Su, F.; Niu, H.; Wood, C. D.; Campbell, N. L.; Khimyak, Y. Z.; Cooper, A. I., Conjugated microporous poly(phenylene butadiynylene)s. *Chemical Communications*, **2008**, (4), 486-488.

[47] Zhuang, X.; Zhang, F.; Wu, D.; Forler, N.; Liang, H.; Wagner, M.; Gehrig, D.; Hansen, M. R.; Laquai, F.; Feng, X., Two-Dimensional Sandwich-Type, Graphene-Based Conjugated Microporous Polymers. *Angewandte Chemie International Edition*, **2013**, *52* (37), 9668-9672.

[48] Dawson, R.; Adams, D. J.; Cooper, A. I., Chemical tuning of CO_2 sorption in robust nanoporous organic polymers. *Chemical Science*, **2011**, *2* (6), 1173-1177.

[49] Ghosh, S.; Kouamé, N. A.; Ramos, L.; Remita, S.; Dazzi, A.; Deniset-Besseau, A.; Beaunier, P.; Goubard, F.; Aubert, P.-H.; Remita, H., Conducting polymer nanostructures for photocatalysis under visible light. *Nature Materials*, **2015**, *14* (5), 505-511.

[50] Xu, Y.; Chen, L.; Guo, Z.; Nagai, A.; Jiang, D., Light-Emitting Conjugated Polymers with Microporous Network Architecture: Interweaving Scaffold Promotes Electronic Conjugation, Facilitates Exciton Migration, and Improves Luminescence. *Journal of the American Chemical Society*, **2011**, *133* (44), 17622-17625.

[51] Chen, L.; Honsho, Y.; Seki, S.; Jiang, D., Light-Harvesting Conjugated Microporous Polymers: Rapid and Highly Efficient Flow of Light Energy with a Porous Polyphenylene Framework as Antenna. *Journal of the American Chemical Society*, **2010**, *132* (19), 6742-6748.

[52] Saeki, A.; Seki, S.; Sunagawa, T.; Ushida, K.; Tagawa, S., Charge-carrier dynamics in polythiophene films studied by in-situ measurement of flash-photolysis time-resolved microwave conductivity (FP-TRMC) and transient optical spectroscopy (TOS). *Philosophical Magazine*, **2006**, *86* (9), 1261-1276.

[53] Krishnan, C. V.; Sutin, N., Homogeneous catalysis of the photoreduction of water by visible light. 2. Mediation by a tris(2,2'-bipyridine)ruthenium(II)-cobalt(II) bipyridine system. *Journal of the American Chemical Society*, **1981**, *103* (8), 2141-2142.

[54] Wang, S.; Guan, B. Y.; Lu, Y.; Lou, X. W. D., Formation of Hierarchical $In_2S_3CdIn_2S_4$ Heterostructured Nanotubes for Efficient and Stable Visible Light CO_2 Reduction. *Journal of the American Chemical Society*, **2017**, *139* (48), 17305-17308.

[55] Chen, L.; Wang, Z.; Kang, P., Efficient photoelectrocatalytic CO_2 reduction by cobalt complexes at silicon electrode. *Chinese Journal of Catalysis*, **2018**, *39* (3), 413-420.

[56] Meng, X.; Yu, Q.; Liu, G.; Shi, L.; Zhao, G.; Liu, H.; Li, P.; Chang, K.; Kako, T.; Ye, J., Efficient photocatalytic CO_2 reduction in all-inorganic aqueous environment: Cooperation between reaction medium and Cd(II) modified colloidal ZnS. *Nano Energy*, **2017**, *34*, 524-532.

[57] Guan, X.; Chen, G; Shang, C., ATR-FTIR and XPS study on the structure of complexes formed upon the adsorption of simple organic acids on aluminum hydroxide. *Journal of Environmental Sciences*, **2007**, *19* (4), 438-443.

[58] Liu, M.; Pang, Y.; Zhang, B.; De Luna, P.; Voznyy, O.; Xu, J.; Zheng, X.; Dinh, C. T.; Fan, F.; Cao, C.; de Arquer, F. P. G.; Safaei, T. S.; Mepham, A.; Klinkova, A.; Kumacheva, E.; Filleter, T.; Sinton, D.; Kelley, S. O.; Sargent, E. H., Enhanced electrocatalytic CO_2 reduction via field-induced reagent concentration. *Nature*, **2016**, *537* (7620), 382-386.

[59] Ouyang, T.; Huang, H.-H.; Wang, J.-W.; Zhong, D.-C.; Lu, T.-B., A Dinuclear Cobalt Cryptate as a Homogeneous Photocatalyst for Highly Selective and Efficient Visible-Light Driven CO_2 Reduction to CO in CH_3CN/H_2O Solution. *Angewandte Chemie International Edition*, **2017**, *56* (3), 738-743.

[60] Jiang, J.-X.; Su, F.; Trewin, A.; Wood, C. D.; Niu, H.; Jones, J. T. A.; Khimyak, Y. Z.; Cooper, A. I., Synthetic Control of the Pore Dimension and Surface Area in Conjugated Microporous Polymer and Copolymer Networks. *Journal of the American Chemical Society*, **2008**, *130* (24), 7710-7720.

[61] Ren, S.-B.; Li, P.-X.; Stephenson, A.; Chen, L.; Briggs, M. E.; Clowes, R.; Alahmed, A.; Li, K.-K.; Jia, W.-P.; Han, D.-M., 1,3-Diyne-Linked Conjugated Microporous Polymer for Selective CO_2 Capture. *Industrial & Engineering Chemistry Research*, **2018**, *57* (28), 9254-9260.

[62] Yang, C., Huang, W., da Silva, L. C., Zhang, K. A.; Wang, X. Functional conjugated polymers for CO_2 reduction using visible light. *Chemistry-A European Journal*, **2018**, *24*, 17454-17458.

[63] Zhou, M., Wang, S., Yang, P., Huang, C.; Wang, X. Boron carbon nitride semiconductors decorated with CdS nanoparticles for photocatalytic reduction of CO_2. *ACS Catalys*, **2018**, *8*, 4928-4936.

[64] Huang, C.; Chen, C.; Zhang, M.; Lin, L.; Ye, X.; Lin, S; Antonietti, M.; Wang, X. Carbon-doped BN nanosheets for metal-free photoredox catalysis. *Nature Communications*, **2015**, *6*, 7698.

[65] Lin, J., Pan, Z.; Wang, X. Photochemical reduction of CO_2 by graphitic carbon nitride polymers. *ACS Sustainable Chemistry & Engineering*, **2013**, *2*, 353-358 (2013).

[66] Qin, J., Wang, S., Ren, H., Hou, Y.; Wang, X. Photocatalytic reduction of CO_2 by graphitic carbon nitride polymers derived from urea and barbituric acid. *Applied Catalysis B: Environmental*, **2015**, *179*, 1-8.

Chapter 6 . General conclusion and future prospects

6.1 General conclusion

In this dissertation, the carrier dynamics in photocatalytic materials were evaluated using ultra-fast spectroscopy. I selected and analyzed $SrTiO_3$, a typical oxide photocatalyst, and a recently reported conjugated polymer photocatalyst as model materials. For $SrTiO_3$, the effect of La, Cr doping for the visible light response, and the loading of Pt cocatalyst for high hydrogen evolution, on the carrier dynamics in $SrTiO_3$ were evaluated. In the conjugated polymer photocatalyst, by focusing on the bonding state between component molecules and used various ultra-fast spectroscopy, the transfer process of the electrons generated in the photocatalyst was clarified and the reasonable mechanism of carbon dioxide reduction reaction has been proposed.

In Chapter 2, the measurement principle of transient absorption spectroscopy used in this study was explained. The set-up and configuration of the ns-ms transient absorption spectrometer composed of an Nd: YAG laser and Xe lump, and the ps-ns transient absorption spectrometer composed of the femtosecond titanium sapphire laser with a regenerative amplifier were introduced. In addition, some analysis methods of the obtained data were introduced, and the validity of the fitting method considering fractal kinetics mainly applied over the ns-ms transient absorption spectrometer in this study was explained.

In Chapter 3, the transient absorption measurement has been performed over La, Cr doped $SrTiO_3$, aimed at achieving a visible light response by using the ns-ms transient absorption spectrometer. In the transient absorption spectrum of undoped $SrTiO_3$, a signal derived from photo-generated holes were observed in the entire visible light range. After La doping, a signal derived from photo-generated electrons and holes were simultaneously observed in the visible light range. This suggests that the impurity level of La formed in the conduction band can capture electrons, which contributes to a longer lifetime of photoexcited carriers. Therefore, La doping was shown to be useful for improving the photocatalytic activity of $SrTiO_3$. Conversely, in the case of Cr doping, the transient absorption spectrum drastically changed because of the impurity level in the band gap formed by Cr, resulting in the transient signal derived from electron in the visible light region. Interestingly, from the transient absorption spectrum after Cr doping, the signal derived from holes originally observed in $SrTiO_3$ could not be observed. This is probably due to the fact that most of the carriers excited by ultraviolet light are from Cr impurity band, and these carriers have poor reactivity and short lifetime, so that the photocatalytic activity in the entire UV and visible region has been greatly reduced. Based on these results, in designing an oxide semiconductor with a higher photocatalytic activity while maintaining the high photocatalytic activity inherent in the

oxide semiconductor, it is not the impurity level in the band gap, but the impurity in the conduction band plays an important role. The hybridizing of the levels in the conduction band is expected to improve the photocatalytic activity in the entire ultraviolet and visible regions.

In Chapter 4, the transient absorption spectrum of $SrTiO_3$ loaded with Pt cocatalysts was measured by using the ns-μs transient absorption spectrometer. In the case of $SrTiO_3$ without Pt loading, the transient signal derived from photo-generated holes locates around 765 nm. This signal derived from holes is measured by changing the loading amount of Pt cocatalyst, and the decay constant is calculated by fitting in consideration of fractal kinetics. It was shown that the decay constant increased linearly with the increase in the Pt loading amount in N_2 and O_2 atmosphere. Furthermore by comparing to increasing rate of decay constant in Ni cocatalyst, Pt cocatalyst obviously accelerate the recombination of photogenerated charge carriers. These results indicate that the Pt cocatalysts is trapping holes on the measured time scale, which is different from the previously proposed dynamics in which only electrons move and participate in the reaction. In addition, the increasing recombination ratio retard in the presence of MeOH vapor as hole scavenger, which indicate that Pt would not act as recombination center with sacrificial reagents. Thus, Pt loaded $SrTiO_3$ exhibit outstanding photocatalytic hydrogen evolution performance among inorganic semiconductor. Furthermore, the measurement results of the ps-ns transient absorption spectrum confirmed that holes generated near the surface were trapped by the Pt cocatalyst within 400 ps. Thus, in the case of a noble metal cocatalyst such as a Pt cocatalyst, which owns a broad density of state capable of covering valence band and conduction band of an oxide semiconductor, the cocatalyst might function as a recombination center without any sacrificial reagents. In order to achieve the efficient overall water splitting, it is highly desired to design the cocatalyst with the feature of localized density of state and favorable hydrogen absorption/desorption energy.

In Chapter 5, the behavior of photo- generated electrons in a conjugated polymer photocatalyst is analyzed using ps-ns transient absorption spectrum, time-resolved microwave conductivity, and time-resolved PL spectroscopy. The process of charge transfer to carbon dioxide was discussed. From the results of time-resolved microwave spectroscopy measurement, it was found that when the alkynyl C-C bond constructs the conjugated polymer, the photoexcitation electrons are delocalized and have high mobility. Whereas the mobility of photoexcited electrons is comparably low in a conjugated polymer connected by a C-C single bond. It is predicted that this electron localization greatly assists the electron transfer from the conjugated polymer to the cocatalyst molecule due to strong interaction, and the results of ps-ns transient absorption spectroscopy show that the delocalized electrons unlikely transfer to cocatalyst, whereas conjugated polymers with localized electron start charge transfer within $\sim$5 ps. Furthermore, time-resolved PL spectroscopy measurement has performed in the presence and absence of carbon dioxide. It was observed that the decay rate of photo luminescence was drastically accelerated by consuming electrons in the carbon dioxide reduction reaction. It is obvious that elucidating the electron transfer process in the conjugated polymer will help to design a useful material among the conjugated polymers.

6.2 Future prospects

The ultra-fast spectroscopy allows us to observe the temporal event in the photoexcited state of photocatalytic materials such as oxide semiconductor and conjugated polymer photocatalysts, photovoltaic materials, photosynthetic reaction mechanisms in plants that contribute to solving environmental and energy issues. By analyzing these photoexcited state behavior, it is possible to elucidate unknown mechanisms, discover new high-speed optical functions, or achieve higher functions. However, these ultra-fast spectroscopic experiments are not widely used, and research on understanding photocatalytic reactions is not sufficient. Mentioning about the transient absorption spectroscopy, the choice of taking the time difference Δt between the pump light and the probe light must be made either optical delay or electrical trigger. In the case of optical delay for the time differentials, measurements can be made at the time resolution of fs-ps, but the time differentials must be adjusted by an optical delay path. For example, since light travels 300 mm during 1 ns, an extremely long optical delay path (1.5 m) is needed to obtain a 10 ns delay. When applying electrical trigger for the delay, the electrical signal is relatively slower than optical signal that the response speed of the signal amplifier cannot keep up with it, resulting in a time resolution of a few ns at most. While electrical trigger enable the time difference up to laser frequency. Therefore, the 3-20 ns range is used to be a blank range that disable to measure seamlessly thought fs-ms. In 2016, a computational technique called the Random Interleaved Pulse Train method (RIPT) is establishing a transient absorption spectroscopy that covers this blank range.[1] However, it is still difficult to apply it to home build TA set up. One of the advantages of the home build set-up, not only for transient absorption spectroscopy, the selection of sample holders is relatively free, it is possible to measure the in situ ultra-fast phenomena such as photoelectrochemical reactions with applying voltage, photocatalytic CO_2 reduction reaction under CO_2 gas flow and photocatalytic nitrogen fixation with N_2 gas flow in H_2O. It is expected that these in situ ultra-fast spectroscopy methods will be actively researched in the future.

References

[1] Nakagawa, T.; Okamoto, K.; Hanada, H.; Katoh, R., Probing with randomly interleaved pulse train bridges the gap between ultrafast pump-probe and nanosecond flash photolysis. *Optics. Letters*, **2016**, 41 (7), 1498-1501.

Acknowledgment

本論文は、北海道大学大学院総合化学院後期課程在籍中、葉金花教授のもとで行った研究内容により構成されています。葉金花教授には本論文作成の御指導は基より、研究の方向性や実験、データの解釈、論文投稿に至るまで、常に的確な御指摘、丁寧な御指導を賜りました。また、研究以外の生活においても多大なる御支援および御配慮頂きました事を、心より御礼申し上げます。

御多忙の中、主査として本論文を審査して頂いき、貴重な御指導・助言を賜りました村越敬教授に心より御礼を申し上げます。同じく副査として本論文を審査して頂いきました　佐田和己教授、忠永清治教授、白幡直人教授には、論文作成 にあたり詳しく御検討いただき、貴重な御教示を賜りました。ここに深く感謝いたします。葉金花研究室では、先輩・同期・後輩関係なく、研究室の皆さまから、研究を進めるにあたって様々な御支援を頂きました。特に、研究のみならず多岐にわたりご指導を賜りました加古哲也博士に深く感謝いたします。超高速分光を測定するにあたって共同研究を快く引き受けてくださり、御指導・助言を賜りました Leibniz Universität Hannover の Detlef W. Bahnemann 教授、Fabian Sieland 博士、物質・材料研究機構、機能性材料研究拠点の和田芳樹博士に深く感謝いたします。

最後に、両親には今日に至るまでの長い間、円滑に研究を行うことができる環境を整えて頂きました。以上の方々に、深く謝意を表します。

2020 年 9 月 市原　文彦